

AN ABSTRACT OF THE THESIS OF

David W. Murray for the degree of Doctor of Philosophy  
in Oceanography presented on January 30, 1987

Title: Spatial and Temporal Variations in Sediment Accumulation  
in the Central Tropical Pacific

Abstract Approved: Redacted for Privacy *by L. H. H.*  
G. Ross Heath

Pelagic tropical Pacific sites at 1° and 11°N have strikingly different Recent depositional histories. Both sites are largely supplied by biogenic remains of plankton settling through the water column and fine particles transported by winds. Although separated by only 10° of latitude, the composition of their sediments is substantially different. Site C (1°N, 139°W) is a carbonate-rich site typical of the carbonate ooze belt of the central equatorial Pacific, whereas Site S (11°N, 140°W), a siliceous clay site lacking Recent carbonate material, is typical of the region between the Clarion and Clipperton Fracture Zones where most of the world's Cu- and Ni-enriched, deep-sea ferromanganese nodules are located.

A time scale developed from oxygen isotopic stratigraphy, allows temporal and spatial variations in the accumulation of biogenic and non-biogenic sediment components at Site C to be resolved during the last 200,000 years. Changes in calcium carbonate accumulation, largely attributed to dissolution, are primarily responsible for temporal variations in bulk sedimentation. Spatial variations in sedimentation can be attributed to accelerated bottom-water flow around small bounding seamounts. Changes in calcium carbonate and aluminum accumulation in five intervals

calcium carbonate and aluminum accumulation in five intervals spanning the last 200,000 years, suggest a flow toward the east or northeast prior to 9,000 years ago with a change toward the west or southwest since that time.

Site S sediments show pronounced spatial and temporal variations in accumulation. A thin Quaternary layer (<20-cm thick) containing reworked Tertiary microfossils is found over either a unit with reworked Tertiary microfossils, a non-fossiliferous clay, or a nannofossil ooze ranging from Oligocene to early Miocene in age. A multi-tracer model that uses radionuclide and conservative tracers allows the Recent deposition at this site to be deciphered. Following a period of extensive erosion, the most recent episode of deposition began within the last 130,000 years. A factor of three increase in accumulation during the Holocene is evident in cores from the deepest basin in the site. An increase in the input of both Recent opaline material and reworked Tertiary sediments can explain the near-surface concentration changes. More than 50% of the concentration of some elements can be traced to a Tertiary source.

The ratio of water column fluxes measured in sediment traps to sediment accumulation rates provides an estimate of the magnitude of recycling of bioactive components in the lower water column and near-surface sediments. At Site C, a simple mass balance calculation forms the basis for this comparison, whereas at Site S, erosion and redeposition of older material must be taken into account before realistic estimates of modern recycling can be derived.

SPATIAL AND TEMPORAL VARIATIONS IN SEDIMENT ACCUMULATION  
IN THE CENTRAL TROPICAL PACIFIC

by

David W. Murray

A THESIS

submitted to

Oregon State University

in partial fulfillment of  
the requirements for  
the degree of

Doctor of Philosophy

Completed January 30, 1987

Commencement June 1987

APPROVED:

Redacted for Privacy

\_\_\_\_\_  
Professor of Oceanography in charge of major

Redacted for Privacy

\_\_\_\_\_  
Dean of College of Oceanography

Redacted for Privacy

\_\_\_\_\_  
Dean of Graduate School

Date thesis is presented January 30, 1987

Typed by David W. Murray and Jackie Poppleton

I dedicate this thesis to my Grandfather Murray.

"Pop" took an interest in my education at an early age  
and provided support, encouragement and bribes along the way.

## ACKNOWLEDGEMENT

Many thanks go to my major professor, Ross Heath, for his advice and support along the way. The guidance of Nick Pias, my unofficial co-major professor, was instrumental in this work. Both advisors have been an inspiration to me. I thank the rest of my committee, Larry Small, Van Volk and David Thomas for their help during the thesis work.

Mitch Lyle provided the groundwork for much of this study and I appreciate his contributions and valuable insights. Jack Dymond freely supplied sediment trap samples and data. His fine group, headed by Chris Moser, provided the technical support for the collection of these unique samples. David Kadko provided the original version of the sedimentation model, the nuclide data for the Site S study, and my support for the last two years. Oxygen and carbon isotope data for 14 GC were generated by Warren Prell, and Mitch Lyle furnished organic carbon data for this core. Dave Rea kindly made the RC11-210 data available prior to publication. Alan Mix supplied preliminary foram data from Site C sediment traps, and Roger Mahanah phoned "hot-off-the-counter" thorium data to me.

Reliable XRF data was produced through a major effort by Greg Campi. Jim Robbins, Andy Ungerer, Bobbi Conard, Cydne Perhats, Pat Collier, and Dick Kovar all helped with laboratory procedures and analyses. I hope the OSU faculty realize their immense value as analysts, technicians, and human beings (Pat may not qualify for the latter). Bill Rugh deserves credit for trouble-shooting and fixing sick equipment. I thank the "girls" in Nick's lab: Pat,

Charlene, Adrienne, Katy, Johanna, Martha, and Stacy, who assisted and tolerated me. Julie Borden was an immense help with the XRD work. Dave Reinert, Pat Collier, Emily Verplanck, Annette deCharon, and Marta vonBreyman all helped with drafting. Special thanks to Emily for her last minute work before the defense. Deadlines could not have been met without the rapid processing of my Federal Express packages by Jackie Poppleton and Annette. Thanks to Jackie for her help in preparing the final version of this thesis.

To the faculty, staff, and graduate students in the College of Oceanography, friends in Corvallis, friends who have moved on and MANOP participants who, over the years, enriched my scientific and social life, a sincere THANKS!!! Special thanks to: my office-mate, Marta, who provided me with a chemist's view of marine geology and much needed help and friendship along the way; Todd, Gina and Caleb, who provided a wonderful home life; John, who endured a year on the farm and introduced me to rugby and the "European way"; Bruce, whose friendship and insights on science, flyfishing, soccer, poker, canoeing, squash, and women, are greatly appreciated; Ian, who tackled the resuspension problem among other things; Kris, who corrected my letters; and Dave D., Anne, and Becky who gave me support from afar.

Finally, love and encouragement from Annette kept me going during the final stages. Her help is greatly appreciated.

This research was supported by NSF grants OCE-84-15723-01 and ATM-83-19731-01.

## TABLE OF CONTENTS

	GENERAL INTRODUCTION .....	1
CHAPTER I	A HIGH RESOLUTION RECORD OF SEDIMENT ACCUMULATION IN THE CENTRAL EQUATORIAL PACIFIC DURING THE LAST 200,000 YEARS .....	4
	ABSTRACT .....	5
	INTRODUCTION .....	7
	MATERIALS .....	8
	SEDIMENT ACCUMULATION RATES .....	11
	Concentration .....	11
	Sedimentation Rates .....	15
	Sediment Density .....	27
	RESULTS AND DISCUSSION .....	34
	Sediment Accumulations .....	34
	Calcium Carbonate .....	34
	Opal .....	43
	Organic Carbon .....	46
	Non-Biogenic Components .....	50
	Sediment - Sediment Trap Comparison .....	67
	Input to the Sediments .....	68
	Sediment Trap - Sediment Calibration .....	77
	Temporal Estimates of Benthic Recycling ..	79
	Calcite Storage .....	84
	SUMMARY AND CONCLUSIONS .....	92
	REFERENCES .....	95
CHAPTER II	SPATIAL VARIATIONS IN SEDIMENT ACCUMULATION AT MANOP SITE C, CENTRAL EQUATORIAL PACIFIC: EVIDENCE FOR EASTWARD FLOWING BOTTOM-WATERS PRIOR TO 9,000 YEARS AGO .....	107
	ABSTRACT .....	108
	INTRODUCTION .....	109



	SITE DESCRIPTION .....	113
	METHODS .....	118
	Solid Phase Chemistry .....	118
	Correlations .....	119
	Accumulation Rates .....	126
	RESULTS .....	127
	DISCUSSION .....	145
	CONCLUSIONS .....	153
	REFERENCES .....	154
CHAPTER III	WATER COLUMN WEIGHT FLUXES OF OPAL AND CALCAREOUS MICROFOSSILS IN THE CENTRAL EQUATORIAL PACIFIC: PALEO- OCEANOGRAPHIC IMPLICATIONS .....	157
	ABSTRACT .....	158
	INTRODUCTION .....	160
	METHODS .....	164
	RESULTS AND DISCUSSION .....	169
	Characteristics of the Flux .....	169
	Partitioning the Flux into Plankton Groups .....	174
	Water Column Weight Fluxes of Microfossils .....	176
	Comparison of Trap Fluxes and Sediment Accumulations .....	184
	CONCLUSIONS .....	195
	REFERENCES .....	197
CHAPTER IV	SEDIMENT ACCUMULATION AT MANOP SITE S, CENTRAL TROPICAL PACIFIC: LOCAL REWORKING AND A LATE QUATERNARY INCREASE IN SEDI- MENT ACCUMULATION .....	200
	ABSTRACT .....	201
	INTRODUCTION .....	202
	SITE DESCRIPTION .....	204

METHODS .....	211
RESULTS AND DISCUSSION .....	214
Facies Compositions .....	214
Sedimentation Model .....	229
Application of Model .....	243
Sediment Trap - Surface	
Sediment Comparison .....	268
CONCLUSIONS .....	270
REFERENCES .....	271
BIBLIOGRAPHY .....	275
APPENDICES .....	292
APPENDIX I .....	292
APPENDIX II .....	326
APPENDIX III .....	340
APPENDIX IV .....	342

# LIST OF FIGURES

## CHAPTER I

<u>Figure</u>	<u>Title</u>	<u>Page</u>
I-1	Bathymetry at MANOP Site C based on 12 kHz records obtained during OSU cruise W8402A and a Deep-Tow Survey .....	9
I-2	Downcore records of calcium carbonate concentration (%) for (A) 14 GC and (B) RC11-210 versus depth sub-bottom (cm). <u>G. tumida</u> $\delta^{18}\text{O}$ versus depth for (C) 14 GC and (D) RC11-210 .....	21
I-3	(A) Results of the correlation of $\delta^{18}\text{O}$ records from RC11-210 and 14 GC to the reference stack. (B) Record of calcium carbonate concentration in RC11-210 and 14 GC based on correlations in Figure I-3A. (C) Calcium carbonate concentration versus age (kyr) for 14 GC .....	24
I-4	Comparison of dry bulk density measured from volumetric ring samples ( $\text{g cm}^{-3}$ ) versus dry bulk density ( $\text{g cm}^{-3}$ ) calculated from salt content of the sample using the equation of Kominz et al. (1979) .....	29
I-5	Dry bulk density ( $\text{g cm}^{-3}$ ) calculated from calcium carbonate content (%) based on equations of Luz and Shackleton (1974), Lyle and Dymond (1976), and this study .....	32
I-6	Downcore record of accumulation in $\text{mg cm}^{-2} \text{ kyr}^{-1}$ of (A) calcium carbonate, (B) opal, (C) organic carbon, (E) manganese versus age (kyr). The profile of organic carbon corrected for the calcium carbonate content is also given (D) .....	35
I-7	Downcore record of accumulation in $\text{mg cm}^{-2} \text{ kyr}^{-1}$ of (A) aluminum, (B) barium, (C) titanium, (D) phosphorus, and (E) iron versus age (kyr) .....	37

<u>Figure</u>	<u>Title</u>	<u>Page</u>
I-8	(A) Variance and coherency spectra calculated between calcium carbonate accumulation and the oxygen isotope record of Imbrie et al. (1984). (B) Phase spectrum of carbonate accumulation versus the $\delta^{18}\text{O}$ record .....	40
I-9	Solid phase record of opal accumulation ( $\text{mg cm}^{-2} \text{ kyr}^{-1}$ ) versus sub-bottom depth for the upper section of core 14 GC. The average pore water profile for silica ( $\mu\text{mole kg}^{-1}$ , at Site C is also shown .....	44
I-10	Ratio of predicted organic carbon concentration for a constant primary productivity of $46 \text{ gC (m}^{-2}\text{y}^{-1})$ to the measured concentration in 14 GC versus age (kyr) .....	48
I-11	Iron versus aluminum from Site C sediment trap and BNTH III 11 box core samples .....	54
I-12	Accumulation ( $\text{mg cm}^{-2} \text{ kyr}^{-1}$ ) versus age (kyr) of total iron partitioned into detrital and excess phases .....	56
I-13	Partitioning of total phosphorus accumulation ( $\text{mg cm}^{-2} \text{ kyr}^{-1}$ ) versus age (kyr) into fractions associated with calcium carbonate, oxyhydroxides, and residual .....	61
I-14	Partitioning of total titanium accumulation ( $\text{mg cm}^{-2} \text{ kyr}$ ) versus age ( $\text{kyr}^{-1}$ ) into fractions associated with detrital, oxyhydroxides, and residual .....	64
I-15	Bulk flux ( $\text{mg cm}^{-2} \text{ kyr}^{-1}$ ) measured by two sediment trap deployments at MANOP Site C .....	71
I-16	Extrapolated flux of calcium carbonate, opal, and organic carbon ( $\mu\text{g cm}^{-2} \text{ yr}^{-1}$ ) to the sediment water interface from the two experiments at MANOP Site C .....	75
I-17	Opal rain rate ( $\text{mg cm}^{-2} \text{ kyr}^{-1}$ ) predicted from Broecker and Peng (1982; eq. 2-4) versus age (kyr) .....	82

<u>Figure</u>	<u>Title</u>	<u>Page</u>
I-18	Calcium carbonate accumulation ( $\text{mg cm}^{-2} \text{ kyr}^{-1}$ ) versus age (kyr) for cores (A) 14 GC and (B) RC11-210 .....	85
I-19	Isopleths of calcium carbonate accumulation ( $\text{mg cm}^{-2} \text{ kyr}^{-1}$ ) for the area bounded by 0-5°N and 130-155°W using cores shown in (A) for (B) Recent; carbonate-poor, (C) 10-64 kyr; carbonate-rich, and (D) 64-120 kyr; carbonate-poor .....	88
CHAPTER II		
II-1	Bathymetry of MANOP Site C constructed from 12 kHz records obtained during the W8402A cruise .....	110
II-2	Correlations based on color changes .....	116
II-3	Calcium carbonate concentration (%) versus sub-bottom depth (cm) for seven Site C cores in addition to nearby core RC11-210 .....	121
II-4	(A) Calcium carbonate concentration (%) versus age (kyr) for cores W8402A 14 GC, BENTHIC III 21 GC, BENTHIC III 25 GC, and K7905 16 GC. (B) As A, but for cores W8402A 14 GC, BENTHIC III 18 GC, BENTHIC III 12 GC, and RAMA I 6 GC .....	124
II-5	Manganese concentration (%) versus age (kyr) in Site C cores .....	130
II-6	Contoured maps of sediment thickness between correlated horizons .....	132
II-7	Sediment thickness (cm) contours in a distance from 4000 m bathymetric contour versus water depth (m) coordinate system .....	134
II-8	Aluminum and calcite accumulation rate excess or deficit in selected cores relative to 14 GC during five time intervals over the last 200 kyr .....	138

<u>Figure</u>	<u>Title</u>	<u>Page</u>
II-9	Calcium carbonate accumulation rate versus water depth for five selected time intervals during the last 200 kyr .....	142
II-10	(A) Calcite to aluminum ratio for eroded or excess material corrected for dissolution for five intervals in Site C cores spanning the last 200 kyr. (B) As A, but not corrected for calcite dissolution ...	146
II-11	Depths in Site C cores (cm) versus corre- sponding depth in 14 GC (cm) .....	151
CHAPTER III		
III-1	Sea-surface temperature (°C) at MANOP Site C (1°N, 139°W) for 1983 and 1984 .....	161
III-2	Partitioning of the calcium carbonate, opal and residual fluxes ( $\mu\text{g cm}^{-2} \text{ yr}^{-1}$ ) in nine sampling intervals from two sedi- ment trap deployments at MANOP Site C into four size fractions; <38, 38-63, 63- 150, and >150 $\mu\text{m}$ .....	170
III-3	Percent of total opal and calcium car- bonate contained in four size fractions for each sample .....	172
III-4	Calcite/opal flux ratio in site fractions; <38 $\mu\text{m}$ , 38-63, 63-150, and >150 $\mu\text{m}$ .....	182
III-5	A comparison of calcium carbonate flux ( $\mu\text{g cm}^{-2} \text{ yr}^{-1}$ ) between the time weighted mean of the two trap deployments and sedi- ment samples .....	186
III-6	Record of calcium carbonate accumulation ( $\text{mg cm}^{-2} \text{ kyr}^{-1}$ ) during the last 450 kyr for cores (A) W8402A 14 GC and (B) RC11-210 ....	188
III-7	A comparison of the time weighted mean opal flux ( $\mu\text{g}\cdot\text{cm}^{-2} \text{ yr}^{-1}$ ) measured in two sediment trap deployments to opal accumula- tion in sediments from MANOP Site C .....	192

<u>Figure</u>	<u>Title</u>	<u>Page</u>
CHAPTER IV		
IV-1	Bathymetry of MANOP Site S constructed from data obtained during cruises MN75-05 and MN76-01 (Karas, 1978) with additional 12 kHz data from the W8402A cruise .....	205
IV-2	Schematic W-E profile across Site S, for the area below 4800 m, illustrating the stratigraphic relationship of Units 1-4 .....	208
IV-3	Downcore profile of selected solid-phase components in addition to % illite/% smectite ratio and % Quaternary radiolarians for core K7905 82 GC .....	216
IV-4	Downcore profiles of opal, manganese, % illite/% smectite and % Quaternary radiolarians from representative box cores located in the central basin .....	218
IV-5	Downcore profiles of opal, manganese, % illite/% smectite and % Quaternary radiolarians for core BENTHIC III 31 BC .....	220
IV-6	Downcore profiles of selected solid-phase components for core K7905 97 GC .....	222
IV-7	Downcore profiles of calcium carbonate, opal, manganese, % illite/% smectite and % Quaternary radiolarians from core K7905 106 BC .....	224
IV-8	Schematic diagram of sedimentation modified from Kadko (1983) .....	231
IV-9	Modelled profiles of a nuclide (A) and a conservative tracer (B) showing the impact of duration of sedimentation .....	234
IV-10	Parameters as Figure IV-9, but duration is held constant at 150 kyr and S, the sedimentation rate, varies as indicated .....	236
IV-11	Parameters as Figure IV-9, but duration is held constant at 150 kyr and E, erosion rate, varies as indicated .....	238

<u>Figure</u>	<u>Title</u>	<u>Page</u>
IV-12	Modelled profiles for a nuclide with a 75 kyr half-life. (A) shows variations in the mixing depth, L; (B) shows variations in the rate of mixing .....	240
IV-13	Downcore profiles of (A) $^{230}\text{Th}$ and $^{231}\text{Pa}$ , (B) manganese, (C) opal and (D) Quaternary and Tertiary radiolarians in the top 25 cm of basin box core K7905 47 BC .....	246
IV-14	Observed and modelled $^{230}\text{Th}$ and $^{231}\text{Pa}$ profiles from core K7905 47 BC .....	248
IV-15	Observed and modelled Tertiary and Quaternary radiolarian profiles from basin core K7905 47 BC .....	251
IV-16	Modelled manganese profile showing partitioning of box core K7905 47 BC sediments into Recent and reworked Tertiary contributions .....	254
IV-17	Modelled profile showing partitioning of box core K7905 47 BC sediments into Recent and reworked Tertiary material .....	257
IV-18	Modelled aluminum profile showing partitioning of box core K7905 47 BC sediments into Recent and reworked Tertiary material .....	260
IV-19	Observed and modelled: (A) $^{230}\text{Th}$ and $^{231}\text{Pa}$ , (B) manganese and (C) radiolarian concentration profiles for core BENTHIC III 31 BC .....	263
IV-20	Observed and modelled profiles of (A) $^{230}\text{Th}$ and $^{231}\text{Pa}$ and (B) radiolarian concentration for core K7905 106 BC from the western flank of the Site S basin .....	266



# LIST OF TABLES

## CHAPTER I

<u>Table</u>	<u>Title</u>	<u>Page</u>
I-1	Bulk chemistry in wt % for W8402A 14 GC samples - salt corrected; measured by X-ray fluorescence unless noted .....	12
I-2	W8402A 14 GC data; depth, age, sedimentation rate, $\delta C^{13}$ , $\delta O^{18}$ , salt content, water content and dry bulk density .....	16
I-3	Ages of datums .....	19
I-4	Sediment trap fluxes and surface sediment accumulation .....	59

## CHAPTER II

II-1	Gravity Cores from MANOP Site C .....	112
II-2	Coherencies of the correlations to 14 GC .....	123
II-3	Depths of Correlated Horizons (cm) .....	128
II-4	Aluminum Budget .....	140
II-5	Calcium Carbonate Budget .....	141

## CHAPTER III

III-1	Sediment trap fluxes and surface sediment accumulation .....	165
III-2	Size fraction fluxes ( $\mu g \cdot cm^{-2} \cdot yr^{-1}$ ) for the average trap and surface sediments .....	177

<u>Table</u>	<u>Title</u>	<u>Page</u>
CHAPTER IV		
IV-1	Cores from MANOP Site S .....	215
IV-2	Mean Composition of Tertiary Facies .....	227
IV-3	Model Parameters which result in profile "a" of sensitivity tests .....	242
IV-4	Sediment trap fluxes at MANOP Site S, 3400 m level .....	244

# SPATIAL AND TEMPORAL VARIATIONS IN SEDIMENT ACCUMULATION IN THE CENTRAL TROPICAL PACIFIC

## GENERAL INTRODUCTION

Sediment accumulation in the tropical Pacific is largely the result of particulate settling through the water column, degradation and decomposition of the biogenic components within the water column and/or sediments, and erosion and redeposition of sediment components. Recently, large integrated projects, such as the Manganese Nodule Program (MANOP), have tried to assemble the necessary data to estimate the magnitude of these fluxes and processes which ultimately determine the rates of accumulation and composition of the preserved sediment record. An understanding of the present relationship between the water column particle flux, benthic regeneration, and surficial sediment accumulations should provide a basis for estimating past changes in the water column flux from the sediment record.

The focus of this study is to provide solid phase chemical data from sediments at two pelagic sites, which can be compared to measurements of the water column particle rain rates. Temporal records of sediment accumulation are interpreted as variations in this relationship. This thesis is divided into four chapters. In the first three chapters, sedimentation at MANOP Site C, a carbonate-rich site typical of the carbonate ooze belt of the central equatorial Pacific, is examined. The last chapter gives the results of a study of sedimentation at MANOP Site S, a siliceous

clay site characteristic of the region between the Clarion and Clipperton Fracture Zones.

The temporal variations at Site C are examined in Chapter I. A high-resolution time scale based on oxygen isotopic stratigraphy is developed for the past 200,000 years, and the records of accumulation for various biogenic and non-biogenic components are determined. A comparison is made between the water column flux and the preserved record to estimate the magnitude of benthic recycling of calcium carbonate, opal and organic carbon.

Chapter II presents the spatial pattern of deposition within two carbonate-rich and two carbonate-poor intervals, in addition to the Recent period of deposition. Bulk chemical data are used to separate total sediment accumulation variations due to carbonate solution from other processes.

The present relationship between the siliceous and carbonate components of the water column flux and the accumulation in underlying sediments is examined in Chapter III. The flux is separated into contributions from zooplankton and phytoplankton remains, and the seasonal change in the magnitude of these fluxes is determined.

In the final chapter, a multi-tracer approach is used to decipher sedimentation at MANOP Site S, where a lateral source of eroded material is input to the surface sediments in addition to the vertical rain rate. The inputs of Quaternary opal and carbonate are compared to measured sediment trap fluxes to estimate the magnitude of benthic recycling of these components.

Nick Pisias, Mitch Lyle and G. Ross Heath share authorship in Chapters I, II and IV. All three were involved in generating and interpreting solid phase elemental data from MANOP Sites C and S. Jack Dymond and Warren Prell, who supplied sediment trap and oxygen isotope data, respectively, share authorship on Chapter I. Nick Pisias furnished sediment trap samples for plankton analysis and is a co-author on Chapter III. David Kadko, a co-author on Chapter IV, provided nuclide data for Site S cores and collaborated on the modelling.

## CHAPTER I

# A HIGH RESOLUTION RECORD OF SEDIMENT ACCUMULATION IN THE CENTRAL EQUATORIAL PACIFIC DURING THE LAST 200,000 YEARS

## ABSTRACT

The existence of a reference high resolution oxygen isotope stratigraphy (Imbrie et al., 1984), allows relatively high frequency changes in pelagic sedimentation during the last 200 kyr at MANOP Site C (1°N, 139°W) to be defined. This site is characteristic of the central equatorial Pacific carbonate ooze belt. Calcite is the dominant sediment component. Changes in its rate of accumulation largely control total sedimentation rates in the study area. A factor of four variation in accumulation rates between carbonate-rich and -poor intervals marks glacial and interglacial stages, respectively. The primary cause of the variation is changes in dissolution. Cross-spectral analysis of calcium carbonate accumulation rates and the oxygen isotopic values at Site C suggests that sea level variations associated with the waxing and waning of continental ice sheets are responsible for much of the variation in the pelagic record of calcium carbonate dissolution.

The large variations in calcite accumulation recorded at Site C represent changes in the amount of calcite removed from the oceanic system. Using calcite accumulation records in 12 cores from the central tropical Pacific, we estimate that an additional 3.4% of the present river input is stored in this region during carbonate-rich periods compared to carbonate-poor intervals.

Unexpectedly, the records of biogenic carbonate, opal, and organic carbon are not correlated. High opal accumulation at 5-15 kyr and 130-145 kyr reflects enhanced preservation of the remains of siliceous phytoplankton. A minimum in opal accumulation at

30-60 kyr corresponds to a carbonate-rich interval. The absence of significant downcore variations in the organic carbon record suggests that the reliability of this component as a recorder of paleoproductivity at Site C is not understood.

The rates of accumulation of non-biogenic components are indicative of more than one source. An aluminosilicate (detrital) fraction is inversely correlated with sedimentation rate and accumulated most rapidly during glacial stage 4. Phosphorus, titanium, iron, and manganese have a source that is acquired in the lower water column or at the sediment-water interface. Their deposition is highly correlated with the rate of calcium carbonate accumulation. The distribution of manganese is attributed of post-depositional remobilization which has produced a number of peaks downcore.

The long term sediment accumulation rate data are complemented by sediment-trap flux data which can be used to estimate benthic fluxes of labile components and thereby aid in the interpretation of the geologic record. The fluxes of detrital Al, Fe, and Mn in the traps and surface sediments are comparable. However, we find that 60-62% of the calcium carbonate, 89-92% of the opal, 98-99% of the organic carbon, and 55% of the primary barium fluxes are recycled in the lower water column and surficial sediments. Increases in the present-day opal and carbonate fluxes to the sediments rather than just enhanced preservation are required to account for their downcore maximum accumulation rates.



## INTRODUCTION

The sediments in the central equatorial Pacific consist largely of the calcium carbonate skeletal remains of coccolithophores and foraminifera. The opaline tests of diatoms and radiolarians are of secondary importance. Terrigenous clay material generally contributes less than 10% by weight of these sediments. Variations in the relative proportions of the three components which are commonly observed over short intervals are thought to be related to paleoceanographic changes either in the production of biogenic detritus in the upper water column or in the corrosiveness of bottom waters.

Large-amplitude cycles in calcium carbonate concentration, attributed mostly to dissolution and roughly corresponding to glacial/interglacial periods, have been well documented in sediments from this region (i.e., Arrhenius, 1952; Hays et al., 1969; Berger, 1973, Valencia, 1977). Owing to the dominance of calcite in these sediments, variations of most non-carbonate components are inverse to those of the carbonate, thereby raising the concern that they may reflect only calcite dilution. By expressing downcore compositional changes as mass fluxes, the dependence upon calcium carbonate is ameliorated. In earlier studies, the resolution of such flux changes has been limited by the lack of a detailed history of sedimentation rate variations. From the recently developed high-resolution oxygen isotope stratigraphy for the late Pleistocene (Imbrie et al., 1984), however, sedimentation rate changes within glacial/interglacial cycles can be determined.

Already, Boyle (1983) has demonstrated that high resolution accumulation (mass flux) records of non-carbonate chemical components in the eastern equatorial Pacific record recent climatic fluctuations.

In this study, we focus on sediment accumulation during the last 200 kyr at a site in the central equatorial Pacific. To aid in interpreting the temporal record of accumulation, sediment trap data available for the site are used to quantify the relationship between the flux of material to the sediment-water interface and the sediment accumulation rate. By calibrating the modern sediment record against the water column flux, downcore accumulation changes can be directly related to temporal variations in the flux to the sediment-water interface. These results can help define elemental cycling and removal within glacial and interglacial oceans.

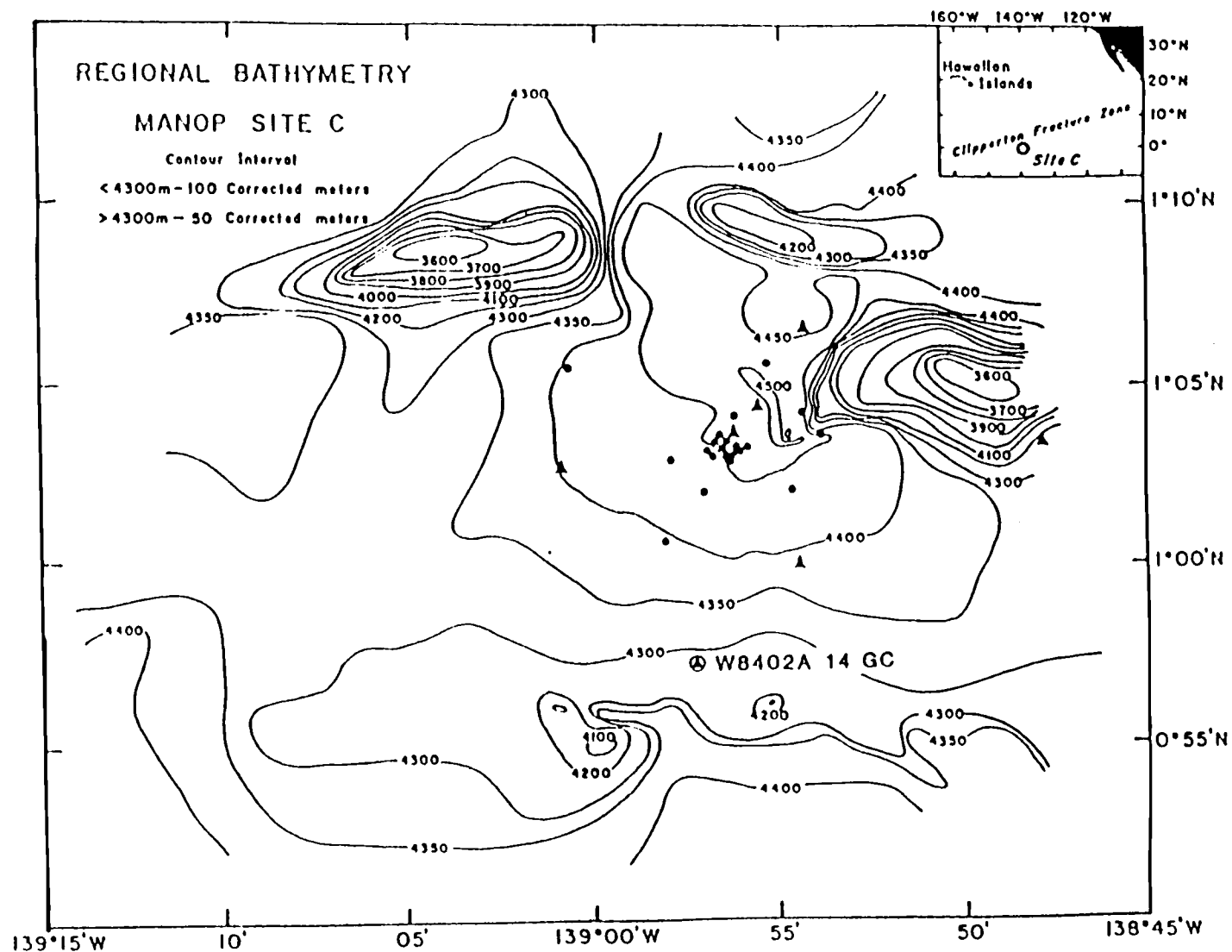
#### MATERIALS

During the Manganese Nodule Project (MANOP), 28 gravity cores were collected from Site C (1°N, 139°W) in the carbonate ooze province of the central equatorial Pacific (Figure I-1). All of the cores show "Pacific-type" carbonate variations in which preservation is enhanced during glacial periods (Arrhenius, 1952; Hays et al., 1969). Core W8402A 14 GC (0° 57.2'N, 138° 57.3'W) from the Oregon State University collection was selected for detailed chemical and oxygen isotopic analysis, because it is from the shallowest location (4287 m), has the thickest carbonate-rich and -poor sections, and exhibits no major disturbances (see Chapter II).

Figure I-1

Bathymetry at MANOP Site C based on 12 kHz records obtained during OSU cruise W8402A and a Deep-Tow Survey (Spiess and Weydert, 1984). Gravity core locations are indicated by dots and triangles.

Figure I-1



## SEDIMENT ACCUMULATION RATES

Elemental mass accumulation rates for the sediments are calculated from the equation  $A = C \times D \times S$  where A is the accumulation rate in  $\text{mg} \cdot \text{cm}^{-2} \text{ kyr}^{-1}$ , C is the concentration in  $\text{mg} \cdot \text{g}^{-1}$ , D is the dry weight per wet sediment volume (dry bulk density) in  $\text{g} \cdot \text{cm}^{-3}$  and S is the sedimentation rate in  $\text{cm} \cdot \text{kyr}^{-1}$ . The following sections document the determination of C, D, and S.

Concentration

Elemental concentrations listed in Table I-1 were determined using a wavelength dispersive Phillips P.W. 1600 simultaneous X-ray fluorescence (XRF) spectrometer. The samples were freeze dried and ground into a fine powder by shaking with methacrylate spheres in polycarbonate sample tubes. Approximately 2.5 g of sample were pressed at 5 tons pressure into XRF discs with a cellulose backing. Samples were kept in a dessicator prior to analysis to prevent rehydration. Each batch of 18 samples was analyzed using an internal monitor to check for instrument drift and a USGS standard to check for accuracy between runs.

The spectrometer is controlled by a Digital Equipment Corp. PDP 11/34 minicomputer which also runs the data collection and reduction programs. A fundamental parameters program developed by Criss Software Inc. (c.f. Criss et al., 1978) in addition to a background stripping program developed at Oregon State University is used for the data reduction (G. Campi, written comm.). A set of 64 rock and sediment standards from the U.S. Geological Survey,

Table I-1. Bulk chemistry in wt % for W8402A 14 GC samples - salt corrected;  
measured by X-ray fluorescence unless noted.

Depth (CM)	Al	Si	P	Ca	Ti	Mn	Fe	Sr	Ba	Opal	CaCO <sub>3</sub>	CaCO <sub>3</sub> LECO	C-org LECO	Sum of oxides
0.5	0.4898	7.9940	0.0416	30.5373	0.0348	0.1812	0.4065	0.1273	0.1995	15.1	76.2	79.82	0.304	97.2
3.5	0.4791	8.1044	0.0401	30.8898	0.0324	0.1616	0.3793	0.1216	0.1847	15.5	77.1	81.98	0.252	98.2
6.5	0.4296	7.8760	0.0373	31.0174	0.0327	0.1515	0.3621	0.1241	0.1796	15.4	77.5	81.39	0.231	97.5
9.5	0.3645	7.9592	0.0345	31.1870	0.0302	0.1433	0.3292	0.1221	0.1554	16.3	77.9	83.05	0.226	98.1
12.5	0.3130	7.4818	0.0321	31.9054	0.0320	0.2336	0.3013	0.1223	0.1525	15.6	79.7	84.13	0.182	98.7
15.5	0.3070	7.0678	0.0310	32.3188	0.0291	0.1428	0.2990	0.1235	0.1339	14.5	80.8	88.09	0.182	98.6
18.5	0.3115	5.4732	0.0300	33.3423	0.0299	0.2638	0.2983	0.1257	0.1353	10.5	83.4	91.00	0.152	97.8
21.5	0.3093	5.0862	0.0305	33.2009	0.0285	0.5945	0.2783	0.1249	0.1236	9.6	83.0	89.08	0.152	97.2
24.5	0.2802	4.9583	0.0284	33.8782	0.0284	0.2530	0.2814	0.1255	0.1090	9.6	84.7	92.63	0.205	98.0
27.5	0.3101	5.3687	0.0317	33.6881	0.0290	0.2744	0.2970	0.1257	0.1244	10.3	84.2	91.41	0.180	98.6
30.5	0.3056	4.9005	0.0310	33.9832	0.0301	0.0570	0.3101	0.1264	0.1205	9.2	85.0	91.81	0.345	97.9
33.5	0.3169	3.7426	0.0306	34.8418	0.0293	0.0665	0.3075	0.1279	0.1165	6.2	87.2	92.27	0.289	97.6
36.5	0.3167	3.6875	0.0301	34.6648	0.0278	0.0617	0.3072	0.1266	0.1152	6.0	86.7	91.92	0.246	97.0
39.5	0.3101	3.5547	0.0298	34.9373	0.0299	0.0615	0.3024	0.1276	0.1140	5.7	87.4	94.94	0.214	97.3
45.5	0.3261	3.5597	0.0298	34.8875	0.0312	0.0730	0.3081	0.1276	0.1184	5.6	87.3	90.66	0.162	97.3
51.5	0.3061	3.4694	0.0292	34.8450	0.0292	0.0707	0.3087	0.1292	0.0973	5.6	87.2	92.28	0.135	96.9
57.5	0.2285	2.9053	0.0260	35.3079	0.0275	0.0658	0.2736	0.1264	0.0782	5.0	88.4	95.60	0.110	96.4
63.5	0.2168	3.0042	0.0280	35.3312	0.0269	0.0705	0.2618	0.1273	0.0729	5.4	88.4	92.13	0.101	96.7
69.5	0.2375	2.8401	0.0262	35.0302	0.0281	0.0777	0.2666	0.1297	0.0729	4.7	87.7	93.20	0.101	95.6
75.5	0.2375	2.5694	0.0260	35.7158	0.0262	0.0879	0.2750	0.1313	0.0660	4.0	89.4	93.70	0.084	96.7
81.5	0.2296	2.9738	0.0248	34.8483	0.0274	0.0911	0.2679	0.1288	0.0778	5.2	87.2	93.27	0.111	95.5
87.5	0.2375	3.1881	0.0255	34.8274	0.0270	0.0847	0.2645	0.1272	0.0753	5.5	87.1	93.36	0.113	95.9
90.5	0.2703	3.2421	0.0288	34.8408	0.0277	0.0743	0.2832	0.1292	0.0821	5.4	87.2	92.99	0.130	96.1
93.5	0.2238	2.0875	0.0253	35.5077	0.0285	0.0810	0.2587	0.1280	0.0664	3.0	88.9	95.19	0.092	95.1
96.5	0.2384	2.4550	0.0271	35.3603	0.0268	0.0799	0.2715	0.1287	0.0677	3.7	88.5	94.14	0.108	95.7
99.5	0.2524	2.6549	0.0298	35.1707	0.0271	0.0759	0.2805	0.1287	0.0703	4.1	88.0	92.89	0.154	95.7
102.5	0.2819	3.2743	0.0298	34.5625	0.0276	0.0883	0.2985	0.1266	0.0833	5.6	86.5	91.15	0.142	95.6
105.5	0.3758	3.5453	0.0337	34.1980	0.0321	0.1008	0.3458	0.1261	0.1062	5.1	85.5	90.61	0.187	95.8
108.5	0.4748	4.5300	0.0356	33.5158	0.0360	0.1088	0.4005	0.1257	0.1471	6.6	83.8	88.49	0.202	96.7
111.5	0.6884	6.3499	0.0436	31.2610	0.0401	0.1406	0.5136	0.1216	0.1909	9.0	78.1	83.02	0.158	96.0
114.5	0.7126	6.5674	0.0445	31.0332	0.0415	0.1622	0.5371	0.1221	0.2226	9.3	77.5	82.10	0.107	96.0
117.5	0.9407	7.9426	0.0502	29.1837	0.0463	0.1839	0.6452	0.1152	0.2799	10.4	72.8	79.14	0.176	95.4
120.5	1.1892	9.5179	0.0578	28.2524	0.0533	0.2393	0.7489	0.1115	0.3534	11.9	70.4	74.96	0.130	97.7
123.5	1.0017	8.2033	0.0490	29.0490	0.0467	0.1700	0.6552	0.1125	0.2972	10.5	72.5	77.65	0.100	95.9
126.5	0.8339	7.0668	0.0434	30.2560	0.0448	0.1367	0.5859	0.1180	0.2601	9.3	75.5	78.98	0.112	95.5
129.5	0.8553	7.3749	0.0446	29.9895	0.0454	0.1014	0.5844	0.1151	0.2565	9.9	74.8	80.64	0.121	95.8
131.5	0.9149	7.8159	0.0463	29.6094	0.0448	0.1086	0.6125	0.1141	0.2615	10.3	73.9	78.10	0.125	95.9
134.5	0.8471	7.8532	0.0443	29.6900	0.0446	0.1364	0.5847	0.1140	0.2641	11.2	74.1	80.28	0.086	96.0

Table I-1 ... continued

Depth (CM)	Al	Si	P	Ca	Ti	Mn	Fe	Sr	Ba	Opal	CaCO <sub>3</sub>	CaCO <sub>3</sub> LECO	C-org LECO	Sum of oxides
138.5	0.9758	9.0427	0.0450	28.7432	0.0465	0.1697	0.6353	0.1101	0.3054	12.8	71.7	78.40	0.094	96.7
141.5	1.0621	10.2575	0.0468	27.1852	0.0487	0.1484	0.6940	0.1080	0.3383	15.0	67.7	71.73	0.105	95.8
144.5	0.9025	8.8478	0.0450	28.9778	0.0454	0.1223	0.6155	0.1130	0.2939	13.1	72.3	77.78	0.098	96.5
147.5	0.8693	8.7862	0.0442	28.9857	0.0429	0.0804	0.5947	0.1144	0.2877	13.3	72.3	73.93	0.156	96.2
150.5	0.7964	8.1845	0.0429	29.8052	0.0441	0.1402	0.5565	0.1156	0.2819	12.4	74.4	81.18	0.152	96.7
153.5	0.9183	9.2324	0.0460	28.5736	0.0468	0.1724	0.6149	0.1142	0.3158	13.9	71.2	80.29	0.180	96.5
156.5	1.0857	10.9407	0.0528	26.8768	0.0510	0.2135	0.6903	0.1107	0.3722	16.5	66.9	76.68	0.122	96.7
159.5	0.9808	10.5782	0.0492	27.3715	0.0467	0.2186	0.6278	0.1102	0.3255	16.4	68.2	75.08	0.125	96.7
162.5	0.9865	12.3395	0.0487	26.0351	0.0448	0.2696	0.6210	0.1075	0.3420	21.0	64.8	71.92	0.116	97.3
165.5	0.7517	10.7451	0.0424	28.1396	0.0386	0.3929	0.4793	0.1145	0.2811	19.3	70.1	76.50	0.167	98.3
168.5	0.6541	8.6973	0.0403	29.2760	0.0366	0.3766	0.4300	0.1154	0.2322	15.2	73.0	81.62	0.161	96.3
171.5	0.5603	7.1245	0.0367	30.7877	0.0332	0.4839	0.3672	0.1195	0.1868	12.2	76.9	83.66	0.166	96.3
174.5	0.4733	6.9315	0.0335	30.8915	0.0329	0.4571	0.3250	0.1208	0.1514	12.5	77.1	85.14	0.155	95.7
177.5	0.4478	7.2960	0.0327	30.8384	0.0328	0.3025	0.3220	0.1202	0.1556	13.8	77.0	84.63	0.119	96.0
180.5	0.3831	8.0398	0.0306	30.3685	0.0308	0.2642	0.2979	0.1183	0.1479	16.3	75.8	83.21	0.155	96.2
183.5	0.3866	8.5969	0.0301	30.3524	0.0287	0.2336	0.2787	0.1159	0.1254	17.6	75.8	84.04	0.171	97.2
187.5	0.3920	8.8535	0.0305	30.8283	0.0294	0.1956	0.2753	0.1171	0.1249	18.2	77.0	83.67	0.172	98.9
189.5	0.3983	7.9297	0.0300	31.5230	0.0286	0.0950	0.2942	0.1148	0.1230	15.8	78.7	83.09	0.158	98.6
195.5	0.3788	5.9764	0.0317	32.4189	0.0298	0.1627	0.3399	0.1181	0.1187	11.1	81.0	86.50	0.165	96.9
201.5	0.3582	7.8728	0.0322	30.9641	0.0281	0.1737	0.2898	0.1161	0.1242	16.1	77.3	84.48	0.127	97.1
207.5	0.3516	8.0439	0.0319	30.6674	0.0268	0.0995	0.3006	0.1155	0.1118	16.6	76.6	84.86	0.172	96.6
213.5	0.4289	5.5660	0.0352	32.2605	0.0310	0.1421	0.3474	0.1227	0.1115	9.6	80.6	79.79	0.146	95.6
219.5	0.3805	5.4602	0.0343	32.6651	0.0311	0.0919	0.3552	0.1233	0.1161	9.9	81.6	85.94	0.173	96.1
225.5	0.3963	6.1220	0.0342	31.8448	0.0338	0.0860	0.3645	0.1236	0.1422	11.3	79.6	85.74	0.184	95.5
231.5	0.4017	6.4269	0.0337	31.6708	0.0335	0.0816	0.3739	0.1250	0.1405	12.1	79.1	89.58	0.243	95.8
237.5	0.3793	4.4715	0.0360	32.9854	0.0345	0.0953	0.3828	0.1314	0.1460	7.4	82.5	89.04	0.131	94.7
243.5	0.4678	4.9409	0.0388	32.0833	0.0369	0.3123	0.4312	0.1273	0.1600	7.7	80.2	84.85	0.133	94.1
249.5	0.5957	6.4173	0.0425	30.4820	0.0426	0.4678	0.5082	0.1245	0.2249	10.0	76.1	82.70	0.203	94.1
254.5	1.0585	10.9258	0.0545	25.7646	0.0567	0.0861	0.8369	0.1149	0.3760	16.7	64.1	73.76	0.227	93.9
261.5	1.4562	13.6498	0.0650	23.4856	0.0678	0.0773	1.0204	0.1065	0.4862	19.5	58.3	64.02	0.363	95.8
267.5	1.4694	14.0378	0.0630	23.1151	0.0678	0.0773	0.9990	0.1070	0.4906	20.4	57.4	63.63	0.473	95.6
273.5	0.8179	7.8123	0.0467	29.3424	0.0460	0.1006	0.5951	0.1265	0.2940	11.4	73.2	81.08	0.200	94.8
279.5	0.5832	6.1198	0.0395	31.0281	0.0362	0.0993	0.4681	0.1288	0.2068	9.5	77.5	84.45	0.117	94.2
283.5	0.5048	4.4851	0.0378	32.2155	0.0333	0.1189	0.4223	0.1327	0.1712	7.4	80.5	89.73	0.139	94.4
291.5	0.5804	5.8936	0.0434	30.9792	0.0355	0.4643	0.4424	0.1287	0.1947	8.8	77.4	83.99	0.119	94.2
297.5	0.5829	5.9494	0.0392	31.5201	0.0347	0.0951	0.4451	0.1289	0.1909	9.0	78.7	86.61	0.150	95.0
303.5	0.6946	8.6135	0.0419	29.4691	0.0378	0.0798	0.4872	0.1251	0.2434	14.5	73.5	78.57	0.187	96.3
309.5	0.4149	4.1986	0.0368	33.2016	0.0309	0.0966	0.3624	0.1320	0.1273	6.3	83.0	91.33	0.112	94.8
315.5	0.3633	4.1958	0.0356	32.9727	0.0325	0.2358	0.3308	0.1318	0.1083	6.9	82.4	91.34	0.108	94.1

National Bureau of Standards, Canada, and France, as well as in-house clay standards are used to calibrate the data reduction program. The precision for the reported elements is within 3% and, except for chlorine, accuracies are within 7%.

Calcium carbonate and organic carbon concentrations were measured using the wet oxidation LECO technique described by Weliky et al. (1983). This method assumes that calcium carbonate is the dominant carbonate phase in the samples. Acetic acid leach studies of Site C sediments confirms this assumption (Lyle, unpublished data). Calcium carbonate concentrations determined by LECO and Ca measured by atomic absorption spectrometry (AAS) are systematically 5-7% higher than those calculated from the XRF data. Both LECO and XRF concentrations are reported in Table I-1. The XRF values are used to calculate the calcium carbonate fluxes reported in this study.

Opal concentrations were determined by a normative calculation based on a detrital Si/Al ratio of 4:1. This value was determined by leaching the opal-Si from 11 Site C samples with a hot 2 M  $\text{Na}_2\text{CO}_3$  solution. The difference between the total Si (XRF) and opal-Si values yields residual Si values that are approximately four times the Al concentrations in the same samples; i.e.,  $\text{total Si} - \text{opal-Si} = 4.0 \times \text{Al}$ . We assume that this fraction consists of Si in detrital clay minerals and quartz. Since quartz comprises a significant portion of the terrigenous detritus in this region (Moore and Heath, 1978; Leinen et al., 1986) our ratio is higher than those which consider only the Si contained in clay minerals (Leinen, 1977; Dymond, 1981). We also assume that biogenic opal is



14.3% water (i.e.,  $\text{SiO}_2(\text{H}_2\text{O})_{0.56}$ ). This value is obtained from van Bennekom and van der Gaast's (1976) data by assuming that the weight loss on ignition is due to organic matter and the bound water in opal.

All concentrations reported are salt corrected. The reported salt contents (Table I-2) were determined by multiplying adjusted chlorine concentrations by 1.715, the ratio of Cl to total salt in seawater with a salinity of 34.7‰. Chlorine was adjusted because salt contents calculated from raw Cl (XRF) values were 32% higher than those calculated from weight loss due to drying. Fischer (1983) found good agreement between INAA measured Cl and Cl determined from weight loss measurements for sediment trap samples. Her results and our observation that the Cl discrepancy is not evident in samples low in calcium carbonate (see Chapter IV) suggest that Ca is interfering with the Cl determinations in carbonate-rich samples, and form the basis for decreasing Cl-based salt concentrations by 32% in this data set. Additionally, the reported concentrations of Ca and Sr have been corrected for sea-salt contributions.

#### Sedimentation Rates

A number of methods have been employed to determine sedimentation rates in carbonate-rich sediments from the tropical Pacific. The most common approach is to identify dated horizons and assume a constant sedimentation rate between them. Hays et al. (1969), for example, identified the Brunhes-Matuyama boundary in their cores and assumed a constant rate of sedimentation for the last 700 kyr.

Table I-2. W8402A 14 GC data; depth, age, sedimentation rate,  $\delta C^{13}$ ,  $\delta O^{18}$ , salt content, water content, and dry bulk density.

Depth (cm)	Age kyr	Sed. Rate $\text{cm} \cdot \text{kyr}^{-1}$	$\delta C^{13}$ ‰	$\delta O^{18}$ ‰	Salt %	H <sub>2</sub> O %	Dry Density $\text{g} \cdot \text{cm}^{-3}$
0.5	0.30	1.690	1.50	0.06	5.6	62.7	0.494
3.5	2.07	1.690	1.51	0.00	5.0	60.0	0.545
6.5	3.85	1.690	1.57	-0.03	4.6	57.7	0.584
9.5	5.62	1.690	1.40	0.06	4.9	59.4	0.554
12.5	7.40	1.680	1.47	0.06	4.6	57.8	0.584
15.5	9.19	1.690	1.23	0.21	4.5	57.2	0.594
18.5	10.95	1.700	1.22	0.43	4.2	55.9	0.628
21.5	12.72	1.669	1.23	0.67	4.1	55.2	0.641
24.5	14.50	1.690	1.19	0.58	4.1	55.0	0.641
27.5	16.26	1.690	1.23	1.04	4.1	54.9	0.641
30.5	18.05	1.681	1.26	1.17	4.1	55.2	0.641
33.5	19.83	1.714	1.38	1.10	4.0	54.5	0.653
36.5	21.55	1.734	1.44	1.09	3.8	52.9	0.680
39.5	23.29	1.673	1.51	0.92	3.8	52.8	0.680
45.5	26.93	1.674	1.66	0.94	3.6	51.3	0.709
51.5	30.46	1.765	1.62	0.82	3.6	51.5	0.709
57.5	33.73	1.884	1.47	0.77	3.3	49.2	0.757
63.5	36.83	1.951	1.47	0.54	3.4	50.4	0.740
69.5	39.88	1.970	1.46	0.52	3.3	49.5	0.757
75.5	42.92	2.013	1.32	0.44	3.1	47.7	0.793
81.5	45.84	2.076	1.44	0.41	3.4	49.8	0.740
87.5	48.70	2.098	1.39	0.54	3.3	49.6	0.757
90.5	50.13	2.055	1.58	0.44	3.4	49.9	0.740
93.5	51.62	2.020	1.43	0.31	3.2	48.8	0.775
96.5	53.10	2.062	1.43	0.44	3.3	49.7	0.757
99.5	54.53	2.083	1.42	0.57	3.3	49.2	0.757
102.5	55.98	1.980	1.46	0.80	3.3	49.7	0.757
105.5	57.56	1.802	1.47	0.71	3.4	50.3	0.740
108.5	59.31	1.662	1.31	0.69	3.6	51.9	0.709
111.5	61.17	1.583	1.47	0.92	4.0	54.1	0.653
114.5	63.10	1.515	1.61	0.92	4.1	54.8	0.641
117.5	65.13	1.425	1.71	1.25	4.4	56.9	0.605
120.5	67.31	1.367	1.87	1.12	4.9	59.5	0.554
123.5	69.52	1.345	1.77	0.73	4.6	57.7	0.584
126.5	71.77	1.302	1.71	0.53	4.1	54.9	0.641
129.5	74.13	1.259	1.62	0.13	4.3	56.3	0.617
131.5	75.74	1.217	1.55	0.20	4.3	56.2	0.617
134.5	78.24	1.155	1.51	0.29	4.2	55.7	0.628
138.5	81.80	1.082	1.59	0.22	4.3	56.0	0.617
141.5	84.71	0.974	1.63	0.41	4.5	57.5	0.594
144.5	87.96	0.984	1.63	0.37	4.3	56.1	0.617

Table I-2 ... continued

Depth (cm)	Age kyr	Sed. Rate cm·kyr <sup>-1</sup>	$\delta C^{13}$ ‰	$\delta O^{18}$ ‰	Salt %	H <sub>2</sub> O %	Dry Density g·cm <sup>-3</sup>
147.5	90.81	0.968	1.54	0.14	4.5	57.1	0.594
150.5	94.16	0.846	1.45	0.11	4.1	55.3	0.641
153.5	97.90	0.775	1.45	0.48	4.3	56.2	0.617
156.5	101.90	0.732	1.40	0.22	4.7	58.3	0.573
159.5	106.10	0.741	1.41	0.32	4.5	57.5	0.594
162.5	110.00	0.822	1.47	0.46	5.0	60.2	0.545
165.5	113.40	0.909	1.24	0.24	4.8	59.0	0.564
168.5	116.60	0.937	1.13	0.56	4.4	56.6	0.605
171.5	119.80	0.952	1.14	0.26	4.0	54.0	0.653
174.5	122.90	1.017	1.09	0.28	3.9	53.8	0.666
177.5	125.70	1.091	1.04	0.25	3.9	54.0	0.666
180.5	128.40	1.200	1.17	0.74	4.3	55.9	0.617
183.5	130.70	1.346	1.23	0.94	4.2	55.8	0.628
187.5	133.60	1.364	1.27	0.82	3.9	54.0	0.666
189.5	135.10	1.404	1.25	1.01	3.9	53.7	0.666
195.5	139.30	1.481	1.22	0.85	4.0	54.4	0.653
201.5	143.20	1.644	1.23	0.95	4.3	55.9	0.617
207.5	146.60	1.690	1.19	0.84	4.2	55.8	0.628
213.5	150.30	1.579	1.14	1.21	3.9	53.9	0.666
219.5	154.20	1.558	1.25	1.01	4.2	55.7	0.628
225.5	158.00	1.538	1.30	0.71	4.2	55.4	0.628
231.5	162.00	1.446	1.22	0.61	4.3	56.5	0.617
237.5	166.30	1.304	1.16	0.51	3.5	51.2	0.724
243.5	171.20	1.188	1.22	0.81	3.8	53.0	0.680
249.5	176.40	1.111	1.30	0.90	4.2	55.7	0.628
254.5	181.10	1.008	1.19	1.06	6.1	65.0	0.459
261.5	188.30	0.935	1.46	0.83	6.8	67.6	0.416
267.5	195.00	0.863	1.49	0.58	7.1	68.6	0.400
273.5	202.20	0.839	1.48	0.49	4.4	56.9	0.605
279.5	209.30	0.862	1.52	0.47	3.9	53.4	0.666
283.5	213.80	0.902	1.24	0.54	3.6	51.9	0.709
291.5	222.60	0.927	1.33	1.00	4.0	54.3	0.653
297.5	228.90	1.000	1.39	0.92	4.3	56.2	0.617
303.5	234.60	1.062	1.29	0.87	5.4	62.1	0.510
309.5	240.20	1.017	1.24	0.47	3.5	51.2	0.724
315.5	246.40	0.984	1.26	0.68	3.6	51.4	0.709

Thompson and Saito (1974) showed, by identifying additional stratigraphic levels, that sedimentation rates in core RC11-210 were not uniform during this period. Thompson and Saito (1974) and, more recently Gardner (1982) and Rea (1982), still assume a constant rate of sedimentation through at least one cycle of calcite variation, however. This assumption forces artificial changes in the magnitude of the accumulation rates of the various sediment components. In particular, it requires an increase in non-carbonate accumulation rates during periods when the concentration of calcium carbonate was low.

Arrhenius (1952), Pisias (1976), and Kominz et al. (1979) developed time scales for carbonate-rich cores from the assumption that a particular sediment component accumulated at a constant rate. In such models, analytical data can be used to generate high-resolution sedimentation rates profiles, which do not depend directly on carbonate variations. The profiles are accurate, however, only to the extent that the assumption of a constant input is valid. For example, the time scale of Arrhenius (1952) for central Pacific carbonate variations, which assumes a constant input of titanium, gives ages for carbonate transitions that are 60-80 kyr older than those which are based on the global oxygen isotope stratigraphy (i.e., Hays et al., 1969; see Table I-3). Adjustment of the flux of Ti would yield better agreement, but would also yield Ti accumulation rates, an order of magnitude higher than expected for this region (Bostrom et al., 1973).

Boyle (1983) used a linear relationship between the aluminum accumulation rate and the Ti/Al ratio to obtain a high resolution

Table I-3. Ages of Datums.

CaCO <sub>3</sub> Transitions: See Figure I-2							
	<sup>14</sup> GC	RC11-210	Ave	Broecker (1971)	Hays et al. (1969)	Luz and Shackleton (1975)	Arrhenius (1952)
1	9.1	12.4	10.8	11	10	--	10
2	63.1	64.2	63.7	75	75	63	90
3	118	123	121	127	130	109	160
4	171	187	183	--	170	--	270
5	200	211	206	--	200	--	330
= = = = =							

Oxygen isotope datums: Imbrie et al. (1984) terminology

	<sup>14</sup> GC	RC11-210	Ave	Imbrie et al. (1984)	Martinson et al. (in press)	Morley & Hays (1981)	Shackleton & Opdyke (1973)
1.1	3.6	2.6	3.2	6	2.3	--	--
2.0	12.7	11.5	12.1	12	12.1	11	13
2.2	18.1	16.7	17.4	19	17.9	--	--
3.0	27.0	28.5	27.8	24	24.1	27	32
3.3	51.6	61.0	56.3	53	50.2	--	--
4.0	59.0	62.8	60.9	59	59.0	58	64
4.2	65.0	64.6	64.8	65	64.1	--	--
5.0	69.5	73.0	71.7	71	73.9	72	75
6.0	128.0	129.0	128.5	128	129.8	128	128
6.4	150.3	153.6	152.0	151	152.6	--	--
6.5	166.3	164.0	165.1	171	175.1	--	--
6.6	182.0	172.0	177.0	183	183.3	--	--
7.0	188.0	--	--	186	189.6	--	--
7.4	222.6	--	--	228	224.9	--	--
7.5	240.2	--	--	238	240.2	--	--

record of the accumulation rates of various components in core V19-29. The Ti/Al fluctuations are attributed to changes in the intensity of eolian transport at this site (3°35'S, 83°56'W). Because of the decreasing resolution of this transport signal away from land, however, such a technique has limited applicability in the central equatorial Pacific.

More recently, a high resolution time scale has been developed for the temporal variations in the oxygen isotopic composition of seawater as recorded in foraminiferal shells (Imbrie et al., 1984). We have used this oxygen isotope stratigraphy to establish a high resolution time scale for core W8402A 14 GC (14 GC). This method permits variations in sedimentation rate within a single carbonate cycle, since the time scale is independent of carbonate variations. It is, of course, necessary to assume that the reference time scale for oxygen isotope variations is valid and that the oxygen isotopic variations in foraminiferal shells are dominated by global ice volume changes.

An oxygen isotope record from the planktic foraminiferan Globorotalia tumida (355-500  $\mu\text{m}$ ) was obtained for 14 GC. Samples were taken at 3-6 cm intervals (Figure I-2) and analyses were made at Brown University using a VG Sira 24 mass spectrometer (Table I-2). The precision of the data is  $\pm 0.11\text{‰}$ . A similar isotope record was obtained for the nearby 14 m long core RC11-210 (1°49'N, 140° 03'W; 4420 m) using a sample spacing of 8-10 cm. For this core, analyses were performed at the Stable Isotope Laboratory, Department of Geological Science, University of Michigan, under the direction of K.C. Lohmann. The precision for the data are

Figure I-2

Downcore records of calcium carbonate concentration (%) for (A) 14 GC and (B) RC11-210 versus depth sub-bottom (cm). G. tumida  $\delta^{18}\text{O}$  versus depth for (C) 14 GC and (D) RC11-210. Positive  $\delta^{18}\text{O}$  values increase to top of page. Circled  $\delta^{18}\text{O}$  value in RC11-210 record is considered anomalous. Age for noted transitions and isotopic events are given in Table I-3.

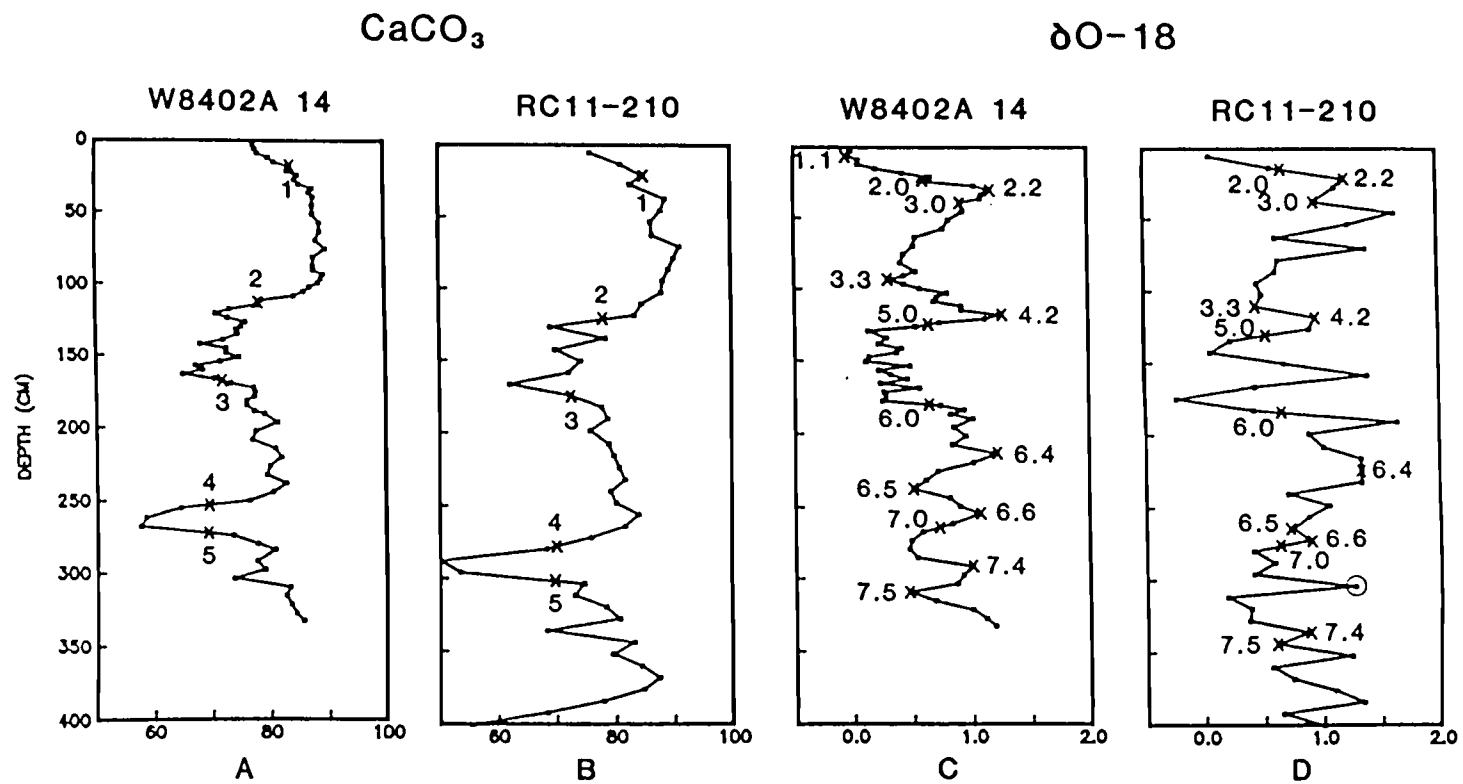


Figure I-2



$\pm 0.08\text{‰}$ . The calcium carbonate content of the RC11-210 samples was determined by the carbonate bomb volumetric technique (Chuey et al., in prep.). For the stratigraphic interval common to both cores, the RC11-210 calcium carbonate and oxygen isotope data display the same cycles as those found in 14 GC (Figure I-2).

Age scales were assigned to the two cores by independently correlating their oxygen isotope records to the SPECMAP stack (Imbrie et al., 1984), using the signal correlation technique of Martinson et al. (1982; Figure I-3). A careful application of the Martinson et al. technique is required to avoid anomalous stretching and squeezing of the records. This is due, in part, to the poor resolution of the records from RC11-210 and 14 GC (i.e., stages 5 and 7, Figure I-2) and differences in the amplitude of particular isotopic events in these cores and in the reference stack. The signal correlation technique is very sensitive to the amplitude differences and the correlation of each core to the reference stack produces records with major hiatuses and intervals of rapid accumulation. We have no other evidence that such events occurred in the central equatorial Pacific and view these results as anomalous.

To avoid this problem, an age scale was developed for RC11-210 using age picks for 17 isotopic events during the last 780 kyr and assuming a linear rate of sedimentation between events. With this age scale as an initial estimate of the correlation between RC11-210 and the reference stack, and 21 coefficients to define the

Figure I-3

(A) Results of the correlation of  $\delta^{18}\text{O}$  records from RC11-210 (large dash) and 14 GC (small dash) to the reference stack (solid). RC11-210 and 14 GC records in per mil variations with positive values increasing toward top of page. Reference stacked record of Imbrie et al. (1984) expressed in standard deviation units about a mean of zero (scale on right side of diagram). (B) Record of calcium carbonate concentration (%) in RC11-210 (dashed) and 14 GC (solid) based on correlations in Figure I-3A. (C) Calcium carbonate concentration (%) versus age (kyr) for 14 GC. Ages based on a constant rate of titanium accumulation (long dash), constant aluminum accumulation (small dash) and  $\delta^{18}\text{O}$  correlation to reference isotope record (solid). The age model of constant titanium accumulation is used as the initial approximation in developing the mapping function for the correlation of 14 GC to the reference stack. See text for discussion.

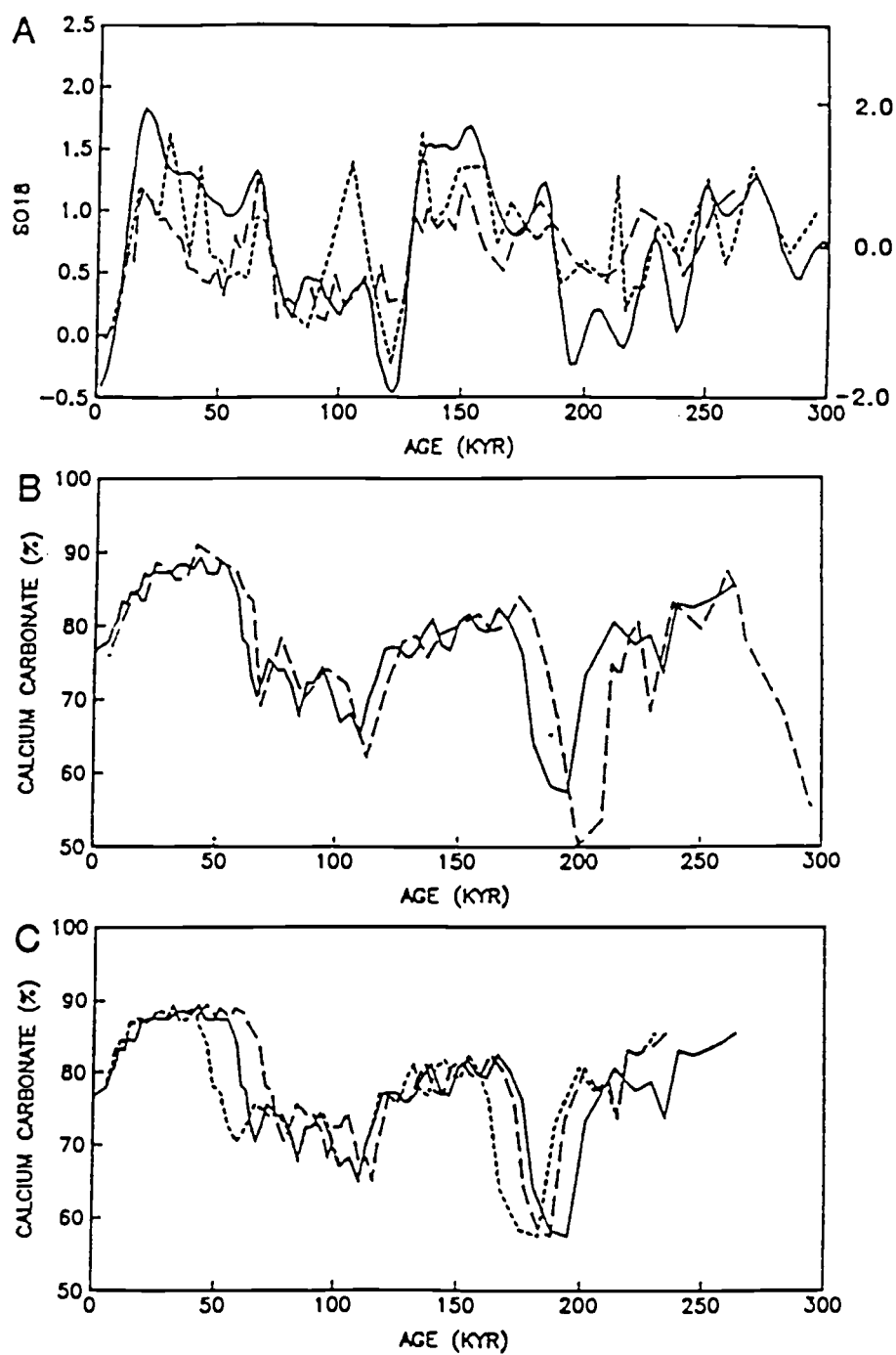


Figure I-3

mapping function, an age model was assigned to RC11-210. In this study we present the last 230 kyr (Figure I-3).

A preliminary age scale for 14 GC was constructed assuming a constant accumulation rate for titanium (Figure I-3). This time scale is used as an initial approximation to develop the mapping function for the correlation of 14 GC to the reference stack. To obtain a correlation map for the last 230 kyr in 14 GC, maintaining the same resolution as in RC11-210, six coefficients were used to define the mapping function. A similar time scale was obtained using a constant accumulation of Al as an initial age approximation for the correlation of 14 GC to the reference stack. The continuous mapping function obtained from the Martinson et al. technique provides an age estimate for each level in 14 GC. Sedimentation rates at each sample depth were derived from the differences in depth and age of the adjacent samples (Table I-2). Because of the poor stratigraphic control near the top of the core, the sedimentation rate for the upper 10 cm (last 6,000 years) is assumed to be constant.

The time scale estimates for both 14 GC and RC11-210 produce a major discrepancy between the carbonate records of the cores at approximately 180 kyr (Figure I-3). This can be attributed partly to the poor isotopic control within isotope stage 7 for both RC11-210 and 14 GC. Correlation of the carbonate records in the two cores does not resolve the problem because such a correlation produces an even larger discrepancy in the oxygen isotope records. The difference cannot be resolved with the present data set. The age pick for the carbonate minimum is  $195 \pm 8$  kyr. Although off-

set, the carbonate-poor interval spans approximately 20 kyr in each record (Figure I-3B). Based on both carbonate and oxygen isotope data sets, the maximum time length of the interval may be 25% larger and the corresponding sedimentation rates may be 25% lower than our estimated values. Consequently, only accumulation rate variations in excess of 25% are considered significant in the lower section of 14 GC.

A similar age discrepancy near 120 kyr affects the age of the high to low carbonate transition in early isotope stage 5. An average age for the transition is  $118 \pm 5$  kyr. Ages of selected datums from both the isotope and carbonate records are listed in Table I-3 for comparison with earlier studies.

#### Sediment Density

Physical property measurements were not available for all samples but the salt content of each sample was measured. Therefore, dry bulk densities (Table I-2) were calculated using the equation of Kominz et al. (1979):

$$\text{bulk density (g}\cdot\text{cm}^{-3}) = \frac{1-x}{27.85x + (1-x)/2.7}$$

where  $x$  is the weight fraction of salt in the sample and 27.85 is the conversion from g salt/g sample to  $\text{cm}^3$  seawater/g sample, assuming a salinity of 34.7‰. The inferred particle density of  $2.7 \text{ g}\cdot\text{cm}^{-3}$  is reasonable for the Site C sediments. Furthermore, the calculation is much more sensitive to the salt content changes than it is to variations in the particle density. A comparison

between dry bulk densities measured by calculating the dry weight in a known ring volume and those calculated from the salt contents is given in Figure I-4. Although the variances between the two methods are not significantly different, the 5% difference between the means is statistically significant. This difference is attributed to the fact that the Kominz et al. equation adjusts for the salt content of a sample whereas this correction has not been applied to the densities measured by the ring method. The equation based on the salt content of a sample is appropriate in our study where the elemental data has been salt corrected.

In a later section of this paper, dry bulk densities are required for samples where neither physical property nor salt contents are available. Luz and Shackleton (1975) and Lyle and Dymond (1976) have published equations for determining dry bulk densities from calcium carbonate contents. These equations are not based on a large number of high carbonate samples and we propose that they are not the best predictors of dry bulk density in the equatorial Pacific carbonate ooze belt. Therefore, we have derived a new empirical relation to predict dry bulk density from carbonate content using available data from all the cores taken at Site C. The regression equation:

$$\text{Dry bulk density (g}\cdot\text{cm}^{-3}) = \frac{1}{4.207 - (3.395 \times \% \text{CaCO}_3 / 100)}$$

is based on a data set containing 192 dry bulk density values measured by the volumetric ring method including 14 values from Lyle and Dymond (1976). The correlation coefficient for the

Figure I-4

Comparison of dry bulk density measured from volumetric ring samples ( $\text{g cm}^{-3}$ ) versus dry bulk density ( $\text{g cm}^{-3}$ ) calculated from salt content of the sample using the equation of Kominz et al. (1979). A total of 178 samples from MANOP Site C were used. The dashed line represents a 1:1 correlation.

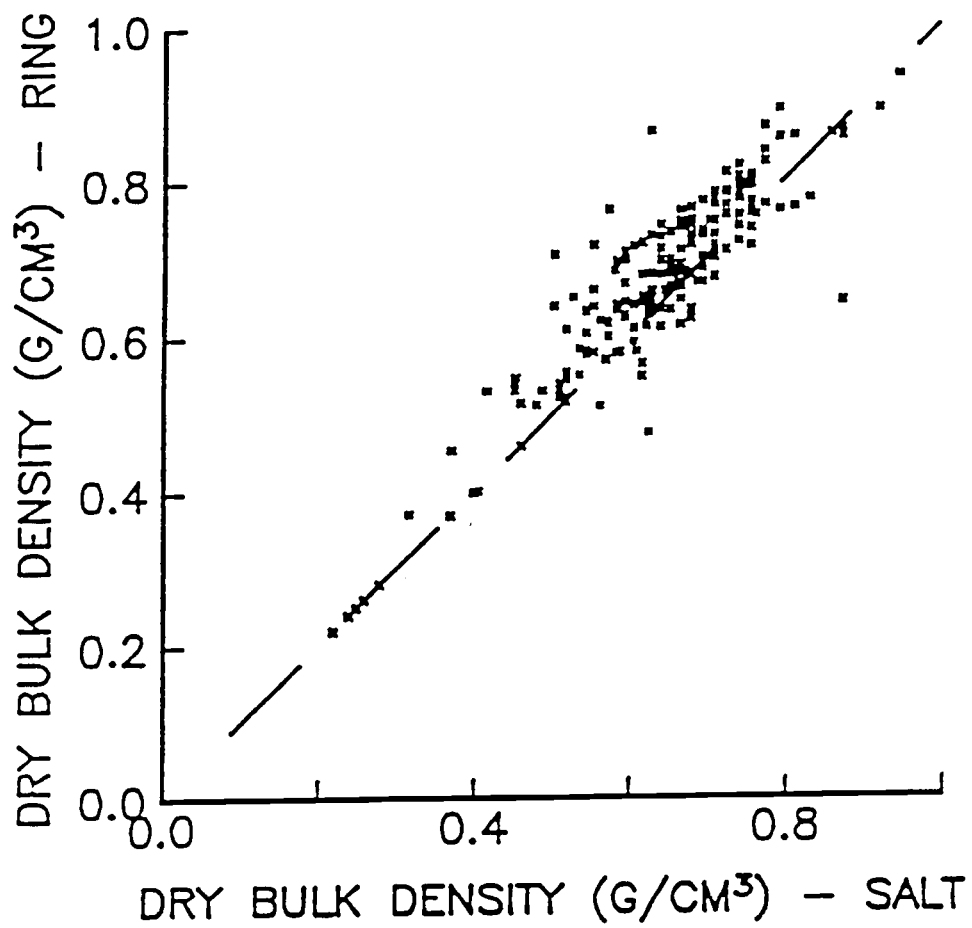


Figure I-4

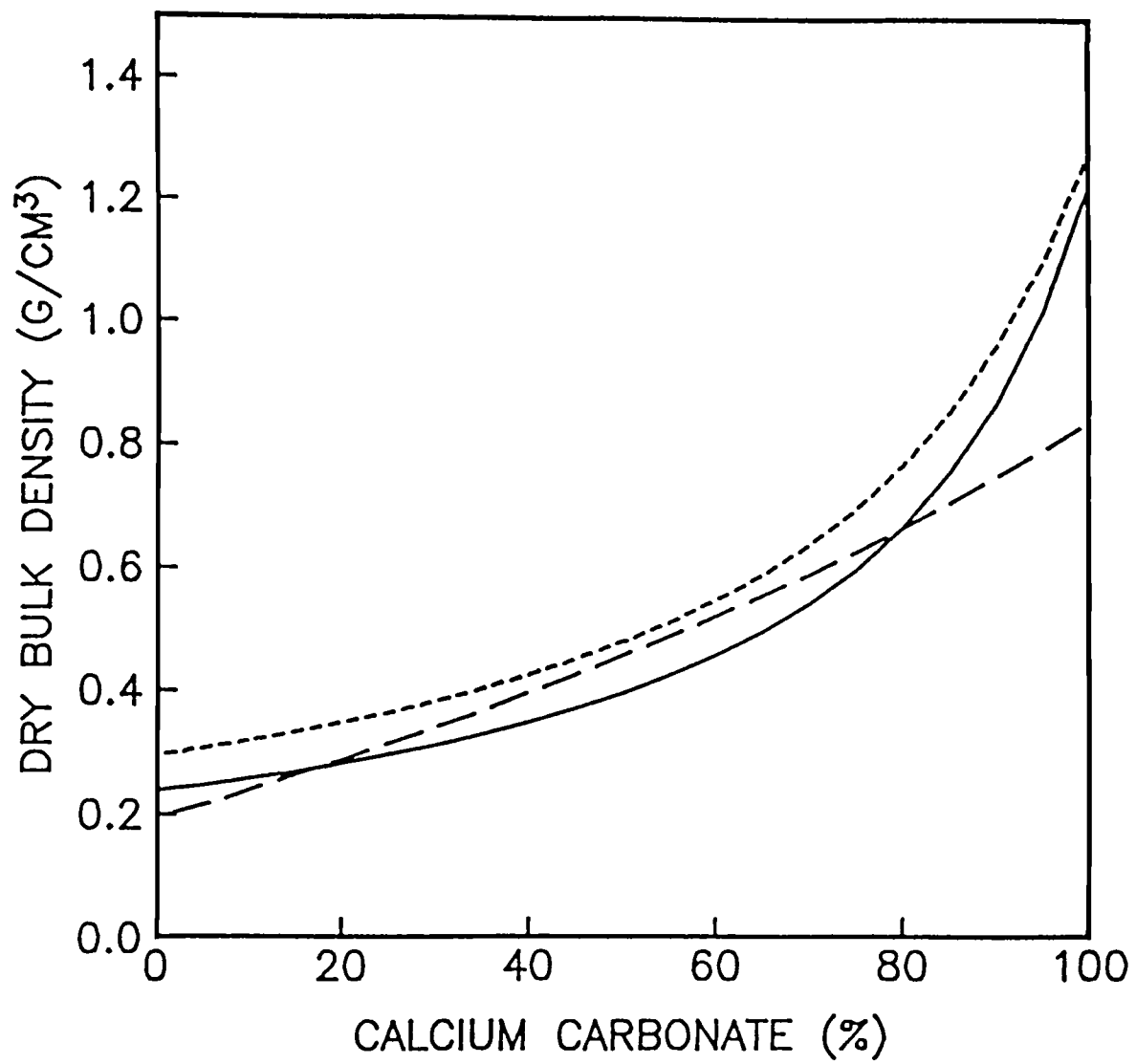


equation is 0.961 and the standard error of estimate is 0.071  $\text{g}\cdot\text{cm}^{-3}$ . Profiles derived from the Luz and Shackleton (1975) and Lyle and Dymond (1976) equations in addition to our new relation are shown in Figure I-5.

Figure I-5

Dry bulk density ( $\text{g cm}^{-3}$ ) calculated from calcium carbonate content (%) based on equations of Luz and Shackleton (1974, small dash), Lyle and Dymond (1976, large dash), and this study (solid).

Figure I-5



## RESULTS AND DISCUSSION

### Sediment Accumulations

The sediment data are reported as accumulation rates vs age for the last 200,000 years (Figures I-6 and I-7). First, we evaluate the records of accumulation of the biogenic components ( $\text{CaCO}_3$ , opal, and organic carbon) which show no apparent correlation (Figure I-6). The downcore variations in the non-biogenic components are then considered.

### Calcium Carbonate

In a review of Pleistocene carbonate fluctuations, Volat et al. (1980) state that three factors govern the carbonate content of the sediments; productivity of calcareous plankton, dilution by non-carbonate material, and intensity of carbonate dissolution. Benthic foraminifera generally make up less than 10% of the foraminiferal assemblage in this region and are not important contributors to the total carbonate signal.

Dilution is a factor in regions where the input of the non-carbonate fraction changes markedly (Gardner, 1982). If the flux of calcite does not change but the non-carbonate flux increases substantially, the concentration of calcium carbonate will decrease (Dean et al., 1981). By converting concentration to accumulation-rate (flux) profiles, the dilution problem is eliminated, allowing the variations in each component to be examined separately. In 14 GC, non-carbonate accumulation rate changes cannot account for the observed changes in the calcium carbonate record; in fact, the

Figure I-6

Downcore record of accumulation in  $\text{mg cm}^{-2} \text{ kyr}^{-1}$  of (A) calcium carbonate, (B) opal, (C) organic carbon, (E) manganese versus age (kyr). The profile of organic carbon (%) corrected for the calcium carbonate content is also given (D).

ACCUMULATIONS (mg/cm<sup>2</sup>/kyr)

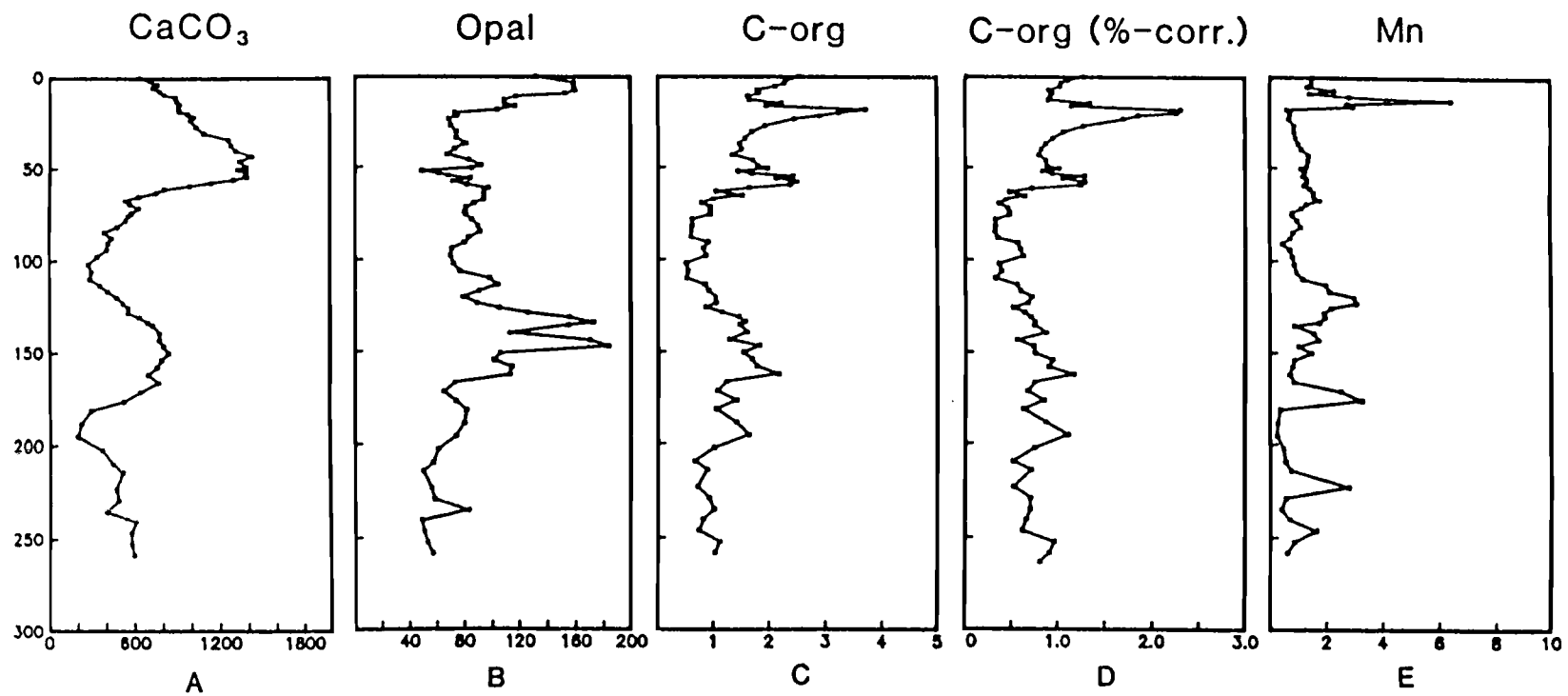


Figure I-6

Figure I-7

Downcore record of accumulation in  $\text{mg cm}^{-2} \text{ kyr}^{-1}$  of (A) aluminum, (B) barium, (C) titanium, (D) phosphorus, and (E) iron versus age (kyr).

ACCUMULATIONS (mg/cm<sup>2</sup>/kyr)

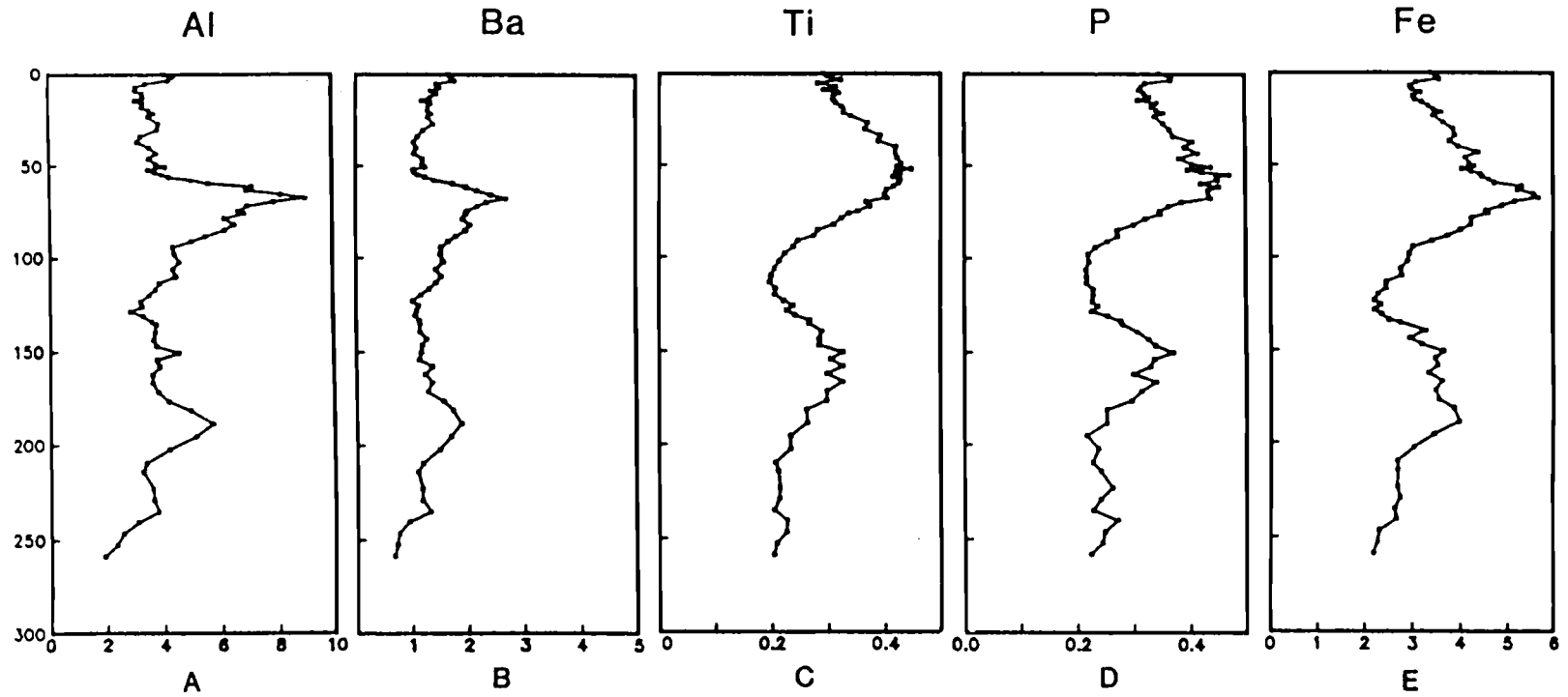


Figure I-7



amplitude of the calcium carbonate signal is significantly enhanced when presented as accumulations rather than concentrations. Thus, we conclude that most of the concentration changes are controlled by the rate of accumulation of calcium carbonate through either productivity or dissolution variations or a combination of the two. The similarity of our calcite record with those from nearby sites where dissolution is primarily responsible for the variations (Broecker, 1971; Berger, 1973; Adelseck and Anderson, 1978; Ku and Oba, 1978), suggests that the recorded Site C calcium carbonate accumulations result from dissolution.

Since the calcium carbonate record mostly reflects dissolution cycles, a comparison of calcite accumulation with records of global climatic change may help to understand the cause of the cycles. In the tropical Pacific, a strong tie has been shown between carbonate concentration changes and global ice volume as recorded by the oxygen isotopic composition of foraminifera (Broecker, 1971; Moore et al., 1977; Moore et al., 1982; Pisias and Prell, 1985). At Site C, a cross-spectral analysis (Jenkins and Watts, 1968) of calcium carbonate accumulation rate and the oxygen isotopic record of Imbrie et al. (1984) reveals high coherencies at periods of 100, 38 and 23.5 kyr (Figure I-8A). These values are similar to the periods associated with variations of the earth's orbital parameters (Imbrie et al., 1984), supporting the hypothesis that both the carbonate system and global ice volume changes are responding to the same global climatic forcing. Maximum correlation occurred with a phase lag of 8 kyr indicating that maximum (minimum) ice volume precedes calcium carbonate accumulation maxima (minima) by

Figure I-8

(A) Variance and coherency spectra calculated between calcium carbonate accumulation and the oxygen isotope record of Imbrie et al. (1984). The variance spectra of calcium carbonate accumulation (dotted line) and the  $\delta^{18}\text{O}$  record (thick solid line) are plotted as arbitrary log scales. The coherency spectrum (thin solid line) is plotted on a hyperbolic arctangent scale. The bandwidth and 5% significance level (dashed line) is shown. Frequencies are in cycles per thousand years. (B) Phase spectrum of carbonate accumulation versus the  $\delta^{18}\text{O}$  record. Error bars give the 95% confidence interval. Frequencies are in cycles per thousand years.

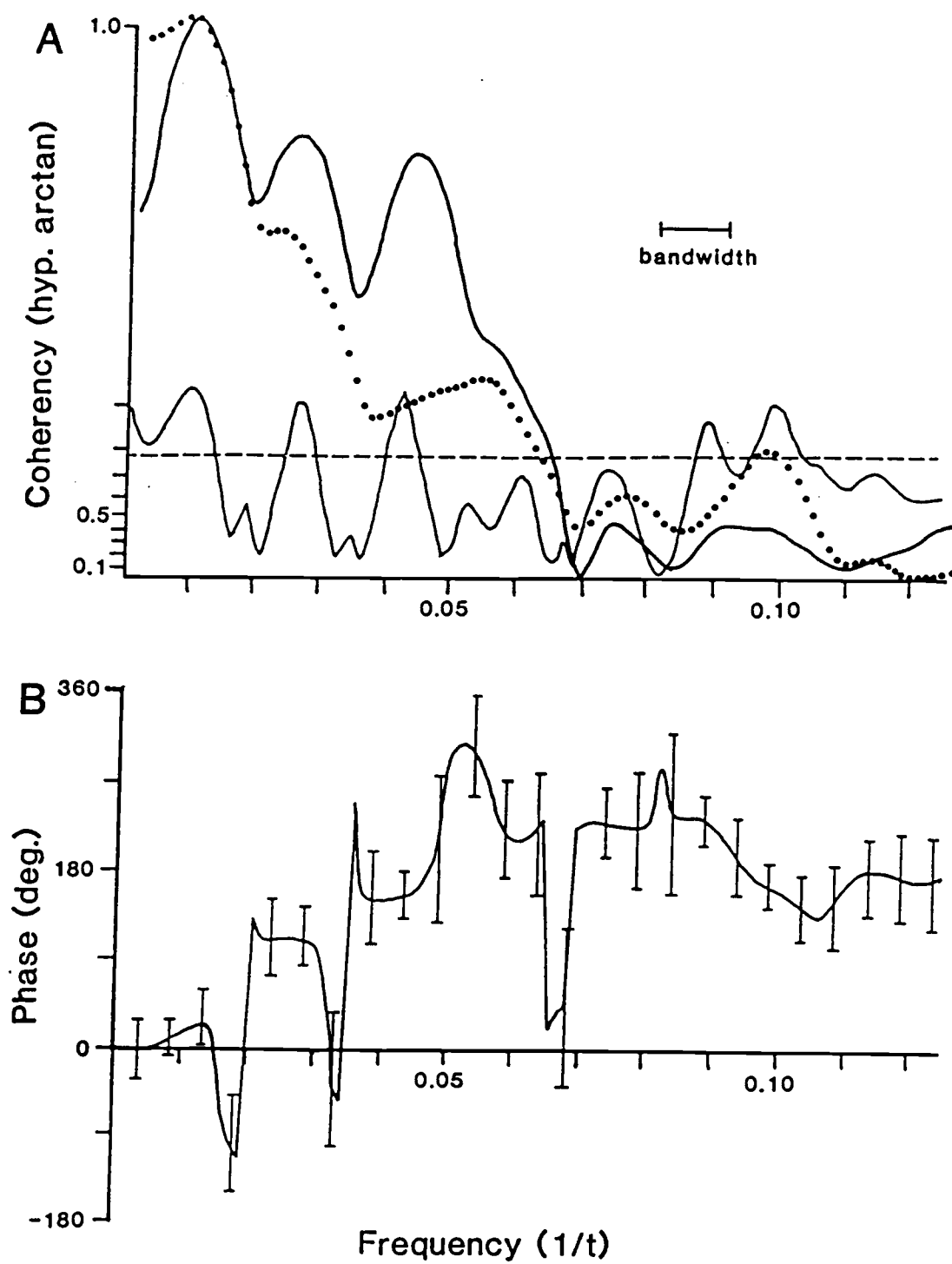


Figure I-8

8 kyr. Examination of the phase relationship between the record of carbonate accumulation and ice volume changes in the frequency bands associated with variations in the earth's orbital parameters provides further insight into this relationship (Figure I-8B).

We observe that, at the 100 kyr spectral band corresponding to the eccentricity of the earth's orbit, maximum ice volume ( $\delta^{18}\text{O}$ -enriched) is in phase with maximum carbonate accumulation (Figure I-8B). This low frequency band accounts for the largest variance in both the carbonate accumulation and ice volume records. The in-phase relationship, in this spectral band, suggests that when sea level drops, a corresponding increase in carbonate accumulation (preservation) is observed. With a model developed to examine the association of oceanic  $\text{CO}_2$  changes and dissolution cycles recorded in sediments during the last 120,000 years, Keir and Berger (1983) predict that maximum and minimum calcium carbonate accumulation in the sediments should be in phase with the maximum rate of change of sea level. Our record does not exhibit a dominant response of calcite accumulation to the rate of sea level change; rather a direct response of calcite accumulation variations to sealevel changes. In the band associated with obliquity of the earth's axis (41 kyr), maximum carbonate accumulation precedes maximum sea level by about  $70^\circ$  or 8 kyr. Thus, in agreement with Keir and Berger (1983), at this frequency, the maximum rate of sea level rise is in phase with maximum calcite accumulation. In the 23 kyr band, associated with the precession of the equinoxes, ice volume and carbonate accumulation rate changes are out of phase.

Although our data do not agree with the predicted response of the Keir and Berger (1983) model, another mechanism such as a simple response of calcite preservation to sealevel variations cannot explain the phase relationship in the higher frequencies. Other effects controlling the accumulation of carbonate at the 41 and 23 kyr frequencies must be included to fully explain the variation in the record. Calcite flux changes in response to global climate change may account for the added variance in the higher frequencies. Because of the dominance of the dissolution signal, any variations due to changes in calcite fixation in surface waters are difficult to extract from this record. This issue is revisited later in the paper.

### Opal

The opal accumulation rate varies by a factor of three down-core in 14 GC (Figure I-6B). Accumulation rates were greatest at 5-15 and 130-145 kyr. Because opal dissolves in Site C sediments to a depth of 15-20 cm (Jahnke et al., 1982), the near-surface accumulation rate maximum is ephemeral and will decrease in magnitude until it is advected below the corrosion zone. However, the recent increase in opal accumulation rate which begins below the corrosion zone (Figure I-9) is real, and will be preserved in the geologic record.

A qualitative examination of sediments from the intervals of faster and slower opal accumulation indicates more abundant and better preserved diatoms and silicoflagellates in samples with larger opal fluxes. The opal flux variations are not, however,

Figure I-9

Solid phase record of opal accumulation ( $\text{mg cm}^{-2} \text{ kyr}^{-1}$ , upper scale) versus sub-bottom depth for the upper section of core 14 GC (solid). The average pore water profile for silica ( $\mu\text{mole kg}^{-1}$ , lower scale) at Site C (Jahnke et al., 1982) is also shown (dotted). Star at 2.5 cm is the e-folding depth (i.e., the depth at which the difference of bottom water concentration and the asymptotic concentration decreases by a factor of  $1/e$ ). Inverted triangle ( $\nabla$ ) is the bottom water concentration of silica at Site C.

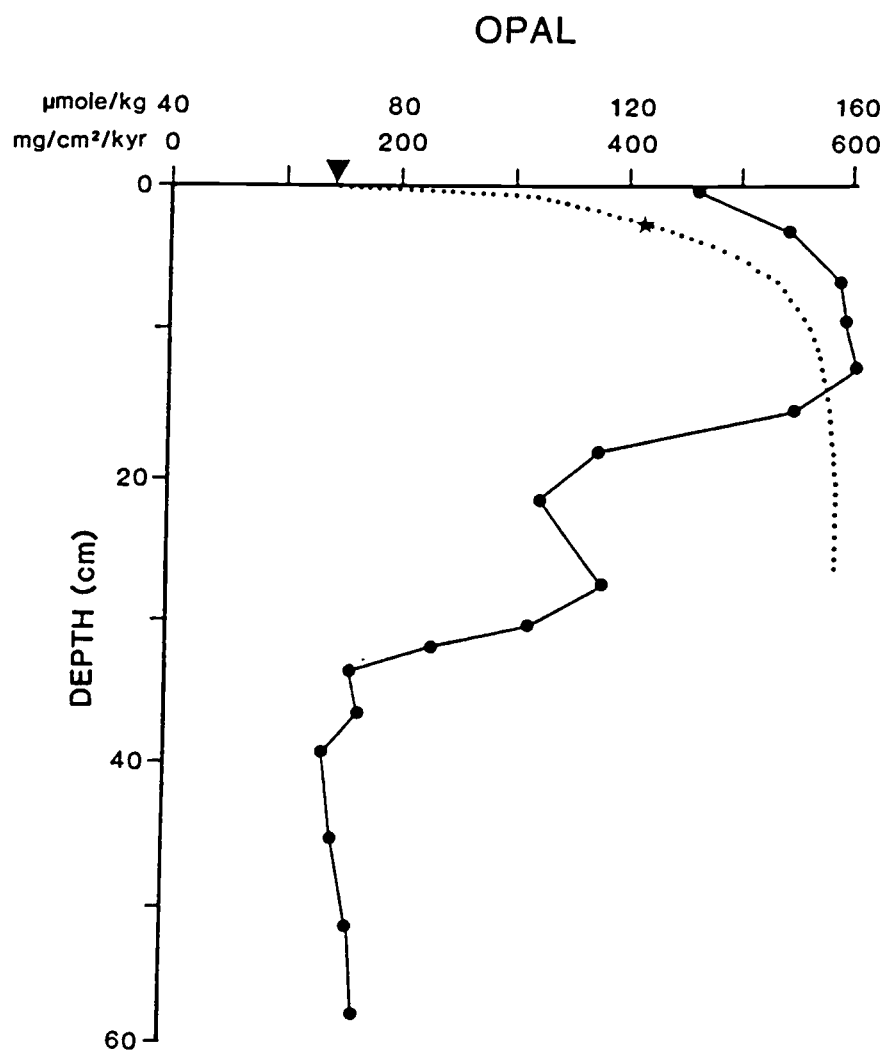


Figure I-9

reflected in the relative proportions of radiolarian species in the sediments. In nearby SDSE cores 60 and 61, as well as RC11-210, radiolarian assemblages show no significant variations for the past 300 kyr (Nigrini, 1971; Pisias, unpublished data). In fact, in RC11-210 the number of radiolarians/gram of  $\text{CaCO}_3$ -free sediment decreases from  $6 \times 10^5$  during periods of low opal accumulation to  $2 \times 10^5$  during periods of high accumulation. Thus, increased opal flux to the sediments must be due to the enhanced preservation or input of the remains of siliceous phytoplankton (i.e. diatoms and silicoflagellates). These periods of enhanced opal deposition do not correlate with increases in other biogenic constituents. In a later section, we discuss the factors controlling increases in opal deposition and conclude that these changes represent opal flux variations.

### Organic Carbon

In core 14 GC, the rate of accumulation of organic carbon has varied by more than a factor of four during the last 200 kyr (Figure I-6C). Similar large variations in organic carbon accumulation are observed in eastern Pacific sediments (Pederson, 1983; Gardner, 1982; Finney, 1986; Rea et al., in press) and have been interpreted as reflecting surface productivity changes. The carbonate-free downcore profile of organic carbon (Figure I-6D) has many of the same features as the record of organic carbon accumulation suggesting little dependence on the age model. There is no significant difference in the I:C-org ratio between samples from rapidly and slowly accumulated organic carbon sections, implying



that preservation is not controlling the organic carbon accumulation rate variations (Pederson, 1983). All the 14 GC organic matter is highly degraded.

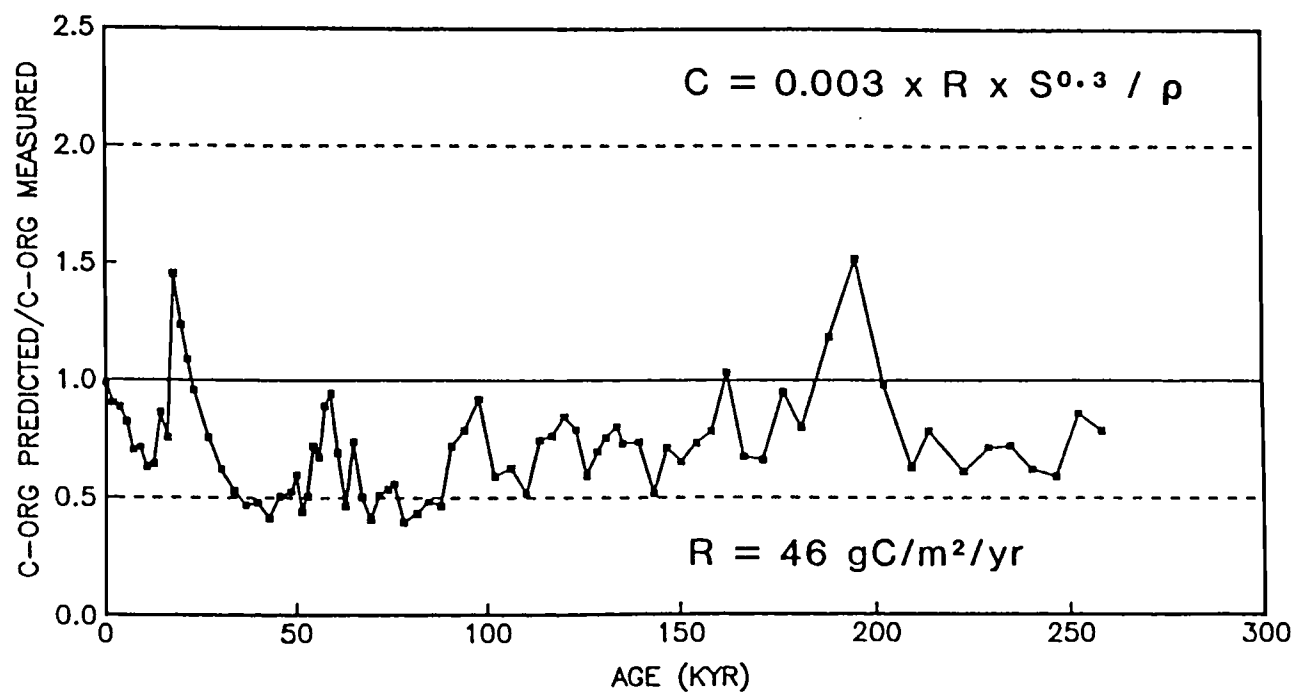
The model of Müller and Suess (1979) provides insight to the degree to which the preserved organic carbon variations can be attributed to temporal changes in productivity. In Figure I-10, we ratio the organic carbon concentration attributed to sedimentation rate and density variations (equation 6 of Müller and Suess, 1979) to the measured values (Table I-1), assuming no change in primary productivity. Variations in this ratio of more than a factor of two would imply a significant carbon flux change. Based on Figure I-10, the primary productivity at Site C was never significantly greater than at present. Significant decreases at 35-53 kyr and 68-90 kyr correspond to interglacial stages 3 and 5, respectively. These findings are consistent with other studies (Müller et al., 1983) which infer a decrease in the rate of burial of organic carbon in the deep sea during interglacial periods. We note that the predicted primary productivity from the surficial organic carbon content ( $46 \text{ gC m}^{-2} \text{ yr}^{-1}$ ) is approximately 20% below the primary productivity estimates of Koblentz-Mishke (1970) for this region. Therefore, less carbon is preserved at this site than is predicted by the equation of Müller and Suess (1979). This value is not beyond their error estimates, however.

The study of Emerson et al. (1985), working with porewater and sediment data from Site C, suggests that organic carbon records in deep-sea sediments do not reliably reflect surface productivity variations. Since the accumulation rate records of the other

Figure I-10

Ratio of predicted organic carbon concentration for a constant primary productivity of  $46 \text{ gC (m}^{-2}\text{y}^{-1}\text{)}$ , (equation 6 of Müller and Suess, 1979) to the measured concentration in 14 GC (Table I-1) versus age (kyr). Variations in the predicted concentration result from sedimentation rate and density changes. The dashed lines represent factor of two changes from the present ratio.

Figure I-10



biogenic components do not show the same variations as the organic carbon records, we are inclined to agree with Emerson et al. (1985). Core K7905 16 GC (4467 m water depth) from the central depression at Site C records only the 18 kyr increase in organic carbon accumulation. Prior to 60 kyr this core had a sedimentation rate 30-50% lower than 14 GC (see Chapter II). According to the models of Müller and Suess (1979) and Emerson (1985), sedimentation rate changes of this magnitude cannot account for the absence of the 14 GC variations in organic carbon accumulation at this coring site. Other factors, such as lateral fractionation, must be invoked to account for the spatial variations in organic carbon accumulations at Site C.

#### Non-Biogenic Components

Downcore rates of accumulation for selected non-biogenic components are shown in Figures I-6E and I-7. The profiles of aluminum and barium are highly correlated ( $r = 0.93$ ) as are those of titanium and phosphorous ( $r = 0.96$ ). Iron has affinities with both Al-Ba and Ti-P.

The high correlation of Al and Ba is surprising since Al is considered to reflect the input of detrital aluminosilicates, whereas Ba, in the form of barite, is thought to reflect biogenic input (Dymond, 1981). Since barium and aluminum covary, the accumulation rate variations of barite at Site C are difficult to attribute to paleoproductivity changes unless the aluminosilicate accumulation rate also reflects a biogenic flux. If the aluminum accumulation rate is a proxy for productivity, a direct correlation

of the organic carbon water column flux (reflecting productivity; Deuser, 1986) and the aluminum flux to the sediments should be evident in data from environments with differing Al fluxes and productivity levels.

Data from sediment traps in a given area do show a high correlation among the bulk, organic carbon, and aluminum fluxes. This link reflects the common biologically mediated mode of transfer of particulates to the deep-sea (Deuser et al., 1983). Since aluminum concentrations do not build up in surface waters, removal by the biota is relatively efficient. When data obtained from OSU traps deployed in a number of oceanographically distinct environments are pooled, however, the organic carbon flux can no longer be predicted from the aluminum flux (Fischer et al., 1986; Dymond and Collier, in prep.; Dymond, unpublished data). Thus, it appears that although seasonal variations of the flux of aluminosilicates to the deep-sea reflect productivity variations (Deuser et al., 1983), the long term flux is determined by the atmospheric input.

Atmospheric fallout is the dominant source of aluminum to Site C. Thus, the factor-of-two flux increase during isotope stage 4 likely results from greater eolian transport of particles to the site. At present, Site C lies beneath the Southeast Trades. An intensification of these winds could transport a greater amount of material further offshore. Proxy indicators of atmospheric circulation changes in eastern equatorial sediments (Molina-Cruz, 1977; Romine and Moore, 1981; Schramm, 1985) imply an intensification of the trade winds during glacial stages 2 and 4. At Site C the increase in eolian input is only observed during stage 4.

Romine (1982) suggests a 5° southward shift of the trade winds relative to their modern location prior to 80 kyr. This would move the intertropical convergence zone closer to the site and produce an increase in rainfall. Uematsu et al. (1985b) have shown that wet deposition of airborne particles accounts for 75-85% of the total input. Thus, an increase in rainfall during a period of high atmospheric dust concentrations would be expected to increase the input. At present, however, particle supply and not rainfall appears to be the factor limiting detrital deposition at the equator. Uematsu et al. (1985a) suggest that the present low dust loads in the equatorial regions reflect the influence of southern hemisphere air. Thus, an increase in the dust load of the Southeast Trades during stage 4, as suggested by Molina-Cruz (1977), could account for the Al flux increase observed at Site C. We cannot distinguish this possibility from a shift in the trade winds that led to a greater influence of Northeast Trades, which carry a greater particulate load, however.

Both titanium and phosphorus accumulation rate profiles resemble that of calcium carbonate (Figures I-6 and I-7). A comparison of Ti and P with the record of Al accumulation suggests that their deposition is unrelated to aluminosilicate input. Since a constant titanium accumulation model was used as a preliminary age model, the Ti variations are a direct result of the correlation of <sup>14</sup>GC to the reference isotope stack (Figure I-3). Iron reflects accumulation of both the Al-Ba and Ti-P sources.

At Site C, 30-45% of the total iron is in an oxyhydroxide phase that can be extracted with a buffered hydroxylamine hydro-

chloride leach (Robbins et al., 1984). Most of the remaining iron is associated with aluminosilicates. Results from a sequential leach of Site C sediments, (Box core BNTH III 11 BC; Lyle, unpublished data) using a pH 5 acetic acid-sodium acetate extractant, a hot pH 9.2 sodium dodecyl sulfate-sodium bicarbonate extractant, a pH 5 hydroxylamine hydrochloride-sodium citrate extractant, and a hot pH 12.1 sodium carbonate extractant, allow the total iron measured by XRF to be partitioned into detrital and "excess" or oxyhydroxide fractions (Figure I-11).

The ratio of Fe to Al in the residue from the sequential leach of 0.45:1 represents the ratio in aluminosilicate material. Bischoff et al. (1979) and Boyle (1983) obtained a similar value in tropical Pacific sediments. We use the normative equations:

$$\%Fe \text{ (detrital)} = [0.45 \times 0.78 \times \%Al \text{ (XRF)}] + 0.09$$

$$\%Fe \text{ (excess)} = [0.88 \times \%Fe \text{ (XRF)}] - Fe \text{ (detrital)}$$

to obtain the iron concentrations in the aluminosilicate (detrital) and oxyhydroxide (excess) phases; where 0.45:1 is the Fe/Al ratio in the residual of the sequential leach, 0.78 is the proportion of the total Al content in the residual fraction, 0.09 is the systematic offset between the bulk concentrations measured by atomic absorption spectroscopy (AAS) and XRF (Figure I-10), and 0.88 is the proportion of the total Fe content in the sum of the residual and oxyhydroxide fractions. The %Al (XRF) and %Fe (XRF) values are obtained from Table I-1. The accumulation-rate profiles for detrital and excess iron are presented in Figure I-12; alumino-

Figure I-11

Iron versus aluminum from Site C sediment trap and BNTH III 11 box core samples. Diamonds = sediment trap samples measuring the primary flux of material; Plus's (+) = sediment trap samples containing resuspended sediments in addition to the primary flux; Upward arrows ( $\uparrow$ ) = total concentration measured by AA; x's = total concentration measured by XRF; Squares = the concentration of Al and Fe in the residue of sediment samples treated by a sequential leach (Robbins et al., 1984); Triangles ( $\blacktriangle$ ) = concentrations in the oxyhydroxide phase in the sediments. The slope of the regression line passing through the primary flux measured by sediment traps and the leach residue is 0.45. The average Fe/Al ratio for the oxyhydroxide fraction (1.77) is also shown. Totals can be represented as a mixing of these two end-member phases.



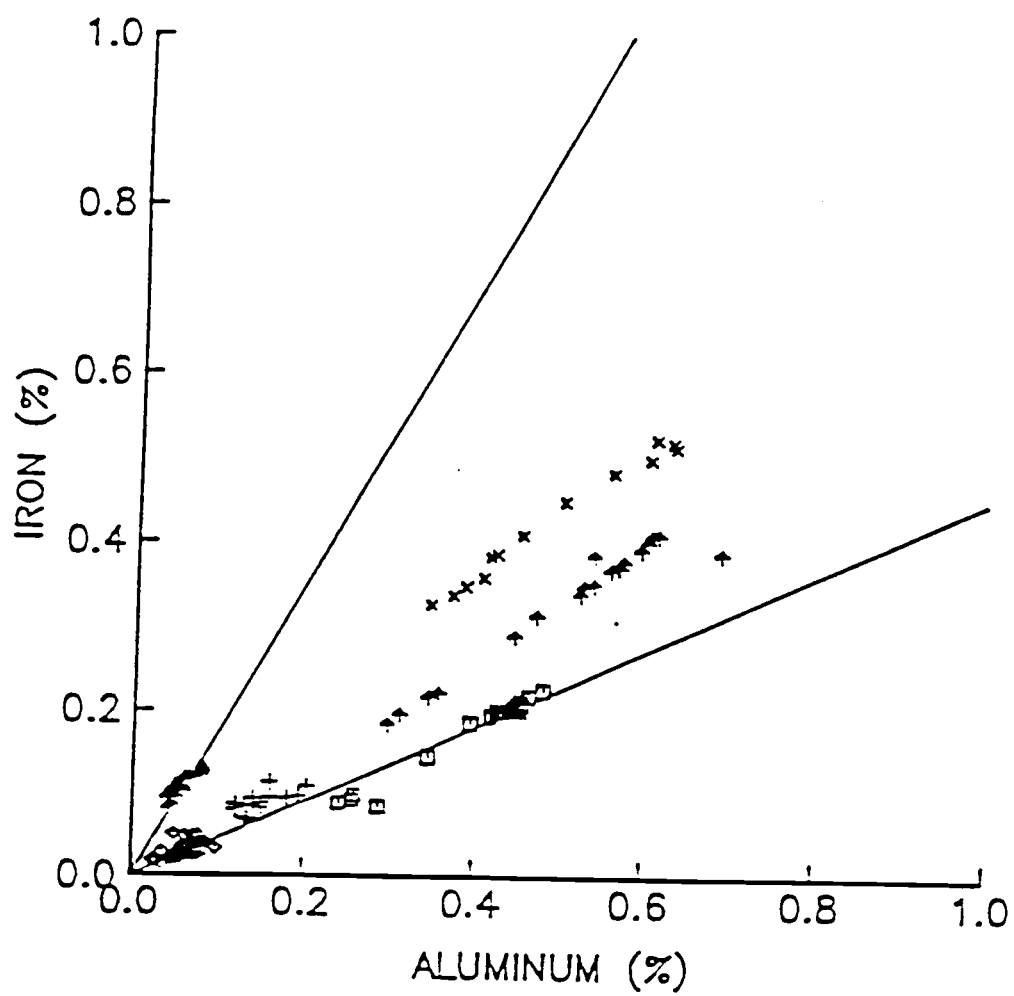


Figure I-11

Figure I-12

Accumulation ( $\text{mg cm}^{-2} \text{ kyr}^{-1}$ ) versus age (kyr) of total iron (solid line with squares) partitioned into detrital (dashed line) and excess (solid line) phases.

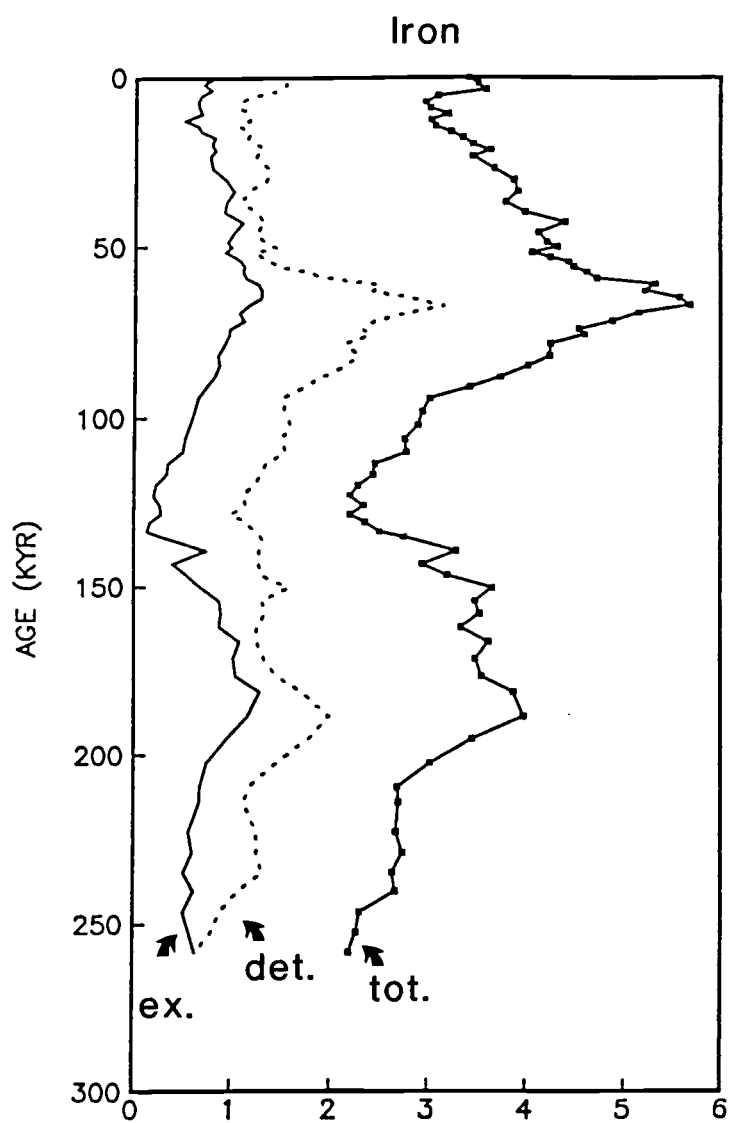


Figure I-12

silicate-associated iron is the dominant form of this element at Site C.

The rate of accumulation of excess Fe is similar in magnitude to Krishnaswami's (1976) estimate of authigenic Fe deposition. However, if this component is truly authigenic, its accumulation rate should vary little through time. In fact, the excess Fe is positively correlated with sedimentation rate ( $r = 0.37$ ) and shows a factor-of-six variation between periods of maximum and minimum accumulation. Because the Fe/Al ratio in particles captured by sediment traps above the resuspension zone is the same as detrital material (Table I-4; Figure I-11), the excess Fe component must originate at the sediment-water interface or in the lower water column where particles have a relatively long residence time. In pelagic sites far removed from the continental margins, Dymond (1984) attributes a flux increase with depth for refractory elements to scavenging of dissolved species by falling particles. The composition of this component should reflect both the character of primary detritus and the length of time particles are in contact with seawater. We propose that the oxyhydroxide phase of iron in the Site C sediments originates in this way. The flux of excess iron is highly correlated with those of Ti and P ( $r = 0.72$  and  $0.68$  respectively) suggesting that they reside in the same phase. Since particulate scavenging by iron oxides is proposed as a source of sedimentary phosphorus near rise crests, a similar process could be supplying P at Site C. The ratio of total phosphorus to excess iron is an order of magnitude higher than the measured ratio in

Table I-4. Sediment trap fluxes and surface sediment accumulation.

Sampling Period					Fluxes ( $\mu\text{g cm}^{-2} \text{ yr}^{-1}$ )										
		Open	Closed	Days	Total <sup>a</sup>	CaCO <sub>3</sub>	Opal <sup>b</sup>	C-org	Si-Tot	Al	Fe	Ba	Mn	C-org/ C-CaCO <sub>3</sub>	
<u>Deployment 1 (1°02.41'N, 138°56.10'W; 4445 m water depth)</u>															
1895 m	Cup 2	12/23/82	04/03/83	100	1905	1330	330	93.3	137	1.26	0.709	2.40	0.0367	0.58	
	Cup 3	04/03/83	07/12/83	100	2482	1581	536	169.	222	1.85	0.701	2.98	0.0385	0.89	
	Cup 4	07/12/83	10/20/83	100	3013	1573	1172	193.	478	2.29	0.864	4.09	0.0588	1.02	
	Cup 5	10/20/83	02/25/84	128	3216	1579	1344	163.	547	2.37	0.837	3.89	0.0527	0.86	
	Ave C2-4	12/23/82	10/20/83	300	2467	1495	679	152.	279	1.80	0.758	3.16	0.0447	0.84	
3495 m	Cup 2	12/23/82	04/03/83	100	1872	1265	383	87.0	158	1.20	0.925	2.57	0.1297	0.57	
	Cup 3	04/03/83	07/12/83	100	2363	1473	580	133.	239	1.76	1.180	3.37	0.1614	0.75	
	Cup 4	07/12/83	10/20/83	100	2830	1362	1034	179.	423	2.32	1.440	4.32	0.1411	1.10	
	Cup 5	10/20/83	02/25/84	128	1758	912	667	86.1	273	1.59	0.713	2.20	0.0451	0.79	
	Ave C2-4	12/23/82	10/20/83	300	2355	1367	666	133.	273	1.76	1.180	3.42	0.1441	0.81	
<u>Deployment 2 (1°03.67'N, 138°58.50'W; 4425 m water depth)</u>															
1883 m	Cup 2	02/25/84	04/01/84	36	4627	2266	1876	252.	766	3.86	1.880	5.80	0.0523	0.93	
	Cup 3	04/01/84	07/10/84	100	7632	3975	2735	453.	1115	5.27	2.130	9.25	0.1107	0.95	
	Cup 4	07/10/84	10/18/84	100	4813	2817	1569	197.	640	2.95	1.080	4.76	0.0446	0.58	
	Cup 5	10/18/84	02/25/85	127	4939	2740	1788	168.	727	2.95	1.090	4.00	0.0559	0.51	
	Cup 1	02/22/84	02/25/84	3+68	4667	2507	1764	169.	716	2.46	2.490	3.92	0.0245	0.56	
	Average	02/22/84	05/01/85	434	5460	2965	1960	247.	798	3.48	1.620	5.52	0.0605	0.69	
2980 m	Cup 2	02/25/84	04/01/84	36	3750	1930	1395	189.	570	3.06	1.510	4.06	0.0842	0.81	
	Cup 3	04/01/84	07/10/84	100	3035	1492	1114	164.	455	2.27	1.110	3.11	0.0961	0.86	
	Cup 4	07/10/84	10/18/84	100	6802	3857	2299	324.	941	5.27	2.320	6.61	0.2106	0.70	
	Cup 5	10/18/84	02/25/85	127	3191	1896	1114	112.	453	1.80	0.860	2.47	0.0590	0.49	
	Cup 1	02/22/84	02/25/84	3+68	4048	2127	1615	173.	655	2.24	1.120	2.92	0.0603	0.68	
	Average	02/22/84	05/01/85	434	4174	2295	1499	189.	603	2.88	1.350	3.78	0.1048	0.68	
<u>Flux to Sediments</u>															
Ave W/IC2, IC3		12/23/82	05/01/85	862	--	1729	1109	150.	--	2.41	1.215	3.67	0.1107	0.72	
Ave W/O IC2, IC3		07/12/83	05/01/85	662	--	1856	1305	164.	--	2.70	1.264	3.88	0.1000	0.74	
<u>Sediment Accumulation 14 GC 0-5 cm</u>					--	913	703 <sup>c</sup>	110 <sup>d</sup>	2.37	--	4.29	3.470	1.73	1.5000	0.03
							740 <sup>e</sup>	139 <sup>c</sup>							
<u>Benthic Flux<sup>f</sup></u>					--	--	1153-1116	1195-1166	162.	--	--	--	2.15	---	1.21

<sup>a</sup>Total flux is corrected for salt<sup>b</sup>Except for Na<sub>2</sub>CO<sub>3</sub> leach in 0-5 cm sample, Opal = (Si-tot - (4.0xAl)) x 2.5<sup>c</sup>X-ray fluorescence<sup>d</sup>Na<sub>2</sub>CO<sub>3</sub> leach<sup>e</sup>LECO analysis<sup>f</sup>Flux to sediments - sediment accumulation

metalliferous sediments (Berner, 1973; Froelich et al., 1977); pointing to the existence of additional sources of phosphorus.

Froelich et al. (1982) found that most of the phosphorus in deep-sea sediments can be attributed to organic matter, calcite shells, phosphorites, and iron oxyhydroxides. In carbonate-rich sediments, a substantial portion of phosphorus is in the shells of foraminifera and coccolithophores. At Site C, the weight proportions of 38  $\mu\text{m}$  calcium carbonate (mostly coccoliths) and >38  $\mu\text{m}$  carbonate (only foraminifera) are equal in near-surface sediments (see Chapter III). Froelich et al. (1982) propose 400 ppm as the P concentration in coccolith calcite and 50 ppm as the value in foraminiferal calcite. Since foraminiferal fragments contribute to the 38  $\mu\text{m}$  calcite we assign 200 ppm P/g  $\text{CaCO}_3$  (rather than 225 ppm P/g) to phosphorus incorporated in the shells of microplankton at Site C. Because dissolution is the major cause of the calcium carbonate variations, it is likely that the relative proportions of coccolith to foraminiferal calcite will change temporally. In the absence of data on this change, we assume a constant proportion downcore, suggesting that 20-70% of the phosphorus accumulation can be attributed to microplankton shells (Figure I-13). If dissolution affects foraminifera more than coccoliths (Broecker, 1971; Honjo, 1977), this proportion and the resulting P accumulation will decrease during carbonate-rich and increase during carbonate-poor intervals. Thus, 40-50% is probably a better estimate of the proportion of total phosphorus associated with calcite shells at Site C.

Figure I-13

Partitioning of total phosphorus accumulation ( $\text{mg cm}^{-2} \text{ kyr}^{-1}$ , solid line with squares) versus age (kyr) into fractions associated with calcium carbonate (dotted line), oxyhydroxides (dashed line), and residual (solid line).

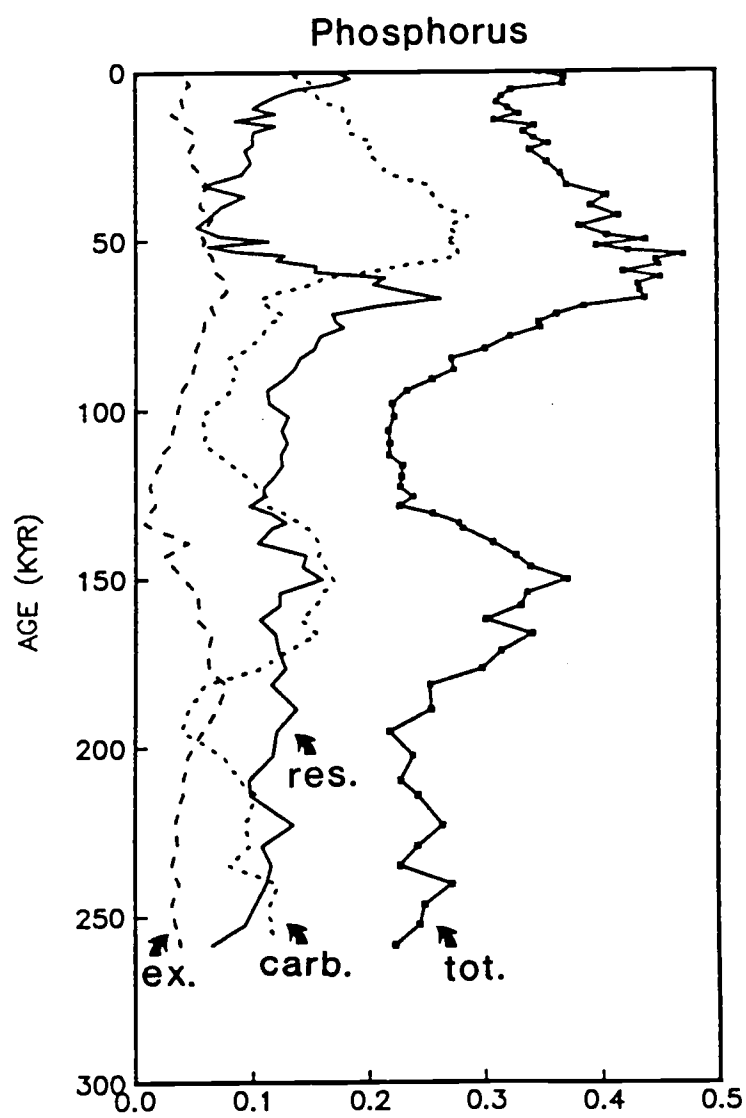


Figure I-13



Froelich et al. (1977) used a P/Fe ratio of 0.06:1 to calculate the amount of phosphorus associated with ferric oxyhydroxides. This phosphorus is believed to be derived from seawater and absorbed on iron oxyhydroxides (Froelich et al., 1982). We assume that only excess Fe (Figure I-12) is involved in P uptake, implying (from Froelich et al.'s ratio) that 3-30% of the total phosphorus deposition can be accounted for in this phase (Figure I-13). The portion not accounted for (14-60%) is shown as residual accumulation (Figure I-13) and its source is not defined. Whether some of this component is associated with organic matter (possibly as much as 20-40% in near-surface sediments) or simply reflects uncertainties in our partitioning procedure is unclear.

The titanium accumulation can be partitioned in a similar way (Figure I-14). The fraction associated with aluminosilicates is calculated by multiplying detrital Fe accumulation (Figure I-12) by 0.07:1 (the mean ratio of Ti/Fe in the residual of the sequential leach of BNTH III 11 BC). Additionally, the record of titanium accumulation in iron oxides is obtained by multiplying excess Fe by the mean Ti/Fe ratio in the hydroxylamine hydrochloride extract (0.04). Only a minor fraction of the total titanium is in this component (Figure I-14). The downcore profile of the remaining 30-70% resembles the calcite accumulation profile. At present, we know of no measurements to test our conclusion that a large portion of sedimentary titanium is associated with calcium carbonate.

The manganese accumulation profile (Figure I-6E) contains a number of peaks which do not correlate with maxima in biogenic or detrital accumulation rates. The high manganese concentration

Figure I-14

Partitioning of total titanium accumulation ( $\text{mg cm}^{-2} \text{ kyr}^{-1}$ , solid line with squares) versus age (kyr) into fractions associated with detrital (dashed line), excess (solid line), and residual (dotted line).

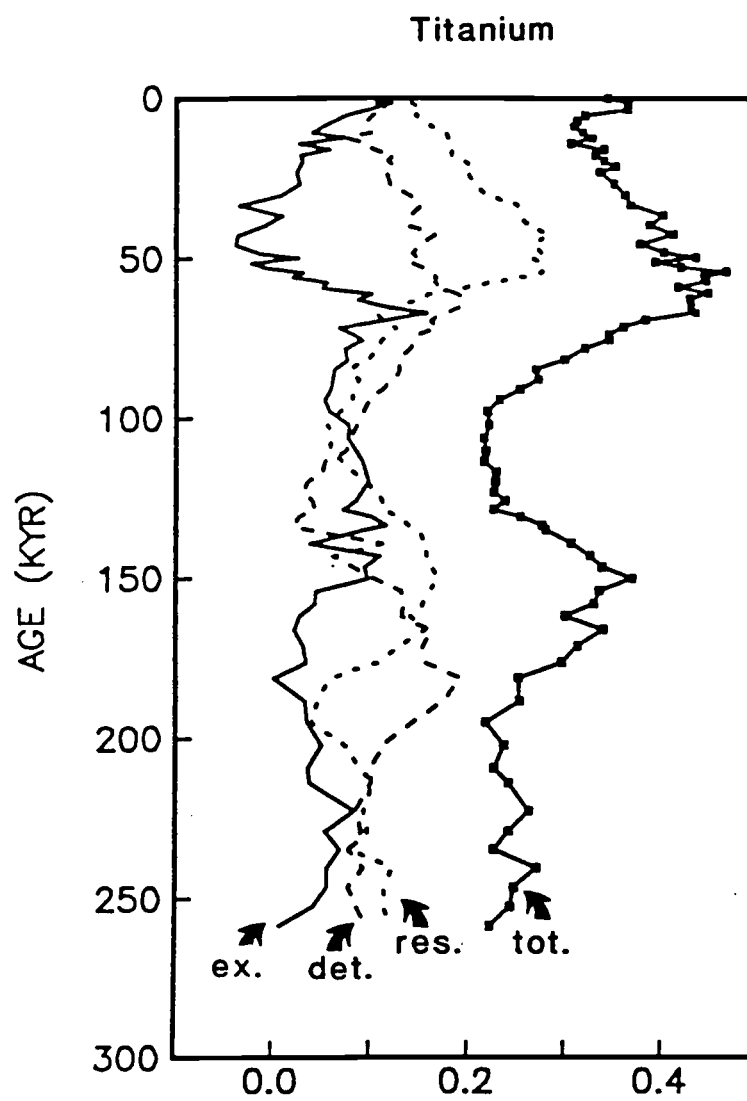


Figure I-14

creates dark bands in the sediments which can be used to visually correlate cores at Site C (see Chapter II). In other areas with similar profiles, post-depositional remobilization of manganese has been proposed as the mechanism for generating peaks in the sediments (Bonatti, 1971; Sawlan and Murray, 1983; Finney, 1986). Pore water profiles at Site C show that the near surface solid phase peak results from upward diffusion of reduced manganese into the surface oxidized zone (Jahnke et al., 1982). At MANOP Site H, Finney (1986) has used sediment redox variations driven by changing organic carbon flux to model the burial of manganese peaks. Although a similar mechanism may explain the cause of manganese variations at Site C, the large changes in organic carbon necessary to generate the observed redox variations are not observed at appropriate intervals downcore. Rather, because the integrated amount of manganese in 14 GC equals the amount obtained by assuming a constant input of  $1.3 \text{ mg} \cdot \text{cm}^{-2} \text{ kyr}^{-1}$  we believe that the peaks reflect post-depositional mobility. This value is close to the average accumulation above the redox boundary ( $1.5 \text{ mg} \cdot \text{cm}^{-2} \text{ kyr}^{-1}$ , Table I-4). If the input rate has not changed significantly during the past 200 kyr, the excess manganese in a peak can be derived from material already incorporated within the sediment column; no additional manganese source is necessary.

In near-surface sediments above the redox boundary, 90-95% of the manganese can be extracted with acetic acid and hydroxylamine hydrochloride. Since the extracted Mn resides in the same phase as excess Fe, we propose that manganese is input to the sediments by a process similar to the scavenging mechanism described for excess

Fe. Thus, the Mn input covaries with excess Fe but the record is altered by post-depositional mobility.

Our results show that, in addition to deposition as detrital, non-biogenic components, a significant portion of the Fe, P, and Mn accumulate with an oxyhydroxide phase. Since the partitioning of the components in 14 GC relies on data obtained from regional studies and a nearby box core (BNTH III 11 BC) which only sampled the top 30 cm of the sediments, these results represent only a first attempt to decipher the record of accumulation of various sediment components. Additional leach studies downcore are needed to verify the temporal variation.

#### Sediment - Sediment Trap Comparison

To quantify the paleo-flux changes recorded as variations in the accumulation rates of sediment components, it is necessary to compare the recent sediment record to fluxes through the water column. The sediments, however, record fluxes averaged over intervals at least three orders of magnitude longer than the water column rain rates estimated from sediment traps. A comparison of the refractory elemental fluxes in both traps and sediments can establish whether the two sets of measurements are compatible (Fischer et al., 1986). Such a comparison, requires that no major flux changes have occurred during the last few thousand years, since the bioturbated surface sample at Site C represents an averaged sample of that interval. We also assume that sediment traps collect most of the particles that transport material to the sediments. If the trap and sediment fluxes of the refractory in-

puts are comparable, then differences in the fluxes of labile components between traps and sediments should be meaningful. Such differences can be used to hindcast flux changes recorded by the downcore accumulation rates of calcite, opal, and organic carbon.

#### Input to the Sediments

The present-day flux to the sediment-water interface at Site C is based on two sediment trap experiments deployed from 26 December 1982 to 1 May 1985. The samples were collected by single-cone OSU traps equipped with 5-cup sample changers and poisoned with sodium azide. Under quiescent conditions, a sediment trap moored close to the ocean bottom should accurately capture the flux of material to the sediments. However, near-bottom traps often contain a large component of resuspended sediment in addition to the primary flux (Rowe and Gardner, 1979; Gardner et al., 1983; Walsh, Fischer, et al., submitted). Thus, it is necessary to use fluxes measured above the resuspension zone to determine the primary input to the sediments.

In this study, traps moored at depths of 1895 and 3495 m from the first deployment and 1883 and 2908 m from the second deployment have been used to estimate the flux of calcium carbonate, opal, organic carbon, Al, Ba, Mn, and Fe to the sediment-water interface (Table I-4). The samples were processed following the methods of Fischer (1983). Calcium carbonate and organic carbon values were measured by a LECO carbon analyzer (Weliky et al., 1983). Si, Al, Ba, Mn, and Fe were measured by atomic absorption spectrometry (AAS) and the opal content was calculated by the normative pro-

cedure discussed earlier. We use a sample designation such that 1C2 refers to cup 2 of the first deployment.

Since Site C is distant from land masses, the main source of particulate Fe and Al is expected to be atmospheric dust. The flux to the sediment-water interface of non-labile components (i.e., Al and Fe) is taken as the measured value in the deepest trap above the resuspended zone for each deployment. This corresponds to the 3495 m level (792 meters above bottom) in the first experiment and 2908 m (1379 meters above bottom) for the second experiment. As discussed earlier, these levels do not contain a significant hydrogeneous component and the measured fluxes of Al and Fe reflect only aluminosilicate material. Dissolution and degradation of calcite, opal, and organic carbon (the major labile components of the flux) in the water column is considered when extrapolating to the sediment-water interface. We use the model of Walsh, Dymond, et al. (submitted) which assumes that decomposition and dissolution follow first order kinetics in the lower water column. The flux decrease with depth between the deepest two traps above the resuspension zone is attributed to these processes. Reaction rates in the near-bottom region are assumed to be the same as those higher in the water column and the model neglects any possible increase in the rate of dissolution of calcium carbonate in the sub-lysoclinial zone.

Fluxes of calcite, opal, and organic carbon components are normalized to Al which is associated with lithogenic particles and is not affected by dissolution or decomposition reactions in the water column (Spencer et al., 1978). This normalization corrects

for disaggregation and horizontal transport processes which affect both biogenic and refractory fluxes. The similarity of normalized and non-normalized profiles indicates that these processes are of minor importance in the lower water column at Site C. The aluminum content of the settling particles is assumed to be fixed at the time of particle formation. At locations such as Site C, where the only source of lithogenic particles in traps is atmospheric fallout, this assumption is reasonable.

Reaction rates for the dissolution and decomposition processes between the pairs of sediment traps in each deployment are given by:

$$k = \frac{(\ln F_i - \ln F_i^0)}{z}$$

where  $k$  is the reaction constant per meter,  $F_i$  and  $F_i^0$  are the ratios of measured fluxes of component  $i$  to the Al flux for the lower and upper traps, respectively, and  $z$  is the difference in depth between the traps in meters (see Walsh (1985) for a more detailed discussion of the model).

Because the pairs of traps were at different levels during the two experiments, organic carbon, opal and calcium carbonate rate constants were calculated for each deployment and the averages were used to extrapolate the fluxes to the sediment-water interface. The difference between the C5 profile and the other profiles in deployment 1 (Figure I-15) may reflect a flux increase that passed the 1895 m level but did not reach the 3495 m level before the mooring was recovered. Data from this cup have not been used to



Figure I-15

Bulk flux ( $\text{mg cm}^{-2} \text{ yr}^{-1}$ ) measured by two sediment trap deployments at MANOP Site C. Solid circles of the first deployment and circles with stars for the second deployment are the average bulk flux for each sampling interval. Refer to Table I-4 for sampling intervals. Circles with stars of first deployment and solid circles for the second are the time-averaged bulk fluxes normalized to one year. The single solid star is the bulk flux measured in a Soutar trap from the first deployment at 2695 m.

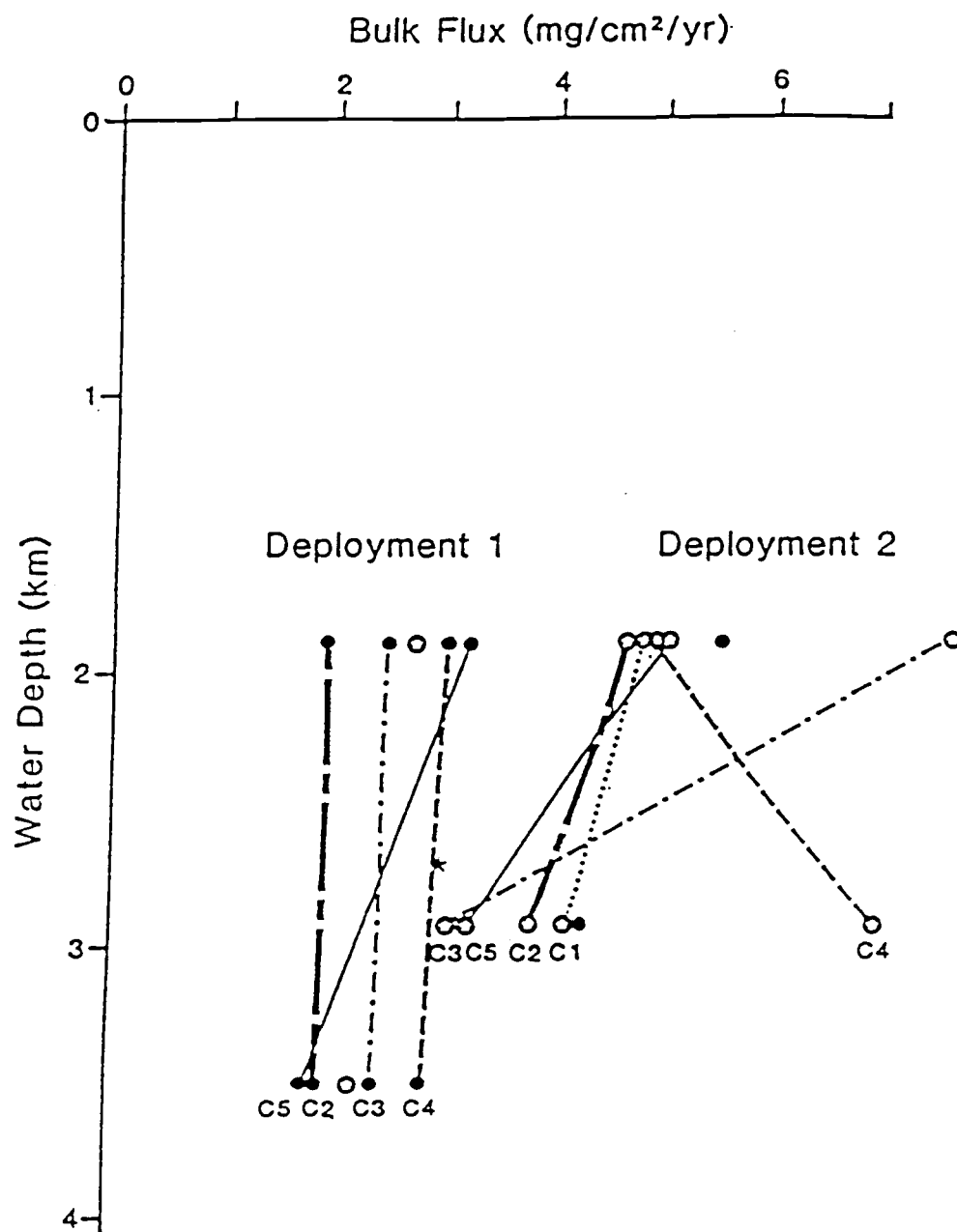


Figure I-15

calculate rate constants. We note that a trap at the 2695 m level, which collected one sample for the whole deployment, recorded a flux similar to the time-averaged flux at 1895 m (Figure I-15). This suggests that the flux increase did reach 2695 m before 25 February 1984. If we assume that the particles settled at 150 m/day (Fowler and Small, 1972; Small et al, 1979) then the near-surface event responsible for the flux increase occurred at least 18 days (2700 m/150 m/day) but not more than 23 days (3500 m/150 m/day) before the experiment was recovered (Feb. 25, 1984). The trap moorings were deployed so that no gaps in the sampling period occurred. Therefore, deep samples from the second experiment should record an increase. However, the lowest trap of the second experiment (2908 m) that sampled only the primary flux during the first sampling period (2C2, Figure I-15) did not record the increase. We propose that the flux increase had already passed the 2900 m level by February 25, 1984 and was captured only by the near-bottom traps. These traps also contain a significant resuspended component, however, which masks the proposed increase in the primary flux.

A second similar event is seen in the 2C3 and 2C4 profiles of the second experiment. Based on the measured fluxes at the 1883 m level, 2C3 sampled half and 2C4 sampled almost twice the expected flux to the 2908 m level during their respective sampling periods. Therefore, the sum of 2C3 and 2C4 equals the sum of the expected fluxes. We propose that the increase observed at the end of the 2C3 sampling period at 1883 m is not sampled until the 2C4 period at the 2908 m level. With a settling rate of 150 m/day, the sur-

face event causing the flux increase occurred after June 21, 1984 but before June 28, 1984. Unfortunately, vertical transmissometer profiles and moored data, which could have traced the flux peak through the water column, are not available for these experiments.

The time-weighted average of the rate constants for the labile components from the first and second deployments are used to extrapolate the measured fluxes to the sediment-water interface. The constants are  $-7.4 \times 10^{-5}$ ,  $-4.5 \times 10^{-5}$ , and  $-5.6 \times 10^{-5} \text{ m}^{-1}$  for organic carbon, opal, and calcium carbonate, respectively. These values are slightly smaller than those of Walsh, Dymond et al. (submitted) who considered only data from the first deployment. These constants are equivalent to a 5-10% flux decrease due to dissolution and decomposition in the lower 1000 m of the water column. Time weighted averages are given in Table I-4 and biogenic fluxes to the sediment-water interface for each sampling period are shown in Figure I-16. Because of the problems discussed earlier, the fluxes for 1C5 are extrapolated from the 1895 m trap.

During the first two sampling periods of the first experiment, anomalously warm waters associated with the 1982-83 El Niño were present at the site (Pisias et al., 1985). Organic carbon and opal fluxes as well as the carbonate fraction due to coccolithophores are lower during this period (Murray and Dymond, 1985). Since these fluxes do not represent "normal" conditions at the site, 1C2 and 1C3 samples are excluded when determining the average flux to the sediments (Table I-4). We assume that this average flux estimate is characteristic of the long-term input to the sediments

Figure I-16

Extrapolated flux of calcium carbonate, opal, and organic carbon ( $\mu\text{g cm}^{-2} \text{ yr}^{-1}$ ) to the sediment-water interface from the two experiments at MANOP Site C. Refer to Table I-4 for the sampling intervals. Histograms with the same patterns sampled similar seasons. The solid line is the time-averaged flux for all sampling periods, and the dashed line represents the time-averaged flux excluding the 1C2 and 1C3 sampling periods. The value for the dashed line is used for the modern flux. The maximum and minimum sediment accumulation rate in 14 GC for calcite, opal and organic carbons during the last 200 kyr are shown to the right of the trap fluxes.

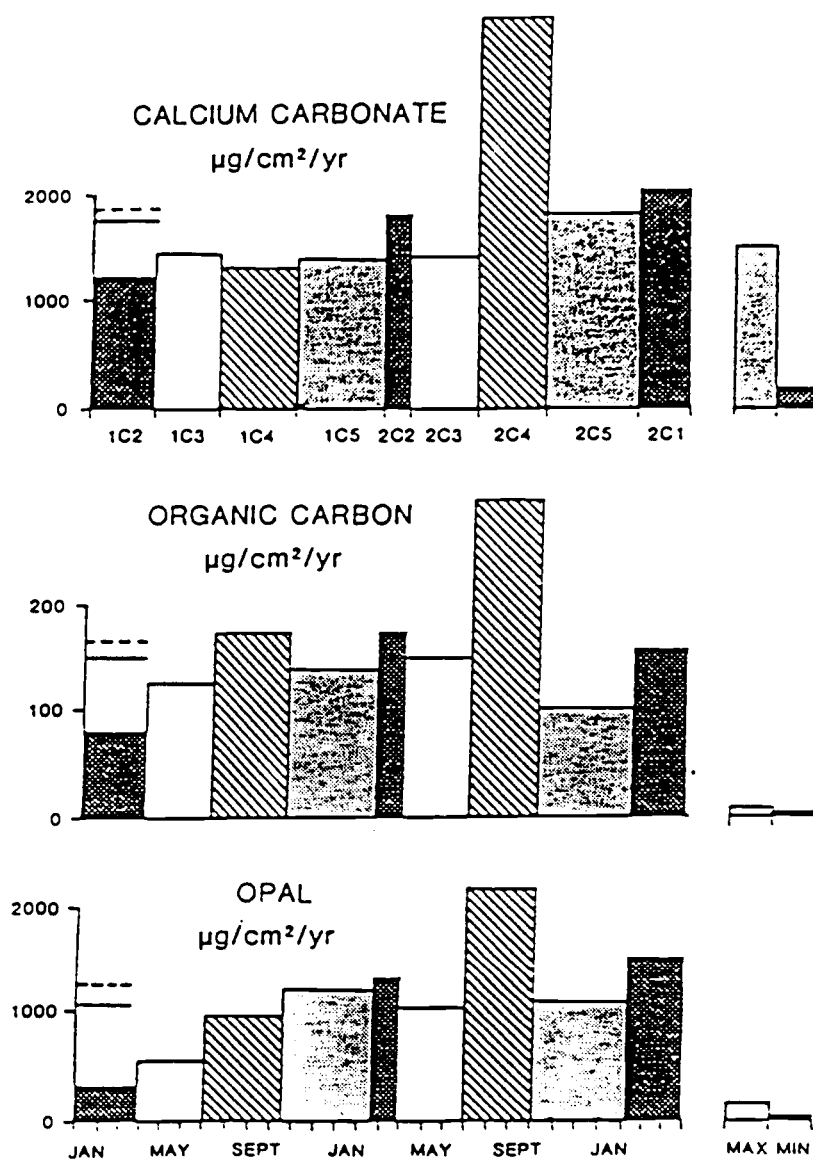


Figure I-16

at Site C and compare it to sediment accumulations measured in the surface layer of core 14 GC.

The average fluxes at Site C are as much as ten times higher than results from other studies of pelagic regions (Honjo et al., 1982; Deuser, 1986; Fischer et al., 1986). The greater flux of organic carbon to the sediment-water interface at Site C compared to MANOP Sites M and H, for example, is reflected in their pore-water oxygen profiles (Reimers et al., 1984; Emerson et al., 1985). Fluxes of carbonate and opal comparable to those at Site C were found in the fertile waters of the Panama Basin during a period of relatively low productivity for that region (Honjo, 1982).

#### Sediment Trap - Sediment Calibration

The flux of aluminum, a refractory element, can be used to determine whether the trap fluxes are similar to the sediment accumulation rate. The interval from 0-5 cm in 14 GC is used to characterize the recent accumulation at Site C (Table I-4). At first glance the fluxes are not comparable; the sediment accumulation rate being 60% higher than the flux measured in the traps. Of the aluminum in sediments at Site C, 10-20% is in an oxyhydroxide phase. Based on the Fe/Al ratio in trap material, such oxyhydroxide material is not a major component of the flux at Site C in water depths less than 3500 m (Figure I-11). Taking into account only the detrital Al accumulation rate in the sediments and the range of sedimentation rates observed at Site C ( $1.4-1.7 \text{ cm} \cdot \text{kyr}^{-1}$ ), leads to in trap and sediment fluxes of Al that differ only by 10-20%. Similarly, the trap-measured Fe flux ( $1.3 \mu\text{g} \cdot \text{cm}^{-2} \text{ yr}^{-1}$ ) is

close to the surface accumulation rate of detrital iron ( $1.3-1.6 \mu\text{g}\cdot\text{cm}^{-2} \text{yr}^{-1}$ ; Figure I-12). In contrast, the sediments are accumulating manganese an order of magnitude more rapidly than the measured trap flux. As discussed earlier in this paper, most of the manganese in Site C sediments is in an oxyhydroxide phase. If only the leach residue manganese (detrital component) is considered, the water column and sediment fluxes of manganese are similar.

The agreement between trap fluxes and accumulation rates of detrital components in Site C sediments forms the basis for our conclusion that the Fe, Al, and Mn oxyhydroxide phase is mostly acquired in the lower water column and at the sediment-water interface. This phase may account for near-bottom increases of "refractory" elements that cannot be attributed to resuspension (Dymond, in prep.). Since the trap-measured fluxes and sediment accumulation rates for aluminosilicate detritus are comparable to within 10-20%, we are confident that the trap fluxes are representative of the Recent input to the site and can be used to estimate the rates of recycling of labile components.

However, we have also considered the possibilities that the two trap deployments do not characterize the flux to the sediments during the last 2000-3000 years, that accumulations in 14 GC are not representative of the primary input to the site, that the traps do not efficiently capture aluminosilicates, or that there is an additional source of detrital components in the near bottom zone.

Using traps of the same design at other deep-sea sites, Fischer et al. (1986) have found good agreement between aluminum



fluxes in traps and sediments. Thus, trapping efficiency should not be a problem. The spatial variations in sediment accumulation at Site C is examined in Chapter II. At present, 14 GC is representative of sedimentation at the site. A sedimentation rate of  $1.1 \text{ cm kyr}^{-1}$  would produce comparable Al fluxes in the traps and sediments. This rate is, however, lower than the range of near-surface sedimentation rates at Site C. Finally, the possibility that 14 GC is receiving additional fine detritus via lateral near-bottom transport cannot be excluded. Accumulations in 14 GC are similar to nearby core RC11-210, however, so 14 GC appears to be representative of the region.

#### Temporal Estimates of Benthic Recycling

Comparison of the input fluxes of the labile components (Table I-4) to the amounts accumulating in the sediments shows that 60-62% of the calcium carbonate, 89-92% of the opal, 98-99% of the organic carbon, and 55% of the barium flux are recycled in the lower water column and near-surface sediments. The estimates of recycling are with reference to a core depth of 4287 m. Since depth-dependent calcite dissolution is evident at Site C (see Chapter II), the calcite recycled should increase with water depth. The proportion of the organic carbon flux degraded at MANOP Sites M and H in the eastern equatorial Pacific is similar (Fischer et al., 1986), but more of the opal and calcium carbonate are preserved at Site C.

Subtraction of the accumulation rate of a labile component from its rain rate yields an estimate of the benthic flux of the component (Table I-4). Downcore accumulation rate changes can be

interpreted as variations in the terms of this balance. Varying the amount of organic carbon recycled between 97.5 and 99.5% covers all the changes observed in organic carbon accumulation during the last 200 kyr. Small perturbations in the input flux, bottom water oxygen concentration, bioturbation rate, or degradation rate can easily account for these variations (Emerson, 1985).

For opal, the benthic flux of 1152-1180  $\mu\text{g cm}^{-2} \text{yr}^{-1}$  is similar to the porewater flux estimate of 910-1190  $\mu\text{g cm}^{-2} \text{yr}^{-1}$  for dissolved silica calculated from Figure I-9 using equation 2-20 of Broecker and Peng (1982) with a whole diffusion coefficient of  $2.43.2 \times 10^{-6} \text{ cm}^2 \text{sec}^{-1}$  and an e-folding depth of 2.5 cm. Similar values are obtained using the model of Schink et al. (1975). These results suggest that most of the dissolution of opal occurs at the sediment-water interface or in surficial sediments and is reflected by the porewater silica gradient.

Opal accumulation rates varied from 49-184  $\text{mg cm}^{-2} \text{kyr}^{-1}$  during the last 200 kyr at Site C (Figure I-6). If the mean opal input remained constant, changing the amount of opal recycled between 86 and 97% can account for the observed accumulation variations. Alternatively, an input change of 10% can explain the variations if the pore water flux is constant. An understanding of the factors controlling this dissolution is necessary for interpreting the record of accumulation.

Broecker and Peng (1982) suggest that the fraction of the opal rain rate that is preserved is largely controlled by the solution rate of opal and dilution by non-opaline material. We rearrange

their equation 2-4 to predict the paleo-flux of opal at Site C (Figure I-17).

$$R = A + (S^* \times C^{1/2})$$

where R is the opal rain rate in  $\text{mg cm}^{-2} \text{ kyr}^{-1}$ ;  $S^*$  is the solution rate of pure opaline sediments in  $\text{mg cm}^{-2} \text{ kyr}^{-1}$ ; and C is the concentration of opal in the sediments in  $\text{mg mg}^{-1}$ . The value for  $S^*$  ( $3000 \text{ mg cm}^{-2} \text{ kyr}^{-1}$ ) is calculated from the balance of the present rain rate and the observed accumulation. This value will increase if the present near-surface opal accumulation rate is reduced by dissolution in the sediments. We assume that this solution rate has been constant over the last 200 kyr and determine that the paleo-flux of opal varied by a factor of two between opal-rich and -poor intervals (Figure I-17). The largest fluxes occurred during the end of glacial stage 6 and the beginning of interglacial stage 5. Opal rain rates were also large during interglacial stages 1 and 7, and minimum opal fluxes occurred during periods of maximum calcite accumulation. Dymond and Lyle (1985) suggest that high opal input and a large calcite rain reflect lower primary productivity conditions. Our results imply that opal production was lower during the glacial stages compared to interglacial periods. A better understanding of the factors controlling opal solution in the sediments should help to verify these conclusions.

Varying the amount of dissolution of the modern calcite flux, as measured by sediment traps, between 25 and 85% can explain all the changes in calcium carbonate accumulation during the last 200 kyr. However, the rate of accumulation of carbonate 350 and 430

Figure I-17

Opal rain rate ( $\text{mg cm}^{-2} \text{ kyr}^{-1}$ ) predicted from Broecker and Peng (1982; eq. 2-4) versus age (kyr).  $S^*$  ( $3000 \text{ mg cm}^{-2} \text{ kyr}^{-1}$ ) is held constant over time. The dashed line is the modern flux rate ( $1305 \text{ mg cm}^{-2} \text{ kyr}^{-1}$ ; Table I-4).

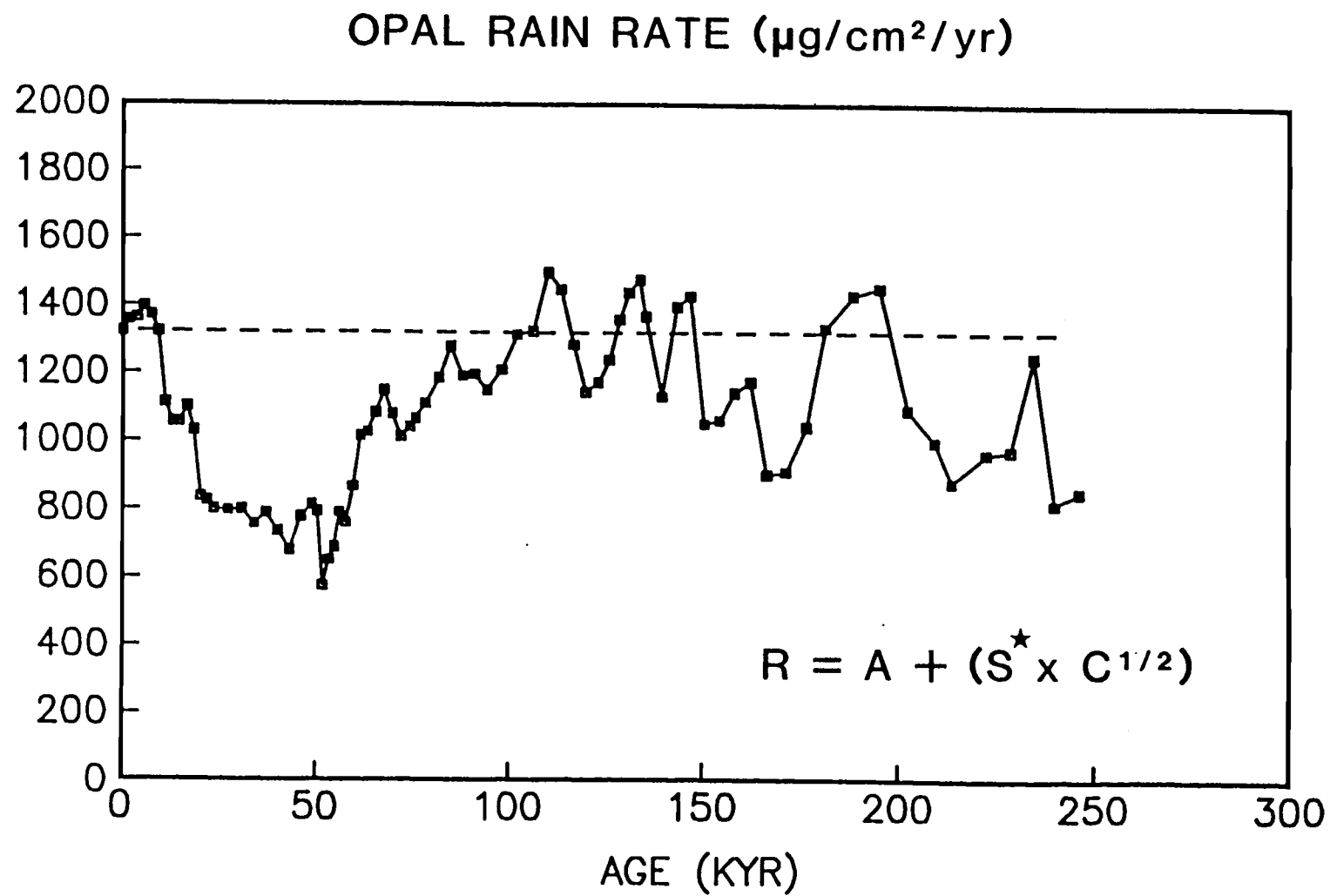


Figure I-17

kyr ago in RC11-210 (Figure I-18) cannot be accounted for by the modern flux; even neglecting dissolution, a 35% increase in calcium carbonate flux would be necessary to account for the observed accumulation. Fluxes of this magnitude are observed in the highly productive Panama Basin region (Honjo, 1982).

We note that calcareous microfossils in RC11-210 (Thompson and Saito, 1974) and nearby IPOD-DSDP Site 573 (Pujos, 1985) provide evidence for dissolution at 350 and 430 kyr. Thus, a flux increase of more than 35% is necessary to explain the record of calcite accumulation at these time intervals. Additionally, we cannot dismiss calcite flux increases during the last 200,000 years without first quantifying the record of paleo-dissolution. If the sediments at 50 kyr in 14 GC (Figure I-18) contain a calcareous microfossil assemblage that represents dissolution of more than 25%, then a flux increase above the modern value is necessary. Supplementing the high resolution record of calcite accumulation with a paleo-dissolution record could help quantify the paleo-calcite fluxes in this area.

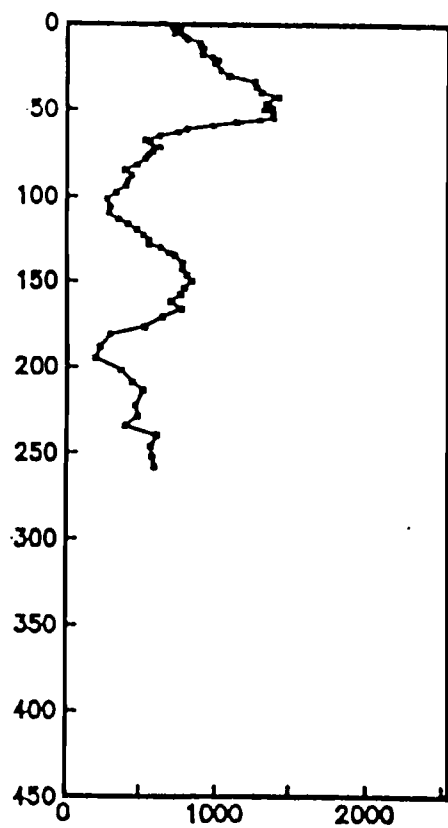
#### Calcite Storage

Previous studies (i.e., Berger, 1973) have shown that calcite dissolution largely controls carbonate cycles in the central equatorial Pacific. The cycles at Site C correspond to a factor of four difference in accumulation between carbonate-rich and -poor intervals. If this site is representative of the region, the central equatorial Pacific stored significantly more calcite during carbonate-rich periods than it does today. To estimate the

Figure I-18

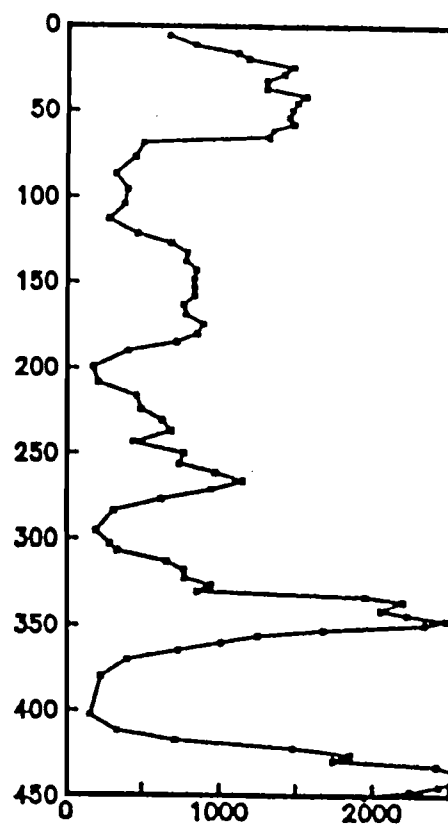
Calcium carbonate accumulation ( $\text{mg cm}^{-2} \text{ kyr}^{-1}$ ) versus age (kyr) for cores (A) 14 GC and (B) RC11-210.

W8402A 14 GC



A

RC11-210



B

Figure I-18



magnitude of this increase, we use published downcore records of calcium carbonate concentration (Arrhenius, 1952; Hays et al., 1969; Mayer, 1979) to construct patterns of accumulation during carbonate-rich and -poor intervals in the region from 0-5°N and 155-130°W (Figure I-19). This region is characterized by an increase in water depth to the west, and no major gradient with latitude between the equator and the Clipperton Fracture Zone. North of the fracture zone, however, the regional depth drops below the calcite compensation depth and calcite is not preserved in the sediments.

Contoured maps of accumulation from the Recent and the last two carbonate cycles are constructed using data from 12 cores in this region (Figure I-19). Ages for the transitions between high and low carbonate intervals are taken as the average of the 14 GC and RC11-210 transition ages (Table I-3). We assume that calcium carbonate variations are synchronous and that the non-carbonate component does little to alter the profiles at each site. To our knowledge, no evidence exists to suggest that the carbonate transitions are not isochronous in the central equatorial Pacific. The dry bulk density is determined from the calcite concentration using the empirical relationship derived earlier. The average accumulation rate for each carbonate-rich and -poor interval is calculated from the integrated carbonate content ( $\text{mg cm}^{-2}$ ) between transitions, divided by the time span of the interval. These calculated rates include values within the transitions, so are conservative estimates of the difference between carbonate-rich and -poor intervals. The sedimentation rates used to construct the

Figure I-19

Isopleths of calcium carbonate accumulation ( $\text{mg cm}^{-2} \text{ kyr}^{-1}$ ) for the area bounded by 0-5°N and 130-155°W using cores shown in (A) for (B) Recent; carbonate-poor, (C) 10-64 kyr; carbonate-rich, and (D) 64-120 kyr; carbonate-poor. A geometric contour interval is used.

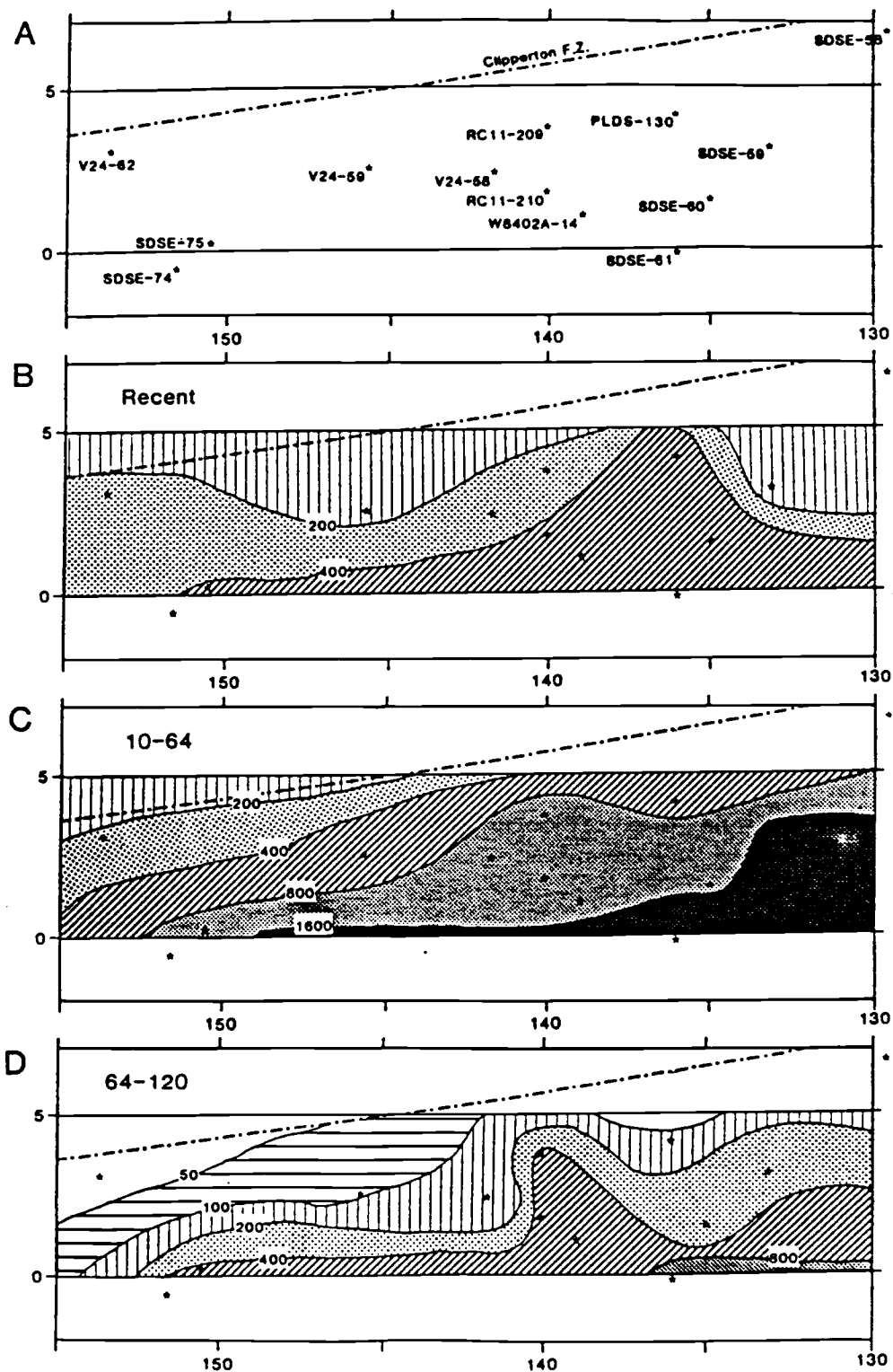


Figure I-19

pattern of Recent accumulation are determined from the difference between the depth of the 10 kyr datum and the surface. Any loss of near-surface material due to coring will bias these calculated rates, so these data are the least reliable of our calculations.

The most striking feature of these patterns is the decrease in accumulation away from the equator independent of water depth. This gradient dominates decreasing carbonate accumulation with increasing depth to the west. An increase in sedimentation rate as the equator is approached has been documented by previous studies (Arrhenius, 1952; Hays et al., 1969) and is attributed to elevated fluxes in the area of equatorial divergence. It is interesting to note that, although accumulation rates increase toward the equator, concentrations do not change significantly (Arrhenius, 1952); the decrease in carbonate concentration has a much stronger relationship to water depth. This implies that the rate of accumulation of non-carbonate material as well as of carbonate material increases in sediments beneath the equatorial divergence.

The patterns of accumulation are used to calculate the rate of removal of inorganic carbon during carbonate-rich and poor periods for the region of study. At the present time,  $5.32 \times 10^{12} \text{ g} \cdot \text{CaCO}_3 \text{ yr}^{-1}$  are removed from the oceanic system within this region. Although the data are spotty, we infer a symmetrical pattern of accumulation south of the equator and in a similar longitudinal band to the east (Figure 38 of van Andel et al., 1975). Thus, for the area bounded by  $5^\circ\text{N}$  and  $5^\circ\text{S}$  between  $105^\circ$  and  $155^\circ\text{W}$ , we estimate the present removal rate to be  $0.24 \times 10^{14} \text{ g} \cdot \text{CaCO}_3 \text{ yr}^{-1}$ . This value is 1.7% of the river input (Garrels and MacKenzie, 1971) for

an area covering 1.7% of the oceans. These figures are comparable to the accumulation estimates for the last 1 million years (Pisias and Prell, 1985).

Of greater interest is the additional calcite stored in this region during carbonate-rich intervals compared to calcite-poor periods. The interval from 10-64 kyr is used to represent a period of rapid removal and 64-120 kyr to represent a period of slower accumulation. We estimate that an additional  $0.42 \times 10^{14}$  g  $\text{CaCO}_3$   $\text{yr}^{-1}$  (3.4% of the present river input) is stored in this region during carbonate-rich intervals. We consider this estimate to represent the minimum change, because average and not the extreme conditions are used. If the river input is constant, a change of this magnitude, unless compensated for elsewhere in the ocean, would soon have a major impact on the carbonate content of seawater and the ability of the oceans to store  $\text{CO}_2$ . The significance of this removal can only be evaluated when similar calculations are available for other regions where high amplitude changes occur.

## SUMMARY AND CONCLUSIONS

This study shows that by calibrating water column flux data to surficial sediment accumulations, downcore records of accumulation can be used both to estimate paleo-fluxes and to quantify the temporal changes in recycling of labile material. Such studies are now feasible because of the development of a high-resolution oxygen isotope stratigraphy for the Pleistocene. A high resolution 200 kyr age scale based on a correlation of central equatorial Pacific core W8402A 14 GC to the reference isotope stack of Imbrie et al. (1984) can be combined with bulk chemical data obtained at the same sampling resolution as for the oxygen isotopes to develop elemental accumulation records for this site.

Calcium carbonate accumulation, which varies by a factor of four downcore, largely controls bulk sedimentation in the study area. At a 100 kyr period, the frequency band accounting for the greatest fraction of the variance in the accumulation rate record, the maximum accumulation rate (preservation) is in phase with ice volume changes, implying that the accumulation rate, which is largely controlled by dissolution, may simply reflect sea level variations. Of the present trap-measured calcite flux to the sediment-water interface, 40% is preserved. Varying the amount of dissolution between 25 and 85% can explain all the changes in calcium carbonate accumulation during the last 200 kyr. However, dissolution variations cannot account for the observed calcite accumulation at 350 and 430 kyr in nearby core RC11-210, which requires a 35% increase in the calcium carbonate flux even for 100%

preservation. The large variations in accumulation rate reflect changes in calcium carbonate storage between calcite-rich and -poor intervals. For the central equatorial Pacific (1.7% of the area of the oceans) the difference in the rate of accumulation of calcite between carbonate-rich and -poor intervals is 3.4% of the present river input. If the river input has been constant, this change must be compensated in another region to prevent a geologically instantaneous change in the  $\text{CO}_2$  content of the oceans.

No correlation exists between variations in the calcium carbonate, biogenic opal, and organic carbon accumulation rates. Presently 89-92% of the opal and 98-99% of the organic carbon fluxes are recycled in the lower water column and near-surface sediments. Opal-enriched intervals record enhanced preservation of diatoms and silicoflagellates. The paleo-flux estimates of opal suggest that opal rain rates were greatest during interglacials. The organic carbon record does not reflect these changes.

The non-biogenic fluxes can be partitioned into more than one input phase. Al, Fe, Ba, Ti, and Mn all enter the sediments in both an oxyhydroxide and detrital component. Near-surface detrital accumulation rates are comparable to the elemental fluxes measured by sediment traps. A factor of four increase in the detrital input during isotope stage 4 probably reflects an increase in particle concentration in the trade winds. The oxyhydroxide component, which is positively correlated with the calcium carbonate flux, is acquired in the lower water column or surficial sediments. Scavenging of dissolved elements by particles is the mechanism that most likely introduces this material to the sediment record. About

50% of the phosphorus is associated with oxyhydroxide and organic phases, but 40-50% also appears to be associated with the calcite shells of microplankton. Manganese input is mostly associated with the oxyhydroxide phase, but variations in the preserved record of manganese accumulation is attributed to post-depositional mobility of this element.



## REFERENCES

- Adelseck, C.G., Jr. and T.F. Anderson, The late Pleistocene record of productivity fluctuations in the eastern equatorial Pacific Ocean, Geology, 6, 388-391, 1978.
- Arrhenius, G., Sediment cores from the east Pacific, Pt. 1, In: Reports of the Swedish Deep-Sea Expeditions 1947-1948, edited by H. Pettersson, 5, p. 227, Elanders, Goteborg, 1952.
- Berger, W.H., Deep-sea carbonates: Pleistocene dissolution cycles, J. Foram. Res., 3, 187-195, 1973.
- Berner, R., Phosphate removal from sea water by absorption on volcanogenic ferric oxides, Earth Planet. Sci. Lett., 18, 77-86, 1973.
- Bischoff, J.L., G.R. Heath and M. Leinen, Geochemistry of deep-sea sediments from the Pacific manganese nodule province: Domes sites A, B, and C, In: Marine Geology and Oceanography of the Pacific Manganese Nodule Province, edited by J.L. Bischoff and D.Z. Piper, Plenum Press, New York, pp. 397-436, 1979.
- Bonatti, E., Manganese fluctuations in Caribbean sediment cores due to post depositional remobilization, Bull. Mar. Sci., 21, 510-518, 1971.
- Bostrom, K., T. Karenen and S. Gartner, Provenance and accumulation rates of silica, Al, Ti, Fe, Mn, Cu, Ni, and Co in Pacific pelagic sediments, Chem. Geol., 11, 123-148, 1973.
- Boyle, E.A., Chemical accumulation variations under the Peru Current during the past 130,000 years, J. Geophys. Res., 88, 7667-7680, 1983.

- Broecker, W.S., Calcite accumulation rates and glacial to inter-glacial changes in oceanic mixing, In: The Late Cenozoic Ice Ages, edited by K.K. Turekian, pp. 239-265, Yale University, New Haven, CT, 1971.
- Broecker, W.S. and T.-H. Peng, Tracers in the Sea, Eldigio Press, Palisades, New York, 690 pp., 1982.
- Criss, J.W., L.S. Birks and J.V. Gilfrich, Versatile X-ray analysis program combining fundamental parameters and empirical coefficients, Anal. Chem., 50, 33-37, 1978.
- Dean, W.E., J.V. Gardner and P. Cepek, Tertiary carbonate-dissolution cycles on the Sierra Leone Rise, eastern equatorial Atlantic Ocean, Mar. Geol., 39, 81-101, 1981.
- Deuser, W.G., Seasonal and interannual variations in deep-water particle fluxes in the Sargasso Sea and their relation to surface hydrography, Deep-Sea Res., 33, 225-246, 1986.
- Deuser, W.G., P.G. Brewer, T.D. Jickells and R.F. Commeau, Biological control of the removal of abiogenic particles from the surface ocean, Science, 219, 388-391, 1983.
- Dymond, J., Geochemistry of Nazca Plate surface sediments: An evaluation of hydrothermal, biogenic, detrital, and hydro-genous sources, In: Nazca Plate: Crustal Formation and Andean Convergence, edited by L.D. Kulm, J. Dymond et al., Geological Society of America Memoir, 154, pp. 133-174, 1981.
- Dymond, J., Sediment traps, particle fluxes, and benthic boundary layer processes, In: Global Ocean flux Study: Proceedings of a Workshop, September 10-14, 1984, National Academy of Science, Washington, DC, pp. 260-284, 1984.

- Dymond, J. and M. Lyle, Flux comparisons between sediments and sediment traps in the eastern tropical Pacific: Implications for atmospheric CO<sub>2</sub> variations during the Pleistocene, Limnol. Oceanogr., 30, 699-712, 1985.
- Emerson, S., Organic carbon preservation in marine sediments, In: The Carbon Cycle and Atmospheric CO<sub>2</sub>: Natural Variations Archean to Present, edited by E.T. Sundquist and W.S. Broecker, Geophysical Monograph 32, American Geophysical Union, Washington, DC, pp. 78-87, 1985.
- Emerson, S., K. Fischer, C. Reimers and D. Heggie, Organic carbon dynamics and preservation in deep-sea sediments, Deep-Sea Res., 32, 1-21, 1985.
- Finney, B.P., Paleoclimatic influence on sedimentation and manganese nodule growth during the past 400,000 years at MANOP Site H (eastern equatorial Pacific), Ph.D. Thesis, Oregon State University, Corvallis, 195 pp., 1986.
- Fischer, K., Particle fluxes to the eastern tropical Pacific Ocean Sources and Processes, Ph.D. Thesis, Oregon State University, Corvallis, 225 pp., 1983.
- Fischer, K., J. Dymond, M. Lyle, A. Soutar and S. Rau, The benthic cycle of copper: Evidence from sediment trap experiments in the eastern tropical North Pacific Ocean, Geochim. Cosmochim. Acta, 50, 1535-1543, 1986.
- Fowler, S.W. and L.F. Small, Sinking rates of euphausiid fecal pellets, Limnol. Oceanogr., 17, 293-296, 1972.

- Froelich, P.N., M.L. Bender and G.R. Heath, Phosphorus accumulation rates in metalliferous sediments on the East Pacific Rise, Earth Planet. Sci. Lett., 34, 351-359, 1977.
- Froelich, P.N., M.L. Bender, N.A. Luedke, G.R. Heath and T. DeVries, The marine phosphorus cycle, Am. J. Sci., 282, 474-511, 1982.
- Gardner, J.V., High-resolution carbonate and organic-carbon stratigraphies for the late Neogene and Quaternary from the western Caribbean and eastern equatorial Pacific, In: Initial Reports of the Deep Sea Drilling Project, 68, pp. 347-364, 1982.
- Gardner, W.D., M.J. Richardson, K.R. Hinga and P.E. Biscaye, Resuspension measured with sediment traps in a high-energy environment, Earth Planet. Sci. Lett., 66, 262-278, 1983.
- Garrels, R.M. and F.T. MacKenzie, Evolution of Sedimentary Rocks, W.W. Norton & Co., New York, 397 pp., 1971.
- Hays, J.D., T. Saito, N.D. Opdyke and L.H. Burckle, Pliocene-Pleistocene sediments of the equatorial Pacific: Their paleomagnetic, biostratigraphic and climatic record, Geol. Soc. Am. Bull., 80, 1481-1514, 1969.
- Honjo, S., Biogenic carbonate particles in the Ocean: Do they dissolve in the water column? In: The Fate of Fossil Fuel CO<sub>2</sub> in the Oceans, edited by N.R. Anderson and A. Malahoff, Plenum Press, New York, pp. 269-294, 1977.
- Honjo, S., Seasonality and interaction of biogenic and lithogenic particulate flux at the Panama Basin, Science, 218, 883-884, 1982.

- Honjo, S., S.J. Manganini and J.J. Cole, Sedimentation of biogenic matter in the deep ocean, Deep-Sea Res., 29, 609-625, 1982.
- Imbrie, J., J.D. Hays, D.G. Martinson, A. McIntyre, A.C. Mix, J.J. Morley, N.G. Pisias, W.L. Prell, and N.J. Shackleton, The orbital theory of Pleistocene climate: support from a revised chronology of the marine  $\delta^{18}O$  record, in Milankovitch and Climate, Pt. I, edited by A. Berger, J. Imbrie et al., Reidel Pub. Co., Boston, pp. 269-305, 1984.
- Jahnke, R.A., D. Heggie, S.R. Emerson and V. Grundmanis, Pore waters of the central Pacific Ocean: Nutrient results, Earth Planet. Sci. Lett., 61, 233-256, 1982.
- Jenkins, G.M. and D.G. Watts, Spectral Analysis and its Applications, 525 pp., Holden-Day, San Francisco, 1968.
- Keir, R.S. and W.H. Berger, Atmospheric  $CO_2$  content in the last 120,000 years: The phosphate-extraction model, J. Geophys. Res., 88, 6027-6038, 1983.
- Koblentz-Mishke, O.J., V.V. Volkovinsky and J.G. Kabanova, Plankton primary production of the world oceans, In: Scientific Exploration of the South Pacific, edited by W.S. Wooster, National Academy of Sciences, Washington, DC, pp. 183-193, 1970.
- Kominz, M.A., G.R. Heath, T.-L. Ku and N.G. Pisias, Brunhes time scales and the interpretation of climatic change, Earth Planet. Sci. Lett., 45, 394-410, 1979.
- Krishnaswami, S., Authigenic transition elements in Pacific pelagic clays, Geochim. Cosmochim. Acta, 40, 425-434, 1976.

- Ku, T.-L. and T. Oba, A method for quantitative evaluation of carbonate dissolution in deep-sea sediments and its application to paleoceanographic reconstruction, Quat. Res., 10, 112-129, 1978.
- Leinen, M., A normative calculation technique for determining opal in deep-sea sediments, Geochim. Cosmochim. Acta, 41, 671-676, 1977.
- Leinen, M., D. Cwienk, G.R. Heath, P.E. Biscaye, V. Kolla, J. Thiede and J.P. Dauphin, Distribution of biogenic silica and quartz in recent deep sea sediments, Geology, 14, 199-203, 1986.
- Luz, B. and N.J. Shackleton,  $\text{CaCO}_3$  solution in the tropical Pacific during the past 130,000 years, In: Dissolution of Deep-Sea Carbonates, edited by W.V. Sliter, A.W.H. Be, et al., Cushman Found. Foram. Res., Special Publication, 13, 142-150, 1975.
- Lyle, M. and J. Dymond, Metal accumulation rates in the Southeast Pacific: Errors introduced from assumed bulk densities, Earth Planet. Sci. Lett., 30, 164-168, 1976.
- Martinson, D.G., W. Menke and P. Stoffa, An inverse approach to signal correlation, J. Geophys. Res., 87, 4807-4818, 1982.
- Martinson, D.G., N.G. Pisias, J.D. Hays, T.C. Moore, J. Imbrie and N.J. Shackleton, Age dating and the orbital theory of the ice ages: Development of a high resolution 0-300 kyr chronostratigraphy, Quat. Res., in press.
- Mayer, L.A., The origin and geologic setting of high-frequency acoustic reflectors in deep-sea carbonates, Ph.D. Thesis, University of California, San Diego, 159 pp., 1979.

- Molina-Cruz, A., The relation of the southern tradewinds to upwelling processes during the last 75,000 years, Quat. Res., 8, 324-338, 1977.
- Moore, T.C., Jr., N.G. Pisias and G.R. Heath, Climate changes and lags in Pacific carbonate preservation, sea surface temperature and global ice volume, In: The Fate of Fossil Fuel CO<sub>2</sub> in the Oceans, edited by N.R. Anderson and A. Malahoff, Plenum Press, New York, pp. 145-165, 1977.
- Moore, T.C., Jr. and G.R. Heath, Sea-floor sampling techniques, In: Chemical Oceanography, edited by J.P. Riley and R. Chester, Academic Press, New York, pp. 75-126, 1978.
- Moore, T.C., Jr., N.G. Pisias and D.A. Dunn, Carbonate time series of the Quaternary and Late Miocene sediments in the Pacific Ocean: A spectral comparison, Mar. Geol., 46, 217-233, 1982.
- Morley, J.J. and J.D. Hays, Towards a high-resolution, global, deep-sea chronology for the last 750,000 years, Earth Planet. Sci. Lett., 53, 279-295, 1981.
- Müller, P.J. and E. Suess, Productivity, sedimentation rate and sedimentary organic matter in the oceans, 1, Organic carbon preservation, Deep-Sea Res., 26, 1347-1362, 1979.
- Müller, P.J., H. Erlenkeuser and R. von Grafenstein, Glacial-interglacial cycles in oceanic productivity inferred from organic carbon contents in eastern North Atlantic sediment cores, In: Coastal Upwelling: Its Sediment Record, Part B, edited by J. Thiede and E. Suess, pp. 365-398, 1983.

- Murray, D.W. and J. Dymond, The seasonal rain of microfossils and organic carbon to the deep sea in the equatorial Pacific (abstr.), Transactions, American Geophysical Union, EOS, 66, p. 1275, 1985.
- Nigrini, C.A., Radiolarian zones in the Quaternary of the equatorial Pacific Ocean, In: The Micropaleontology of the Oceans, edited by B.M. Funnell and W.R. Riedel, Cambridge University Press, Great Britain, pp. 443-461, 1971.
- Pedersen, T.F., Increased productivity in the eastern equatorial Pacific during the last glacial maximum (19,000 to 14,000 yrs B.P.), Geology, 11, 16-19, 1983.
- Pisias, N.G., Late Quaternary sediment of the Panama Basin: Sedimentation rates, periodicities, and controls of carbonate and opal accumulation, Geol. Soc. Am. Mem., 145, 375-391, 1976.
- Pisias, N.G. and W.L. Prell, Changes in calcium carbonate accumulation in the equatorial Pacific during the Late Cenozoic: Evidence from HPC Site 572, In: The Carbon Cycle and Atmospheric CO<sub>2</sub>: Natural Variations Archean to Present, Geophysical Monograph 32, American Geophysical Union, Washington, DC, pp. 443-454, 1985.
- Pisias, N.G., D.W. Murray and A.K. Roelofs, Radiolarian and silicoflagellate response to oceanographic changes associated with the 1983 El Niño, Nature, 320, 259-262, 1986.



- Pujos, A., Nannofossils from Quaternary deposits in the high-productivity area of the central equatorial Pacific, DSDP Leg 85, In: Initial Reports of the Deep Sea Drilling Project, 85, pp. 553-619, U.S. Government Printing Office, Washington, DC, 1985.
- Rea, D.K., Fluctuation in eolian sedimentation during the past five glacial-interglacial cycles: A preliminary examination of data from Deep-Sea Drilling Project Hole 503B, eastern equatorial Pacific, In: Initial Reports of the Deep Sea Drilling Project, 68, pp. 409-415, U.S. Government Printing Office, Washington, DC, 1982.
- Rea, D.K., L.W. Chambers, J.M. Chuey, T.R. Janecek, M. Leinen and N.G. Pisias, A 450,000-year record of cyclicity in oceanic and atmospheric processes from the eastern equatorial Pacific, Paleoceanography, in press.
- Reimers, C.E., S. Kalhorn, S. Emerson and K.H. Nealson, Oxygen consumption rates in pelagic sediments from the central Pacific: First estimates from microelectrode profiles, Geochim. Cosmochim. Acta, 48, 903-910, 1984.
- Robbins, J., G.R. Heath and M.W. Lyle, A sequential extraction procedure for partitioning elements among co-existing phases in marine sediments, College of Oceanography Ref. 84-3, Oregon State University, Corvallis, 55 pp, 1984.
- Romine, K., Late Quaternary history of atmospheric and oceanic circulation in the eastern equatorial Pacific, Mar. Micropaleo., 7, 163-187, 1982.

- Romine, K. and T.C. Moore, Jr., Radiolarian assemblage distributions and paleoceanography of the eastern equatorial Pacific Ocean during the last 127,000 years, Paleoceanogr. Paleoclim. Paleoecol., 35, 281-314, 1981.
- Rowe, G.T. and W.D. Gardner, Sedimentation rates on the slope water of the northwest Atlantic Ocean measured directly with sediment traps, J. Mar. Res., 37, 581-600, 1979.
- Sawlan, J.J. and J.W. Murray, Trace metal remobilization in the interstitial waters of red clay and hemipelagic marine sediments, Earth Planet. Sci. Lett., 64, 213-230, 1983.
- Schink, D.R., N.L. Guinasso, Jr. and K.A. Fanning, Processes affecting the concentration of silica at the sediment-water interface of the Atlantic Ocean, J. Geophys. Res., 8, 3013-3031, 1975.
- Schramm, C.T., Implications of radiolarian assemblages for the late Quaternary paleoceanography at the eastern equatorial Pacific, Quar. Res., 24, 204-218, 1985.
- Shackleton, N.J., and N.D. Opdyke, Oxygen isotope and paleomagnetic stratigraphy of equatorial Pacific core V28-238: Oxygen isotope temperatures and ice volumes on a  $10^5$  and  $10^6$  year scale, Quat. Res., 3, 39-55, 1973.
- Small, L.F., S.W. Fowler and M.Y. Unlu, Sinking rates of natural copepod fecal pellets, Mar. Biol., 51, 233-241, 1979.
- Spencer, D.W., P.G. Brewer, A. Fleer, S. Honjo, S. Krishnaswami and Y. Nozaki, Chemical fluxes from a sediment trap experiment in the deep Sargasso Sea, J. Mar. Res., 36, 493-523, 1978.

- Spiess, F.N. and M. Weydert, Cruise report: Rama Leg 1, MANOP Sites C and R, SIO Ref. 84-8, Marine Physical Laboratory, Scripps Institute of Oceanography, San Diego, CA, 23 pp., 1984.
- Thompson, P.R. and T. Saito, Pacific Pleistocene sediments: Planktonic foraminifera dissolution cycles and geochronology, Geology, 2, 333-335, 1974.
- Uematsu, M., R.A. Duce, S. Nakaya and S. Tsunogai, Short-term temporal variability of eolian particles in surface waters of the Northwestern North Pacific, J. Geophys. Res., 90, 1167-1172, 1985a.
- Uematsu, M., R.A. Duce and J.M. Prosperó, Deposition of atmospheric mineral particles to the north Pacific Ocean, J. Atmos. Chem., 3, 123-138, 1985b.
- Valencia, M.J., Pacific Pleistocene paleoclimatic stratigraphies: A comparative analysis of results, Quat. Res., 8, 339-354, 1977.
- van Andel, T.H., G.R. Heath and T.C. Moore, Jr., Cenozoic Tectonics, sedimentation, and paleoceanography of the central equatorial Pacific, Geol. Soc. Am. Mem., 143, 134 pp., 1975.
- van Bennekom, A.J. and S.J. van der Gaast, Possible clay structures in frustules of living diatoms, Geochim. Cosmochim. Acta, 40, 1149-1152, 1976.
- Volat, J.-L., L. Pastouret and C. Vergnaud-Grazzini, Dissolution and carbonate fluctuations in Pleistocene deep-sea cores: A review, Mar. Geol., 34, 1028, 1980.

- Walsh, I., Resuspension and the rebound process: Implications of sediment trap studies in the Northern Pacific, M.S. Thesis, Oregon State University, Corvallis, 108 pp., 1985.
- Walsh, I., J. Dymond and R. Collier, Rates of recycling of biogenic components of fast settling particles derived from sediment trap experiments, Deep-Sea Res., submitted.
- Walsh, I., K. Fischer, D.W. Murray and J. Dymond, Evidence for resuspension of virgin particles from near-bottom sediment traps, Deep-Sea Res., submitted.
- Weliky, K., E. Suess, C.A. Ungerer, P.J. Müller and K. Fischer, Problems with accurate carbon measurements in marine sediments and particulate matter in seawater: A new approach, Limnol. Oceanogr., 28, 1252-1259, 1983.

## CHAPTER II

SPATIAL VARIATIONS IN SEDIMENT ACCUMULATION AT MANOP

SITE C, CENTRAL EQUATORIAL PACIFIC: EVIDENCE

FOR EASTWARD FLOWING BOTTOM-WATERS

PRIOR TO 9,000 YEARS AGO

## ABSTRACT

Relative to cores from the central basin at MANOP Site C, a pelagic carbonate-rich site in the central equatorial Pacific, cores 150-200 m shallower and 6-10 km further from topographic highs have accumulated 50% more pelagic sediment during the last 200,000 years. The core to core differences are attributed to a combination of depth-dependent calcium carbonate solution and lateral transport of fine material by accelerated bottom-water flow around topographic highs.

Spatial variations in calcium carbonate and aluminum deposition can be used to differentiate these two processes. From 0 to 9000 years ago, excess material has accumulated in the lee of seamounts located to the north and east in response to currents flowing toward the southwest or west. Prior to this time, however, flow toward the east or northeast is necessary to explain the observed depositional patterns. This flow was strongest prior to 63,000 years ago.

## INTRODUCTION

During the Manganese Nodule Project (MANOP) the water column and underlying sediments were extensively sampled at five sites in the eastern Pacific. These sites were chosen to represent the five major Pacific sediment types (carbonate ooze, siliceous clay, red clay, metalliferous clay, and hemipelagic clay). At the carbonate site (Site C), 28 gravity cores were collected between 4280 and 4480 meters water depth in an area 25 km by 20 km (Figure II-1, Table II-1). These cores, which penetrated up to 3.5 meters sub-bottom, record late-Quaternary sedimentation patterns at the site. A typical core from this region contains alternating carbonate-rich and -poor intervals which correspond to glacial and interglacial periods, respectively (see Chapter I). These glacial/interglacial intervals display the light and dark layering typical of the carbonate ooze belt of the equatorial Pacific (Arrhenius, 1952). A given layer is assumed to be synchronous across the site allowing the visible sequence of light and dark layers to be used to correlate the cores. By visually correlating 13 cores from Site C, Lyle and Heath (1980) showed that layer thicknesses at the deepest locations are only 80% of those from the shallowest sites. Lyle and Heath suggested that the decrease in sedimentation rate with depth could be attributed to either depthdependent dissolution of calcium carbonate or bottom currentdependent sediment deposition.

Figure II-1

Bathymetry of MANOP Site C constructed from 12 kHz records obtained during the W8402A cruise. Deep-Tow data from the area of the small dashed rectangle (Spiess and Weydert, 1984) are also included. Large dashed rectangle shows area of Figure II-6. Triangles ( $\Delta$ ) and closed circles ( $\bullet$ ) are gravity core locations. The seven triangles identify the cores used in the geochemical study. The circled triangle ( $\textcircled{\Delta}$ ) is the location of reference core W8402A 14 GC. Core designations pre-fixed with a W, B, R, and K refer to cruises W8402A, Benthic III, RAMA I, and K7905, respectively. The exact locations of all the K7905 cores in the intensely cored area are given in Spiess and Weydert (1984).



Figure II-1

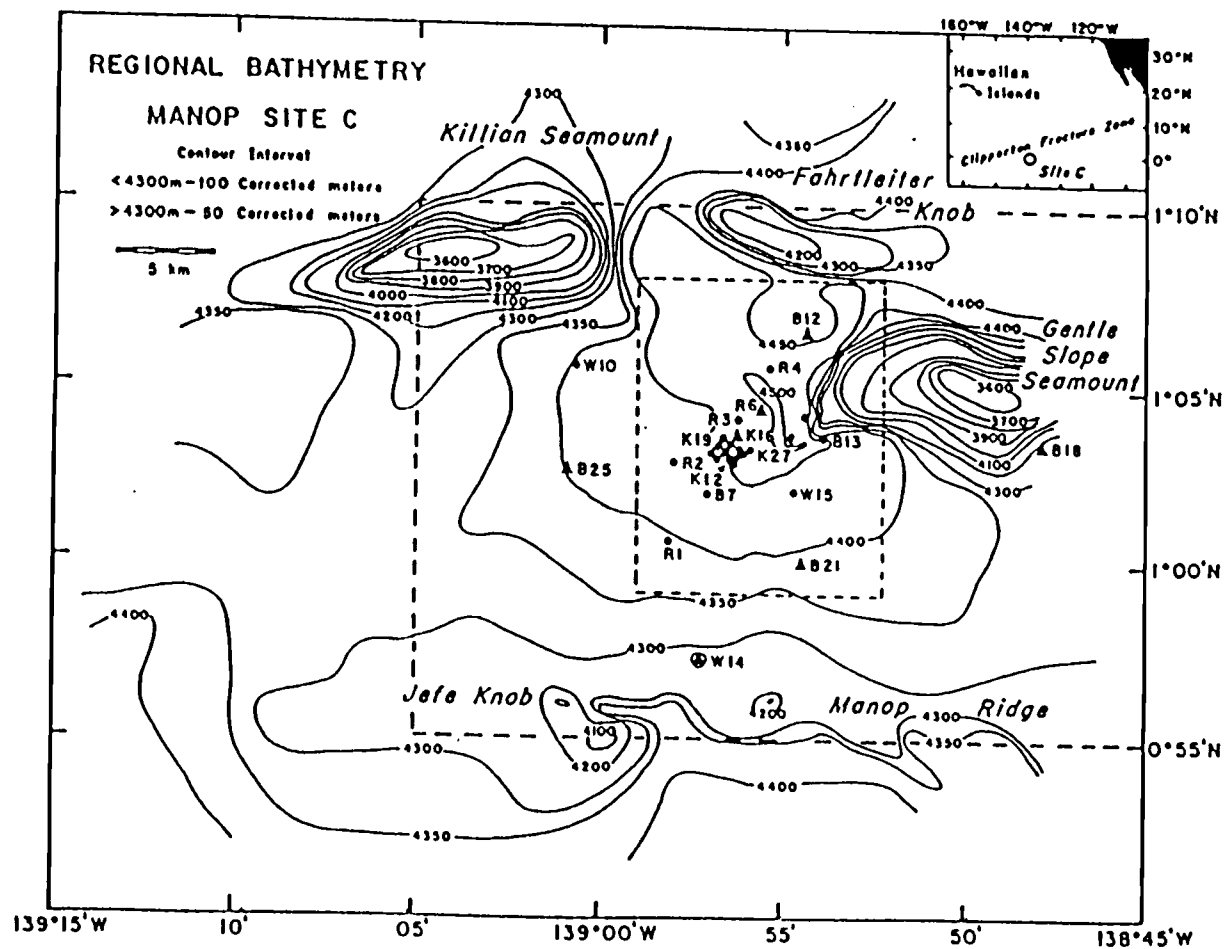


Table II-1. Gravity Cores from MANOP Site C.

Cruise	Core <sup>a</sup>	Location <sup>b</sup> (Lat. N, Long. W)	Water Depth (corrected meters)	Length (cm)
K7905	7	1°3.37', 138°56.49'	4455	273
	12	1°3.00', 138°56.52'	4447	245
	14	1°3.16', 138°56.63'	4447	256
	16	1°3.56', 138°56.32'	4463	279
	19	1°3.35', 138°56.75'	4445	248
	20	1°3.09', 138°57.00'	4440	281 <sup>c</sup>
	24	1°3.02', 138°56.84'	4440	256
	27	1°3.24', 138°55.91'	4464	223
	29	1°3.26', 138°56.23'	4457	238
	31 <sup>d</sup>	1°2.82', 138°56.40'	4452	96
	37	1°3.53', 138°56.64'	4452	51
	40	1°3.12', 138°56.17'	4454	216
	43	1°2.97', 138°56.33'	4449	232
RAMA I	1	1°0.59', 138°58.25'	4372	274
	2	1°2.85', 138°55.07'	4408	269
	3	1°4.07', 138°56.23'	4464	272
	4 <sup>e</sup>	1°5.49', 138°55.36'	4434	366
	6	1°4.34', 138°55.63'	4478	280
BENTHIC III	7	1°02.03', 138°56.79'	4425	258
	12	1°02.03', 138°56.79'	4425	258
	13	1°03.13', 138°53.51'	4425	318
	18	1°03.5', 138°48.0 <sup>f</sup>	4281	278
	19	1°04.06', 138°55.12'	4477	118
	21	1°00.06', 138°54.45'	4379	278
	25	1°02.70', 139°01.00'	4401	286
W8402A	10	1°05.8', 139°00.8 <sup>f</sup>	4404	317
	14	0°57.2', 138°57.3 <sup>f</sup>	4287	333
	15	1°02.0', 138°54.7 <sup>f</sup>	4420	314

<sup>a</sup>All cores stored at OSU unless otherwise noted<sup>b</sup>Unless indicated, locations given by Marine Physical Laboratory, Scripps (Spies and Weydert, 1984; BENTHIC III cruise report)<sup>c</sup>Missing ~10 cm at top<sup>d</sup>Pore water core<sup>e</sup>Stored at Scripps<sup>f</sup>Positions determined by satellite navigation

In this study, we increase the number of cores that are visually correlated to better define the spatial patterns of sediment deposition. We supplement these data with bulk chemical analyses from seven selected cores to help distinguish changes attributed to carbonate dissolution from differential deposition. The spatial variation in sedimentation at this site is examined for five intervals spanning the last 200 kyr. These intervals represent deposition during two separate carbonate-rich and -poor periods in addition to the Recent. Spatial patterns of sediment accumulation for the five intervals are constructed using the sediment thicknesses between visual correlations. Errors in the synchronicity of the datums are evaluated with the chemical data. The chemical data is also used to calculate elemental accumulations within the five intervals. If the variations in sediment accumulation were due only to dissolution, the accumulation rates of non-carbonate refractory components, such as aluminum and titanium, should not vary with depth. The elemental accumulation data can, therefore, be used to test whether the variations in sedimentation can be attributed to depth-dependent carbonate dissolution or whether other processes are necessary to explain the observed patterns.

#### SITE DESCRIPTION

Site C is located in the carbonate ooze belt of the equatorial Pacific. Surface waters in this region are characterized by high primary productivity associated with the equatorial divergence. The sediment is mostly biogenic in origin, consisting primarily of

the shells of calcareous microplankton (foraminifera and coccolithophores), with opal microplankton shells (Radiolaria, diatoms and silicoflagellates) of secondary importance. Terrigenous aluminosilicates transported as eolian dust dominate the non-biogenic component of the sediments. As noted above, the cores exhibit alternating light and dark layers associated with carbonate-rich and -poor intervals, respectively. The intervals of enhanced carbonate preservation were deposited during glacial periods (Arrhenius, 1952; Hays et al., 1969)

The topography of the study area consists of a depression that is bounded to the north and east by small seamounts rising 900 m above the seafloor (Figure II-1). Sidescan sonar shows rock outcrops on the small seamount (Gentle Slope Seamount) to the east of the extensively cored area (Spiess and Weydert, 1984). A small moat, approximately 3 km across and 60 m deep, is evident in the 12 kHz records from the north and south sides of the Gentle Slope Seamount. Similar features observed around other seamounts have been attributed both to tectonic and erosional processes (Menard, 1964; Lowrie and Heezen, 1967; Johnson and Johnson, 1970; Roberts et al., 1974). The moats at Site C are most similar to those described by Johnson and Johnson (1970). We believe that they result from erosion or differential accumulation around the small seamount.

Current meter measurements at Site C support this inference. From 12 December 1982 to 21 February 1984, the mean flow of bottom water at a depth of 4400 m (50 m above bottom) in the central depression was to the southwest; a direction consistent with the location of the observed moats. The average velocity was 5.5 cm

$\text{sec}^{-1}$  with a maximum of  $20 \text{ cm sec}^{-1}$ . Such speeds are capable of redistributing loosely bound bottom sediments (Lampitt, 1985).

In addition to material settling from the water column, the central depression has also accumulated pelagic turbidite deposits. The base of a turbidite that was deposited approximately 20 kyr ago is shown as horizon 2 in Figure II-2. The base is distinguished by a concentration of well-sorted foraminifera. This turbidite is not evident in cores shallower than 4400 m. Fining-upward sequences as much as 78 cm-thick are observed in cores from the deepest part of the depression. Four cores close to Gentle Slope Seamount contain two additional thin coarse-grained layers dominated by foraminifera. The presence of pre-Bruhnes siliceous microfossils in these layers suggest that this material was carried into the basin, rather than being produced from in situ winnowing by bottom currents. We assume that the mini-turbidites represent instantaneous additions of material to the study area, and subtract the turbidites from the sediment section so that we can study "normal" pelagic sediment accumulation processes.

Figure II-2

Correlations based on color changes. Horizon 2 marks the base of a pelagic turbidite. Cores K7905 12 GC and K7905 27 GC bracket the variations observed in the 13 cores studied by Lyle and Heath (1980). The cores are generally arranged with water depth increasing and distance from Gentle Slope Seamount decreasing to the right of the figure.

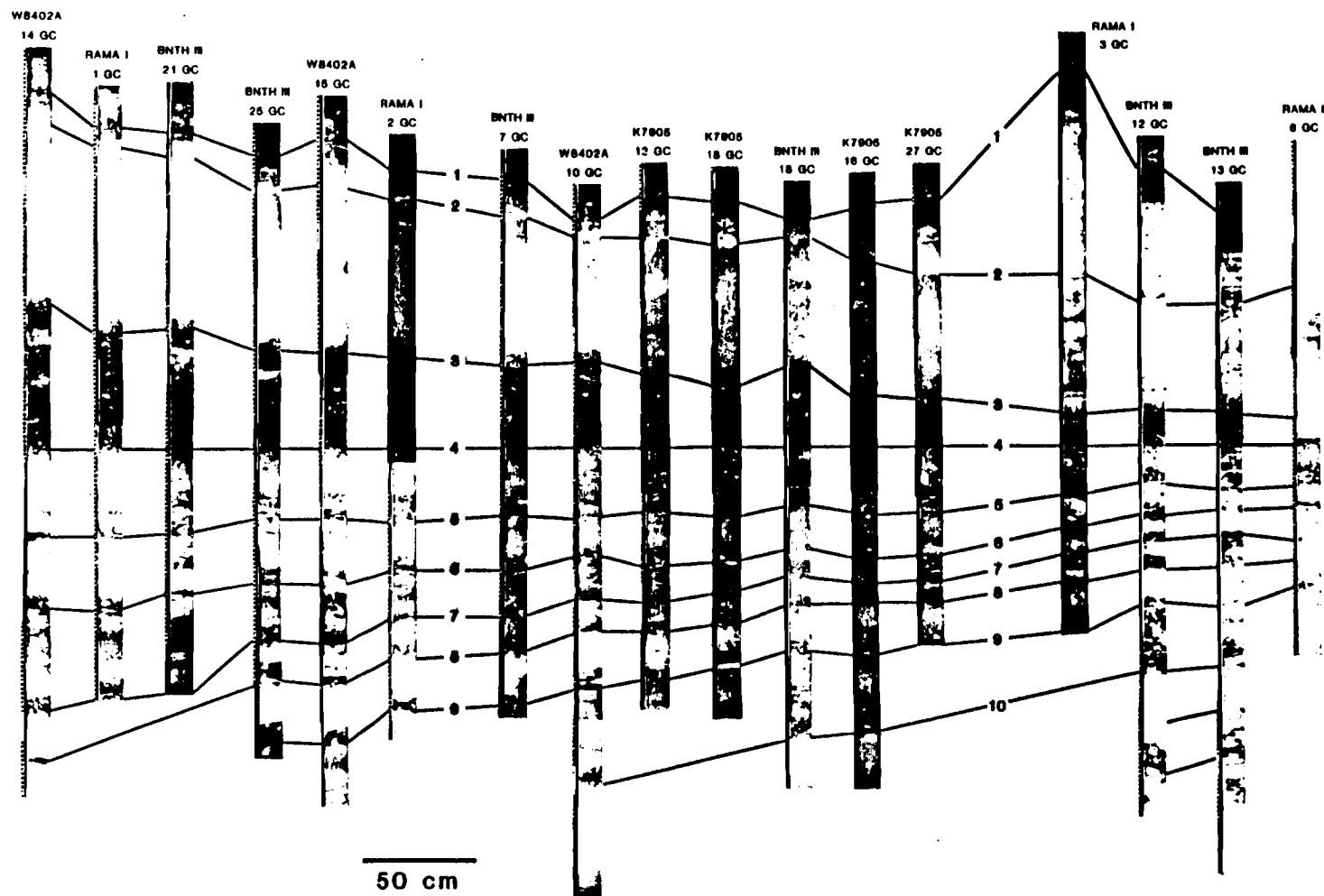


Figure II-2

## METHODS

Solid Phase Chemistry

Seven cores distributed across the site (Figure II-1) were selected for detailed bulk chemical analysis (Appendix 1). Analyses were performed on a wavelength dispersive Phillips P.W. 1600 simultaneous X-ray fluorescence (XRF) spectrometer. Approximately 2.5 g of ground sample were pressed at five tons pressure into XRF discs with a cellulose backing. Batches of 18 samples were analyzed using an internal monitor to check for instrument drift during a run and a USGS standard to check the accuracy between runs. The spectrometer is controlled by a Digital Equipment Corporation PDP 11/34 minicomputer which also manages the data collection and reduction programs. A fundamental parameters program developed by Criss Software, Inc. (c.f. Criss et al., 1978) in addition to a background stripping program developed at Oregon State University are used for the data reduction (G. Campi, written communication, 1986). A set of 64 rock and sediment standards from the U.S. Geological Survey, National Bureau of Standards, Canada and France, as well as in-house clay standards are used to calibrate the data reduction program. The precision for the reported elements is within 3% and the accuracies are within 7%. Opal was calculated as 2.5 times the difference between total Si and detrital Si with detrital Si taken as 4.0 times the Al concentration (see Chapter I). Reported dry bulk densities necessary for calculating elemental accumulations were determined using the equation of Kominz et al. (1979). The inferred particle specific gravity of



$2.7 \text{ g cm}^{-3}$  is reasonable for Site C sediments. Reported core depths reflect adjustments for turbidites as noted in Appendix 1.

### Correlations

Light and dark colored layers have been used for the preliminary correlation of the cores (Figure II-2). For thick, dark layers, both the top and bottom levels are used, whereas, only the bottom of thin, dark layers (horizons 5-8, Figure II-2) are noted. Horizon 1 is the darkest interval within the surface layer. In cores where elemental analyses are available, horizon 1 corresponds to the depth of maximum manganese concentration. Horizon 2 marks the bottom of a pelagic turbidite. In Figure II-2, this horizon is approximated in cores where no turbidite is present, based on the distance of the top of the turbidite from horizon 1 in other cores. At the base of the turbidite, the color appears to be leached from core RAMA I 6 GC. Therefore, the depth of horizon 3 in this core is based on characteristic burrow structures. A thin turbidite layer deposited between horizons 6 and 7 in some of the deeper cores provides an added time marker.

In addition to visual correlations, seven cores were matched using calcium carbonate variations. Other studies of this region (i.e., Arrhenius, 1952; Hays et al., 1969; Valencia, 1977) have shown that the distinctive variations of calcite concentration in equatorial Pacific sediments provide a reliable method for correlating cores. The downcore profiles of calcium carbonate concentration for seven Site C cores are presented in Figure II-3. For comparison of the carbonate cycles, we also show the well

documented record from nearby core RC11-210 ( $1^{\circ}49'N$ ,  $140^{\circ}03'W$ ; 4420 m; Thompson and Saito, 1974; Chuey et al., in prep.).

Calcium carbonate concentrations in all cores were interpolated at 3 cm intervals and correlated to W8402A 14 GC (14 GC in subsequent references) using the signal correlation technique of Martinson et al. (1982). Core 14 GC was chosen as the reference signal because of its thick carbonate-rich and -poor sections and the high resolution age scale based on oxygen isotopic data that has been developed for it (see Chapter I). High coherencies between the reference signal and the correlated carbonate records require only five coefficients to define the mapping functions (Table II-2). For most cores, higher coherencies are obtained using more than five coefficients, but the resulting correlations produced anomalous squeezing and stretching of the records.

The chronostratigraphic framework developed for 14 GC is used to assign age scales to each of the other six cores. The mapping coefficients generated in the correlation of a core (x) to 14 GC are used to obtain depths in 14 GC corresponding to each depth in core x. The age assigned to the 14GC depth based on oxygen isotope stratigraphy is used for the corresponding depth in core x. Using these age scales, a plot of calcium carbonate concentration versus a common age (Figure II-4) gives a sense of how well the other cores mapped to 14 GC, and show variations in the location of the carbonate transitions in each core.

Figure II-3

Calcium carbonate concentration (%) versus sub-bottom depth (cm)  
for seven Site C cores in addition to nearby core RC11-210. Solid  
lines A-E mark the depths of carbonate transition correlations and  
are assumed to be synchronous between cores. Dashed lines 1-7  
correspond to the visual correlations of Figure II-2.

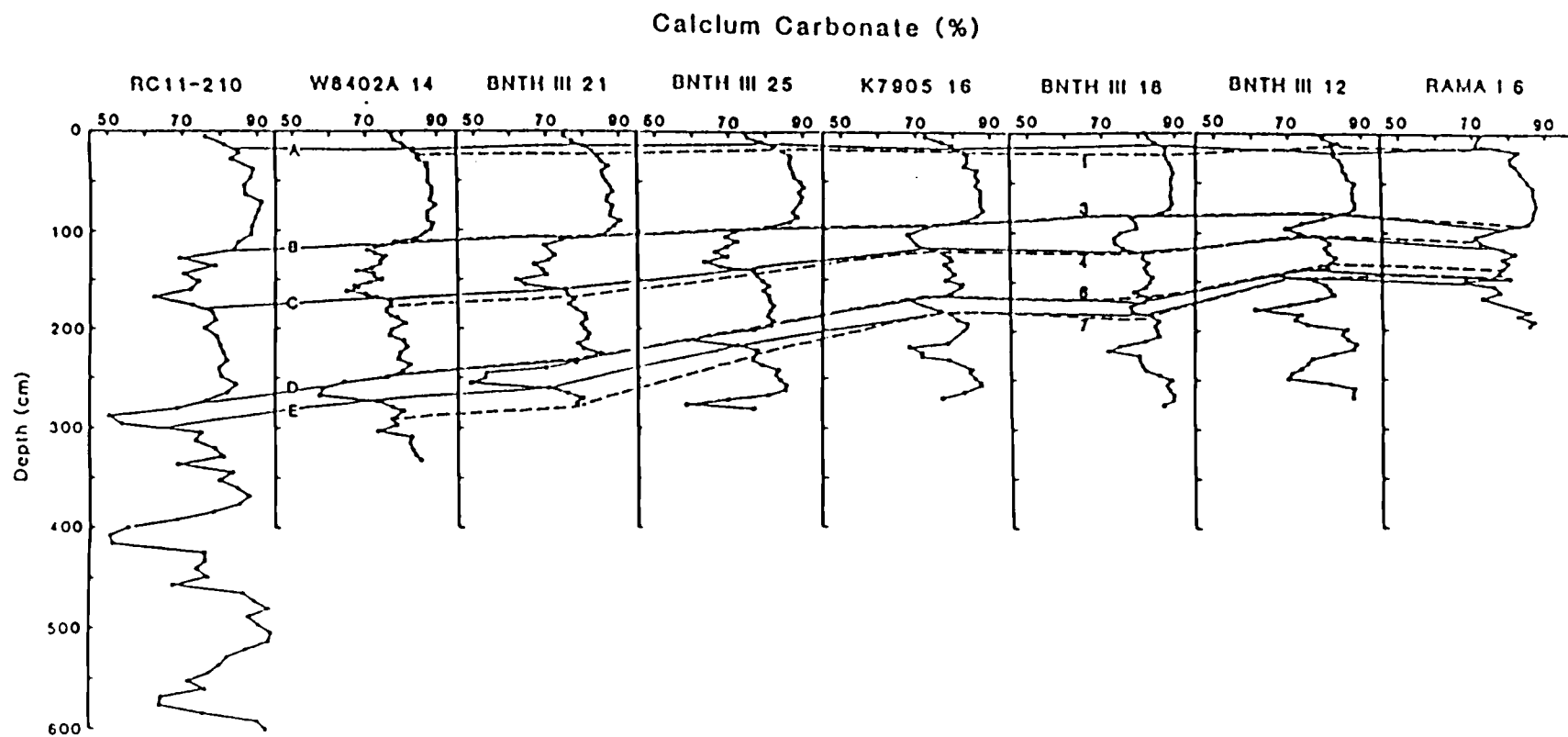


Figure II-3

Table II-2. Coherencies of the correlations to 14 GC

---

<u>Core</u>			<u>Coherency</u>
K7905	I	6 GC	0.89
RAMA	I	6 GC	0.83
BENTHIC	III	12 GC	0.88
BENTHIC	III	18 GC	0.88
BENTHIC	III	21 GC	0.98
BENTHIC	III	25 GC	0.96
RC11-210	PC		0.96

Figure II-4

(A) Calcium carbonate concentration (%) versus age (kyr) for cores W8402A 14 GC (solid), BENTHIC III 21 GC (dashed), BENTHIC III 25 GC (dotted), and K7905 16 GC (solid with squares). Ages are based on the 14 GC time scale correlated to the other cores using the profiles of calcium carbonate concentration. (B) As A, but for cores W8402A 14 GC (solid), BENTHIC III 18 GC (dashed), BENTHIC III 12 GC (dotted) and RAMA I 6 GC (solid with squares).

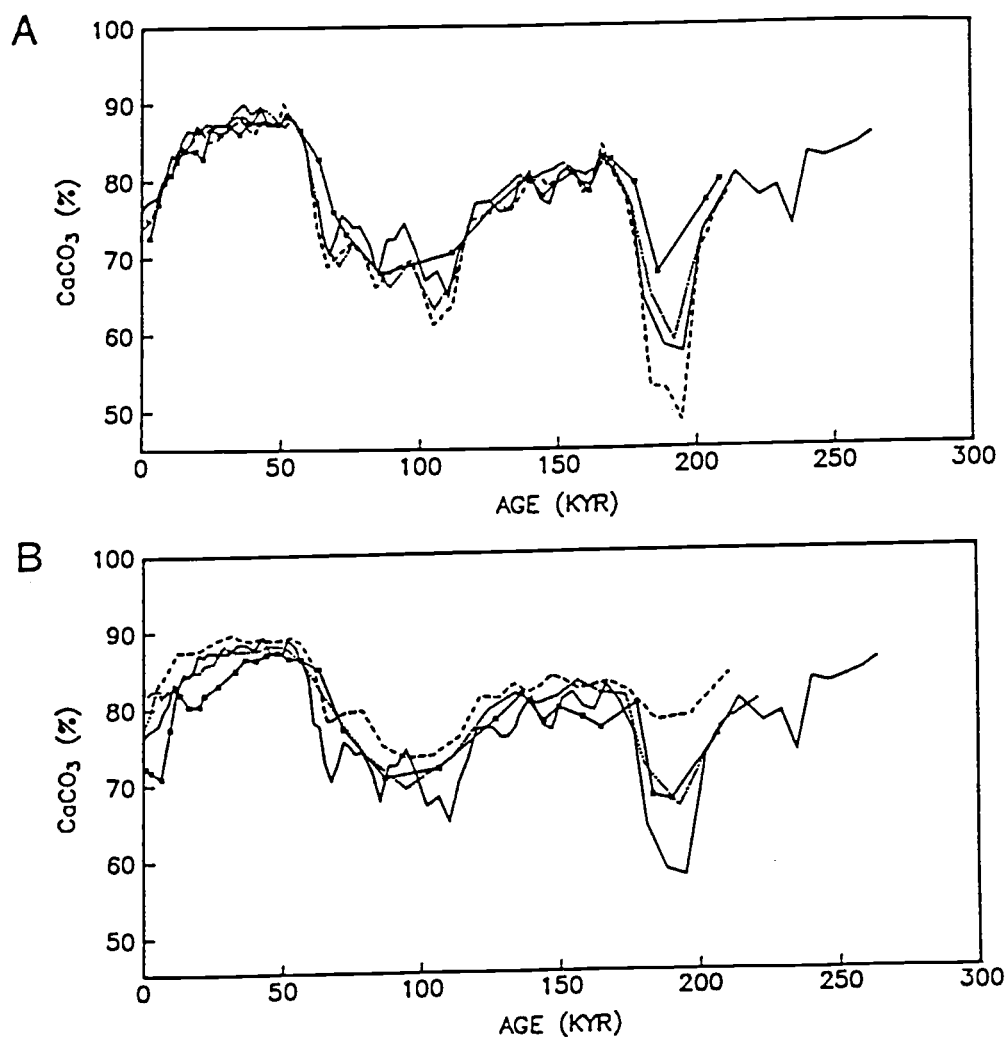


Figure II-4

### Accumulation Rates

Dry bulk density and bulk chemical data were used to calculate the integrated rate of accumulation of each sediment component for a given interval by trapezoidal integration between datum pairs using the equation:

$$A = \sum_{i=1}^n \left[ \frac{x_i d_i + x_{i+1} d_{i+1}}{2} \right] \times L \times 10^3$$

where A is the integrated accumulation in  $\text{mg cm}^{-2}$ ;  $x_i$  is the concentration of an element in a sample;  $d_i$  is the dry bulk density of the sample in  $\text{g cm}^{-3}$ ; L is the distance between samples in cm; and n is the number of samples between datums. Adjustments in L were made when one of the datums fell between samples. The factor of  $10^3$  converts from grams to milligrams. The integrated mass deposited during an interval can be converted to an average accumulation rate by dividing by the time span between correlated datums.



## RESULTS

Before constructing spatial patterns of sediment accumulation at Site C, we examine the temporal variations in the correlation datums. The depth discrepancies between the visual correlations (numbers) and the correlation of transitions in calcium carbonate profiles (letters) are evident in Figure II-3. Visual horizons 1,3,4 and 6 nearly coincide with carbonate transitions A, B, C and D, respectively. Depths corresponding to the calcite transition ages and the depths of the visually correlated horizons are tabulated in Table II-3. Assuming the carbonate correlations are synchronous between cores (Figure II-4), the age scales developed for each core can be used to determine the temporal variability in the visual horizons (Table II-3). Ages for the first two levels are considered synchronous, but horizons 4, 6 and 7 are much more variable.

Since much of the color change is attributed to varying solid-phase manganese concentrations, differing redox conditions between coring sites can account for the temporal variability equivalent to the downcore positions of manganese peaks. Porewater studies at Site C (Jahnke et al., 1982) have shown that post-depositional movement of manganese occurs in these sediments. Additionally, it has been demonstrated that the rapid deposition of turbidite sections in Atlantic cores disturbs the redox conditions (Colley et al., 1984). It is likely that the thick turbidite sections in cores BENTHIC III 12 GC and RAMA I 6 GC affected the prior solid phase manganese profiles and color bands.

Table II-3. Depths<sup>a</sup> of Correlated Horizons (cm).

	Carbonate Transitions					Visual Horizons				
	A	B	C	D	E	1	3	4	6	7
	9	63	118	179	200	11±3 <sup>b</sup> 12±2 <sup>c</sup>	65±2 <sup>b</sup> 65±2 <sup>c</sup>	118±9 <sup>b</sup> 123±4 <sup>c</sup>	172±10 <sup>b</sup> 177±6 <sup>c</sup>	204±25 <sup>b</sup> 216±15 <sup>c</sup>
Age (kyr)										
W8402A 14 GC	15	114	170	152	271	21	114	179	250	295
BENTHIC III 25 GC	14	98	140	203	216	15	98	143	204	237
BENTHIC III 21 GC	15	111	161	241	260	23	110	167	232	278
K7905 16 GC	15	89	116	164	178	16	92	116	165	176
RAMA I 6 GC	14	92	114	148	154	16	96	107	136	145
BENTHIC III 12 GC	18	83	103	138	146	13	84	99	130	135
BENTHIC III 18 GC	12	83	119	173	182	17	84	120	167	181
RC 11-210	15	117	177	275	299	--	--	---	---	---

<sup>a</sup>Listed depths are adjusted as described in Appendix II-1.

<sup>b</sup>Mean age (kyr) and standard deviation of the visually correlated horizons based on all seven cores

<sup>c</sup>Mean age (kyr) and standard deviation of visually correlated horizons excluding RAMA I 6 GC and BENTHIC III 12 GC

The relation of the visually correlated horizons to the manganese profiles are depicted in Figure II-5. Since the correlation lines are not horizontal, it is obvious that some temporal variability exists. There is also substantial lateral variability in the manganese concentrations, but the profiles are similar in cores with high sedimentation rates (i.e. W8402A 14 GC, BENTHIC III 21 GC, and BENTHIC III 25 GC). For most cores without thick turbidite sections, visual correlation horizons 1, 3, 4 and 6, which reflect changes in manganese concentration, can be used as time markers and are surprisingly close to the ages of the calcite transitions.

In lieu of carbonate data for all Site C cores, sediment thicknesses between pairs of visually correlated markers are used to map spatial patterns of sediment accumulation at the site. Because of temporal variability in the visual markers across the site, the variations in accumulation are accentuated. The changes in sediment thickness relative to 14 GC for four intervals during the past 175 kyr are shown in Figure II-6. The total thickness of core 14 GC over this time interval is more than 50% higher than cores from the central depression. Prior to 65 kyr ago, the percent decrease across the site appears to have been greater.

We note that, although the sediment thickness decreases with increasing water depth, proximity to the topographic highs also appears to be important. The relation of water depth and distance from topographic highs to sediment thickness between correlated horizons is shown in Figure II-7. No simple relationship exists and all intervals exhibit the influences of both water depth and

Figure II-5

Manganese concentration (%) versus age (kyr) in Site C cores.

Dotted lines 1-7 correspond to visual correlations in Figure II-2.

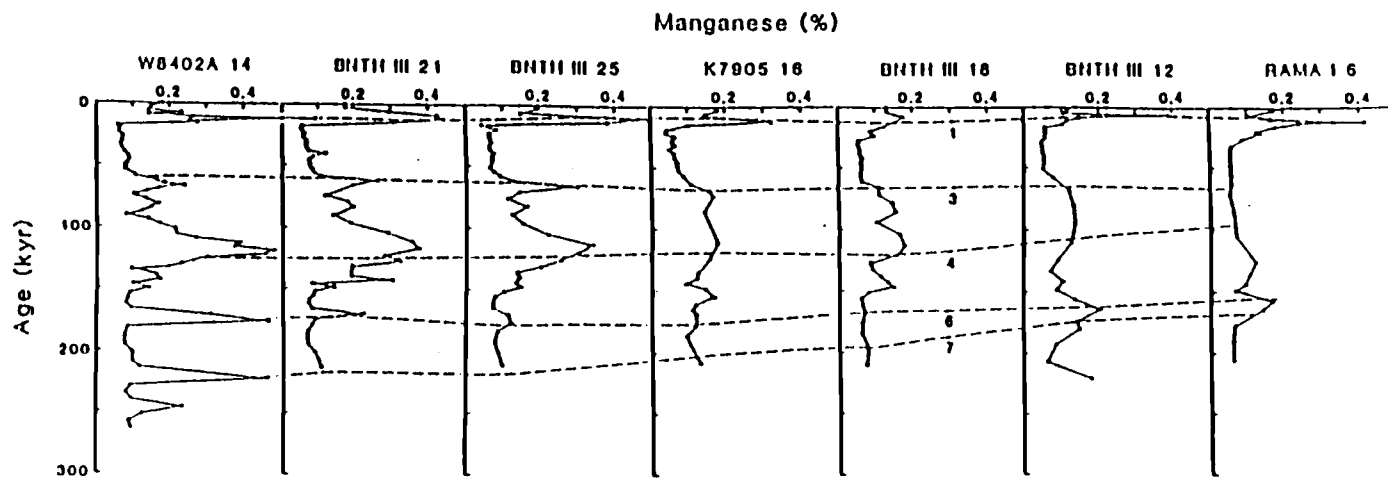


Figure II-5

## Figure II-6

Contoured maps of sediment thickness between correlated horizons. Data are given as % of 14 GC thickness. Figures A, B, C, and D correspond to sections between the surface and horizon 1, horizons 1 and 3, horizons 3 and 4, and horizons 4 and 6, respectively. Age estimates for these horizons are given in Table II-3.

Figure 11-6

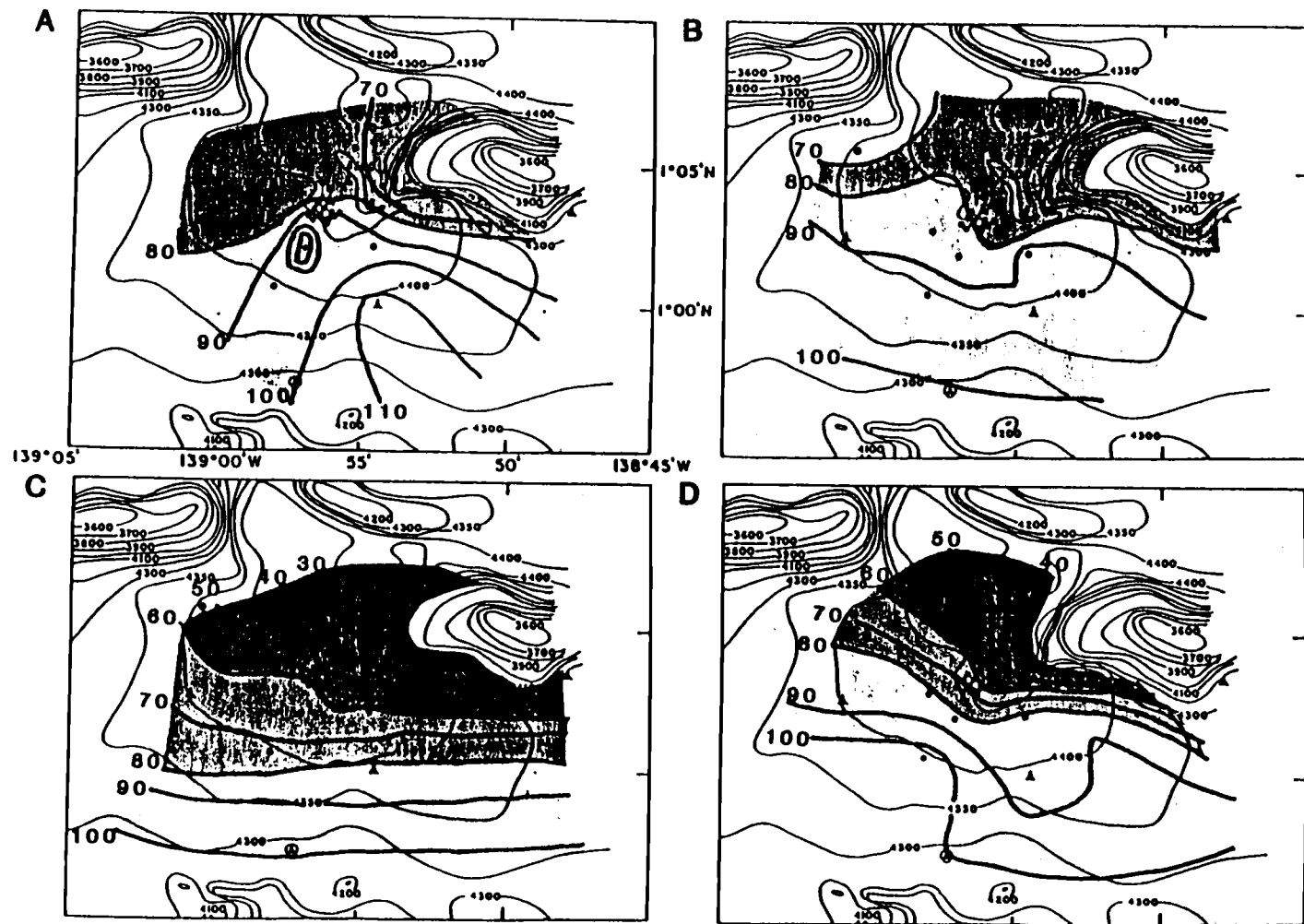
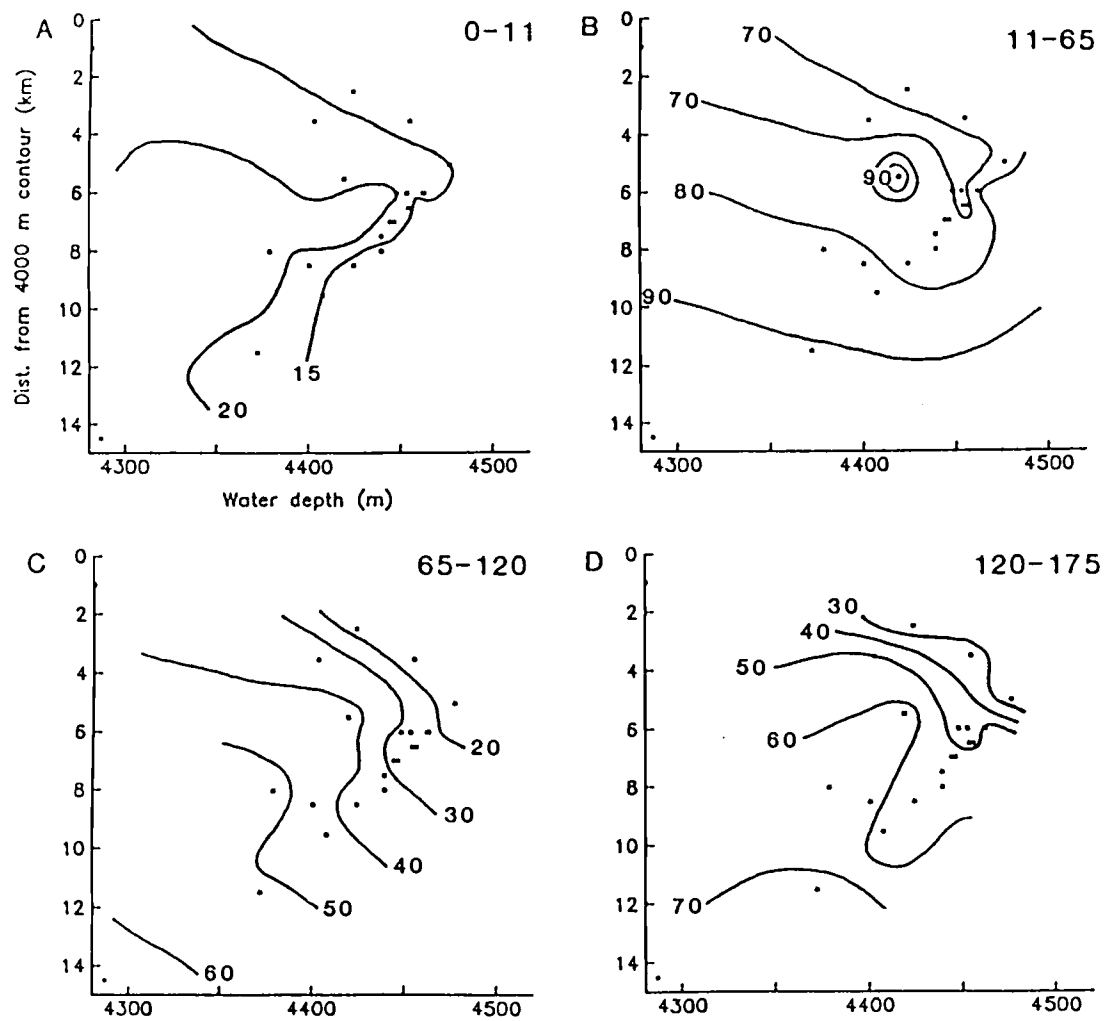


Figure II-7

Sediment thickness (cm) contours in a distance from 4000 m bathymetric contour versus water depth (m) coordinate system. The horizontal gradient reflects water depth dependence and the vertical gradient represents dependence on proximity to topographic highs. Time intervals for A-D are noted.



Figure II-7



proximity to topographic highs on the spatial pattern of sediment accumulation. Thus, depth-dependent carbonate solution cannot be the only process affecting sediment accumulation at Site C.

With these general patterns established, bulk chemical data from seven cores, chosen to span the full range of observed spatial accumulation, are used to separate total sediment accumulation variations due to carbonate solution from other processes. In this study, we use the accumulation of calcite and aluminosilicates to quantify these variations. Previous work at Site C (see Chapter I) has shown that aluminum reliably reflects the accumulation of detrital aluminosilicates in the sediments. These particles are refractory and should not be affected by dissolution at the site. Since the main source of particulate aluminum is particles settling through the water column, spatial variations in its accumulation rate records differential deposition or redistribution of sediment. Spatial variations in the calcite accumulation rate record depth-dependent carbonate dissolution in addition to differential deposition or redeposition.

Because the regional average accumulation rates are unknown, only relative variations in accumulation at Site C are considered. Core 14 GC, the shallowest coring site with the thickest carbonate-rich and -poor sections, has been selected as the reference core. We assume that the thicker sections did not result from deposition of material eroded from nearby coring sites. The similarity of calcium carbonate concentration and total accumulation profiles in 14 GC to a nearby core thought to be representative of the region (RC11-210; Figure II-3) supports the assumption that 14 GC is the

Site C core least affected by localized processes and that it has not received excess material.

Relative to 14 GC, sites closer to the topographic highs are generally deficient in both calcium carbonate and aluminum (Figure II-8). The site closest to Gentle Slope Seamount (BENTHIC III 18 GC) accumulated 32-70% less aluminum and 13-32% less calcite than 14 GC (Tables II-4 and II-5). Since the cores are from similar water depths, the decrease in calcite accumulation must represent differential accumulation; a conclusion supported by the aluminum data.

An estimate of the proportion of "missing" calcite attributable to solution can be generated from cores with similar rates of aluminum accumulation. We assume that cores with the same accumulation rate of aluminum reflect the same sedimentary regime and differences in carbonate accumulation must reflect dissolution effects. We also assume that the dissolution rate changes linearly with depth over the 250 m range at Site C. The cores used and corresponding dissolution rates are given in Figure II-9. Our rates of  $0.3-1.0 \text{ g cm}^{-2} \text{ kyr}^{-1} \text{ km water depth}^{-1}$  are comparable to, but slightly greater than the measured weight loss increase of calcite spheres between 4250 and 4750 m in the equatorial Pacific (Peterson, 1966). They are, however, an order of magnitude less than the regional estimate of Van Andel et al. (1975). Linear extrapolation to a level of no calcite accumulation with our

Figure II-8

Aluminum (solid line with triangles) and calcite accumulation rate (solid lines with solid circles and diamonds) excess or deficit in selected cores relative to 14 GC during five time intervals over the last 200 kyr. The solid lines with solid circles show calcite accumulation rate differences without correcting for calcite dissolution, whereas the solid lines with diamonds represent differences after accounting for depth dependent dissolution. Horizontal axis is the distance (km) of the coring site from the nearest 4000 m bathymetric contour. The cores used are noted on the bottom of the figure.

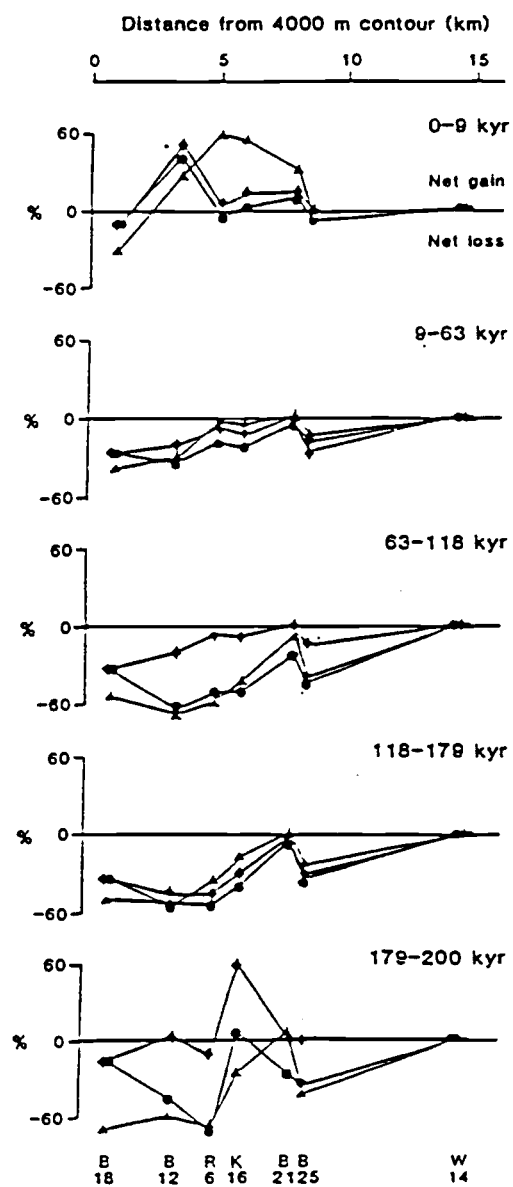


Figure II-8

Table II-4. Aluminum Budget.

Core <sup>a</sup>	0-9 kyr		9-63 kyr		63-118 kyr		118-179 kyr		179-200 kyr	
	MEA. <sup>b</sup>	RES. <sup>c</sup>	MEA.	RES.	MEA.	RES.	MEA.	RES.	MEA.	RES.
W8402A 14 GC	100.	0.0	100.	0.0	100.	0.0	100.	0.0	100.	0.0
BENTHIC III 25 GC	99.2	0.8	75.4	24.5	60.1	39.9	66.7	33.3	59.6	40.4
BENTHIC III 21 GC	132.2	(32.2) <sup>d</sup>	102.8	(2.8)	94.0	6.0	100.5	(0.5)	108.3	(8.3)
K7905 16 GC	154.1	(54.1)	95.3	4.7	57.2	42.8	81.3	18.7	65.9	24.1
RAMA I 6 GC	159.9	(59.9)	99.0	1.0	42.0	58.0	64.0	36.0	31.6	68.4
BENTHIC III 12 GC	126.1	(26.1)	71.8	28.2	33.1	66.9	49.0	51.0	41.2	58.8
BENTHIC III 18 GC	68.3	31.7	65.5	38.5	46.7	53.3	51.5	48.5	30.0	70.0

<sup>a</sup> Cores ordered by decreasing distance from 4000 m contour.

<sup>b</sup> MEA. = (measured Al accumulation in listed core/14 GC Al accumulation) x 100.

<sup>c</sup> RES. = 100-MEA.

<sup>d</sup> Values in parenthesis represent excess accumulation relative to 14 GC.

Table II-5. Calcium Carbonate Budget.

Core <sup>a</sup>	0-9 kyr			9-63 kyr			63-118 kyr			118-179 kyr			179-200 kyr		
	MEA. <sup>b</sup>	DIS. <sup>c</sup>	RES. <sup>d</sup>	MEA.	DIS.	REA.	MEA.	DIS.	REA.	MEA.	DIS.	REA.	MEA.	DIS.	REA.
W8402A 14 GC	99.7	0.3	0.0	98.6	1.4	0.0	99.7	0.3	0.0	98.3	1.7	0.0	98.3	1.7	0.0
BENTHIC III 25 GC	93.3	6.7	0.0	82.5	7.0	10.5	58.2	27.5	14.3	71.5	5.2	23.3	65.8	35.0	(0.8) <sup>e</sup>
BENTHIC III 21 GC	110.6	5.4	(16.0)	96.4	5.7	(2.1)	77.6	22.4	0.0	95.7	4.3	0.0	71.3	28.7	0.0
K7905 16 GC	103.8	10.1	(13.9)	77.8	10.6	11.7	51.2	41.6	7.2	63.0	7.9	29.1	107.7	53.2	(60.9)
RAMA I 6 GC	93.4	10.9	(4.3)	81.2	11.4	7.4	49.8	45.1	5.1	45.4	8.6	46.0	31.1	57.6	11.4
BENTHIC III 12 GC	142.3	9.7	(52.0)	69.5	10.1	20.4	39.2	40.0	20.8	45.8	7.6	46.6	52.9	51.1	(4.0)
BENTHIC III 18 GC	87.0	0.0	13.0	74.8	0.0	25.2	67.7	0.0	32.3	68.4	0.0	31.6	84.7	0.0	15.3

<sup>a</sup> Cores ordered by decreasing distance from 4000 m contour.

<sup>b</sup> MEA. = (Measured CaCO<sub>3</sub> accumulation in listed core/adjusted<sup>f</sup> 14 GC CaCO<sub>3</sub> accumulation) x 100.

<sup>c</sup> DIS. = ((Dissolution rate x (4280 m - core water depth))/adjusted 14 GC CaCO<sub>3</sub> accumulation) x 100.

<sup>d</sup> RES. = 100-MEA-DIS.

<sup>e</sup> Values in parenthesis represent excess accumulation relative to 14 GC.

<sup>f</sup> 14 GC measured accumulation plus (dissolution rate x 7 m).

Figure II-9

Calcium carbonate accumulation rate versus water depth for five selected time intervals during the last 200 kyr. Stars identify cores, with similar aluminum accumulation rates, used to determine calcium carbonate dissolution gradient for each interval. Rates are in  $\text{g}\cdot\text{cm}^{-2} \text{ kyr}^{-1} \text{ km water depth}^{-1}$ .



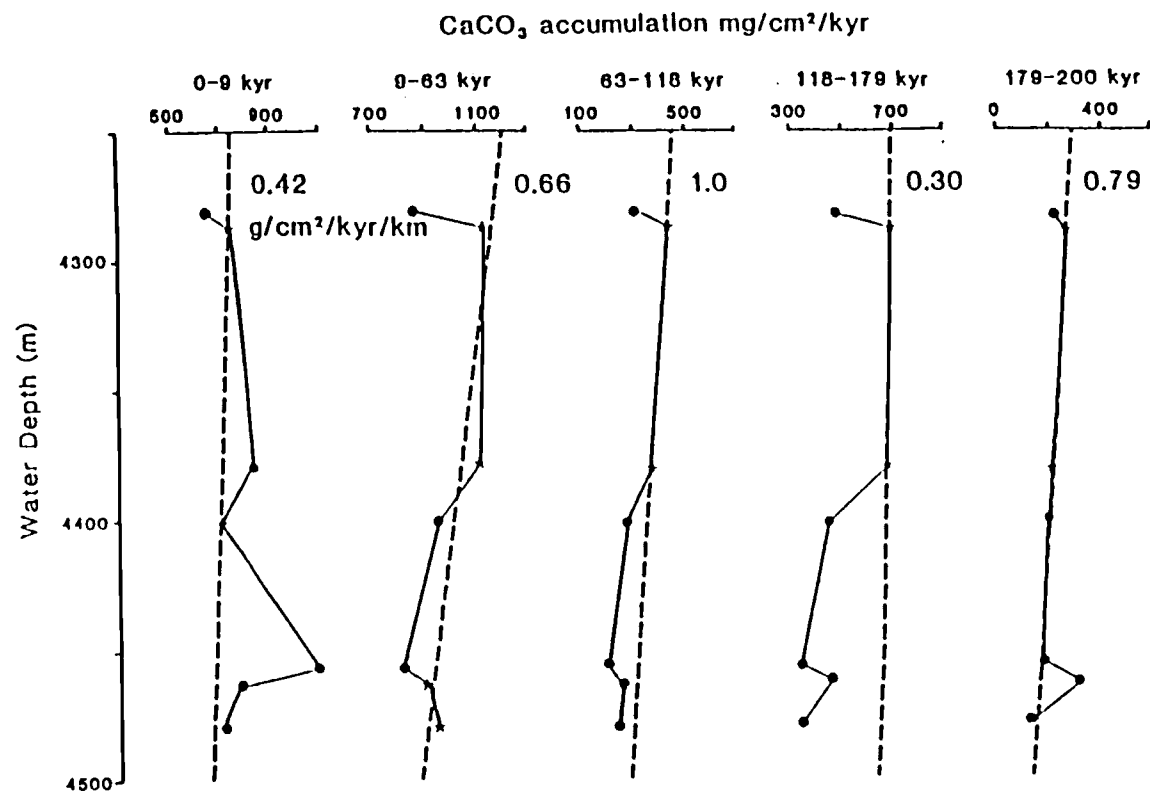


Figure II-9

dissolution rate for 0-9 kyr yields a depth of 6060 m; more than 1000 m below the present regional CCD (Berger et al., 1976). Thus, either the dissolution rate must increase as the compensation depth is approached or Site C values are underestimates of the regional dissolution rates. The calculated dissolution rates have been used to correct the carbonate accumulation rates in all cores to a common depth of 4280 m (the shallowest coring site). Any remaining differences between 14 GC and the other cores (Figure II-8; Table II-5) are attributed to some other process.

## DISCUSSION

Both the results of the visual correlations and chemical accumulation estimates demonstrate that a process in addition to depth-dependent carbonate dissolution is necessary to explain the patterns of sediment accumulation at MANOP Site C. In most cores, the missing or eroded material is enriched in aluminum compared to calcium carbonate. Only in rare instances is the material enriched in calcium carbonate compared to the mean sediment composition of 14 GC for the same interval (Figure II-10A). Even if dissolution is neglected, most of the material removed is still enriched in aluminum relative to correlative 14 GC sediment (Figure II-10B). If, on the other hand, the calcite dissolution rates have been underestimated, then aluminosilicates comprise most of the eroded material. If a redistribution process acts upon particles prior to deposition at the sediment-water interface, the composition of the eroded material should be similar to that measured in sediment traps. However, it is evident from Figure II-10 that the eroded material is depleted in calcium carbonate relative to trap material. In the surface sediments at the site, all the aluminum is concentrated in the silt and clay size fractions, whereas, more than 50% of the calcite is in the coarse silt and sand-size fractions (see Chapter III; Murray, unpublished data). Preferential grain size removal can explain the relative differences in the amount of calcium carbonate eroded compared to aluminum. Thus, we must identify a process that acts upon deposited material,

Figure II-10

(A) Calcite to aluminum ratio for eroded or excess material corrected for dissolution for five intervals in Site C cores spanning the last 200 kyr. Dots represent material eroded, and stars represent material deposited relative to 14 GC. Cores having accumulation rates similar to 14 GC are not shown on this diagram. The vertical bar in each interval corresponds to the ratio in 14 GC. The range of the ratio measured in sediment traps containing only the primary water column flux is shown as the hatched pattern. The range in traps containing resuspended bottom sediments, in addition to the primary flux, is represented by the dotted pattern. (B) As A, but not corrected for calcite dissolution.

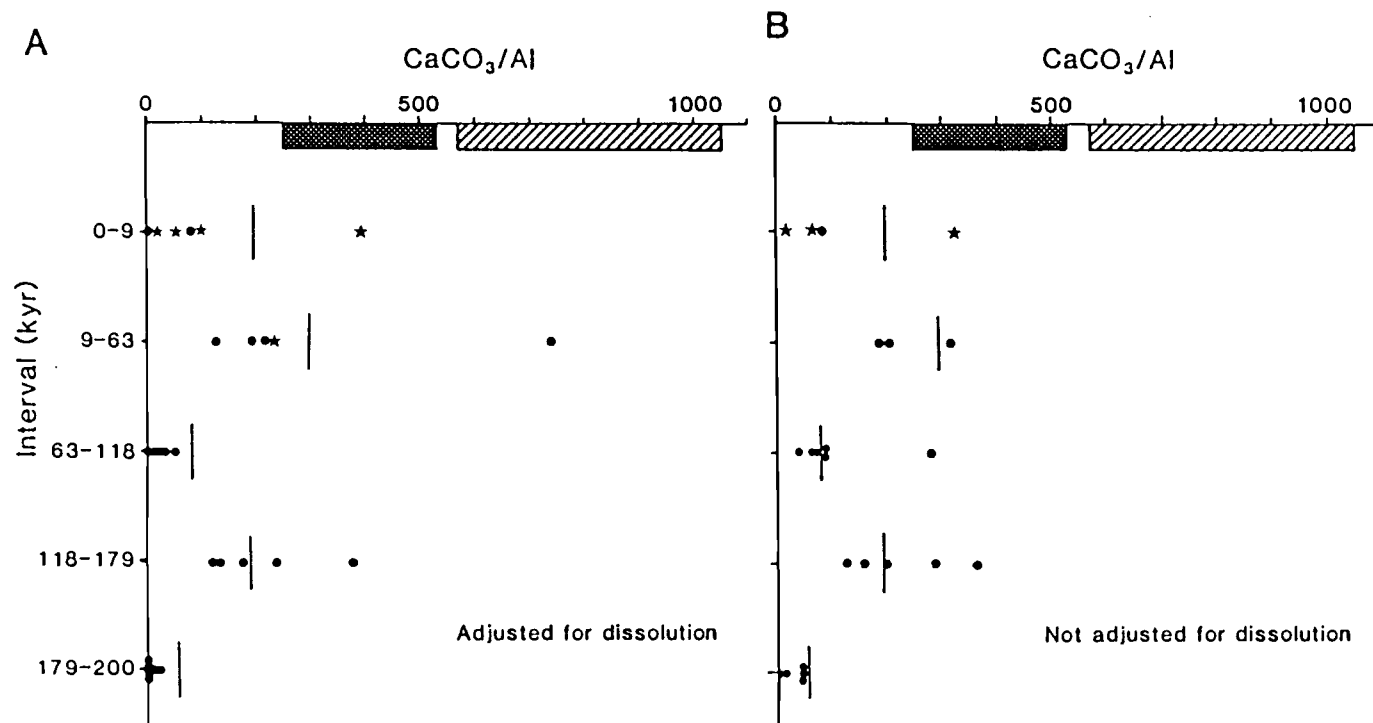


Figure II-10

preferentially removes the fine fraction relative to the coarse fraction, and decreases in strength with increasing distance from topographic highs.

Earlier studies have discussed the influence of topography on local sedimentation (Johnson and Johnson, 1970; Davies and Laughton, 1972; Roberts et al., 1974; Lister, 1976). At sites close to the equator where the coriolis force is negligible, accelerated flow around seamounts generates depositional patterns similar to those described by Johnson and Johnson (1970) and Davies and Laughton (1972). Moats are usually found along the sides of seamounts, with some scouring or winnowing on the upstream sides and deposition in the lees. If such flow is responsible for the Site C variations, the observed depositional patterns can be used to hindcast paleocurrent directions during the last 200 kyrs.

For the youngest interval (0-9 kyr), cores in the central depression are receiving as much as 60% more aluminum than is 14 GC (Figure II-8). The calcite excess is much less, although it would be greater if the estimated dissolution rate is too low. Since this interval is recorded by the top section of the cores, some of the differences may be artifacts of the coring process or misidentification of the detail of the shallowest carbonate transition. A 5 cm-thick layer added to the top of RAMA I 6 GC or lost from the top of 14 GC can explain the difference in aluminum accumulation at the top of each core. However, oxygen isotope data (see Chapter I) show that isotope event 1.1 (2.3-6 kyr; Imbrie et al., 1984; Martinson et al., in press) is at 6.5 cm in core 14 GC. Adding 5 cm above this level would yield sedimentation rate of

1.9-5.0 cm kyr<sup>-1</sup>. These rates are considered high for this site (see Chapter I). Moving the transition boundary would create an excess of aluminum accumulation in the 9-63 kyr interval in RAMA I 6 GC. Thus, unless the coring process and subsequent handling stretched the top 10-20 cm of selected cores or compressed the reference core, the observed excess accumulations are real. In contrast, core BENTHIC III 18 GC, on the south side of Gentle Slope Seamount, has received 15% less calcite and 30% less aluminum during the last 9 kyr than has 14 GC. If the deeper locations are in the lee of the topographic highs and deposits on the south side of Gentle Slope Seamount are being winnowed by currents accelerated around the seamount, then we predict flow toward the southwest or west.

Current meters moored at 4250 and 4400 meters in the central basin from 12 December 1982 to 21 February 1984 both recorded a mean speed of 5.6 cm sec<sup>-1</sup> with the strongest and most persistent flow to the southwest (J. Dymond, personal communication, 1985). Our depositional patterns are consistent with this flow direction, which, we suggest, has persisted for the past 9,000 years.

Prior to this time, however, a flow toward the east or northeast is necessary to explain the lateral variability in sedimentation. If the gradient in aluminosilicate deposition is related to current strength, the flow was stronger prior to 63 kyr. This change is also evident in bulk sediment accumulation (Figure II-11). The depth-depth correlations diverge from 14 GC prior to 63 kyr (114 cm) suggesting a major change in sedimentation occurred at this time. If we assume that the initial grain size of

the carbonate material did not change significantly over time (i.e., the ratio of foraminifera to coccoliths and foraminiferal fragments has been constant), and if our estimate of the carbonate dissolution rate is reasonable, then a greater amount of coarser material was moved between 118 and 179 kyr (glacial stage 6) than before or after this interval.

We emphasize, however, that the moats discussed earlier are the only evidence of erosion by bottom currents; we did not recover any winnowed lag deposits. A quantitative study of the grain sizes of individual layers in the cores might provide the data necessary to verify that the fine fraction in cores closest to topographic highs has been preferentially removed. Additional cores or sub-bottom profiling to the north and east of the seamounts would help define areas of erosion and accumulation that would better constrain our proposed flow directions.



Figure II-11

Depths in Site C cores (cm) versus corresponding depth in 14 GC (cm). Depth correlations are based on matching of the calcium carbonate concentration records. The 14 GC line represents a 1:1 depth correlation. Upside-down triangle at 114 cm is the depth in 14 GC corresponding to 63 kyr.

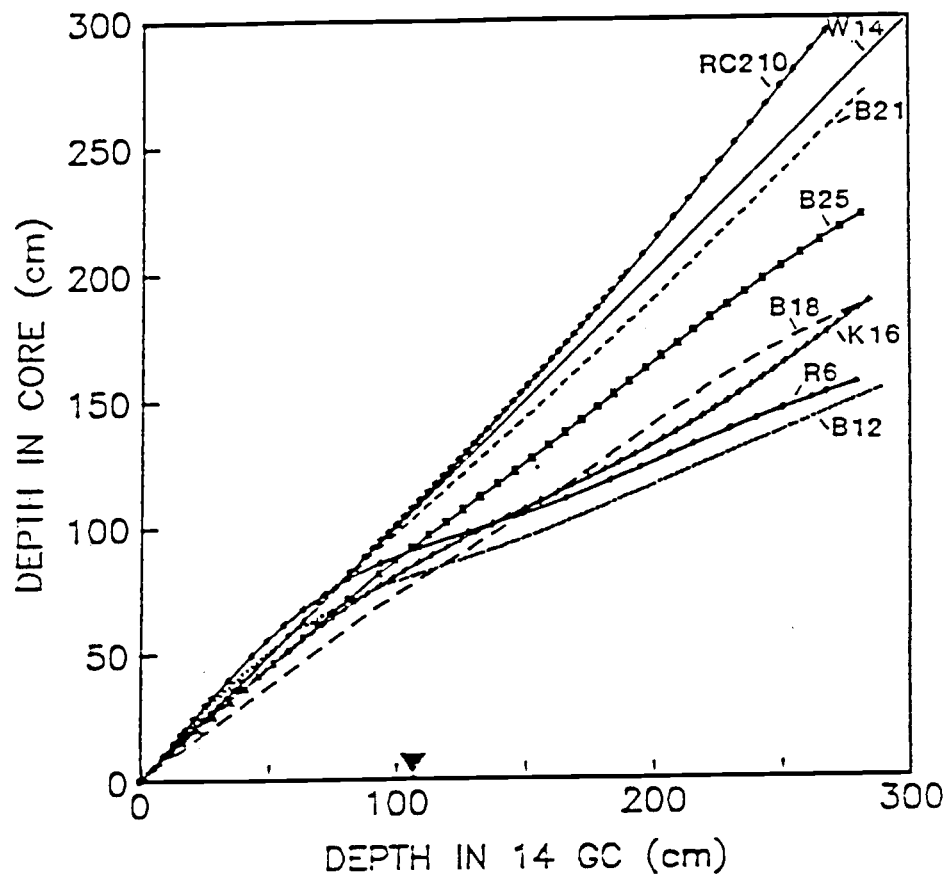


Figure II-11

## CONCLUSIONS

Based on our present understanding of flow around topographic highs in equatorial regions, observed lateral variations in sediment accumulation rates at MANOP Site C can be explained by a combination of depth-dependent calcium carbonate dissolution and material transport by accelerated bottom currents flowing around nearby seamounts. Depth-dependent carbonate solution can account for most of the variations in calcite accumulation, but, transport by bottom currents is necessary to explain the variations of aluminum accumulation and to fully account for calcite deposition. During the last 9,000 years, the observed deposition at Site C is consistent with current-meter determined southwest flowing bottom water. Prior to this time, however, a flow toward the east or northeast is necessary to account for the patterns of sediment accumulation.

## REFERENCES

- Arrhenius, G., Sediment cores from the east Pacific, Pt. 1, In: Reports of the Swedish Deep-Sea Expeditions 1947-1948, edited by H. Pettersson, 5, 227, Elanders, Goteborg, 1952.
- Berger, W.H., C.G. Adelseck, Jr. and L. Mayer, Distribution of carbonate in surface sediments of the Pacific Ocean, J. Geophys. Res., 81, 2617-2627, 1976.
- Colley, S., J. Thomson, T.R.S. Wilson and N.C. Higgs, Post-depositional migration of elements during diagenesis in brown clay and turbidite sequences in the northeast Atlantic, Geochim. Cosmochim. Acta, 48, 1223-1235, 1984.
- Criss, J.W., L.S. Birks and J.V. Gilfrich, Versatile X-ray analysis program combining fundamental parameters and empirical coefficients, Anal. Chem., 50, 33-37, 1978.
- Davies, T. and A.S. Laughton, Sedimentary processes in the north Atlantic, In: Initial Reports of the Deep Sea Drilling Project, edited by A.S. Laughton, W.A. Berggren, et al., U.S. Government Printing Office, Washington, DC, 12, 905-934, 1972.
- Hays, J.D., T. Saito, N.D. Opdyke and L.H. Burckle, Pliocene-Pleistocene sediments of the equatorial Pacific: Their paleomagnetic biostratigraphic and climatic record, Geol. Soc. Am. Bull., 80, 1481-1514, 1969.

- Imbrie, J., J.D. Hays, D.G. Martinson, A. McIntyre, A.C. Mix, J.J. Morley, N.G. Pisias, W.L. Prell and N.J. Shackleton, The orbital theory of Pleistocene climate: Support from a revised chronology of the marine  $\delta^{18}\text{O}$  record, In: Milankovitch and Climate. Pt. 1, edited by A. Berger, J. Imbrie, et al., Reidel Pub. Co., Boston, pp. 269-304, 1984.
- Jahnke, R.A., D. Heggie, S.R. Emerson and V. Grundmanis, Pore waters of the central Pacific Ocean: Nutrient results, Earth Planet. Sci. Lett., 61, 233-256, 1982.
- Johnson, D.A. and T.C. Johnson, Sediment redistribution by bottom currents in the central Pacific, Deep-Sea Res., 17, 157-169, 1970.
- Kominz, M.A., G.R. Heath, T.-L. Ku and N.G. Pisias, Brunhes time scales and the interpretation of climatic change, Earth Planet. Sci. Lett., 45, 394-410, 1979.
- Lampitt, R.S., Evidence for the seasonal deposition of detritus to the deep-sea floor and its subsequent resuspension, Deep-Sea Res., 32, 885-897, 1985.
- Lister, C.R.B., Control of pelagic sediment distribution by internal waves of tidal period: Possible interpretation of data from the southern east Pacific rise, Mar. Geol., 20, 297-313, 1976.
- Lowrie, A. and B.C. Heezen, Knoll and sediment drift near Hudson Canyon, Science, 157, 1552-1553, 1967.
- Lyle, M.W. and G.R. Heath, Carbonate sedimentation at MANOP Site C,  $1^{\circ}\text{N}$ ,  $139^{\circ}\text{W}$ , Equatorial Pacific (abstr.), Transactions, American Geophysical Union, EOS, 60, p. 850, 1979.

- Martinson, D.G., W. Menke and P. Stoffa, An inverse approach to signal correlation, J. Geophys. Res., 87, 4807-4818, 1982.
- Martinson, D.G., N.G. Pisias, J.D. Hays, T.C. Moore, J. Imbrie and N.J. Shackleton, Age dating and the orbital theory of the ice ages: Development of a high resolution 0-300 kyr chronostratigraphy, Quat. Res., in press.
- Menard, H.W., Marine Geology of the Pacific, McGraw-Hill, 271 pp., 1964.
- Peterson, M.N.A., Calcite: Rates of dissolution in a vertical profile in the central Pacific, Science, 154, 1542-1544, 1966.
- Roberts, D.G., N.G. Hogg, D.G. Bishop and C.G. Fleueller, Sediment distribution around moated seamounts in the Rockall Trough, Deep-Sea Res., 21, 175-184, 1974.
- Spiess, F.N. and M. Weydert, Cruise report: Rama Leg 1, MANOP Sites C and R, SIO Ref. 84-8, Marine Physical Laboratory, Scripps Institute of Oceanography, San Diego, CA, 23 pp., 1984.
- Thompson, P.R. and T. Saito, Pacific Pleistocene sediments: Planktonic foraminifera dissolution cycles and geochronology, Geology, 2, 333-335, 1974.
- Valencia, M.J., Pacific Pleistocene paleoclimatic stratigraphies: A comparative analysis of results, Quat. Res., 8, 339-354, 1977.
- van Andel, T.H., G.R. Heath and T.C. Moore, Jr., Cenozoic tectonics, sedimentation and paleoceanography of the central equatorial Pacific, Geol. Soc. Am. Mem., 143, 134 pp., 1975.

CHAPTER III

WATER COLUMN WEIGHT FLUXES OF OPAL AND CALCAREOUS  
MICROFOSSILS IN THE CENTRAL EQUATORIAL PACIFIC:  
PALEOCEANOGRAPHIC IMPLICATIONS

## ABSTRACT

Biogenic opal and calcite measured in four size fractions in sediment trap samples from MANOP Site C, central equatorial Pacific, are used to partition the lower water column particle rain into contributions associated with major microfossil groups. Fine fraction opal (mostly diatom tests) is >50% of the opal flux, whereas, foraminifera shells >150  $\mu\text{m}$  dominate the calcite particle rain.

The 1982-83 ENSO event and seasonal upwelling caused variations in the physical properties of surface waters at Site C during the collection period. These oceanographic changes are reflected in the relative fluxes attributed to various microfossil groups. Below average organic carbon and diatom weight fluxes are recorded in samples obtained during the ENSO event. The weight flux of foraminiferal calcite does not decrease during this period of lower primary productivity, and trapped particles have almost two moles of calcite carbon per one mole of organic carbon. Fine fraction calcite (coccoliths) and organic carbon fluxes are above the mean during the 1983 and 1984 summer upwelling seasons. Foraminifera rain rates are greatest in the summer of 1984, whereas, during the 1983 upwelling season, the >150  $\mu\text{m}$  foraminifera flux is five times lower than the deployment mean. The mean >150  $\mu\text{m}$  opal flux measured in 1984 is more than twice the 1983 coarse fraction flux. This difference is largely attributable to large diatoms contained in the 1984 samples.



The range in composition and magnitude of the particulate rain measured from December 1982 and May 1985 is used to characterize the Recent dissolution-free input to the sediments. A comparison with surface sediment accumulations reveals that, presently, 61-69% of the calcium carbonate and 90-92% of the opal flux is dissolved in the lower water column and surface sediments. This amount of recycling alters the composition of the preserved microfossil assemblage. A change from dominantly coarse fraction calcite particles in sediment traps to fine particles in the sediments reflects both dissolution and mechanical breakage of foraminifera shells. Proportionally, more fine fraction opal is recycled than coarse fraction.

Without altering the composition of the incoming detritus, preservational changes in both calcite and opal in the sediments at Site C can account for accumulation rate variations observed during the last 200,000 years. However, such preservational changes must be quantified before rain rate variations can be dismissed. Additionally, large calcite accumulation rates at 350 and 440 kyr recorded in nearby core RC11-210 provide evidence for paleo-calcite flux changes. These maxima were exceeded in only one of the nine sediment trap sampling periods. To account for these accumulation rates without changing the composition of the incoming detritus, a protracted period of rapid calcite supply, similar in magnitude to that produced during the 1984 upwelling season, with minimal dissolution, is necessary.

## INTRODUCTION

Sediment traps provide a means to capture particles falling through the water column and determine the fluxes of different settling components. The particle rain is generally dominated by biogenic material which undergoes extensive degradation and dissolution in the deep sea. A number of studies have demonstrated a strong seasonality in the flux and related these variations to changes in surface productivity (Deuser and Ross, 1980; Honjo, 1982; Deuser, 1986).

At MANOP Site C in the central equatorial Pacific (1°N, 139°W), samples from two sediment trap moorings deployed from December 1982 to May 1985 contain a record of seasonal flux changes (Pisias et al., 1986; Dymond and Collier, in prep.). In addition, anomalously warm nutrient-poor surface waters associated with the 1982-83 El Niño-Southern Oscillation event (ENSO) were present at the site during the first two sampling periods (Figure III-1). Barber and Chavez (1983) have shown that during the ENSO, primary productivity was lower than normal in the eastern tropical Pacific and the expected flux decrease associated with lower productivity is observed at Site C (Pisias et al., 1986).

Previous studies of sediment trap material have shown that in pelagic regions, as much as 80-90% of the particle flux is composed of the shells of the major microplankton groups (Honjo et al., 1982). As the bulk flux and organic carbon rain rates vary in response to oceanographic changes such as those which occurred at Site C, the relative proportions of the plankton groups should

Figure III-1

Sea-surface temperature ( $^{\circ}\text{C}$ ) at MANOP Site C ( $1^{\circ}\text{N}$ ,  $139^{\circ}\text{W}$ ) for 1983 (solid) and 1984 (dashed). Corresponding time intervals for sediment trap samples are shown at top of diagram. Temperatures extracted from National Weather Service sea-surface temperature maps.

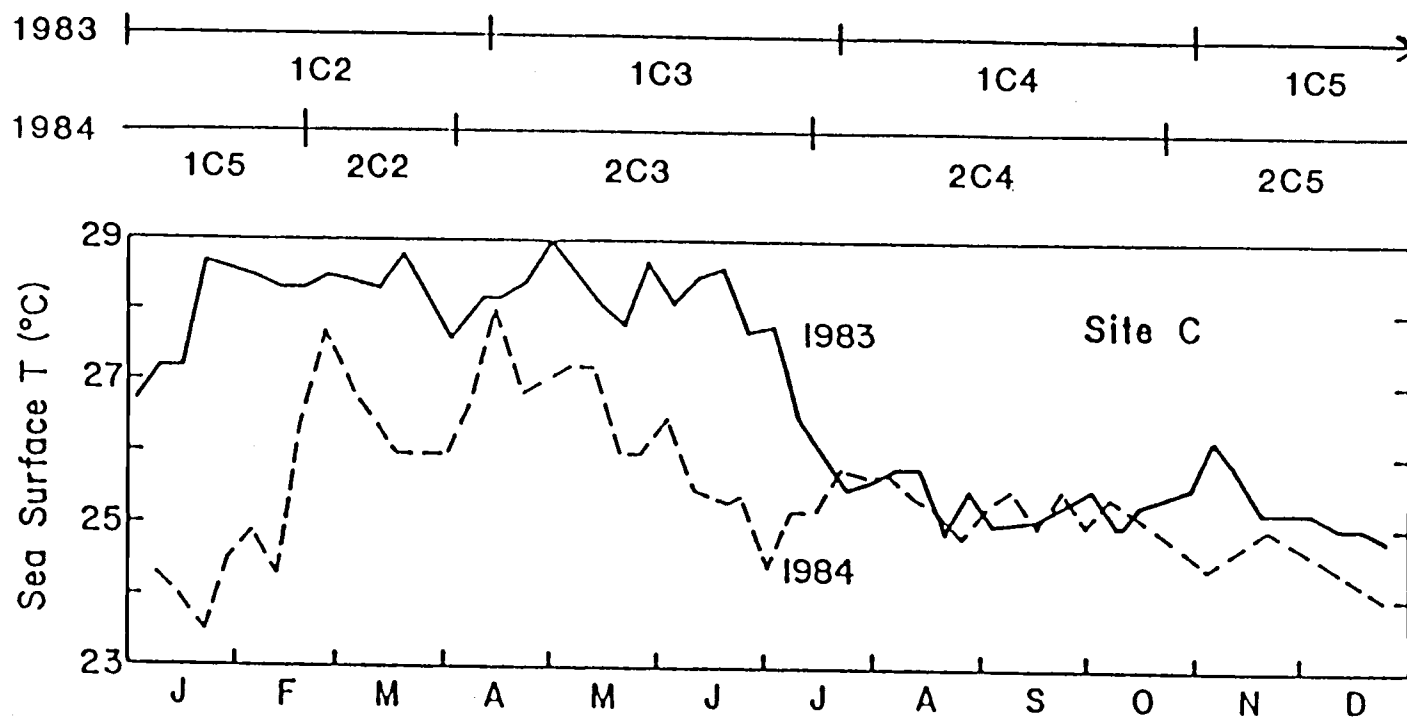


Figure III-1

reflect these changes. It is the mass transfer associated with these biogenic particles (mainly Radiolaria, diatoms, foraminifera, and coccolithophores) which is the focus of this study.

The objectives are to determine the proportion of the seasonal flux of biogenic opal or carbonate that is due to a particular plankton group and how these proportions change during the deployment period in response to surface-water variations. Because these organisms produce the major microfossil assemblages used in the study of deep-sea sediments, we also compare water column fluxes to accumulations in the underlying sediments. These data should improve our understanding of the paleoceanographic signal that is incorporated in the geologic record.

## METHODS

Two consecutive sediment trap experiments were deployed at MANOP Site C between December 26, 1982 and May 1, 1985 (Table III-1). The samples were collected by single-cone OSU traps equipped with five-cup sample changers and poisoned with sodium azide. A sample designation of 1C2 refers to cup 2 of the first deployment. In order to isolate possible shipboard contaminants, the first sample cup (1C1) was rotated out of the collection position seven days after the mooring was in place. During the first experiment, the 14-month sampling period was partitioned into four collecting intervals (1C2, 1C3, 1C4, and 1C5) of approximately 100 days each. The second experiment was designed to sample the same time intervals as the first experiment. Because of a delay in recovery of the first deployment, 2C2 was shortened to 36 days. Thus, only cups 3, 4, and 5 record the same time intervals for both deployments. In addition, the sample changer cycled back to 2C1 before recovery and this sample represents the last 68 days of the deployment.

OSU traps were positioned at six and five levels in the water column during the first and second deployments, respectively. Since fluxes measured in traps are to be compared to sediment accumulations, the trap level which represents the primary input closest to the sediment-water interface and contains a complete set of seasonal samples is selected. Near-bottom sediment traps can collect resuspended aluminosilicate-rich material in addition to the primary flux (Rowe and Gardner, 1979; Gardner et al., 1983;

Table III-1. Sediment trap fluxes and surface sediment accumulation.

Sampling Period					Fluxes ( $\mu\text{g cm}^{-2} \text{ yr}^{-1}$ )						
		Open	Closed	Days	Total <sup>a</sup>	CaCO <sub>3</sub>	Opal <sup>b</sup>	C-org	Si-Tot	Al	
<u>Deployment 1 (1°02.41'N, 138°56.10'W; 4445 m water depth)</u>											
1895 m	Cup 2	12/23/82	04/03/83	100	1905	1330	330	93.3	137	1.26	
	Cup 3	04/03/83	07/12/83	100	2482	1581	536	169.	222	1.85	
	Cup 4	07/12/83	10/20/83	100	3013	1573	1172	193.	478	2.29	
	Cup 5	10/20/83	02/25/84	128	3216	1579	1344	163.	547	2.37	
3495 m	Cup 2	12/23/82	04/03/83	100	1872	1265	383	87.0	158	1.20	
	Cup 3	04/03/83	07/12/83	100	2363	1473	580	133.	239	1.76	
	Cup 4	07/12/83	10/20/83	100	2830	1362	1034	179.	423	2.32	
	Cup 5	10/20/83	02/25/84	128	1758	912	667	86.1	273	1.59	
<u>Deployment 2 (1°03.67'N, 138°58.50'W; 4425 m water depth)</u>											
1883 m	Cup 2	02/25/84	04/01/84	36	4627	2266	1876	252.	766	3.86	
	Cup 3	04/01/84	07/10/84	100	7632	3975	2735	453.	1115	5.27	
	Cup 4	07/10/84	10/18/84	100	4813	2817	1569	197.	640	2.95	
	Cup 5	10/18/84	02/25/85	127	4939	2740	1788	168.	727	2.95	
	Cup 1	02/22/84	02/25/84	3+68	4667	2507	1764	169.	716	2.46	
		02/22/85	05/01/85								
2980 m	Cup 2	02/25/84	04/01/84	36	3750	1930	1395	189.	570	3.06	
	Cup 3	04/01/84	07/10/84	100	3035	1492	1114	164.	455	2.27	
	Cup 4	07/10/84	10/18/84	100	6802	3857	2299	324.	941	5.27	
	Cup 5	10/18/84	02/25/85	127	3191	1896	1114	112.	453	1.80	
	Cup 1	02/22/84	02/25/84	3+68	4048	2127	1615	173.	655	2.24	
		02/22/85	05/01/85								
Ave (1) <sup>c</sup>		12/23/82	05/01/85	862	3399	1866	1186	166.	480	2.41	
Ave (2) <sup>d</sup>		02/25/84	02/25/85	363	4198	2328	1468	192.	600	3.01	
<u>Sediment Accumulation 14 GC 0-5 cm</u>					--	913	703 <sup>e</sup> 730 <sup>f</sup>	139 <sup>e</sup> 119 <sup>f</sup>	2.37	73	4.29 <sup>g</sup>

<sup>a</sup>Total flux is corrected for salt.<sup>b</sup>Except for Na<sub>2</sub>CO<sub>3</sub> Leach in 0-1 cm sample, Opal = (Si-Tot - (4.0xAl))x2.5.<sup>c</sup>Time weighted average flux for full deployment. Trap levels used are given in text.<sup>d</sup>Time weighted average of 2C2-2C5 from 2908 m.<sup>e</sup>Measured by X-ray fluorescence.<sup>f</sup>Sum of Na<sub>2</sub>CO<sub>3</sub> leached size fraction data (0-1 cm sample).<sup>g</sup>20% of Al sediment accumulation is attributed to an oxyhydroxide component not measured in the traps.

Fischer et al., 1986). To avoid this effect, we use samples from traps moored at 3495 m (975 meters above the bottom) during the first experiment and 2908 m (1517 meters above the bottom) during the second experiment to characterize the opal and calcite input to the sediments. Both levels are above the depth of the calcite lysocline in this region (Berger et al., 1976) and should represent a solution-free calcite flux. The particle flux measured in LC5 at 3495 m appears low (see Chapter I), and the 1895 m level is used for this sampling interval.

Sediment trap samples were processed using the methods of Fischer (1983). Elemental concentrations in each sample determined from 3/4 splits of the <1 mm fraction that were freeze-dried and then ground with an agate mortar and pestle. Organic carbon and calcium carbonate were measured using the wet oxidation LECO technique described by Weliky et al. (1983). Al and Si concentrations were determined by flame atomic absorption spectrophotometry (AAS) after hydrofluoric-nitric acid digestion. Opaline silica was calculated as 2.5 times the difference between total Si and detrital Si with detrital Si taken as 4.0 times the Al concentration (see Chapter I).

Surface sediment concentrations of Ca, Al, and Si were measured by X-ray fluorescence and organic carbon was measured by the wet oxidation technique. The concentrations were averaged in samples from the top 5 cm of W8402A 14 GC (4287 m water depth). Bulk sediment accumulation was calculated using a sedimentation rate of  $1.69 \text{ cm kyr}^{-1}$  and a dry bulk density of  $0.54 \text{ g}\cdot\text{cm}^{-3}$  (see Chapter I).



In an effort to differentiate phytoplankton from zooplankton weight fluxes, a 1/32 split of the original <1 mm sample was wet-sieved into four size fractions; <38, 38-63, 63-150, and >150  $\mu\text{m}$ . A 0-1 cm surface sediment sample from W8402A 14 GC was sieved in a similar manner. Each size fraction was examined under a binocular microscope to determine the dominant microfossil groups present, then freeze dried and weighed. Calcium carbonate and opal in these sub-samples were sequentially extracted using leach solutions of buffered acetic acid and sodium carbonate, respectively. The carbonate leach procedure is described in Lyle et al. (1984). Since we use a much smaller sample in this study, 5 ml of 0.516 M acetic acid buffered with 1.0 M sodium acetate was added instead of 20 ml. The samples were placed in a sonic bath for 10 minutes and the supernatant was decanted after centrifuging for 12 minutes at 12500 rpm. After washing twice with 0.2 M NaCl and drying, 5 ml of 2 M sodium carbonate was added. Samples were placed in an 80°C bath for 24 hrs to extract opaline silica. Ca and Si were measured in the supernatants by AAS. As before, % Si was multiplied by 2.5 to convert to % opal.

The opal or calcite flux in each size fraction is the total cup flux ( $\mu\text{g cm}^{-2} \text{ yr}^{-1}$ ) multiplied by the opal or calcite concentration ( $\text{g}\cdot\text{g}^{-1}$ ) times the proportion of the total dry sample weight contained in the size fraction ( $\text{g}\cdot\text{g}^{-1}$ ). The residual flux is calculated as the difference between the total flux and the sum of calcium carbonate and opal fluxes. In trap samples, organic matter ( $\text{CH}_2\text{O}$ ) comprises >95% of the residual, whereas aluminosilicates dominate in the surface sediment.

The fluxes of calcium carbonate and opal in each size fraction of a particular sample were summed to obtain estimates of total calcite and opal for the sample. These estimates are not significantly different from totals measured by wet oxidation, and the normative calculations which are measured on 3/4 splits of the original sample. Since they are based on larger samples, the 3/4 splits should provide better estimates of the elemental fluxes for a sampling period. Therefore, the fluxes in each size fraction for a particular sample were scaled to sum to the flux determined on the 3/4 split. This provides one reported value for the total calcite and opal flux in a sample cup.

## RESULTS AND DISCUSSION

Characteristics of the Flux

Fluxes of calcium carbonate, opal, and residual in each size fraction, in addition to the totals, are presented in Figure III-2. The total carbonate and opal fluxes are much higher than previous studies of Honjo et al. (1982) and Fischer et al. (1986) in the equatorial Atlantic and Pacific. Our data are similar in magnitude to the lower values reported from the Panama Basin which is representative of a high primary productivity area (Honjo, 1982). The amount of material captured in 2C4 is a factor of two above the mean of the other intervals. Sample 2C4 corresponds to seasonal upwelling in the summer of 1984.

The combined fluxes in the  $<38\ \mu\text{m}$  and the  $>150\ \mu\text{m}$  fractions account for most (68-92%) of the total carbonate and opal particles. The calcite flux is generally dominated by larger size particles and most of the opal is concentrated in the fine portion. In eight out of nine samples,  $<38\ \mu\text{m}$  opal is  $>50\%$  of the total (Figure III-3), whereas,  $<38\ \mu\text{m}$  carbonate is  $>50\%$  in only two intervals (1C4 and 2C2).

During the first deployment, much of the residual (i.e., organic matter) is in the fine fraction, whereas it is concentrated in the coarse fraction during the second deployment (Figure III-2). Visual inspection with a binocular microscope reveals that much of the organic matter, generally composed of small particles, is entangled with long needle-like diatoms and radiolarian spines

Figure III-2

Partitioning of the calcium carbonate, opal and residual fluxes ( $\mu\text{g cm}^{-2} \text{ yr}^{-1}$ ) in nine sampling intervals from two sediment trap deployments at MANOP Site C into four size fractions;  $<38$ ,  $38-63$ ,  $63-150$ , and  $>150 \mu\text{m}$ . The key for sampling intervals (i.e., 1C2 = cup 2 of first deployment) with corresponding months 1 = January) and year are shown in lower left histogram. Histograms with the same patterns correspond to samples during the same season. 1C2-1C4 are from the 3495 m level, 1C5 is from 1895 m, and 2C1-2C5 are from 2908 m. The scales for the size fractions are enlarged by a factor of two compared to that of the total flux.

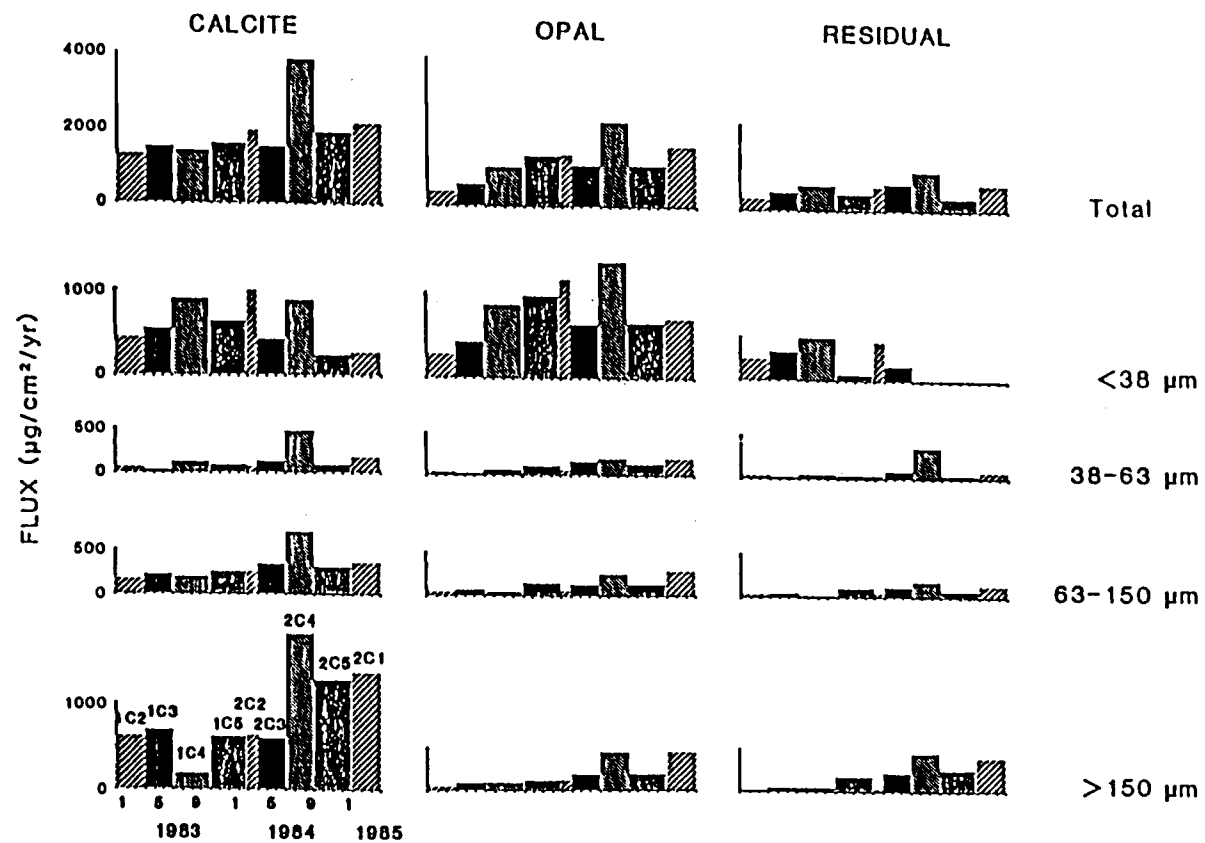


Figure III-2

Figure III-3

Percent of total opal and calcium carbonate contained in four size fractions for each sample. Refer to Table III-1 for dates of sampling intervals. S corresponds to the surface sediment sample. Histograms with same patterns correspond to sampling of the same season.

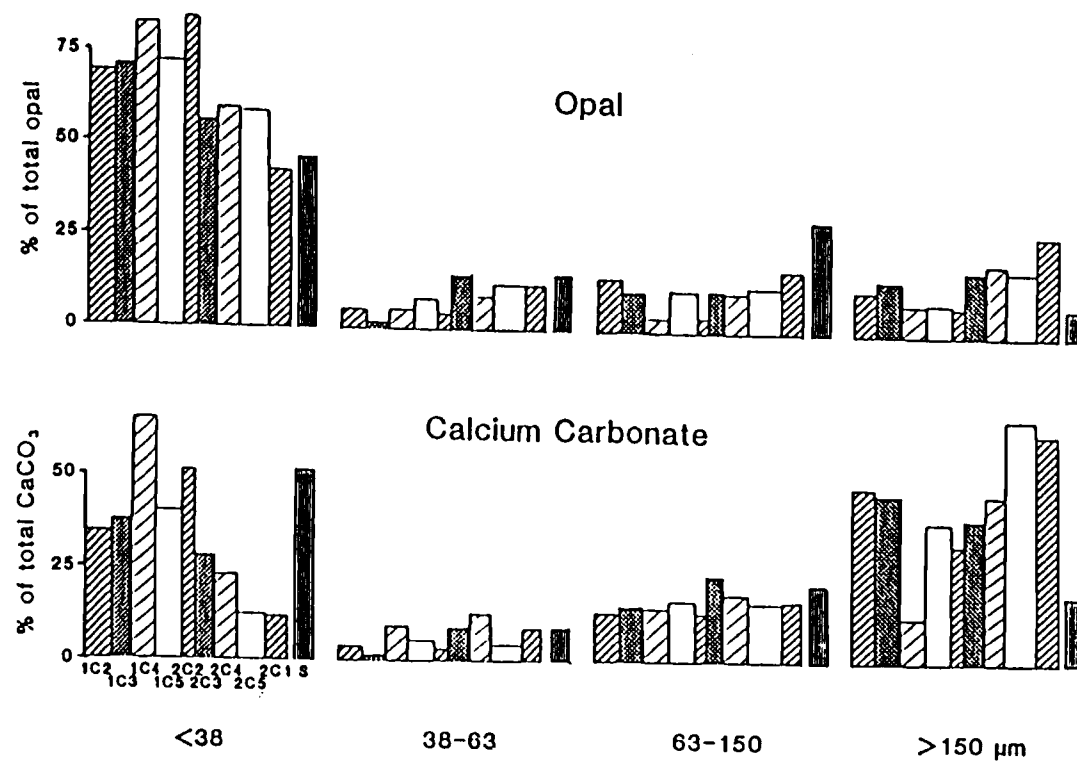


Figure III-3

Figure III-3

which cannot be washed through the sieve. Some fecal pellets are contained in samples  $>63\ \mu\text{m}$  but are not abundant enough to account for the size distribution of the residual particles. The entangled material also accounts for the flux increase of opal  $>150\ \mu\text{m}$ . Thus, size partitioning of the residual flux does not reflect a change in individual organic particles, but a change in the characteristics of particulate opal.

#### Partitioning the Flux into Plankton Groups

Generally, the mean size of individual zooplankton is larger than phytoplankton. Because of this property, we can use a size separation to differentiate between weight fluxes associated with various microfossil groups. Examination of the size fractions with a binocular microscope, in addition to smear slides of the totals, reveals that radiolarians, diatoms, silicoflagellates, coccolithophores, foraminifera, and pteropods are the microfossil groups present. Pteropods are rare in comparison to foraminifera and are not considered separately. Silicoflagellates are always a minor fraction of the siliceous phytoplankton and are grouped with diatoms.

In the carbonate portion of trap samples, coccoliths (phytoplankton) can be differentiated from foraminifera (zooplankton) by a size separation at  $38\ \mu\text{m}$ . Coccolith plates are always  $<38\ \mu\text{m}$  and no whole coccolithophores are observed in the samples. Foraminifera shells are well preserved in trap samples and only rarely are small forms found in the  $<38\ \mu\text{m}$  fraction. Therefore, in the discussion that follows, we will consider all the  $>38\ \mu\text{m}$  calcium



carbonate trap flux to represent foraminifera and  $<38\ \mu\text{m}$  carbonate to represent coccoliths.

The separation between coccoliths and foraminifera is not as clean in sediment samples. Significant fragmentation of foraminiferal tests is evident and  $<38\ \mu\text{m}$  particles include foraminiferal parts. Additionally, some foraminifera  $>38\ \mu\text{m}$  contain coccoliths trapped inside chambers. The  $>38\ \mu\text{m}$  sediment accumulation generally represents foraminiferal calcite, but, the fine fraction represents the accumulation of both coccoliths and foraminifera.

Using a size separation to differentiate between siliceous phytoplankton and zooplankton is more difficult because of overlapping size ranges. Random mounts of the  $>63$  and  $<63\ \mu\text{m}$  siliceous material were made to assist in differentiating diatoms, silicoflagellates, and radiolarian weight fluxes. On the average, particles  $<38\ \mu\text{m}$  comprise more than 65% of the opal flux. Although some radiolarian spines and fragments are  $<38\ \mu\text{m}$ , particles of this size are attributed to phytoplankton. Additionally, as much as one half of the  $>150\ \mu\text{m}$  opal flux measured during the second experiment can be attributed to large centric diatoms (mostly Coscinodiscus nodulifer) and long needle-like tests of Thalassiothrix spp. and Thalassionema spp. which cannot be washed through the  $150\ \mu\text{m}$  sieve. To help separate phytoplankton from zooplankton flux, counts of 500 radiolarians, diatoms, and silicoflagellates in the 38-63, 63-150 and  $>150\ \mu\text{m}$  size ranges were made on random mounts. We assume that no additional breakage occurred during slide preparation. In samples from the first deployment, diatoms and silicoflagellates are 10-30 times more abundant than whole shells and

fragments of Radiolaria in the 38-63  $\mu\text{m}$  size range. Radiolarians are 5-20 times more abundant than the siliceous phytoplankton in the  $>63 \mu\text{m}$  fraction. Therefore, during the first deployment, a separation at 63  $\mu\text{m}$  can effectively differentiate the weight flux of siliceous phytoplankton from zooplankton. This size separation can also be applied to the sediment sample although 10-30% more radiolarian shells and fragments  $<63 \mu\text{m}$  were counted in the surface sediments than in the sediment trap samples.

In the second deployment samples, more than 50% of the  $>150 \mu\text{m}$  opal particles are diatoms. The corresponding flux ( $\sim 130 \mu\text{g cm}^{-2} \text{yr}^{-1}$ ) is similar to the values measured in the 63-150  $\mu\text{m}$  samples ( $\sim 150 \mu\text{g cm}^{-2} \text{yr}^{-1}$ ). Therefore, we use a size separation at 63  $\mu\text{m}$  during the first deployment to differentiate the phytoplankton from zooplankton, whereas we compensate for the large diatoms in the second deployment by only attributing  $>150 \mu\text{m}$  opal to zooplankton in the second deployment.

#### Water Column Weight Fluxes of Microfossils

We use the above size fraction criteria to determine the proportion of calcite and opal that is attributed to each plankton group and to examine how the relative fluxes vary in response to surface water changes.

Foraminifera (i.e.,  $>38 \mu\text{m}$ ) account for 68% of the mean trap measured flux of calcium carbonate (Figure III-3; Table III-2). The dominance of foraminifera is reflected by a high correlation of  $>38 \text{ mm}$  calcite to total calcite ( $r = 0.937$ ). Coccoliths (i.e.,

Table III-2. Size fraction fluxes ( $\mu\text{g}\cdot\text{cm}^{-2}\text{ yr}^{-1}$ ) for the average trap and surface sediments.

	<38 $\mu\text{m}$	38-63 $\mu\text{m}$	63-150 $\mu\text{m}$	>150 $\mu\text{m}$	Total
<u>CaCO<sub>3</sub></u>					
Trap Average <sup>a</sup>	599	116	306	845	1866
Trap Average <sup>b</sup>	532	201	428	1167	2328
Surf Sediment	374	64	155	137	730
% Recycled	30-38	61-68	49-64	84-88	61-69
<u>Opal</u>					
Trap Average <sup>a</sup>	781	101	129	175	1186
Trap Average <sup>b</sup>	901	152	157	258	1468
Surf Sediment	55	18	37	9.1	119
% Recycled	93-94	82-88	71-76	95-97	90-92
<u>Residual</u>					
Trap Average <sup>a</sup>	182	52.5	65.9	168	468
Trap Average <sup>b</sup>	53	126	103	265	547
Surf Sediment	52	3.3	6.9	1.8	64
% Recycled	2-71	94-97	90-93	99	86-88

Trap Average<sup>a</sup> = Time weighted average of samples 1C2-1C4 at 3495 m, 1C5 at 1895 m, and 2C1-2C5 at 2908 m.

Trap Average<sup>b</sup> = Time weighted average of samples 2C2-2C5 at 2908 m.

Surf Sediment = Accumulation at 0-5 cm in core W8402A 14 GC.  
See Chapter I.

% Recycled =  $((\text{Trap Average} - \text{Surf Sediment}) / \text{Trap Average}) \times 100$ ; Range from comparison of Trap Average (a) and (b).

<38  $\mu\text{m}$ ) are >50% in only two of the nine sampling intervals (Figure III-3). Particles >150  $\mu\text{m}$  account for most of the foraminiferal weight flux although there are at least ten times as many shells in the 63-150  $\mu\text{m}$  samples, and a greater number in the 38-63  $\mu\text{m}$  fraction. Studies in the Panama Basin (Thunell et al., 1981; Thunell and Reynolds, 1984) show that large particles, although smaller in number, account for most of the foraminiferal weight flux. This result is important in identifying the plankton group and size fraction responsible for the transfer of inorganic carbon to the deep sea. Knowledge of the number of individuals sedimented does not always relate to the weight flux.

More than 70% of the total opal is attributed to diatoms and this phytoplankton group can be used to represent total opal flux. With a mean flux of 20% of total opal, radiolarians are never a major portion of the flux. This is in contrast to studies of Takahashi and Honjo (1981) and Takahashi (1983) where >50% of total opal is attributed to radiolarians. Their estimates were made by multiplying the shell flux of radiolarians by an average shell weight. Using the same method at Site C, assuming an average weight of 0.20-0.35  $\mu\text{g}/\text{shell}$  (Takahashi and Honjo, 1981), 60-100% of the measured opal in the first deployment can be accounted for by radiolarians. This range is about four times the value based on the size fraction estimates. Better agreement can be obtained by decreasing the average shell weight by an order of magnitude. We note, however, that the period of largest shell flux in the first deployment (1C4) does not correspond to the greatest weight flux due to radiolarians (1C5). Thus, we conclude that size

separations and not average shell weight provide the best estimates of the relative contributions of radiolarians and diatoms to the total opal flux at Site C.

As the surface water properties changed during the sampling period, the fluxes and relative proportions of each plankton group also varied. Coccoliths, which are adapted to nutrient-poor environments (refs. in Dymond and Lyle, 1985), have an unexpectedly high correlation to organic carbon flux ( $r = 0.973$ ) during the first deployment. However, this relationship is not consistent in later samples; resulting in a poor correlation overall ( $r = 0.294$ ). The coccolith portion of the total calcite is greatest during the summer upwelling season of 1983. Although a similar  $<38 \mu\text{m}$  flux is recorded in this season of 1984, the portion of total calcite attributed to coccoliths is much less because of a large increase in foraminiferal shell flux.

A minimum in foraminiferal particulate flux corresponds to the period when nutrient-rich eastern equatorial Pacific waters reached Site C following the ENSO (Cane, 1983). The shell flux of subtropical species Globogerinoides ruber is a factor of 5-6 lower in this interval than in the preceding sampling periods (A. Mix, pers. comm., 1986). Because of its relatively small size, the changes observed in this species cannot account for the large drop in weight flux. Unless the relative proportions of the heavy species changed significantly, a shell production decrease is necessary to explain the large drop in weight flux. At present, these data have not been fully quantified. Preliminary species

data from the second deployment reveals large numbers of G. ruber in 2C4. There is also an increase in the number of heavy shells such as Neogloboquadrina dutertrei, Pulleniatina obliquiloculata, Globigerinella aequilateralis, and Globigerinoides sacculifer. With these preliminary data, we suggest that an increase in shell numbers of the heavy forms, without a major assemblage change or bloom of a particular species, can account for the large calcite flux observed in 2C4.

More than 70% of the total opal is attributed to diatoms, so this phytoplankton group can be used to represent total opal. During the 1982-83 ENSO, measured diatom (opal) fluxes are 2-3 times lower than the deployment mean. These data reflect lower primary productivity conditions associated with the ENSO. Large diatom fluxes are recorded during the 1984 upwelling season (2C4). Calcite and opal fluxes, as well as organic carbon, are greatest during this period.

Radiolarian weight fluxes generally covary with total opal (Figure III-2). However, this correspondence may be masked by an incomplete separation of radiolarians from the phytoplankton. The change in the seasonal pattern of the opal fraction attributed to Radiolaria ( $>63 \mu\text{m}$  for 1C2-1C5 and  $>150 \mu\text{m}$  for 2C1-2C5) is similar to the proportion of calcite corresponding to  $>150 \mu\text{m}$  foraminifera (Figure III-3). The ecological significance of this result is uncertain.

The dominance of calcareous microfossils over opaline forms in the Site C samples is shown in Figure III-4. We note, however, that these values reflect a partially dissolved opal flux, and the

near-surface  $\text{CaCO}_3$ /opal ratio may be lower. Since the samples are obtained above the calcite lysocline, foraminifera and coccolith fluxes should be close to net production values. The largest calcite/ opal values in three of four size fractions are obtained during 1C2. Fine fraction calcite (coccoliths) has a greater flux than fine fraction opal (diatoms). A dominance of coccoliths over diatoms reflects moderate or low nutrient conditions. We have stated that lower than normal opal and organic carbon fluxes recorded in 1C2 reflect lower primary productivity influenced by ENSO. Such conditions provide a mechanism for transferring large calcite fluxes to the deep-sea without a corresponding increase in organic carbon or opal. If similar oceanographic conditions were prevalent in the past, as much as two moles of calcite carbon can be transferred per one mole of organic carbon. Lyle and Dymond (1985) proposed that similar changes could have been responsible in part for Pleistocene  $\text{CO}_2$  variations. Their study focused on phytoplankton changes. Our data show that zooplankton fluxes may also contribute greatly to these variations and should be included in models of past levels of atmospheric  $\text{CO}_2$ .

Figure III-4

Calcite/opal flux ratio in size fractions;  $<38\ \mu\text{m}$  (solid line with circles),  $38-63$  (dashed line with solid circles),  $63-150$  (dashed-dotted line with rectangles), and  $>150\ \mu\text{m}$  (solid line with stars). The ratio in the totals is also given (dotted line with stars). Refer to Table III-1 for dates of the sampling intervals 1C2 to 2C1.



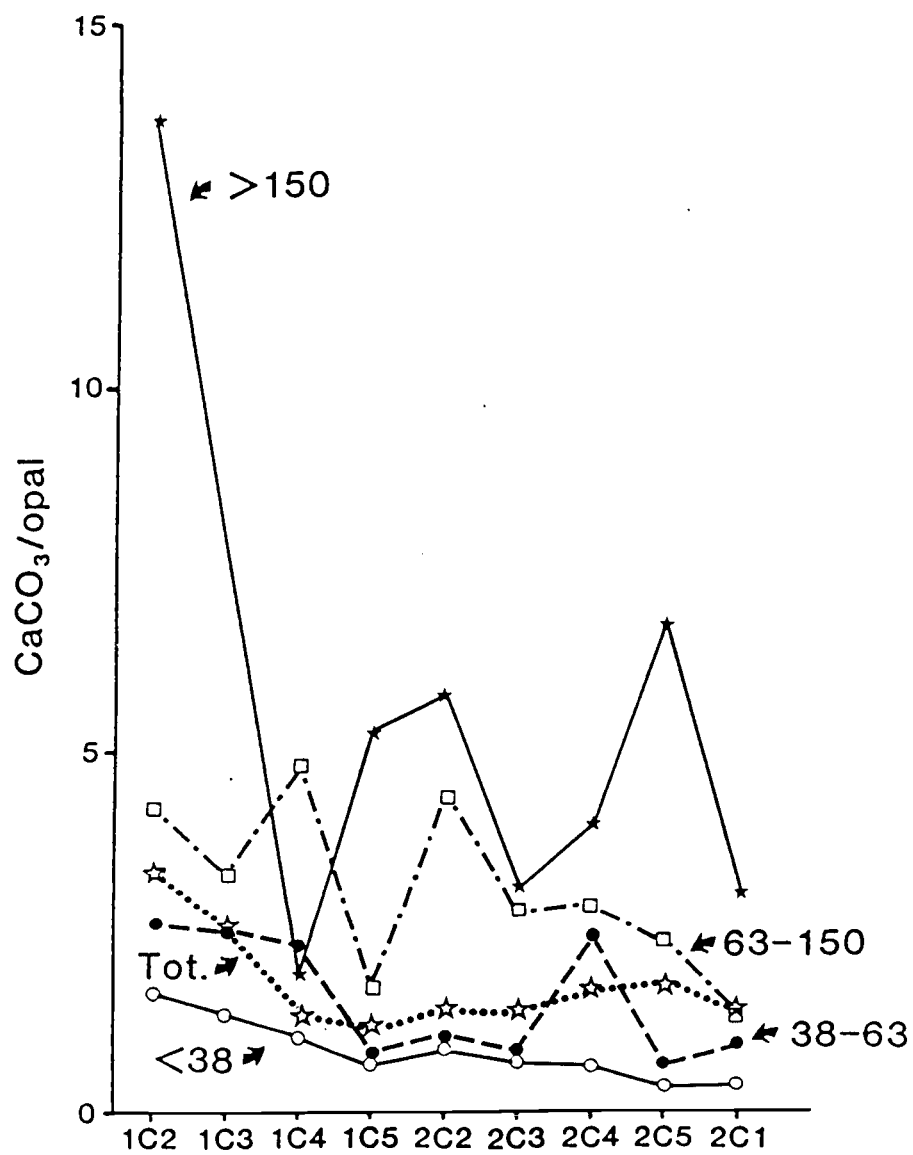


Figure III-4

### Comparison of Trap Fluxes and Sediment Accumulations

Results in Chapter I show that the water-column fluxes of refractory components (i.e., aluminosilicates) measured by the two Site C trap deployments are comparable to accumulations of these same components in the near-surface sediments. These relations are used to support our view that trap fluxes can be compared to accumulations in the sediments even though the time scales of measurement differ by three orders of magnitude. The fluxes of opal, calcite, and residual material measured by the two moorings are used to characterize the inputs to the sediments before dissolution occurs. These values also provide a reference for interpreting paleofluxes from the preserved sediment record. We assume that the flux has had a comparable composition for the last few thousand years. Since the first deployment sampled an anomalous event, we make this comparison with trap ranges that represent the time averaged mean of both deployments, as well as a value that is based only on samples obtained during a "normal" year (2C2-2C5; Table III-2). The sediment accumulation rate is from Chapter I, using a core from a water depth of 4287 m. All estimates of recycling are relative to this water depth; calcite recycling should increase with water depth.

Comparison of water column fluxes to sediment accumulations (Table III-2) shows that 61-69% of the calcium carbonate and 90-92% of the opal flux are recycled in the lower water column and at the sediment-water interface (i.e., below the trap depths). These numbers differ slightly from those in a separate paper by Dymond

(in prep.) because he considers only annual results and corrects for flux changes in the lower water column. The fractions of preserved calcite and opal at Site C are greater than those at MANOP Sites M and H in the eastern tropical Pacific (Fischer et al., 1986).

Size fraction data indicate that a greater proportion of  $>38\ \mu\text{m}$  calcite than  $<38\ \mu\text{m}$  flux is recycled; 72-80% versus 30-38%, respectively (Table III-2; Figure III-5). It is possible that this results from breakage of foraminifera in the  $>38\ \mu\text{m}$  portion rather than a real difference in dissolution. However, visual inspection of the  $<38\ \mu\text{m}$  size fraction shows that foraminifera shells and fragments, although present, do not comprise more than 25% of the  $<38\ \mu\text{m}$  calcite in the sediments. We infer from these data that coccoliths are less affected by dissolution than foraminifera (c.f. Honjo, 1977).

The downcore record of calcite accumulation implies that recycling was less in the past or that the composition and magnitude of the flux changed. Figure III-5 compares the maximum calcite accumulation for the last 200,000 years in Site C core W8402A 14 GC ( $0^{\circ}57.2'\text{N}$ ,  $138^{\circ}57.3'\text{W}$ ; 4287 m water depth) and for the past 450,000 years in nearby core RC11210 ( $1^{\circ}49'\text{N}$ ,  $140^{\circ}03'\text{W}$ ; 4420 m water depth) with the present accumulation rates and the measured trap fluxes. The complete records of calcite accumulation over these time intervals are given in Figure III-6.

Without altering the composition, recycling only 25-40% of the calcite flux could account for the maximum accumulation recorded

Figure III-5

A comparison of calcium carbonate flux ( $\mu\text{g cm}^{-2} \text{ yr}^{-1}$ ) between the time weighted mean of the two trap deployments and sediment samples. The solid bars value for trap mean is the mean for all sampling intervals. The dashed bar is the mean of 2C2-2C5.

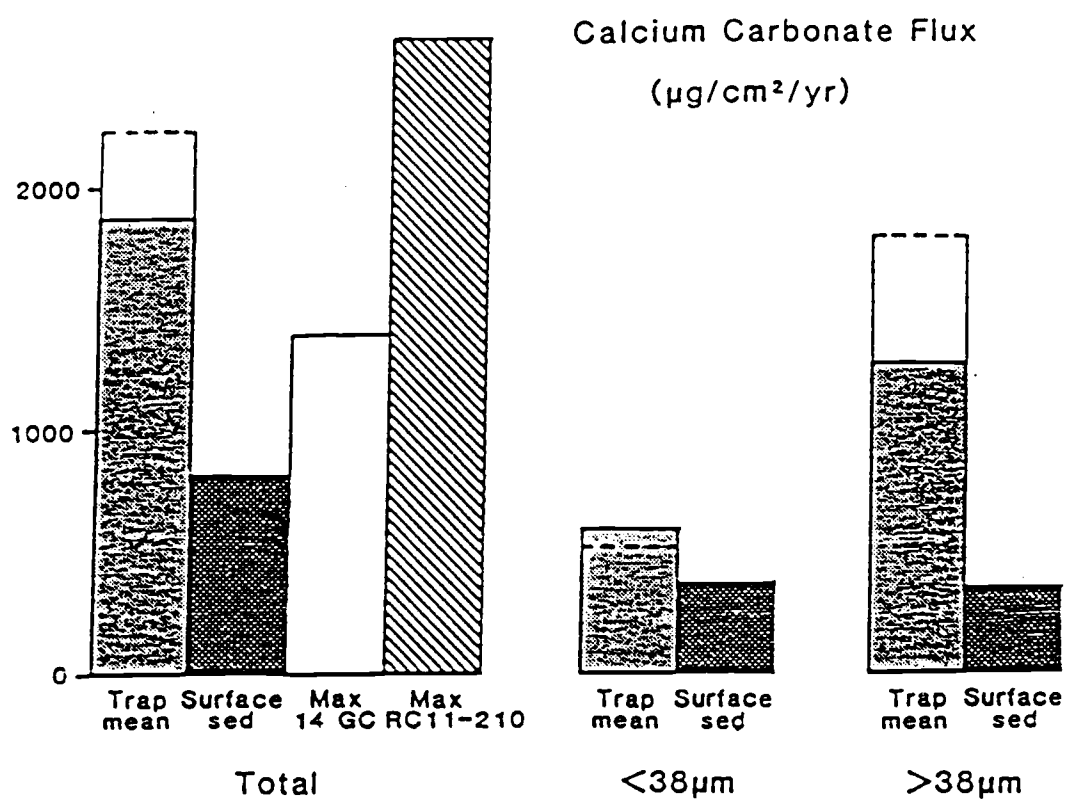
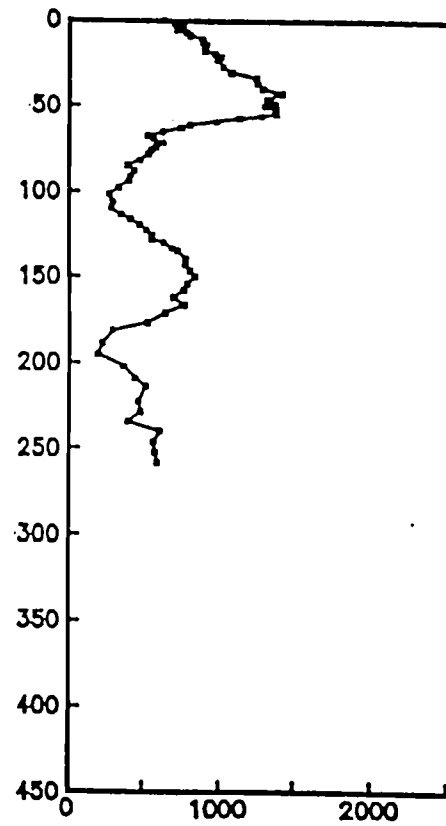


Figure III-5

Figure III-6

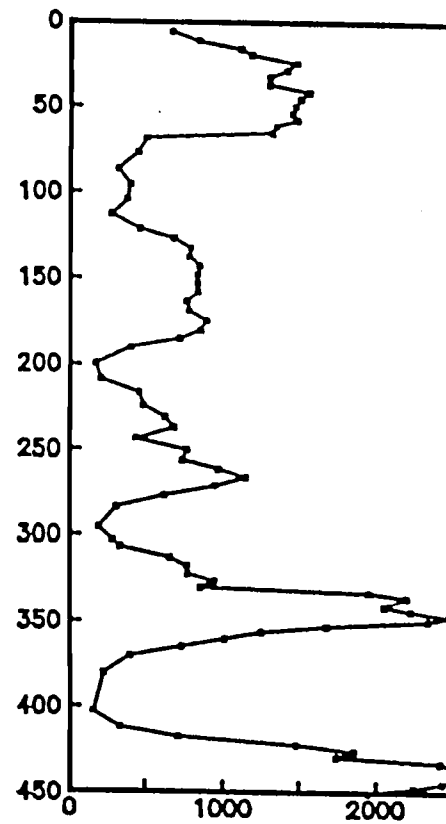
Record of calcium carbonate accumulation ( $\text{mg cm}^{-2} \text{ kyr}^{-1}$ ) during the last 450 kyr for cores (A) W8402A 14 GC and (B) RC11-210.

W8402A 14 GC



A

RC11-210



B

Figure III-6

during the last 200 kyr (Figure III-5). Thompson and Saito (1974) observed time equivalent increases in foraminifera preservation in core RC11-210. Pujos (1985) reported an increase in coccolith preservation in comparable sections of DSDP-IPOD Site 573. Although non-quantitative, there is evidence in this region for the necessary increase in preservation to account for the record of calcite accumulation during the past 200,000 years. We note, however, that the trap foraminiferal assemblage contains species that are very rare, or absent, in sediment samples. If dissolution of these species represents more than 25-40 weight percent of the trap flux, a flux increase during the last 200 kyr is implied. Better estimates of paleo-fluxes will be possible after paleodissolution of the material is quantified.

In contrast, the measured sediment trap fluxes cannot account for calcite accumulation in two intervals during the past 450 kyr in RC11-210 even if all the present trap flux were preserved. The amount of calcite preserved 350 and 440 kyr ago (Figure III-6) is exceeded by the water column fluxes in only one of the nine sampling intervals. These sediment accumulations are 12% higher than the mean flux measured in 2C2-2C5.

A high frequency of well preserved calcite fluxes similar in magnitude to 2C4 and maintained for thousands of years, can account for the recorded increase. Such an increase today is associated with higher opal and organic carbon inputs (Figure III-2), but no evidence of such an association is observed in the Site C sediments (see Chapter I). Extensive recycling of opal and organic carbon would be necessary to explain the lack of correlation. In this



case, these components would not reflect paleoproductivity at Site C. Alternatively, nutrient-poor conditions associated with 1C2 and 1C3 could have provided large fluxes of calcite without raising organic carbon or opal fluxes above present mean levels. In either case, an increase in calcite input above present mean levels is necessary to explain the sediment record at 350 and 440 kyr.

Compared to calcareous microfossils, the siliceous plankton input to the sediments is extensively dissolved in all intervals during the past 200 kyr (Figure III-7). A 5-6% change in recycling can account for accumulation increases. We observe that presently, 85-89% of the  $>63 \mu\text{m}$  opal is recycled or fragmented compared to 92-93% of the  $<63 \mu\text{m}$  opal (Table III-2; Figure III-7). Since some fragments of  $>63 \mu\text{m}$  particles contribute to the  $<63 \mu\text{m}$  fraction, even more than the observed 92-93% of the fine fraction must be recycled. Our data show that dissolution has a greater effect on smaller diatoms than on larger particles. In support of this, Pisias et al. (1986) found that species ratios in trap and sediment samples were similar only for solution-resistant fossil radiolarians. Silicoflagellates and other solution susceptible forms exhibit a poor correspondence between trap and sediment samples. We note that diatom and silicoflagellate assemblages are better preserved in opal-rich intervals. Results in Chapter I show that if dissolution and the porewater flux of opal has been constant in the past, these opal-rich intervals reflect past increases in opal

Figure III-7

A comparison of the time weighted mean opal flux ( $\mu\text{g}\cdot\text{cm}^{-2}\text{ yr}^{-1}$ ) measured in two sediment trap deployments to opal accumulation in sediments from MANOP Site C. Solid line is the mean for all samples. The dashed bar is the mean of samples 2C2-2C5. Surface sediment and maximum accumulation values are from core 14 GC.

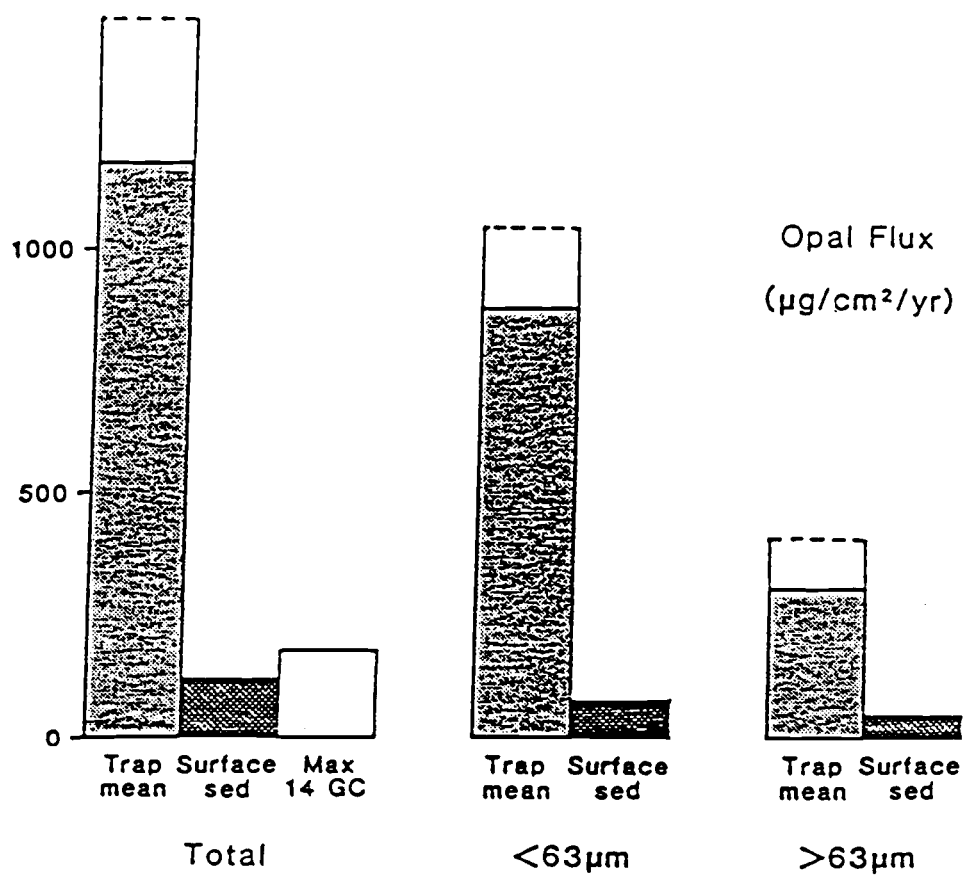


Figure III-7

rain rates. A better understanding of the factors controlling opal dissolution in the sediments is necessary to support this conclusion.

## CONCLUSIONS

Separating the calcite and opal fluxes into various size fractions can effectively differentiate fluxes attributed to phytoplankton from those attributed to zooplankton. At Site C, foraminifera (zooplankton) dominate the calcite input to the sediments, whereas the opal flux is dominated by diatoms (phytoplankton). In samples associated with the 1982-83 ENSO, opal and organic carbon rain rates are below the mean, but calcite fluxes do not decrease. Thus, microplankton population in nutrient-poor waters associated with an ENSO can support a large calcite flux without associated organic carbon to the deep-sea. The zooplankton, which have not received much attention by CO<sub>2</sub> modelers, may play a key role in this transfer.

Using the trap fluxes as standards allows downcore changes in sediment accumulations to be related to paleo-fluxes. These comparisons provide estimates of changes in present conditions that would be necessary to account for the preserved accumulations. Paleo-dissolution must be quantified before accurate calcite paleo-fluxes can be obtained, but if the fluxes have remained relatively constant, variations in preservation can account for the range of calcite accumulation during the past 200,000 years at Site C. A larger flux is necessary to explain the observed accumulation rates at 350 and 440 kyr, however.

Most of the opal that reaches deep waters is recycled in the lower water column and at the sediment-water interface. The species assemblage preserved is only a minor portion of the initial

input, but resistant fossil species have similar ratios in traps and sediments. These results support the use of fossil radiolarian assemblages as recorders of change in water column properties.

## REFERENCES

- Barber, R.T. and F.P. Chavez, Biological consequences of El Niño, Science, 222, 1203-1210, 1983.
- Berger, W.H., G.G. Adelseck, Jr. and L. Mayer, Distribution of carbonate in surface sediments of the Pacific Ocean, J. Geophys. Res., 81, 2617-2627, 1976.
- Cane, M.A., Oceanographic events during El Niño, Science, 222, 1189-1195, 1983.
- Deuser, W.G., Seasonal and interannual variations in deep-water particle fluxes in the Sargasso Sea and their relation to surface hydrography, Deep-Sea Res., 33, 225-246, 1986.
- Deuser, W.G. and E.H. Ross, Seasonal change in the flux of organic carbon to the deep Sargasso Sea, Nature, 283, 364-365, 1980.
- Dymond, J. and M.W. Lyle, Flux comparisons between sediments and sediment traps in the eastern tropical Pacific: Implications for atmospheric CO<sub>2</sub> variations during the Pleistocene, Limnol. Oceanogr., 30, 699-712, 1985.
- Fischer, K., Particle fluxes to the eastern tropical Pacific Ocean - Sources and Processes, Ph.D. Thesis, Oregon State University, Corvallis, 225 pp., 1983.
- Fischer, K., J. Dymond, M.W. Lyle, A. Soutar and S. Rau, The benthic cycle of copper: Evidence from sediment trap experiments in the eastern tropical North Pacific Ocean, Geochim. Cosmochim. Acta, 50, 1535-1543, 1986.

- Gardner, W.D., M.J. Richardson, K.R. Hinga and P.E. Biscaye,  
Resuspension measured with sediment traps in a high-energy  
environment, Earth Planet. Sci. Lett., 66, 262-278, 1983.
- Honjo, S., Biogenic carbonate particles in the ocean: Do they dis-  
solve in the water column? In: The Fate of Fossil Fuel CO<sub>2</sub>  
in the Oceans, edited by N.R. Anderson and A. Malahoff, Plenum  
Press, New York, pp. 269-294, 1977.
- Honjo, S., Seasonality and interaction of biogenic and lithogenic  
particulate flux at the Panama Basin, Science, 218, 883-884,  
1982.
- Honjo, S., S.J. Manganini and J.J. Cole, Sedimentation of biogenic  
matter in the deep ocean, Deep-Sea Res., 29, 609-625, 1982.
- Lyle, M.W., G.R. Heath and J.M. Robbins, Transport and release of  
transition elements during early diagenesis: Sequential  
leaching of sediments from MANOP Sites M and H, Pt. 1, pH 5  
acetic acid leach, Geochim. Cosmochim. Acta, 48, 1705-1715,  
1984.
- Pisias, N.G., D.W. Murray and A.K. Roelofs, Radiolarian and  
silicoflagellate response to oceanographic changes associated  
with the 1983 El Niño, Nature, 320, 259-262, 1986.
- Pujos, A., Nannofossils from Quaternary deposits in the high-  
productivity area of the central equatorial Pacific, Deep Sea  
Drilling Project Leg 85, In: Initial Reports of the Deep-Sea  
Drilling Project, 85, 553-619, U.S. Government Printing  
Office, Washington, DC, 1985.



- Rowe, G.T. and W.D. Gardner, Sedimentation rates on the slope water of the northwest Atlantic Ocean measured directly with sediment traps, J. Mar. Res., 37, 581-600, 1979.
- Takahashi, K., Radiolarian sinking population, standing stock and production rate, Mar. Micropaleo., 8, 171-181, 1983.
- Takahashi, K. and S. Honjo, Vertical flux of Radiolaria: A taxon-quantitative sediment trap study from the western tropical Atlantic, Micropaleontology, 27, 140-190, 1981.
- Thompson, P.R. and T.Saito, Pacific Pleistocene sediments: Planktonic foraminifera dissolution cycles and geochronology, Geology, 2, 333-335, 1974.
- Thunell, R.C., W.B. Curry and S. Honjo, Seasonal variation in the flux of planktonic foraminifera: Time-series sediment trap results from the Panama Basin, Earth Planet. Sci. Lett., 64, 44-55, 1983.
- Thunell, R.C. and L.A. Reynolds, Sedimentation of planktonic foraminifera: Seasonal changes in species flux in the Panama Basin, Micropaleontology, 30, 243-262, 1984.
- Weliky, K., E.Suess, C.A. Ungerer, P.J. Müller and K. Fischer, Problems with accurate carbon measurements in marine sediments and particulate matter in seawater: A new approach, Limnol. Oceanogr., 28, 1252-1259, 1983.

## CHAPTER IV

SEDIMENT ACCUMULATION AT MANOP SITE S, CENTRAL TROPICAL  
PACIFIC: LOCAL REWORKING AND A LATE QUATERNARY  
INCREASE IN SEDIMENT ACCUMULATION

## ABSTRACT

A multi-tracer approach using radionuclide and conservative tracers allows the complex pattern of sedimentation at MANOP Site S (11°N, 140°W) to be deciphered. This area is typical of the region between the Clarion and Clipperton Fracture Zones where most of the world's Cu- and Ni-rich ferromanganese nodules are located. The most recent phase of deposition began within the last 130 kyr and the rate increased by a factor-of-three during the Holocene. Much of this increase can be attributed to Tertiary sediments and Recent opaline material.

A large portion of the near-surface sediment is reworked Tertiary material. Therefore, a simple mass balance between measured water column fluxes and sediment accumulations which does not first account for the input of reworked material, cannot be used to infer the availability of metals to nodules growing at the sediment-water interface.

## INTRODUCTION

During the Manganese Nodule Program (MANOP), numerous measurements were directed towards understanding the cycling of biologically active elements and trace metals in the deep-sea. Extensive analyses of pore waters, sediments and particles settling through the water column were made to understand quantitatively, the flux of elements to and from the seafloor. The results were utilized to identify processes controlling the formation of deep-sea ferromanganese nodules (Moore et al., 1981; Dymond et al., 1984; Lyle et al., 1984; Finney, 1986).

One of the study areas, MANOP Site S (11°N, 140°W), lies within the siliceous clay province of the northeast equatorial Pacific. Sedimentation at this site shares the general characteristics of this region that have been described elsewhere (Moore, 1970; Johnson and Johnson, 1970; Johnson, 1972; von Stackelberg, 1979; Piper et al., 1979). Cores taken within a relatively small area have thicknesses of Quaternary sediment which range from a few meters to only centimeters. Outcrops of Tertiary sediments and the presence of reworked Tertiary radiolarians in surface Quaternary material (Riedel and Funnell, 1964; Moore, 1970; Kadko, 1983) indicate that erosion and redeposition is occurring now or has occurred in the very recent geologic past. A quantitative understanding of the movement of sediment across the seafloor has the potential to help explain the formation and survival of slowly growing manganese nodules which are common at the seafloor in the siliceous clay province.

In a preliminary study of sedimentation at Site S, Kadko (1983) used the downcore concentrations of  $^{230}\text{Th}$ ,  $^{231}\text{Pa}$ , radiolarians, and clay minerals in two box cores to quantify relative and absolute rates of deposition and erosion at these locations. A numerical box model was used to examine the effect of bioturbation and erosion on estimated input rates of the four tracers. Kadko found that subsequent to a period of intense erosion, this site has been experiencing a period of more quiescent sedimentation conditions. The age assigned to the Quaternary radiolarian assemblage suggests that this recent episode of sedimentation began within the last 500,000 years.

In this study, we build upon the initial work of Kadko (1983) and examine the Recent sedimentary history of Site S. Solid phase elemental data is included as an additional tracer and the chemical composition of all observed facies at this site is determined. In addition, analyses of sediment trap samples obtained between December 1982 and February 1984 define the primary input of material to the sediments, and bound the recycling of bio-active components (i.e., opal, organic carbon and calcium carbonate) in the lower water column and near-surface sediments. With the sources better defined than in the initial study, we have re-examined Recent sedimentation in the two cores studied by Kadko (1983), and in an additional core containing a Pliocene(?) non-fossiliferous clay 5 cm below the seafloor. Our goal has been to quantify the roles of the primary input and erosion in determining the composition of near-surface sediments.

## SITE DESCRIPTION

Site S is characterized by a broad north-south trending valley which is bounded by ridges on at least three sides (Figure IV-1). Four kHz reflection profiles reveal a surficial acoustically "transparent" layer in the valley (Karas, 1978). This layer, which is as much as 10 m-thick along the axis of the valley, thins out dramatically toward the walls (as defined by the 4900 m isobath). The "transparent" layer has a maximum thickness of 5 m in the area cored during cruise K7905 (Figure IV-1; Lyle, unpub. data). Calcite-rich layers lower in the stratigraphic column crop out on the flanks of the valley and are evident as truncated reflectors in reflection profiles. Radiolarians from most of these layers belong to the C. tetrapera to S. delmontensis Zones (early Miocene; 18-21.5 myr ago). However, some of the near-surface sediments from the eastern ridges are of Oligocene age (T. tuberosa Zone; 32-36 myr ago).

Examination of the lithologic characteristics from over 60 cores taken at Site S reveals a stratigraphic section containing four facies within the top few meters of sediments. The basal unit (Unit 4) is a nannofossil ooze of Oligocene to early Miocene age depending upon the location within the basin. Calcium carbonate content ranges from 60-95% and radiolarians are well preserved with abundances ranging from  $1-3 \times 10^6$  rads  $\cdot$  (g  $\cdot$  CaCO<sub>3</sub>-free sediment)<sup>-1</sup>. Above the nannofossil ooze lies the basal unit of the "transparent" layer; a non-fossiliferous manganese enriched clay (Unit 3). Preliminary <sup>10</sup>Be data suggest that the age of this layer is Pliocene,

Figure IV-1

Bathymetry of MANOP Site S constructed from data obtained during cruises MN75-05 and MN76-01 (Karas, 1978) with additional 12 kHz data from cruise W8402A. Location of cores used in this study are noted. Core numbers prefixed with a B and K refer to cruises BENTHIC III and K7905, respectively. The small rectangle in the central basin outlines an area where 18 gravity and 16 box cores were collected during cruise K7905.

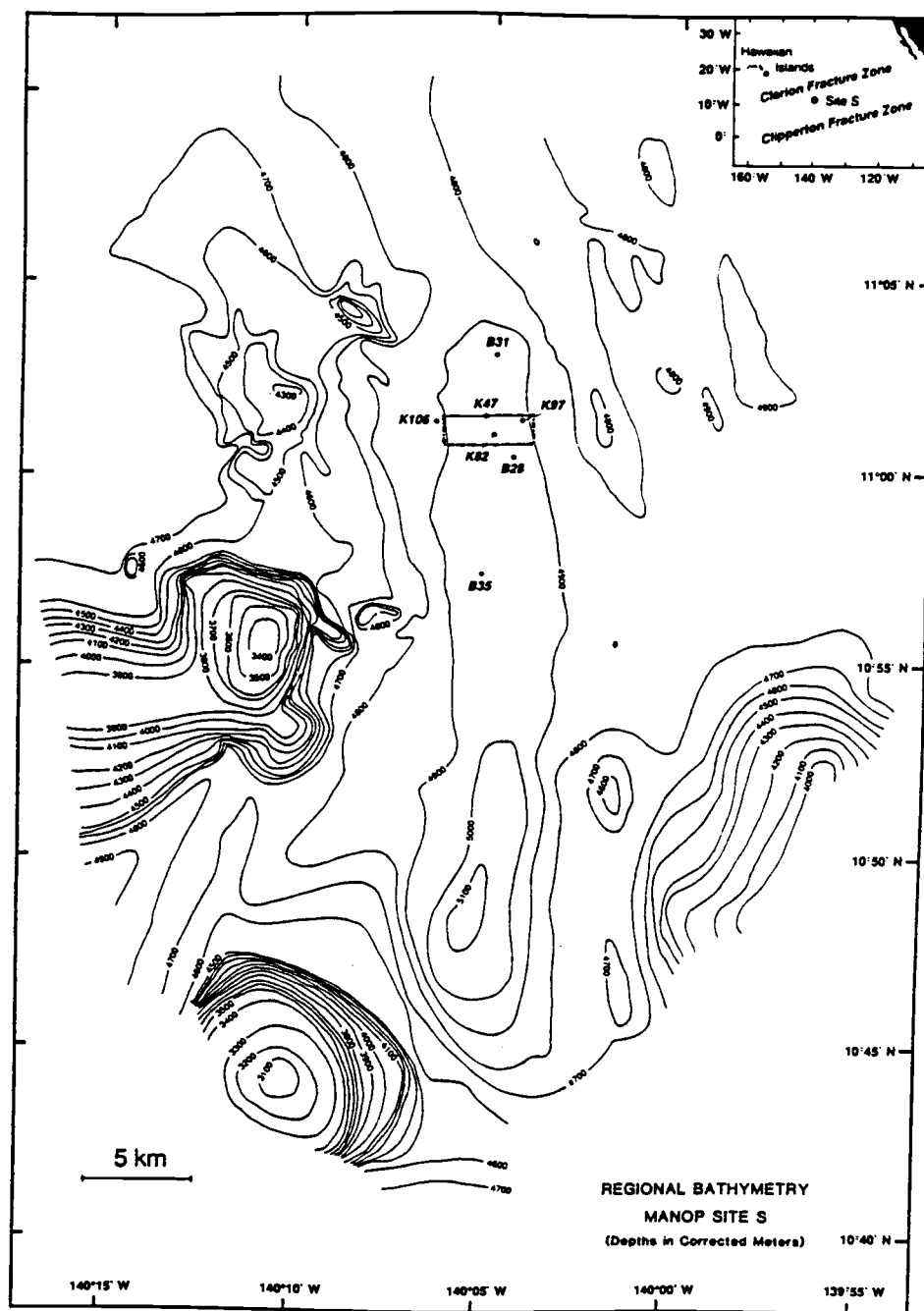


Figure IV-1



although further analyses are necessary before this age can be considered reliable. The contact between the clay and the nannofossil ooze is sharp with little evidence of mixing across the boundary. The upper boundary of the clay can be either sharp or gradational. Above the non-fossiliferous section is a radiolarian clay containing reworked lower Miocene, Oligocene and some Eocene radiolarians with abundances of about  $1 \times 10^5$  rads  $g^{-1}$  (Unit 2). Some cores contain thin manganese enriched sections and, in rare instances, buried manganese nodules. The top of this unit contains Quaternary radiolarians and the contact with the overlying unit is mottled. The top-most layer (Unit 1), a moderate-dark yellowish-brown radiolarian clay, contains Quaternary radiolarians and diatoms as well as some reworked Tertiary siliceous microfossils. Manganese nodules at the seafloor are abundant in cores from the flanks (over  $800 \text{ m}^{-1}$ ), but are sparse ( $<20 \text{ m}^{-1}$ ) in the axis of the basin.

Large-diameter gravity cores from the central basin generally sample Units 1-3, but do not penetrate to the basal unit. Since the transparent layer thins toward the flanks of the basin and Units 2 and 3 are thin or absent, cores taken in water depths near 4900 m penetrate to Unit 4. All cores contain at least 1 cm of the top-most layer which is always less than 10-cm thick. Figure IV-2 presents a generalized west-east profile across Site S and shows the top few meters of sediment from water depths greater than 4800 m. This profile and the relative layer thicknesses are not drawn to scale. However, the figure summarizes the stratigraphic relationship of the four previously described units and illustrates

Figure IV-2

Schematic W-E profile across Site S, for the area below 4800 m, illustrating the stratigraphic relationship of Units 1-4. The profile and the relative layer thicknesses are not drawn to scale. Units 1-3 comprise the "transparent" layer evident on seismic reflection profiles. The core locations, as shown by arrows, illustrate which depositional environments were sampled by the cores used in this study (see Figure IV-1). BBC (Basin Box Cores) refers to cores K47, B28 and B35. The eastward thinning of layers also represents the thinning to the north.

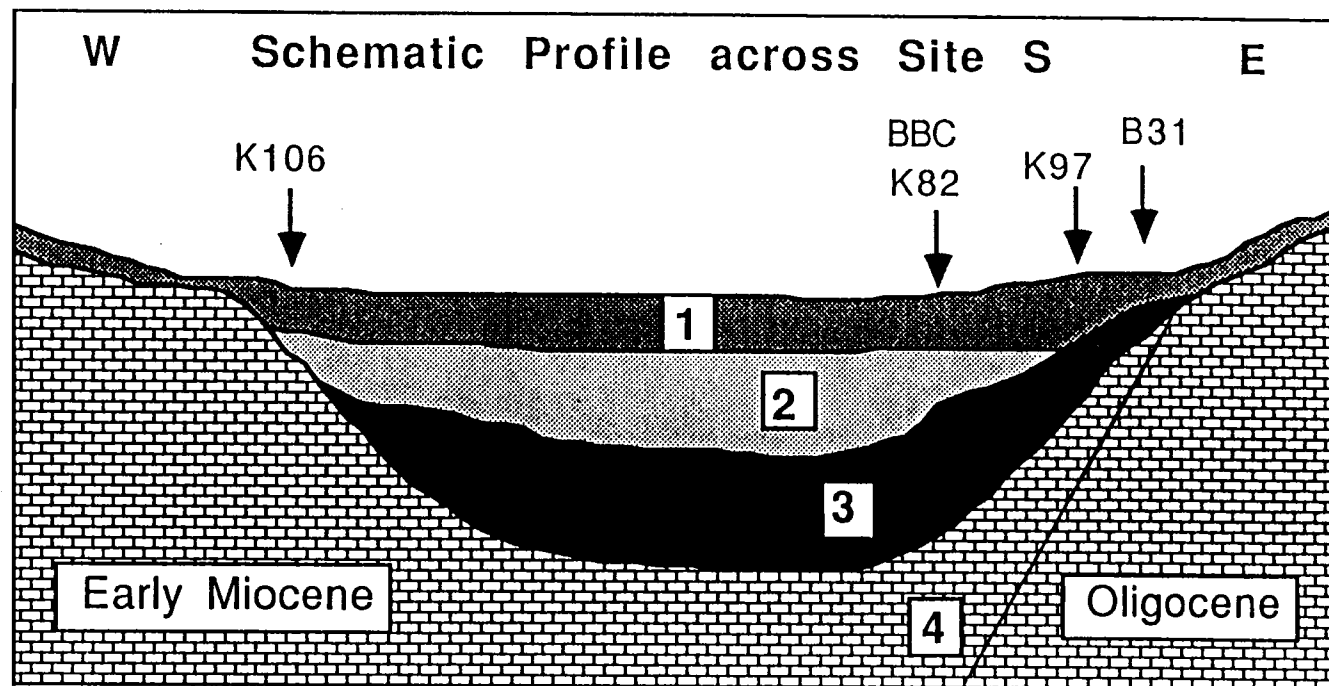


Figure IV-2

how cores located on the flanks of the basin may lack Units 2 and 3. The location of the contact between early Miocene and Oligocene sediments and the structural cause of Oligocene exposures at shallow depths on the eastern wall of the Site S basin are unknown.

## METHODS

Selected cores representing all facies observed at Site S were analyzed for bulk elemental composition (Appendix 2). Analyses were performed on a wavelength dispersive Phillips P.W. 1600 simultaneous X-ray fluorescence (XRF) spectrometer. Approximately 2.5 g of ground sample was pressed at five tons pressure into XRF discs with a cellulose backing. A fundamental parameters program developed by Criss Software, Inc. (c.f. Criss et al., 1978), in addition to a background stripping program developed at Oregon State University (G. Campi, pers. comm., 1986), were used for the data reduction. The precision for the reported concentrations is within 1% and the accuracies are within 5%. Opal was calculated as 2.5 times the difference between total Si and detrital Si with detrital Si taken as 3.4 times the Al concentration. The value of 3.4 represents the ratio of Si to Al in the residual of a sequential leach of Site S sediments (Robbins et al., 1984). Water contents were calculated from chlorine concentrations by attributing all the chlorine in a sample to seawater with a salinity of 34.7‰. Reported dry bulk densities were calculated from the XRF-determined water contents using the equation:

$$\text{Dry density (g}\cdot\text{cm}^{-3}) = 1.051 (-0.01 \times \text{W.C.})$$

where W.C. is the water content in wt %. The equation is based on 46 pairs of values of measured dry weight of a known volume and XRF-water content.

Radiolarian slides of the  $>63\ \mu\text{m}$  fraction were prepared by the method of Roelofs and Pisias (1986) using one gram of dry sample. Abundances are based on counts of more than 500 shells (Appendix 3. The error in the radiolarian content of a sample can be as high as a factor-of-two but commonly is within 20%. Part of this error can be attributed to the large number of radiolarian fragments on each slide.

The  $<63\ \mu\text{m}$  material was saved; treated first with a pH 5 hydroxylamine hydrochloride-sodium citrate solution (Robbins et al., 1984) to remove iron and manganese coatings, and then separated into three fractions:  $<2\ \mu\text{m}$ ,  $2\text{--}20\ \mu\text{m}$ , and  $>20\ \mu\text{m}$ , by repeated Stokes-Law settling. Only the finest fraction has been processed for clay mineral analysis in this study. Samples were saturated with a 0.1N magnesium chloride solution, concentrated by candle filtering, and then freeze-dried. Fifty mg of clay sample was dispersed into 20 ml of distilled water. Fifty mg of  $<2\ \mu\text{m}$  boehmite (internal standard) was also dispersed in 20 ml of distilled water. A mix of 4.5 ml of clay suspension with 0.5 ml of boehmite was diluted with 3 ml of distilled water. Oriented mounts were made by pipetting 4 ml of the homogeneous mixture onto a  $0.45\ \mu\text{m}$  Millipore filter approximately 25 mm in diameter attached to a vacuum flask. The filters were placed on glass slides covered with three drops of a dilute solution of glue. Samples were then dried and solvated with ethylene glycol. Samples were X-rayed on a Scintag diffractometer at  $1^\circ\ 2\theta\ \text{min}^{-1}$  from  $0\text{--}30^\circ\ 2\theta$ . Scintag software was used to strip the background, deconvolve overlapping peaks, and

determine peak areas. The precision of the peak areas is within 20%.

Coefficients determined by Heath and Pisias (1979) were used to convert peak areas to abundances of smectite, illite, kaolinite, and chlorite. A substantial portion of the Site S sediments, generally more than 50%, is unaccounted for by the four clay minerals. Our values for illite (Appendix 3) are comparable to the corrected Biscaye values of Heath and Pisias (1979).

Uranium-series isotope data for cores K7905 47 and 106 BC have been taken from Kadko (1983). Data for BENTHIC III 31 BC (Appendix 4) were measured using the procedure outlined by Kadko (1983).

## RESULTS AND DISCUSSION

Facies Compositions

Downcore profiles of sediment components from selected Site S cores (Table IV-1; Figure IV-1) are presented in Figures IV-3 to IV-7. These cores sample the full range of lithologic variability observed at this site and the data are used to define the composition of each unit. The elemental data are tabulated in Appendix 2 and the clay-mineral and radiolarian data are listed in Appendix 3.

Selected data for gravity core K7905 82 GC from the northern part of the Site S basin which contains the top three sedimentary units are shown in Figure IV-3. Unit 1 is characterized by opal and manganese concentrations of 16-18% and 0.2-0.3%, respectively. Quaternary radiolarians comprise 80% of the radiolarian tests and the % illite/% smectite ratio is near 30. The transition between Units 1 and 2 coincides with a decrease in manganese concentration from 0.2 to less than 0.1% near 7 cm. Because of the oxic nature of Site S sediments (Jahnke et al., 1982), the observed near-surface manganese enrichment (see also Figure IV-4) cannot be attributed to post-depositional migration of manganese in pore waters. Another process, such as a slowdown of detrital sedimentation with a constant input of authigenic manganese or lateral transport of solid-phase manganese, must be responsible for the increase. The source of this near-surface change will be examined in a later section.



Table IV-1. Cores from MANOP Site S.

Cruise	Core <sup>a</sup>	Location <sup>b</sup>		Water Depth (corrected meters)	Length (cm)
		(Lat. N -	Long. W)		
K7905	47 BC	11°01.55'	140°05.11'	4919	35
	82 GC	11°01.09'	140°04.88'	4924	246
	97 GC	11°01.48'	140°04.24'	4912	242
	106 BC	11°02.14'	140°06.41'	4897	31
BENTHIC III	28 BC	11°00.52'	140°03.38'	4932	30
	31 BC	11°03.20'	140°04.86'	4904	31
	35 BC	10°57.44'	140°05.09'	4938	30

<sup>a</sup>All cores stored at Oregon State University; BC = Box Core, GC = Gravity Core.

<sup>b</sup>Locations given by Marine Physical Laboratory, Scripps Institution of Oceanography.

Figure IV-3

Downcore profile of selected solid-phase components in addition to % illite/% smectite ratio and % Quaternary radiolarians for core K7905 82 GC. This core contains a surface layer with mixed Quaternary and Tertiary radiolarians with only Tertiary reworked material between 50 and 190 cm. A Pliocene(?) manganese-rich non-fossiliferous clay lies below 190 cm. The boundaries of Units 1-3B are indicated.

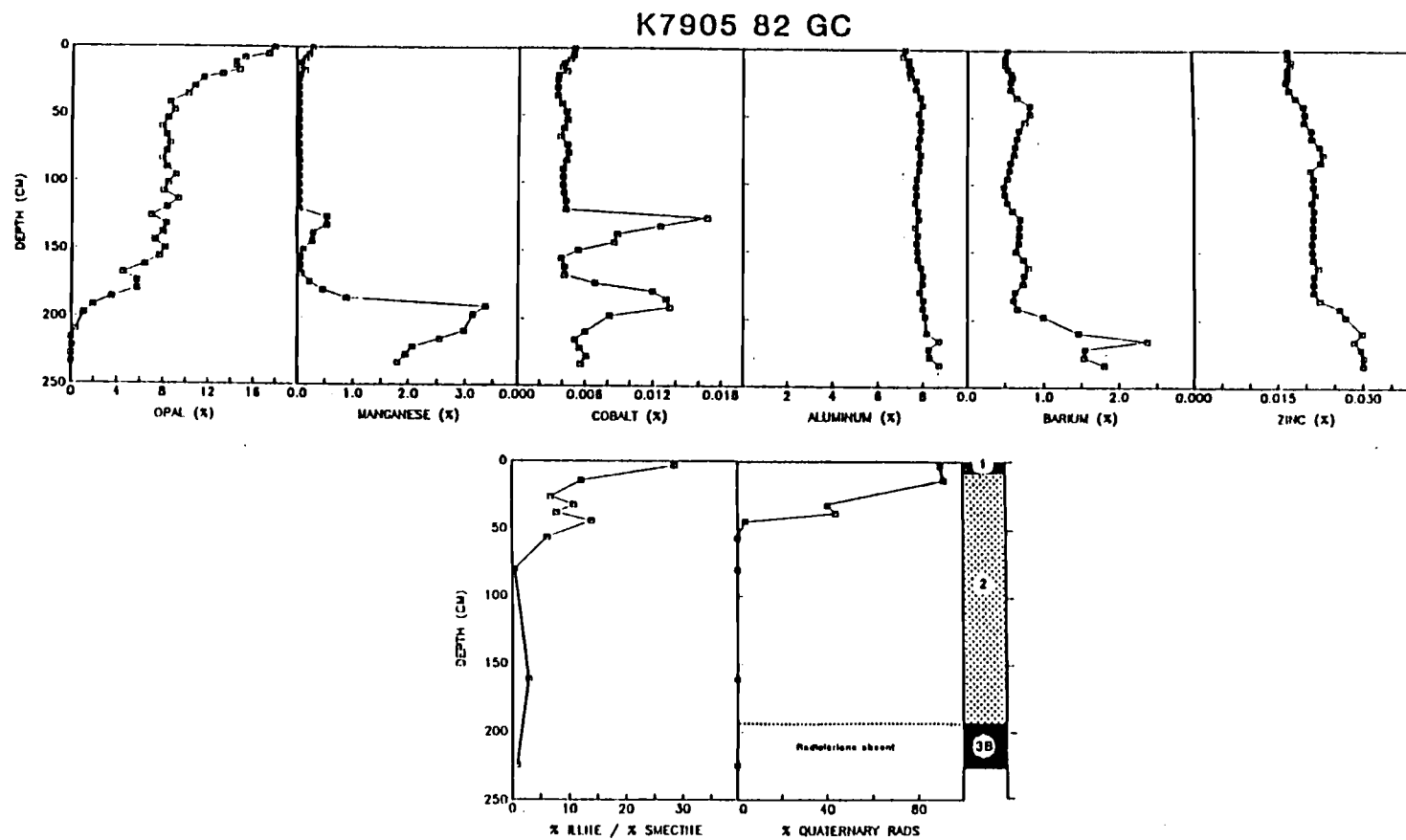


Figure IV-3

Figure IV-4

Downcore profiles of opal, manganese, % illite/% smectite, and % Quaternary radiolarians from representative box cores located in the central basin. Profiles A, B and C refer to cores B28, B35 and K47, respectively. The boundary between Units 1 and 2 is indicated on the right side of the Figure.

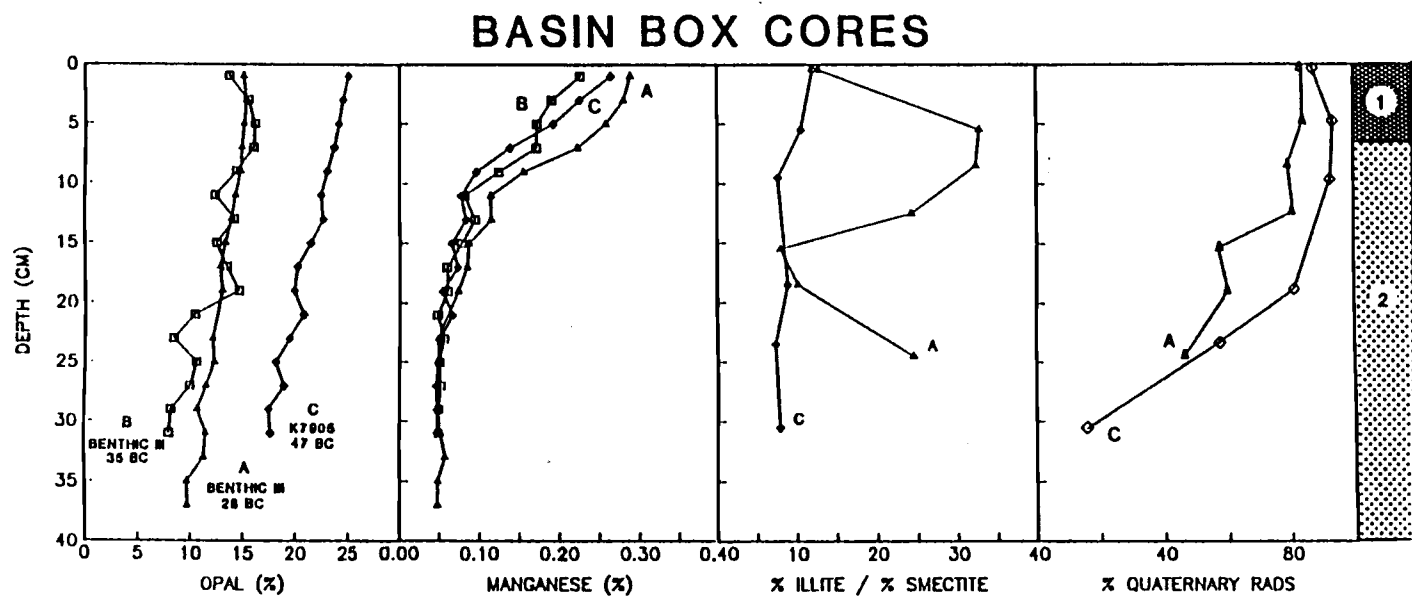


Figure IV-4

## Figure IV-5

Downcore profiles of opal, manganese, % illite/% smectite and % Quaternary radiolarians for core BENTHIC III 31 BC. A Pliocene(?) non-fossiliferous manganese-rich clay is located below 5 cm sub-surface. The Units sampled by this core are indicated.

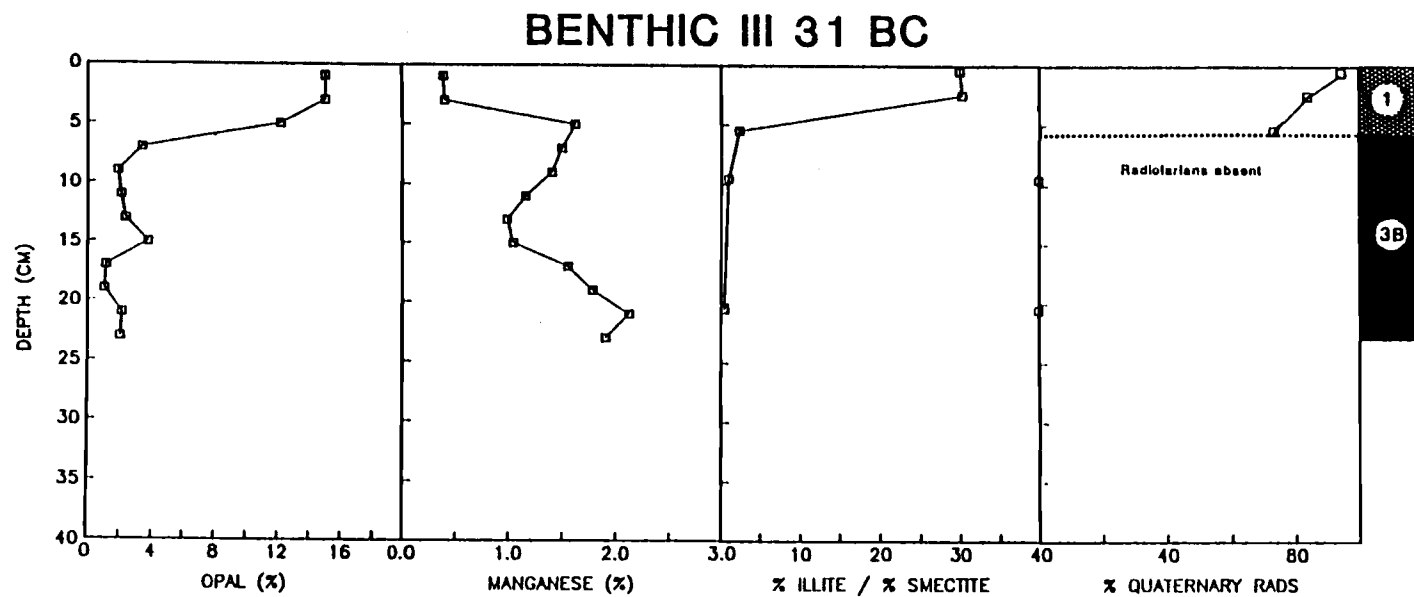


Figure IV-5

Figure IV-6

Downcore profiles of selected solid-phase components for core K7905 97 GC. This core contains a mix of Tertiary and Quaternary radiolarians in the top 20 cm. A Pliocene(?) manganese-rich non-fossiliferous clay (Unit 3A) that is visually and chemically distinct from those in 31 BC and 82 GC is present below 20 cm.



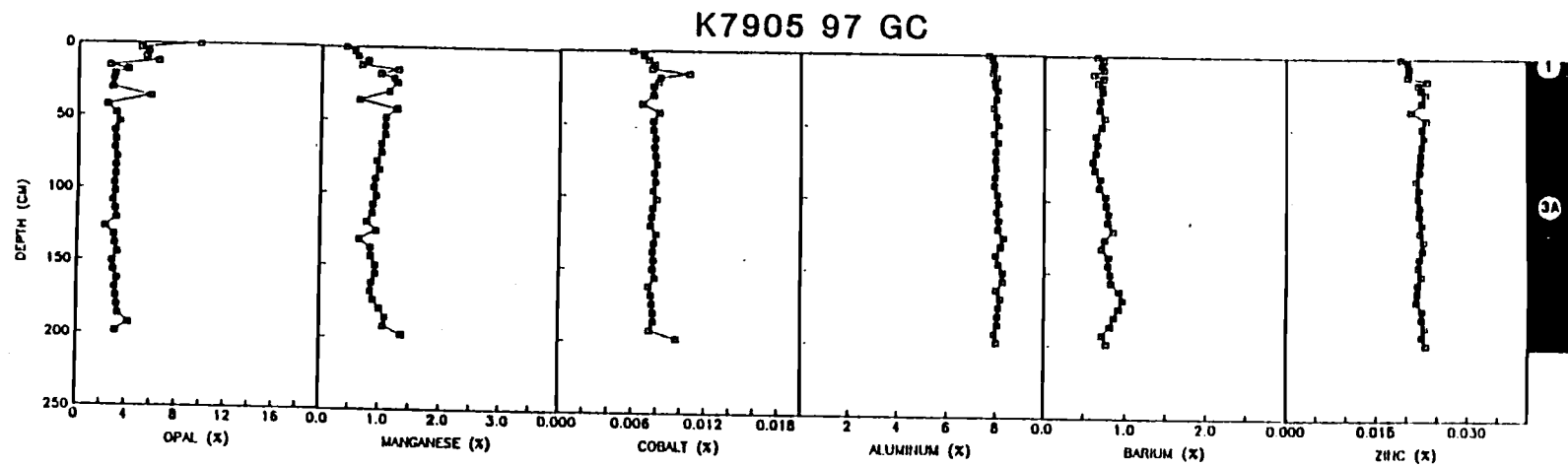


Figure IV-6

## Figure IV-7

Downcore profiles of calcium carbonate, opal, manganese, % illite/  
% smectite and % Quaternary radiolarians from core K7905 106 BC.  
This core contains a lower Miocene nannofossil ooze below 17 cm  
sub-surface. Opal and manganese are presented on a carbonate-free  
basis. The boundaries between Units sampled by this core are  
shown.

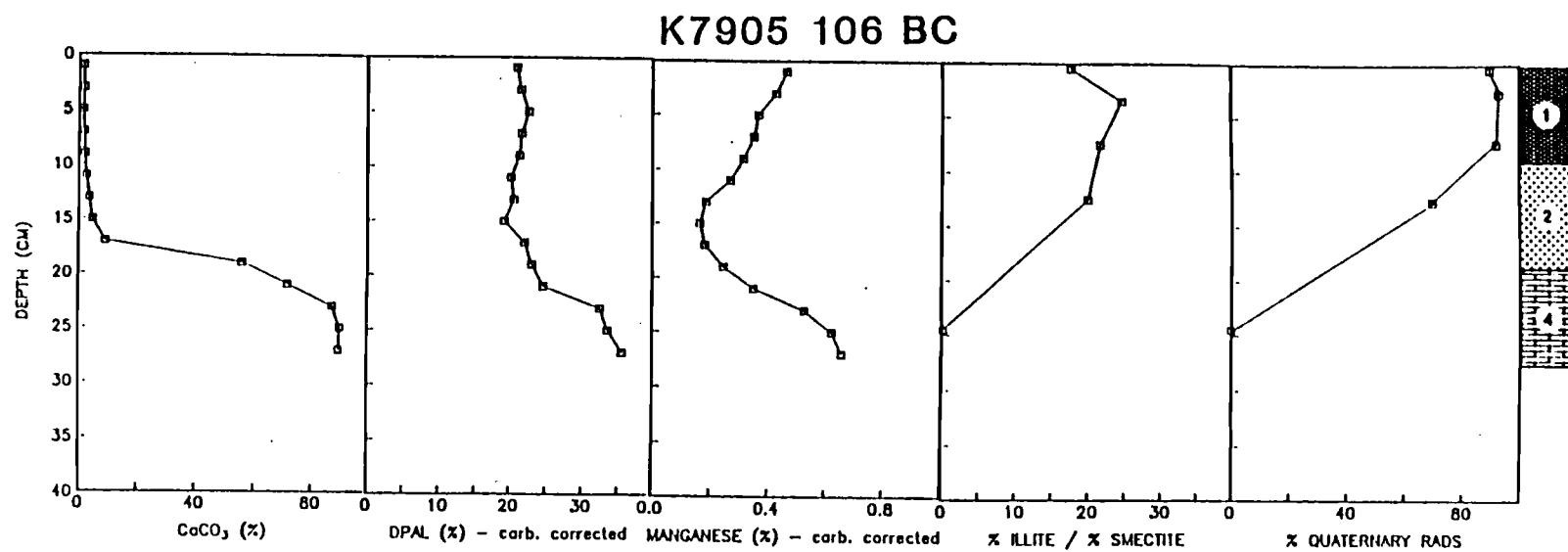


Figure IV-7

The upper part of Unit 2 contains a Quaternary component which decreases with depth. Opal and radiolarian data reflect this decrease. The Quaternary radiolarian assemblage lacks Stylatractus universus Hays which suggests that this component is younger than 400,000 years (Hays and Shackleton, 1976). Illite is enriched in Recent sediments from this region (Heath, 1969), and the values for the % illite/% smectite ratio imply that Quaternary material is present at 55 cm sub-surface. Below 55 cm, Unit 2 is comprised of reworked Tertiary material. The average composition of sediments between 60 and 100 cm is used to characterize a reworked Tertiary sediment component (Table IV-2).

A manganese-rich crust defines the contact between Units 2 and 3 in this core. We infer that this manganese-rich layer and the enrichment near 130 cm record prolonged exposure to seawater so that enrichments of manganese and cobalt are the result of authigenic deposition. For a constant flux of manganese, the high concentrations imply a sedimentation rate of  $0.4 \text{ mm-kyr}^{-1}$  (Krisnaswami, 1976). Further radiometric analyses of long-lived isotopes such as  $^{10}\text{Be}$  are necessary to confirm this interpretation. The section of Unit 3 that was cored by 82 GC is termed 3B. Compared to Unit 3A (see Figure IV-6) this section is enriched in manganese and cobalt which implies a slower deposition rate for 3B.

The Basin Box Cores (Figure IV-4) were taken from the same depositional setting as 82 GC. The large number of samples analyzed from these cores provide high resolution records which overlap with the top 30 cm of 82 GC. The opal content in K7905 47 BC is a factor of two higher than in other cores. This may reflect

Table IV-2. Mean Composition of Tertiary Facies.

	Radiolarians (shells/cm <sup>3</sup> )	Manganese (μg/cm <sup>3</sup> )	Opal (mg/cm <sup>3</sup> )	Aluminum (mg/cm <sup>3</sup> )
Unit 2	30,000	155	24	27
Unit 3A	0	3550	11	28
Unit 3B	0	4200	6	23
Unit 4 <sup>a</sup>	170,000 <sup>b</sup>	1682	95	16

<sup>a</sup>Corrected for calcium carbonate.

<sup>b</sup>Represents a minimum value for this Unit.

selective preservation in 47 BC, although radiolarian abundances of  $2-4 \times 10^5 \text{ rads} \cdot \text{gm}^{-1}$  are comparable in all three box cores.

Core BENTHIC III 31 BC (Figure IV-5) contains a 5 cm-thick section of Unit 1 lying unconformably on Unit 3B. This represents a site that is closer to the basin wall (i.e., the 4900 m isobath) than is 82 GC. Figure IV-2 presents a schematic diagram of the relative positions of these cores in the Site S basin. The samples below 10 cm in core 31 BC are used to define the composition of Unit 3B (Table IV-2).

Core K7905 97 GC (Figure IV-6) contains Unit 3A, a non-fossiliferous manganese-rich clay, below 10 cm. This sediment type is present beneath a thin surface layer in cores on the east flank of the basin near the 4900 m contour (i.e., near 97 GC), and is common in cores in the center of the basin where the transparent layer is more than 5 m-thick. Preliminary  $^{10}\text{Be}$  data suggest a Pliocene age, comparable to that at the base of 82 GC. The two non-fossiliferous clays are visually distinct and the manganese concentration in 97 GC is lower than in either 82 GC or 31 BC (Figures IV-3 and IV-5). If this concentration is the result of authigenic sedimentation of manganese with the rates established by Krisnaswami (1976), then a lower concentration reflects sedimentation rate  $(S = 0.5 \text{ mg} \cdot \text{cm}^{-2} \text{ kyr}^{-1} / (10 \text{ mg Mn} \times 0.35 \text{ g} \cdot \text{cm}^{-3}) = 0.14 \text{ cm} \cdot \text{kyr}^{-1}$  vs  $0.04 \text{ cm} \cdot \text{kyr}^{-1}$  for the manganese crust in 82 GC). The distinction may be simply a function of different detrital accumulation rates at these locations. Future studies will attempt to verify these rates. The section below 50 cm in 97 GC is used to define the composition of Unit 3A (Table IV-2).

Core K7905 106 BC (Figure IV-7) contains the top two units above 20 cm lying uncomformably on an early Miocene nannofossil ooze (Unit 4). Some upward mixing of the nannofossil ooze is evident. Although Quaternary, Oligocene, Eocene and early Miocene radiolarians are present in samples shallower than 15 cm, neither Oligocene nor Eocene microfossils are present in the nannofossil ooze that was deposited when this site was shallower (above the compensation depth) and lay beneath the equatorial high-productivity belt (van Andel et al., 1975). Thus, the pre-early Miocene material above 15 cm cannot be attributed to pure upward mixing of older sediment, but must have been transported to the site from other locations. We use this nannofossil ooze to represent the initial concentration of early Miocene material (Table IV-2).

#### Sedimentation Model

Sediment tracers which characterized the facies compositions (Table IV-2) in conjunction with  $^{230}\text{Th}$  ( $t_{1/2} = 75 \text{ kyr}$ ) and  $^{231}\text{Pa}$  ( $t_{1/2} = 32.5 \text{ kyr}$ ) inventories can be used to quantify the near-surface accumulation of sediment in three Site S box cores. Since they do not decay with time, the sediment tracers are termed conservative in comparison with the nuclides. Two cores previously studied by Kadko (1983) are re-examined using the new tracer data and an additional core, BENTHIC III 31 BC (Figure IV-5) is also considered. These represent three distinct sedimentary environments at Site S.

A numerical mixing model that allows for the erosion of sediments and inputs of both Recent (which western primary) and old (i.e., radioactively dead with respect to the nuclides considered) material is used to quantify the contributions of several components to the sediment compositions of the three box cores. Full details of the model and governing equations are given by Kadko (1983); only the important properties are summarized here.

The model divides the vertical layers, a mixed layer of "L" centimeters where bioturbation proceeds at a constant rate ( $D$ , in  $\text{cm}^2 \cdot \text{kyr}^{-1}$ ) underlain by sediment where  $D$  is zero or decreases as a function of depth ( $D = D_0 \times R^{(Z-L)}$  where  $0 < R < 1$ ) (Figure IV-8). There is an input ( $I$ ) of nuclides ( $\text{dpm} \cdot \text{cm}^{-2} \cdot \text{kyr}^{-1}$ ) and a conservative tracer ( $\text{units} \cdot \text{cm}^{-2} \cdot \text{kyr}^{-1}$ ) which can have a primary and eroded source. The net advection (sedimentation) rate ( $B$ , in  $\text{cm} \cdot \text{kyr}^{-1}$ ) is the balance between the sedimentation rate ( $S$ , in  $\text{cm} \cdot \text{kyr}^{-1}$ ) and the erosion rate ( $E$ , in  $\text{cm} \cdot \text{kyr}^{-1}$ ). A negative value for  $E$  indicates erosion of primary and old material and a positive value reflects net deposition of older reworked material. Thus, if  $-E > S$ , net erosion occurs. If  $-E$  is close to or equal to  $S$ , nuclides and the conservative tracer inputs will accumulate in a mixed layer of length "L". Conditions of  $-E \gg S$  with  $D$  and  $L$  both small will result in the accumulation of only a small fraction of the nuclide in the sediment (Kadko, 1983). In this model,  $I$ , the input flux of conservative tracers, and the corresponding advection rate,  $S$ , consider only resistant material and do not address the dissolution of tracers, such as opal, which are not fully



Figure IV-8

Schematic diagram of sedimentation modified from Kadko (1983). If  $E$  is negative, both primary and old material is eroded. A positive value for  $E$  reflects net deposition of older reworked material.

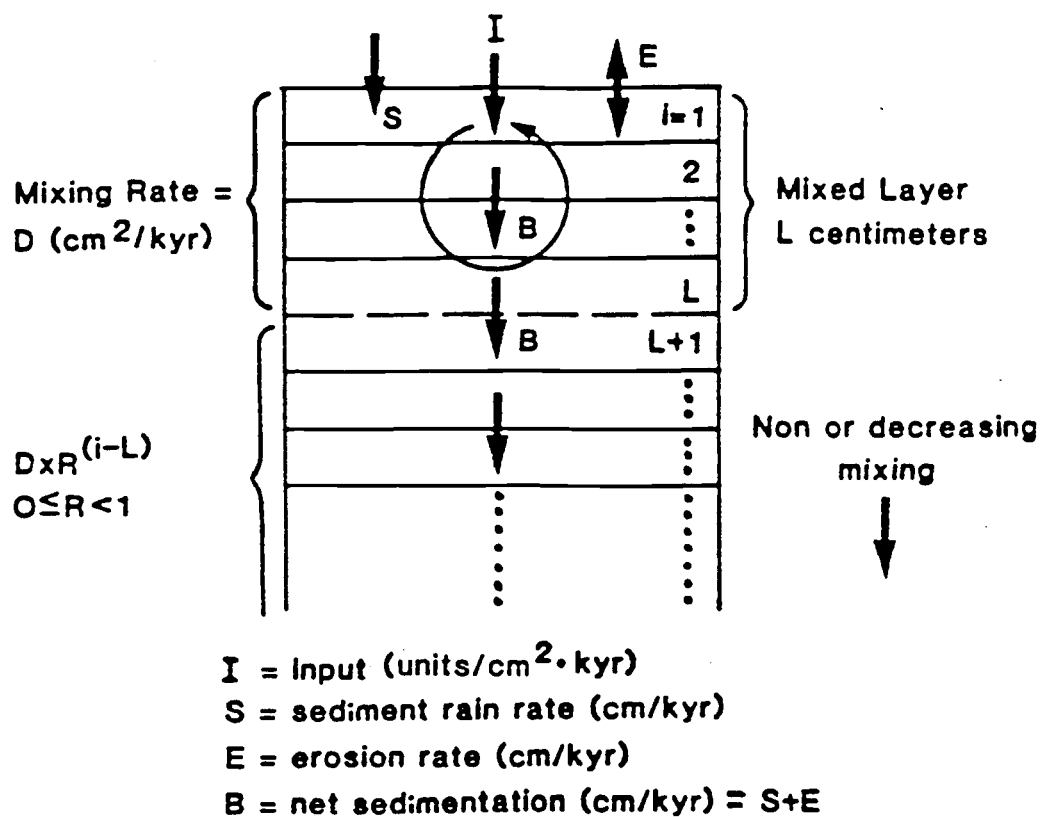


Figure IV-8

conservative. We assume that the major dissolution occurs before the tracers are input to the sediments.

Figures IV-9 to IV-12 show the sensitivity of the model to variations in key parameters. Table IV-3 lists the parameters that are common to profile "a" in these Figures. Figure IV-9 shows that as the duration of a particular sedimentation regime increases, the concentration of the tracers in the mixed layer increases and they penetrate deeper into the sediments until steady-state conditions are reached ("b" curves). Since it does not decay with time, the concentration of the conservative tracer in the near-surface sediments will approach a constant value with depth after long time periods. Its profile can be used, therefore, to estimate the duration of a specific depositional regime. Figure IV-10 shows that small changes in sedimentation rate drastically alters the tracer profiles. At high sedimentation rates, steady-state conditions near the seafloor are reached quickly.

As shown by Figure IV-11, variations in the erosion rate,  $E$ , also drastically affect the resulting profiles. If  $S < -E$ , the inputs are confined to the mixed layer (cases c and d). If  $-E$  is large, the concentration of the tracers in the mixed layer is only a small fraction of the input. If  $E$  has a positive value (case b), the net sedimentation rate increases, but the inventory of the nuclide in the sediments, is the same as when  $E = 0$ .

Figure IV-12 shows the sensitivity with variations in the thickness of the mixed layer ( $A$ ) and the rate of mixing within and below this layer ( $B$ ). The conservative tracers generally exhibit the same patterns. At small values of  $L$  ( $< 5$  cm), the rate of

Figure IV-9

Modelled profiles of a nuclide (A) and a conservative tracer (B) showing the impact of duration of sedimentation. Other model parameters listed in Table IV-3 are held constant.

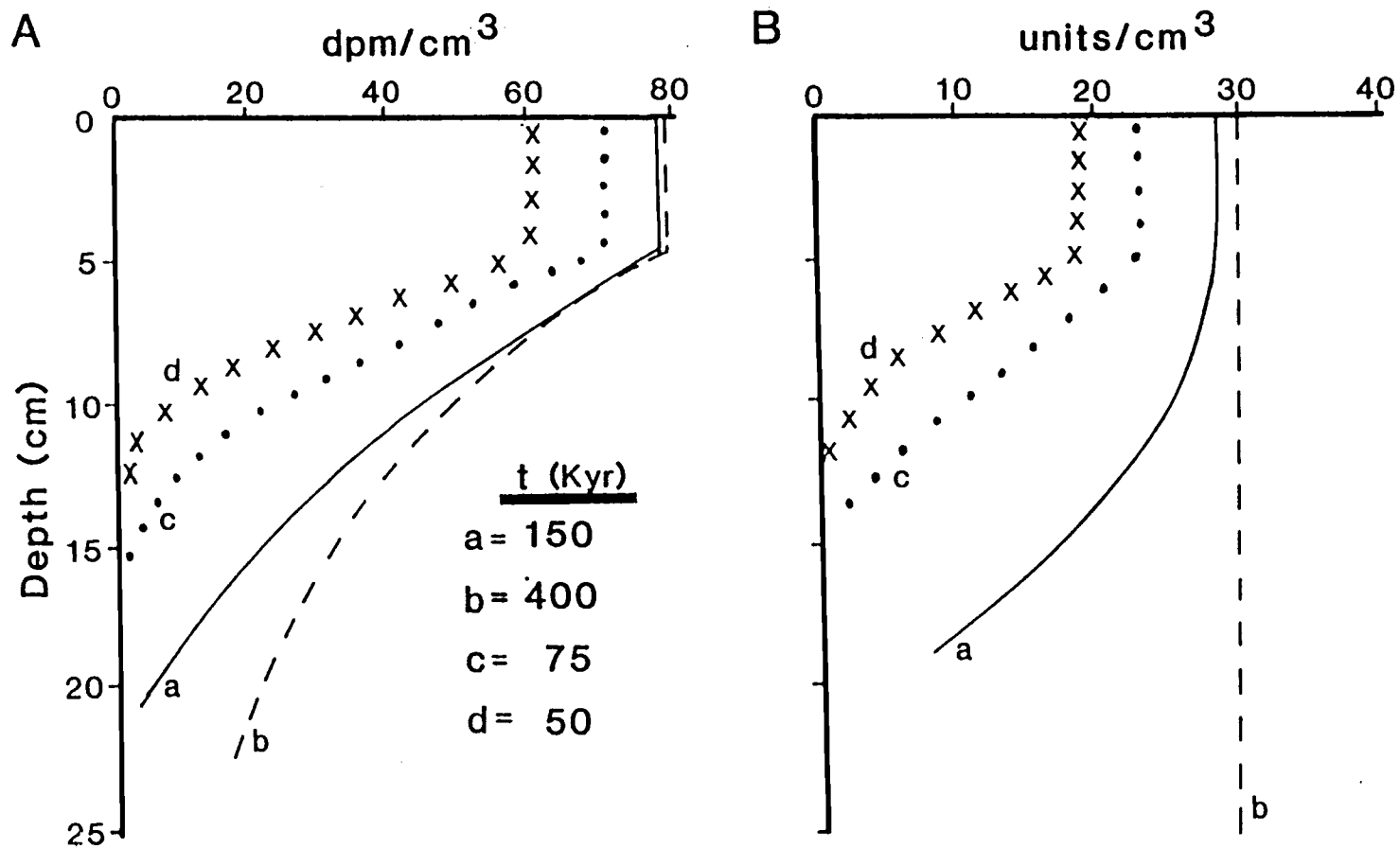


Figure IV-9

Figure IV-10

Parameters as Figure IV-9, but duration is held constant at 150 kyr and S, the sedimentation rate, varies as indicated.

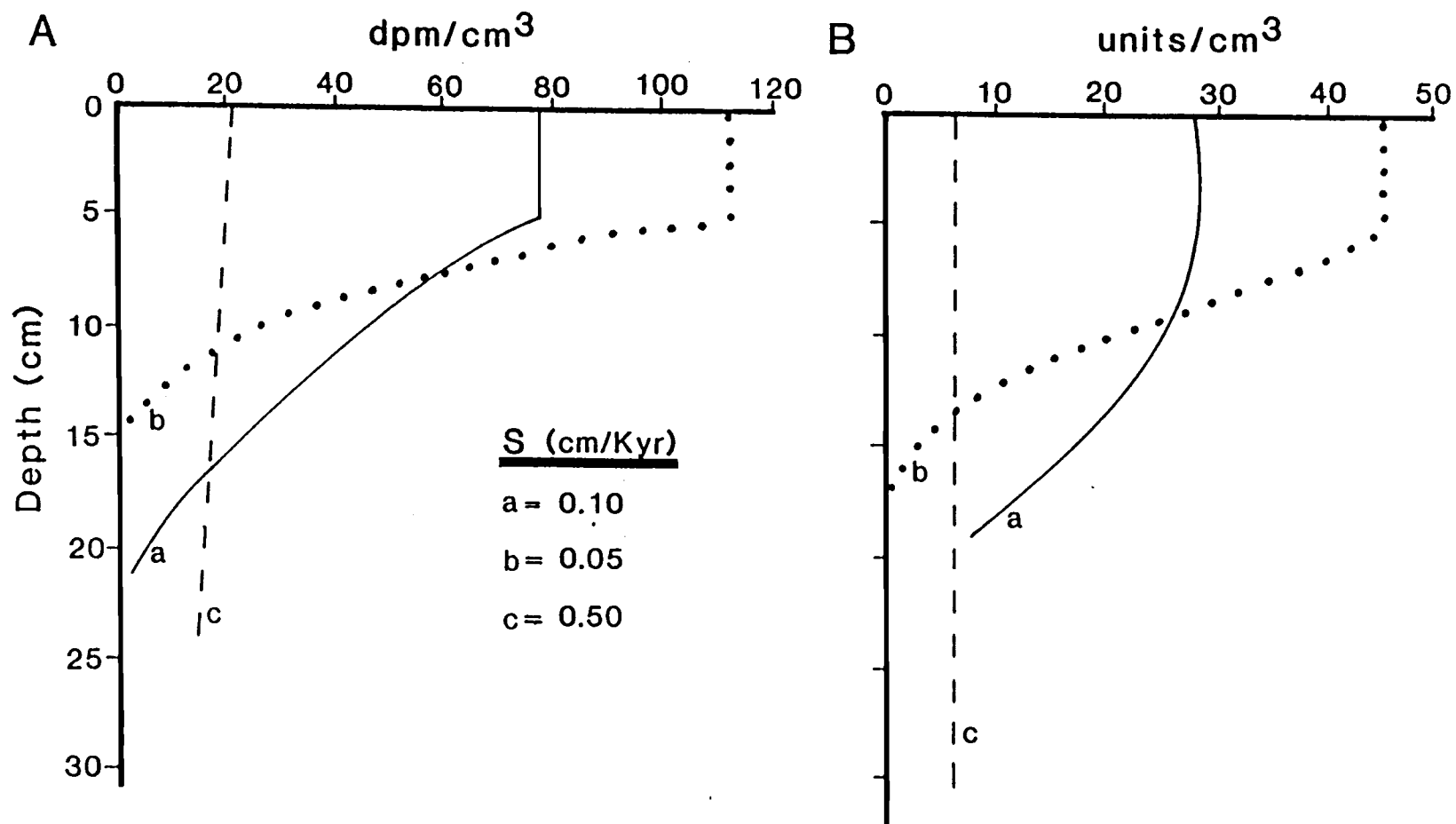


Figure IV-10

Figure IV-11

Parameters as Figure IV-9, but duration is held constant at 150 kyr and E, erosion rate, varies as indicated. A positive value for E results in input of reworked material as well as primary particulates. A negative value represents erosion.



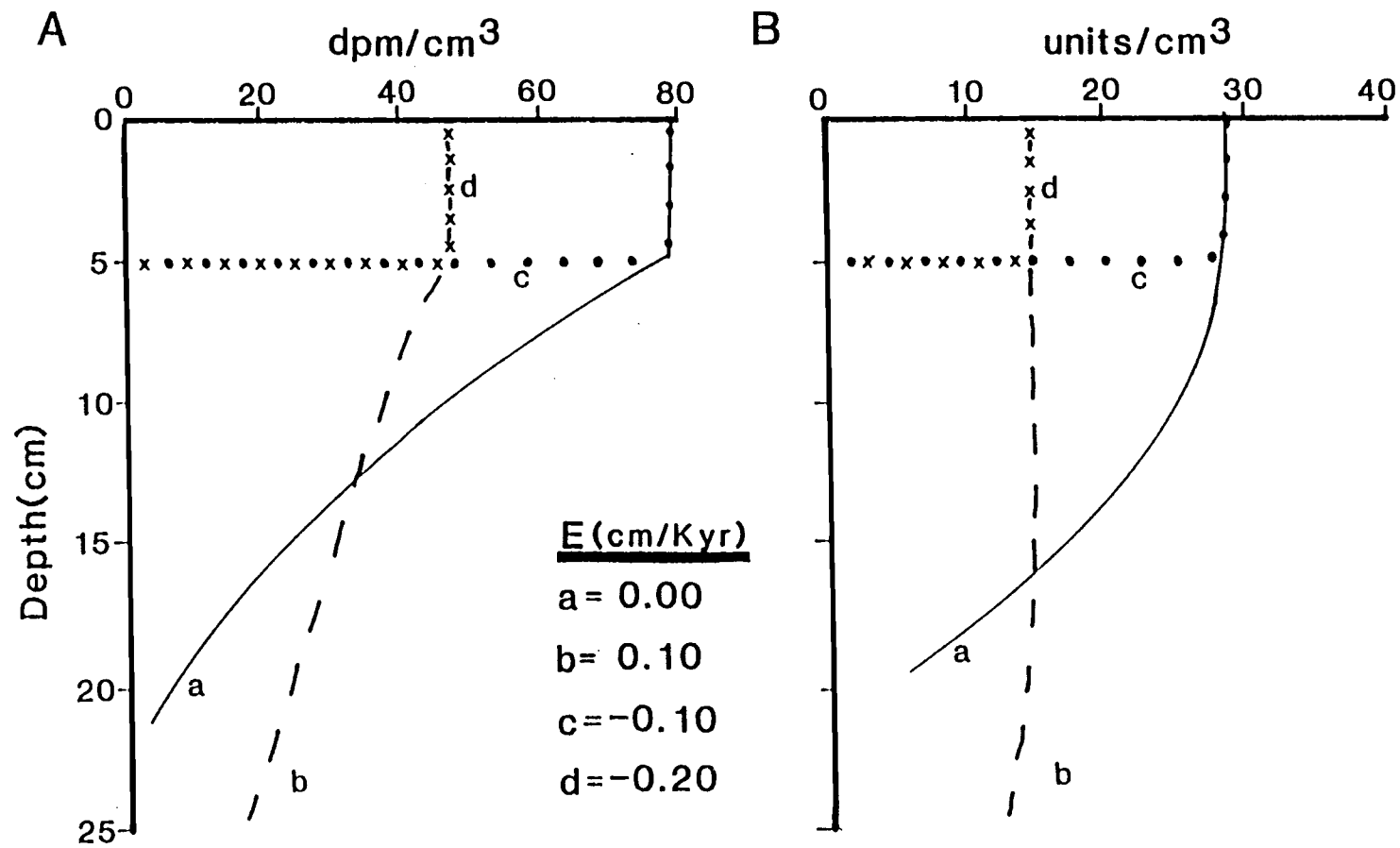


Figure IV-11

Figure IV-12

Modelled profiles for a nuclide with a 75 kyr half-life. (A) shows variations in the mixing depth,  $L$ ; (B) shows variations in the rate of mixing. Apart from the indicated variations in  $L$ ,  $R$  and  $D$ , the other parameters are the same as in Table IV-3.

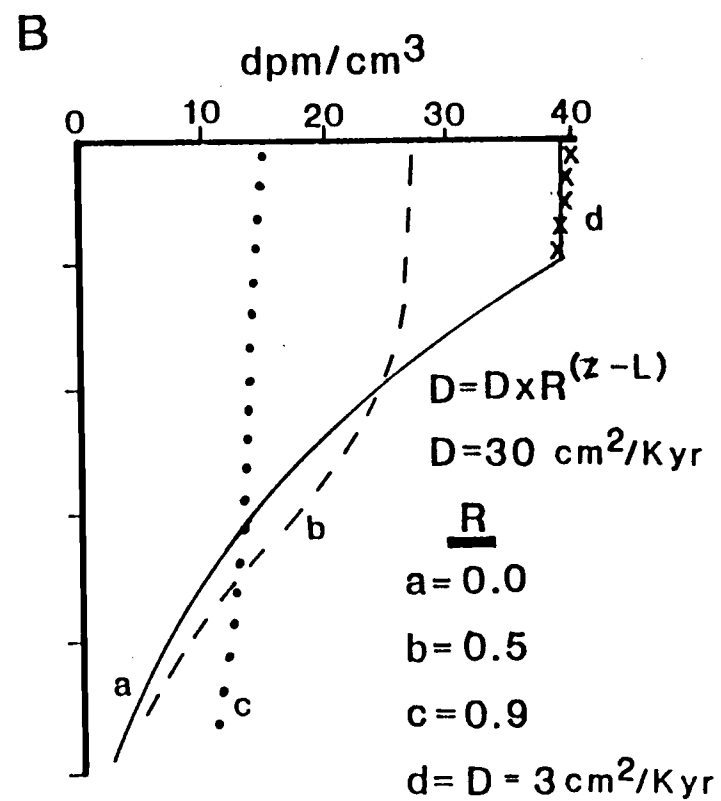
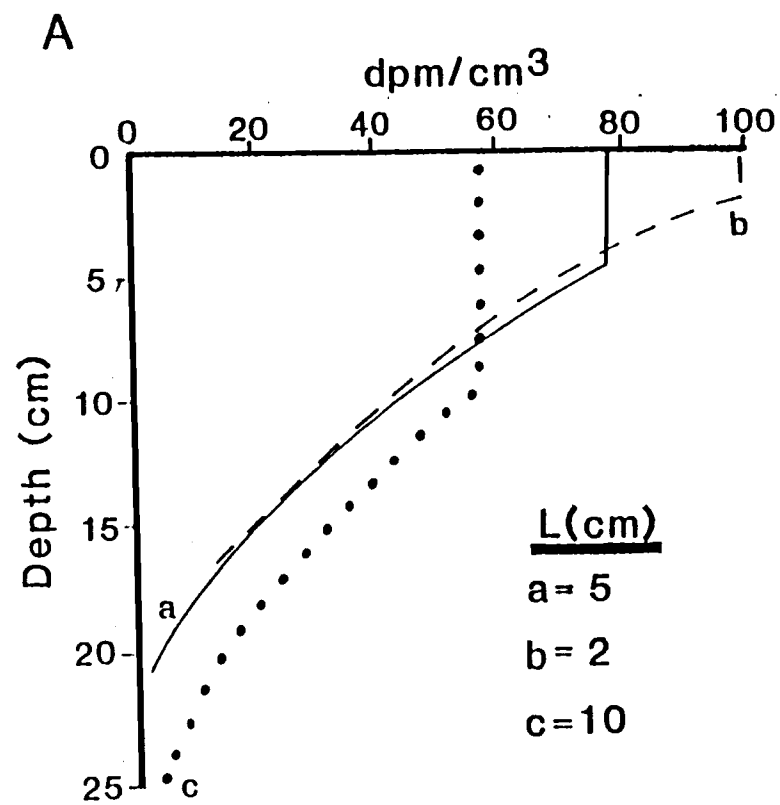


Figure IV-12

Table IV-3. Model Parameters which result in profile "a" of sensitivity tests.

---

(I) nuclide; $tr_2 = 75$ kyr	$= 115.5 \text{ dpm} \cdot \text{cm}^{-2} \cdot \text{kyr}^{-1}$
(I) conservative tracer	$= 3.0 \text{ units} \cdot \text{cm}^{-2} \cdot \text{kyr}^{-1}$
(S) sedimentation rate	$= 0.1 \text{ cm} \cdot \text{kyr}^{-1}$
(E) erosion rate	$= 0.0 \text{ cm} \cdot \text{kyr}^{-1}$
(B) net sedimentation rate	$= 0.1 \text{ cm} \cdot \text{kyr}^{-1}$
(T) duration of sedimentation	$= 150 \text{ kyr}$
(L) mixed layer thickness	$= 5 \text{ cm}$
(D) bioturbation rate	$= 30 \text{ cm}^2 \cdot \text{kyr}^{-1}$
(R) parameter governing rate of mixing below mixed layer	$= 0.0$

mixing and its decrease below the mixed layer, on a thousand year time frame, are not sensitive to changes. As  $L$  increases, the tracers penetrate deeper into the sediment section but the overall concentration is decreased. As the mixing rate becomes small, concentration gradients are maintained in the mixed layer. At Site S, however, surface mixing rates generally exceed  $30 \text{ cm}^2 \text{ kyr}^{-1}$  (Cochran, 1985).

#### Application of Model

The sedimentation model will now be applied to the data from three Site S box cores to examine Recent sedimentation at this site. The goal is to model the sedimentation of the area by a constant primary input across the whole site, while allowing for variations in the erosional and secondary depositional parameters from core to core. We extend the preliminary application of the model by Kadko (1983) to allow for changes in accumulation with time. It was found that downcore tracer distributions could best be modeled by time varying input and sedimentation rates which reflect the changing depositional environment of the region.

Data from a sediment trap deployed from January 1983 to February 1984 at 3400 m are used to provide estimates of the primary input of  $^{230}\text{Th}$ , manganese and aluminum (Table IV-4). Because of dissolution of opal in the lower water column and near-surface sediments, the opal flux measured by the sediment trap represents an upper bound for the primary input. We assume that these input rates remain constant during the Recent episode of sedimentation. Radiolarian data suggest that Recent sedimentation began within the

Table IV-4. Sediment trap fluxes at MANOP Site S, 3400 m level<sup>a</sup>.

	Range <sup>b</sup> ( $\mu\text{g}\cdot\text{cm}^{-2}\text{ yr}^{-1}$ )		Mean ( $\mu\text{g}\cdot\text{cm}^{-2}\text{ yr}^{-1}$ )
Total (salt corrected)	507.	-2734.	1319.
Calcium carbonate	319.	-1419.	729.
Opal	115.	- 920.	389.
Manganese	0.018 -	0.034	0.024
Aluminum	0.098 -	2.94	1.82
-- -- -- --	-- -- -- --	-- -- -- --	-- -- -- --
<sup>230</sup> Th <sup>c</sup>	5.42	11.3 dpm $\cdot\text{cm}^{-2}\text{ kyr}^{-1}$	8.03 dpm $\cdot\text{cm}^{-2}\text{ kyr}^{-1}$

<sup>a</sup>Fluxes from an OSU single cone trap equipped with a 5-cup sample changer, moored at 3400 m; 11° 06'N, 140° 14'W from 29 December 1982 to 14 February 1984. Data provided by J. Dymond, Oregon State University.

<sup>b</sup>Range represents fluxes measured in cups sampling the water column for approximately 100 days each. The first two samples coincide with the end of the 1982-83 ENSO event.

<sup>c</sup>Data provided by R. Mahannah and W.S. Moore, University of South Carolina.

last 400,000 years, therefore,  $T = 400$  kyr is used as the upper limit for the duration of sedimentation. The output for all model runs is in tracer units $\cdot\text{cm}^{-3}$ . These values can be converted to units $\cdot\text{g}^{-1}$  by dividing by the dry bulk density (Appendix 3).

Figure IV-13 summarizes the tracers used to model Recent deposition at basin core 47 BC. An increase in the concentration of  $^{230}\text{Th}$ , opal, and Quaternary radiolarians is observed near 10 cm. The increase in manganese does not occur until 5 cm. Thus it appears that more than one rate of deposition is necessary to obtain agreement with all tracers.

The modelled  $^{230}\text{Th}$  and  $^{231}\text{Pa}$  profiles for core 47 BC are shown in Figure IV-14. We use values of 11.5 and 0.30 dpm $\cdot\text{cm}^{-2}$  kyr $^{-1}$  as the inputs of  $^{230}\text{Th}$  and  $^{231}\text{Pa}$ , respectively. The value for  $^{230}\text{Th}$  represents 91% of the predicted rate at a depth of 4900 m (Kadko, 1980). This equals the percent of the predicted flux measured in a sediment trap moored at 3400 m at Site S (Table IV-4). The  $^{231}\text{Pa}$  flux represents 25% of the predicted value and is within the range measured by Anderson (1981) at 15°N, 150°W. We assume that these rates are constant through time even though the sedimentation rate does change. A value of 30 cm $^2$  kyr $^{-1}$  for the biological mixing rate is used. This value is comparable to the rate used by Kadko (1983) but is below the estimate of 100 cm $^2$  kyr $^{-1}$  (Cochran, 1985) based on  $^{239,240}\text{Pu}$  and  $^{210}\text{Pb}$ . Since our mixed layer depth is always less than 4 cm, the model is not very sensitive to increases in the rate of biological mixing. We assume no mixing below the surface layer (i.e.,  $R = 0$ ) since the effect of this variable is also diminished

Figure IV-13

Downcore profiles of (A)  $^{230}\text{Th}$  and  $^{231}\text{Pa}$ , (B) manganese, (C) opal and (D) Quaternary and Tertiary radiolarians in the top 25 cm of basin box core K7905 47 BC. Original data in  $\text{unit}\cdot\text{mass}^{-1}$  have been multiplied by the dry bulk density to yield  $\text{unit}\cdot\text{vol}^{-1}$ .



# K7905 47BC

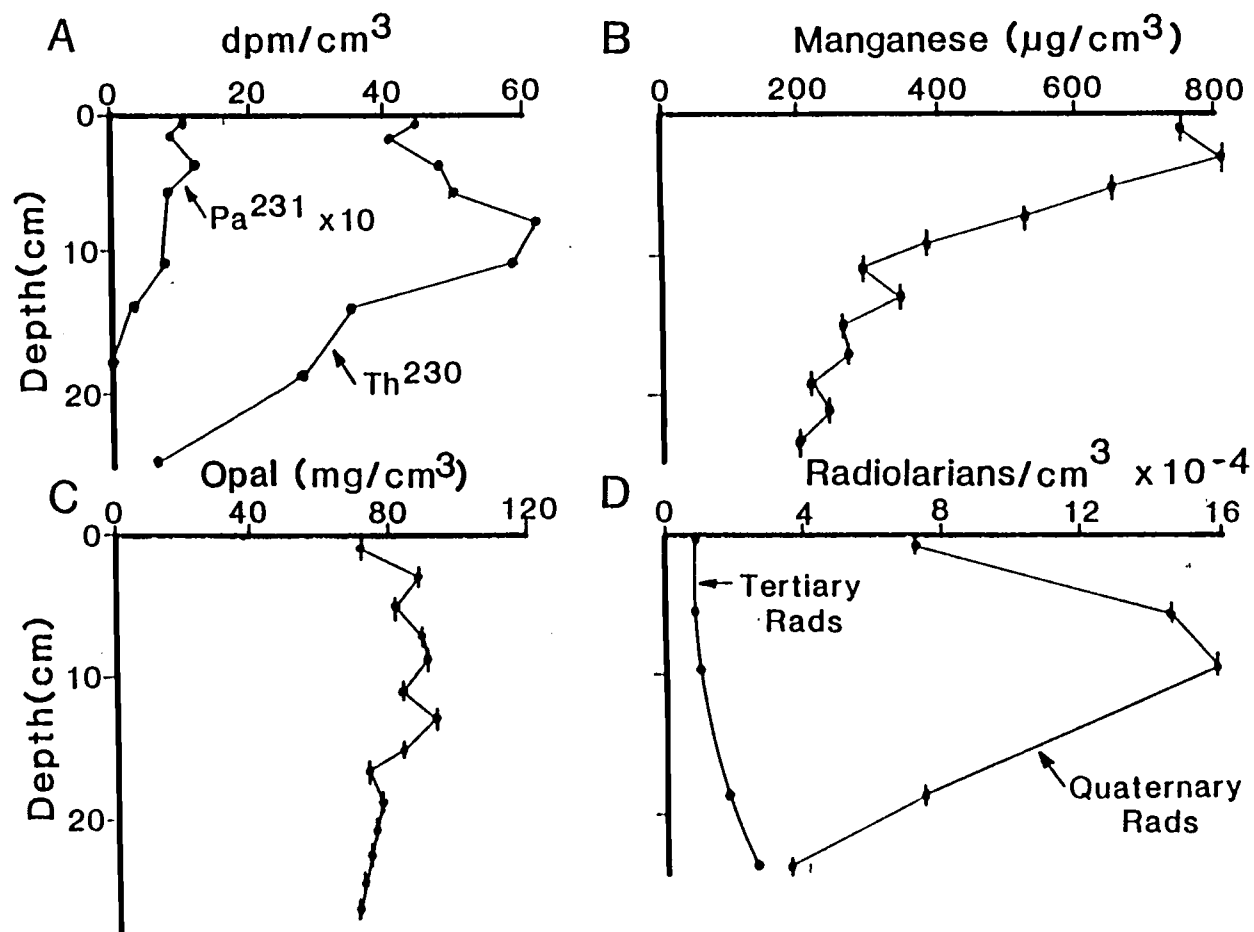


Figure IV-13

Figure IV-14

Observed and modelled  $^{230}\text{Th}$  and  $^{231}\text{Pa}$  profiles from core K7905 47 BC. Vertical bars are the measured  $^{230}\text{Th}$  values and pluses (+) are the  $^{231}\text{Pa} \times 10$  values. Original data in dpm/gm have been converted to  $\text{dpm}/\text{cm}^3$ . Modelled profiles use indicated values of S and E. Other model parameters,  $L = 3 \text{ cm}$ ,  $R = 0.0$ ,  $D = 30 \text{ cm}^2 \text{ kyr}^{-1}$ ,  $^{230}\text{Th}$  input =  $11.5 \text{ dpm cm}^{-2} \text{ kyr}^{-1}$  and  $^{231}\text{Pa}$  input =  $0.30 \text{ dpm} \cdot \text{cm}^{-2} \text{ kyr}^{-1}$  have been held constant through time. See text for details.

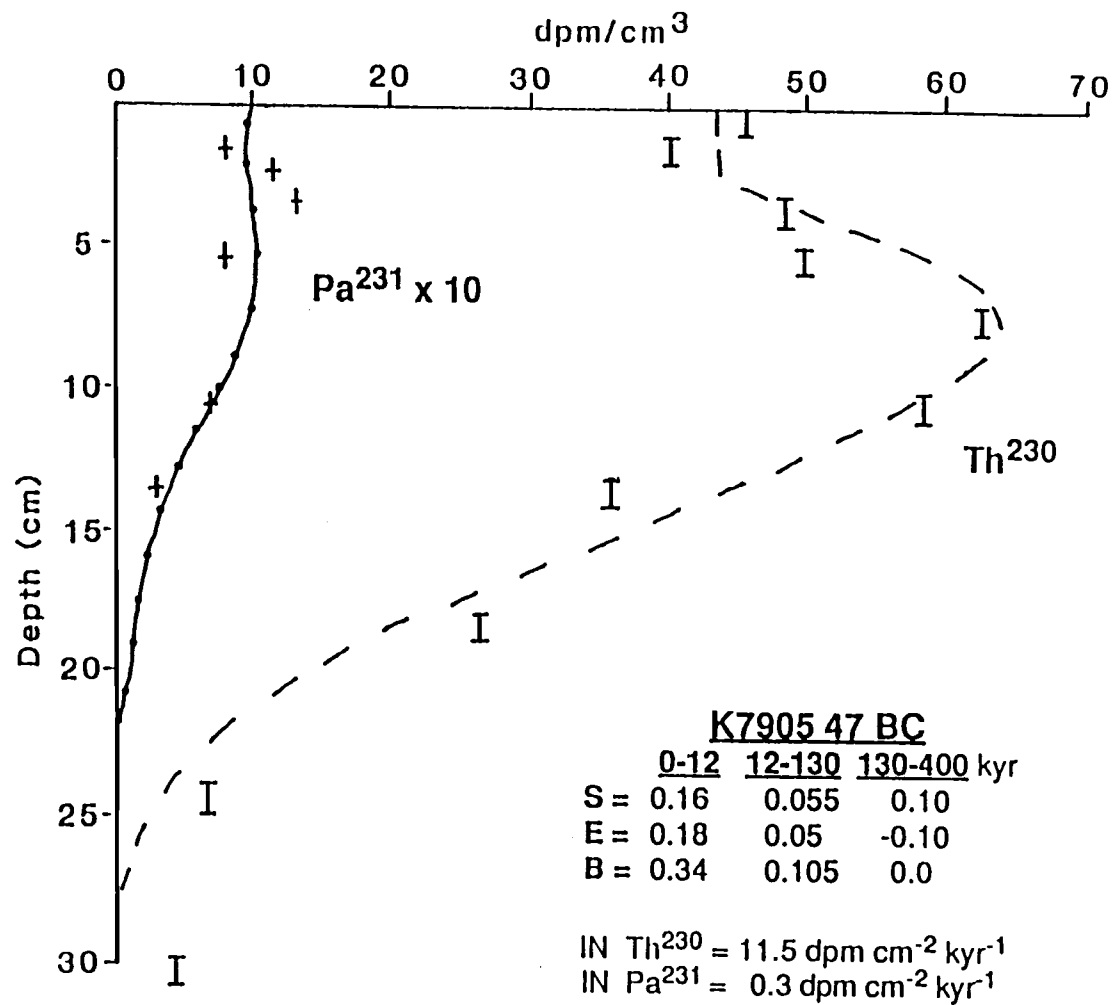


Figure IV-14

because of the thin mixed layer. The assumption of a thin mixed layer is necessary to model the near-surface change in  $^{230}\text{Th}$ .

The model was allowed to run for 400,000 years, however, sediment did not accumulate until 130,000 years ago. This time constraint is imposed because some of the Quaternary tracers (i.e., radiolarians; Figure IV-13) would be found much deeper in the sediment section if a longer period of deposition with a net sedimentation rate of  $0.105 \text{ cm} \cdot \text{kyr}^{-1}$  were maintained. If the sedimentation rate is increased or decreased, the  $^{230}\text{Th}$  profile cannot be accurately modelled. A good fit of both the  $^{231}\text{Pa}$  and  $^{230}\text{Th}$  profiles is obtained with a primary sedimentation rate of  $0.055 \text{ cm} \cdot \text{kyr}^{-1}$  and an erosional input of  $0.05 \text{ cm} \cdot \text{kyr}^{-1}$  between 12 and 130 kyr. During the last 12,000 years, a jump in sedimentation to  $0.16 \text{ cm} \cdot \text{kyr}^{-1}$  for the primary input is necessary to obtain a fit to the near-surface radionuclide decreases. This time corresponds to the glacial-to-Holocene transition. The conservative tracers are modelled with these same parameters.

The model for the radiolarians in 47 BC is shown in Figure IV-15. The decrease in Quaternary radiolarians near the base of this core is assumed to be a function of input, and limits the duration of sedimentation to 130 kyr at a rate of  $0.105 \text{ cm} \cdot \text{kyr}^{-1}$ . The value of  $C(T)$ , the initial concentration of reworked Tertiary radiolarians is taken from Table IV-2. Input rates of 17,500 shells  $\cdot \text{cm}^{-2} \cdot \text{kyr}^{-1}$  from 130-12 kyr ago to 20,000 shells  $\cdot \text{cm}^{-2} \cdot \text{kyr}^{-1}$  for the last 12,000 years provide the best fit to the Quaternary data. These values are 5-30% of the radiolarian flux measured in sediment traps at Site S (Pisias et al., 1986). The Tertiary (A)

Figure IV-15

Observed and modelled Tertiary and Quaternary radiolarian profiles from basin core K7905 47 BC. Vertical bars and pluses (+) are measured values for Quaternary and Tertiary radiolarians, respectively. INQ is the input of Quaternary radiolarians and INT is the input of Tertiary radiolarians ( $\text{rads cm}^{-2} \text{ kyr}^{-1}$ ). Other parameters as in Figure IV-14. C(T) is the initial concentration of radiolarians in Tertiary reworked material (Unit 2; Table IV-2). See text for details.

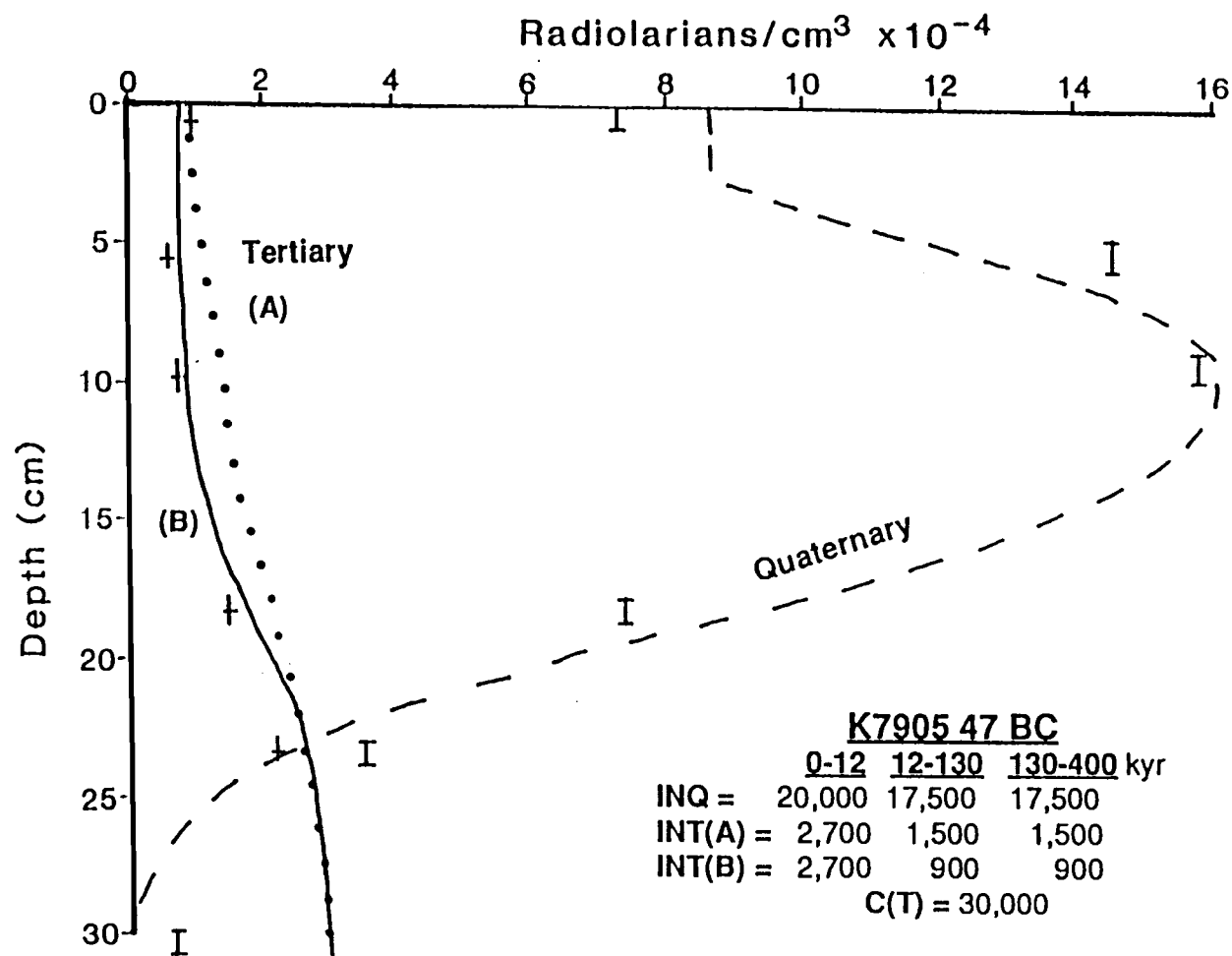


Figure IV-15

profile in Figure IV-15 is derived using input rates of 1500 and 2700 shells  $\text{cm}^{-2}\text{kyr}^{-1}$  for intervals 12-130 and 0-12 kyr, respectively. These values are obtained by multiplying the sedimentation rate of eroded material "E" by the concentration of radiolarians in Unit 2 (Table IV-2). To obtain the low-surface concentrations, we assume that only one-half of the eroded material deposited between 0 and 12 kyr is derived from the source (i.e., E of Unit 2 = 0.09  $\text{cm kyr}^{-1}$ ). The Tertiary input from 12-130 kyr was decreased by 40% in model run (B) to best fit the data. This may reflect added dissolution of material from Unit 2 during lateral transport.

A modelled fit to the manganese profile in 47 BC is shown in Figure IV-16. The value for the Quaternary input is the average value measured in the 3400 m trap at Site S (Table IV-4). This component does not contribute much (<15%) to the total concentration of manganese in near-surface sediments. The values are of similar magnitude to those obtained in the residual of a sequential leach of Site S sediments (Lyle, unpub. data). This residual is assumed to be aluminosilicates. Much of the near-surface increase in manganese is associated with oxyhydroxides and can be extracted with a pH 5 hydroxylamine hydrochloride-sodium citrate solution (Lyle, unpub. data). An input of 320  $\mu\text{g}\cdot\text{cm}^{-2}\text{kyr}^{-1}$  beginning 12 kyr ago is necessary to model the near-surface increase in manganese. This rate corresponds to the manganese concentration core 97 GC (Unit 3A; Table IV-2) multiplied by one-half of the value of E for the input of older material. Therefore, the enrichment can be explained by an input of Tertiary material that is a mixture of Unit 3A plus a manganese depleted component such as Unit 2. The

Figure IV-16

Modelled manganese profile showing partitioning of box core K7905 47 BC sediments into Recent and reworked Tertiary contributions. Pluses (+) are the measured concentrations multiplied by the dry bulk density ( $\mu\text{g cm}^{-3}$ ). INQ and INT are the inputs, in  $\mu\text{g}\cdot\text{cm}^{-2}\text{ kyr}^{-1}$ , for the Quaternary and Tertiary components, respectively. The solid line is the total of Recent and Tertiary manganese using indicated parameters. The dotted line is the modelled Tertiary component, and the dashed line is the modelled Recent Component.



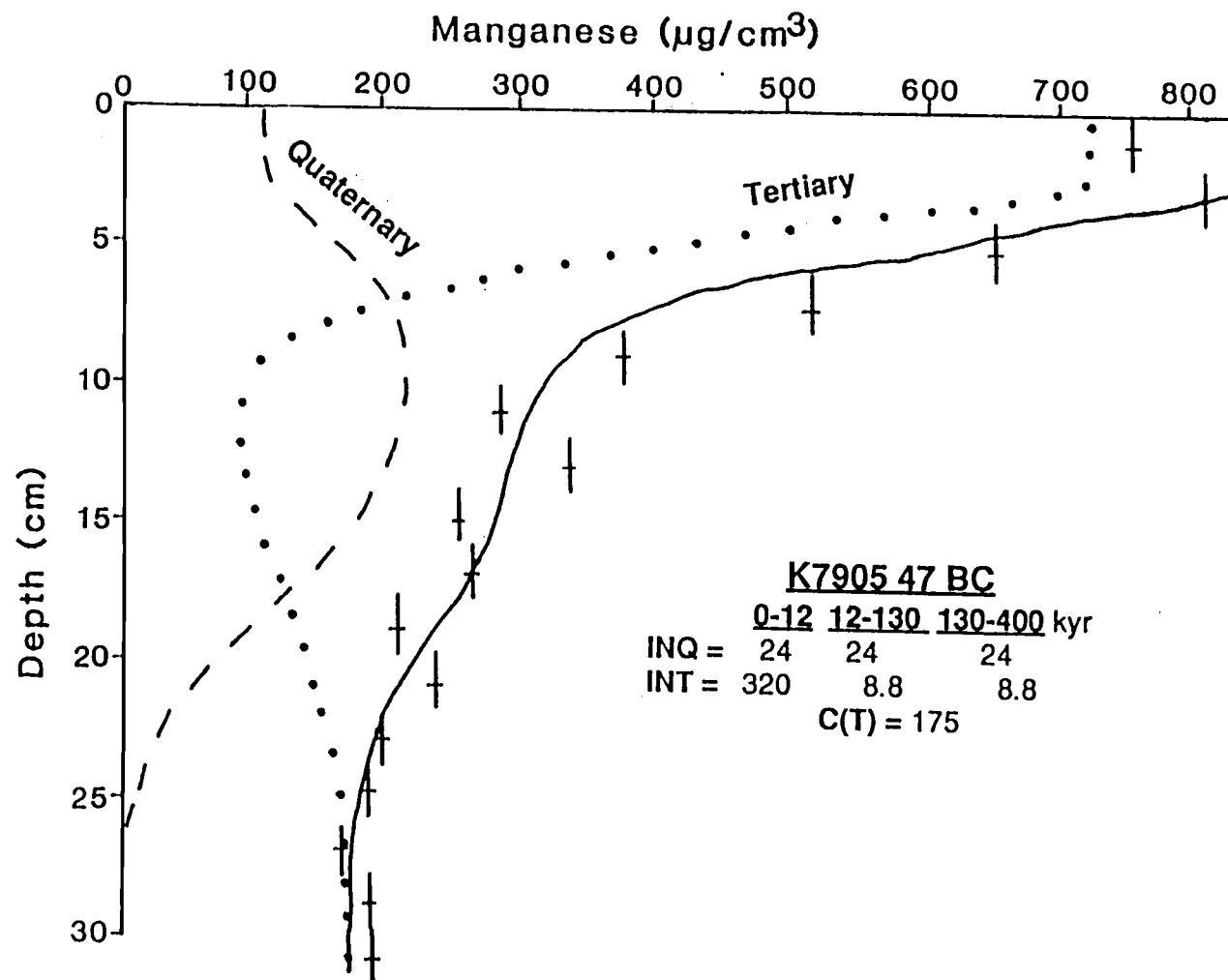


Figure IV-16

radiolarian data concur with this explanation. This manganese-rich source has been tapped only since the last glacial period, even though sediments have been accumulating at 47 BC since 130 kyr! A change in the direction of bottom currents at the end of the last glacial period to its present northwestward direction (J. Dymond, pers. comm.) could account for the source change. Alternatively, a recent erosional event that exposed the non-fossiliferous clay units could also explain the Recent input. It is possible, but unlikely, that an increase in the primary flux of manganese to the site is responsible for the increase in near-surface manganese concentrations since the fluxes would need to increase by an order of magnitude to obtain the necessary rate. Also, the  $^{230}\text{Th}$  enrichment at 10 cm (Figure IV-13) would be expected to coincide with the manganese increase if the source were an increase in the primary rain rate.

The modelled profiles of tracers shown in Figures IV-14 to 16 define the source composition and input rates necessary to best fit the measured data. We use these rates to model the opal component in 47 BC (Figure IV-17) which is not fully conservative and the input rate is not well known. Box core 47 BC contains higher near-surface opal concentrations compared to other cores from this site (Figure IV-4). Therefore, the value for  $C(T)$ , the initial concentration of opal in Tertiary material, is three times typical values of Unit 2 (Table IV-2). This implies that near-surface Tertiary opal is better preserved in 47 BC than in other Site S cores studied. The Tertiary component input (INT) is obtained by multiplying the opal concentration of Unit 2 by the sedimentation rate

Figure IV-17

Modelled opal profile showing partitioning of box core K7905 47 BC sediments into Recent and reworked Tertiary material. Pluses (+) are the measured concentrations multiplied by the dry bulk density ( $\text{mg}\cdot\text{cm}^3$ ). The solid line is the total of Recent and Tertiary opal using indicated parameters. The dotted line is the modelled Tertiary component, and the dashed line is the modelled Recent component. ING and INT are the inputs in  $\text{mg}\cdot\text{cm}^{-2}\text{ kyr}^{-1}$  from the Quaternary and Tertiary material, respectively. The value for  $C(T)$  is three times typical values of Unit 2.

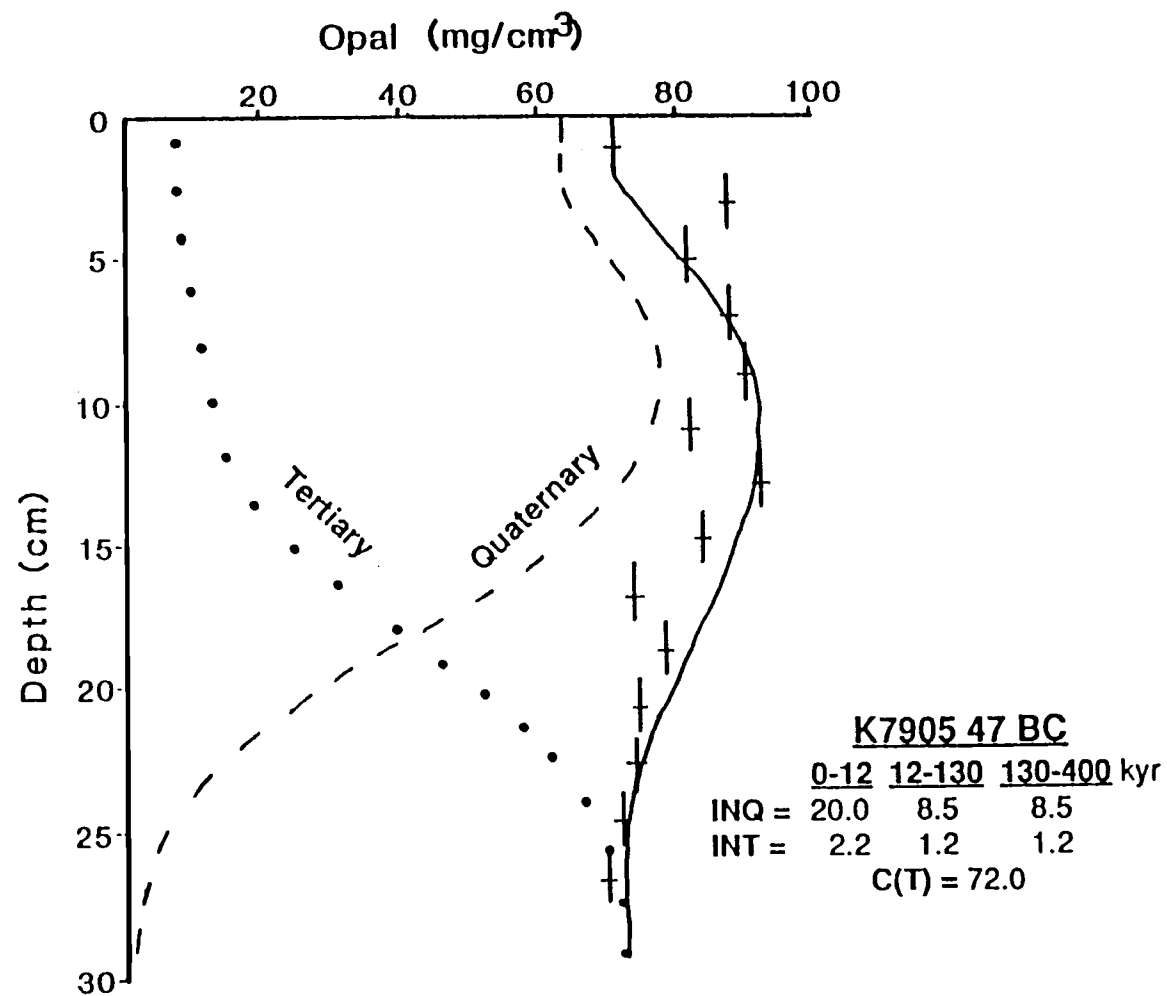


Figure IV-17

of eroded material from this unit as determined by the previous tracers. The corresponding rates of primary opal flux that best fit the data are 2 and 5% of the mean trap-measured flux (Table IV-4) for the interval from 12-130 and 0-12 kyr, respectively. Broecker and Peng (1982) note that opal accumulation is a function of supply (i.e., surface productivity), dissolution rate and net sedimentation rate. During the last 12,000 years, we observe an increase in net sedimentation rate that coincides with more reworked Tertiary material input to the basin. This causes a dilution of the primary input. Thus, better opal preservation may result from this increased dilution rather than a change in the supply rate.

Model parameters obtained from other tracers and a primary input from sediment trap data are used to partition the concentration of aluminum into Recent and reworked Tertiary material (Figure IV-18). The aluminum concentration in Unit 2 is used as the value for  $C(T)$ . A value that is 13% less than in Unit 2 is used for the input of reworked material to provide a better fit of the data. The results show that more than 50% of aluminum in the surface layer is derived from older reworked material. Modelling results from other detrital components in 47 BC, such as iron, support a conclusion that a Tertiary source accounts for more than 50% of the near-surface elemental concentrations in sediments from the Site S basin.

To examine whether a consistent pattern of sedimentation can be obtained for Site S, the input and net sedimentation rates determined for 47 BC are used to model data from core BENTHIC III

Figure IV-18

Modelled aluminum profile showing partitioning of box core K7905 47 BC sediments into Recent and reworked Tertiary material. Pluses (+) are the measured concentrations multiplied by the dry bulk density ( $\text{mg}\cdot\text{cm}^{-3}$ ). The solid line is the total of Recent and Tertiary aluminum using indicated parameters. The dashed line is the modelled Recent component, and the dotted line is the modelled Tertiary component. The value for C(T) represents the concentration in Unit 2.

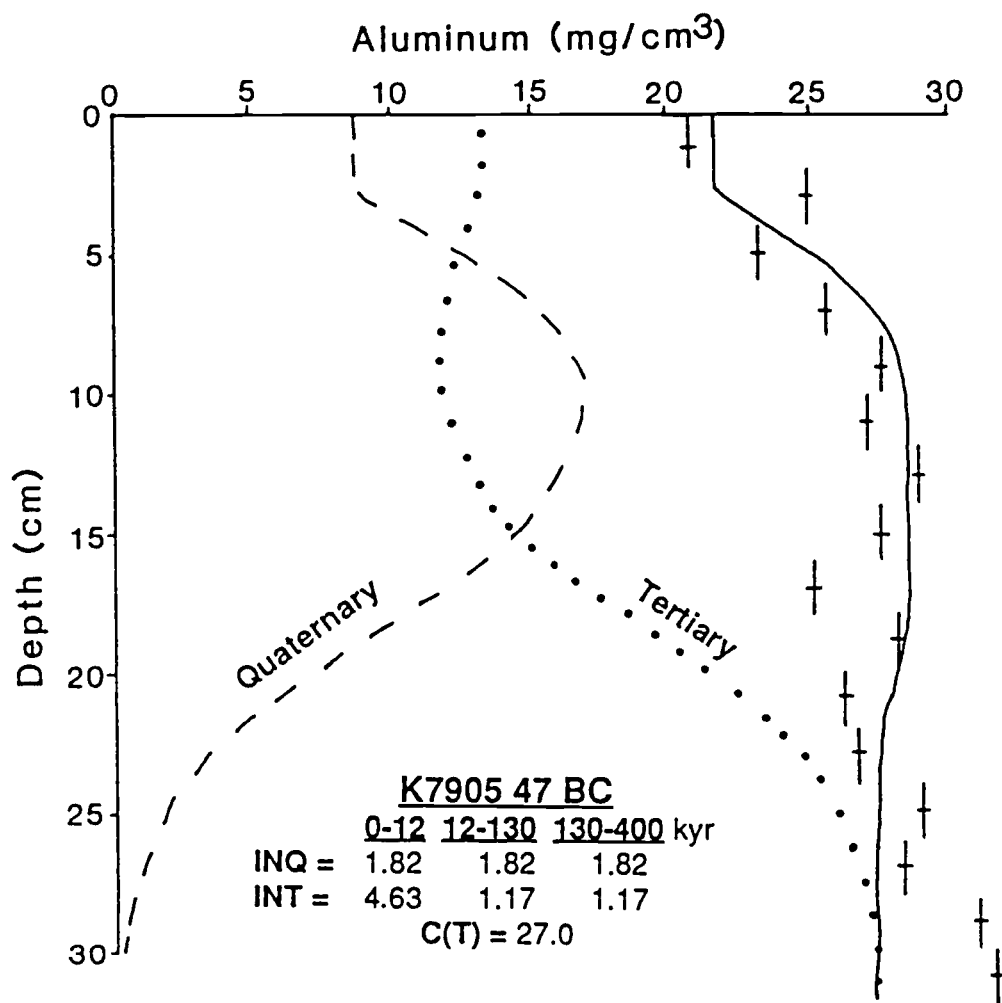


Figure IV-18

37 BC. The core site is located on the northern flank of the Site S basin and contains a 5 cm-thick layer of Unit 1 lying on Unit 3B (Figure IV-5). Model results for the radionuclides, manganese and Quaternary radiolarians are shown in Figure IV-19.

Because the radionuclides are not found below 6 cm in the sediments at this location, Recent sedimentation in 31 BC must be confined to the upper 6 cm. Net sedimentation rates from 47 BC must be associated with high erosion rates when applied to 31 BC. Profile  $^{230}\text{Th}$  (b) is the best fit to the  $^{230}\text{Th}$  data using values for "B" from Figure IV-14. Profile  $^{230}\text{Th}$  (a) results from a decrease in the sedimentation rate and net sedimentation by a factor-of-two. These adjusted rates provide a good fit of the  $^{231}\text{Pa}$  data. Our model does not account for the large variations in radionuclide values near the core top. The large values can result from a much slower net sedimentation rate confined to the upper layer or from the incorporation of  $^{230}\text{Th}$  (excess) enriched material, such as a manganese-rich crust, that has been recently exposed to seawater for a prolonged time interval.

The manganese concentration data is modelled using the same input rates of manganese as for 47 BC. The initial manganese concentration ( $C(T) = 4860 \mu\text{g}\cdot\text{cm}^{-3}$ ) corresponds to the upper section of Unit 3B. Like 47 BC, we conclude that in 31 BC most of the increase in manganese concentration is from a source other than the primary input measured by sediment traps.

To accurately model the Quaternary radiolarian concentrations, it is necessary to decrease the input from those used in 47 BC (Quat. Rads (a)) by at least a factor-of-two (Quat. Rads (b)).



Figure IV-19

Observed and modelled: (A)  $^{230}\text{Th}$  and  $^{231}\text{Pa}$ ; (B) manganese; and (C) radiolarian concentration profiles for core BENTHIC III 31 BC. (A) As in Figure IV-14 with E and S values for  $^{230}\text{Th}$  (a) and  $^{230}\text{Th}$  (b) given in legend. The  $^{231}\text{Pa}$  modelled profile is obtained using E and S values from  $^{230}\text{Th}$  (a). Circled values are not accounted for by the model. (B) As in Figure IV-16 using  $^{230}\text{Th}$  (a) values for E and S, and  $C(T) = 4860 \mu\text{g cm}^{-3}$ . (C) As in Figure IV-15 with Quat. Rads (a) having the same input rates as K7905 47 BC and Quat. Rads (b) representing a factor-of-two decrease in the input rate. The horizontal dashed line represents the unconformity between Units 1 and 2.

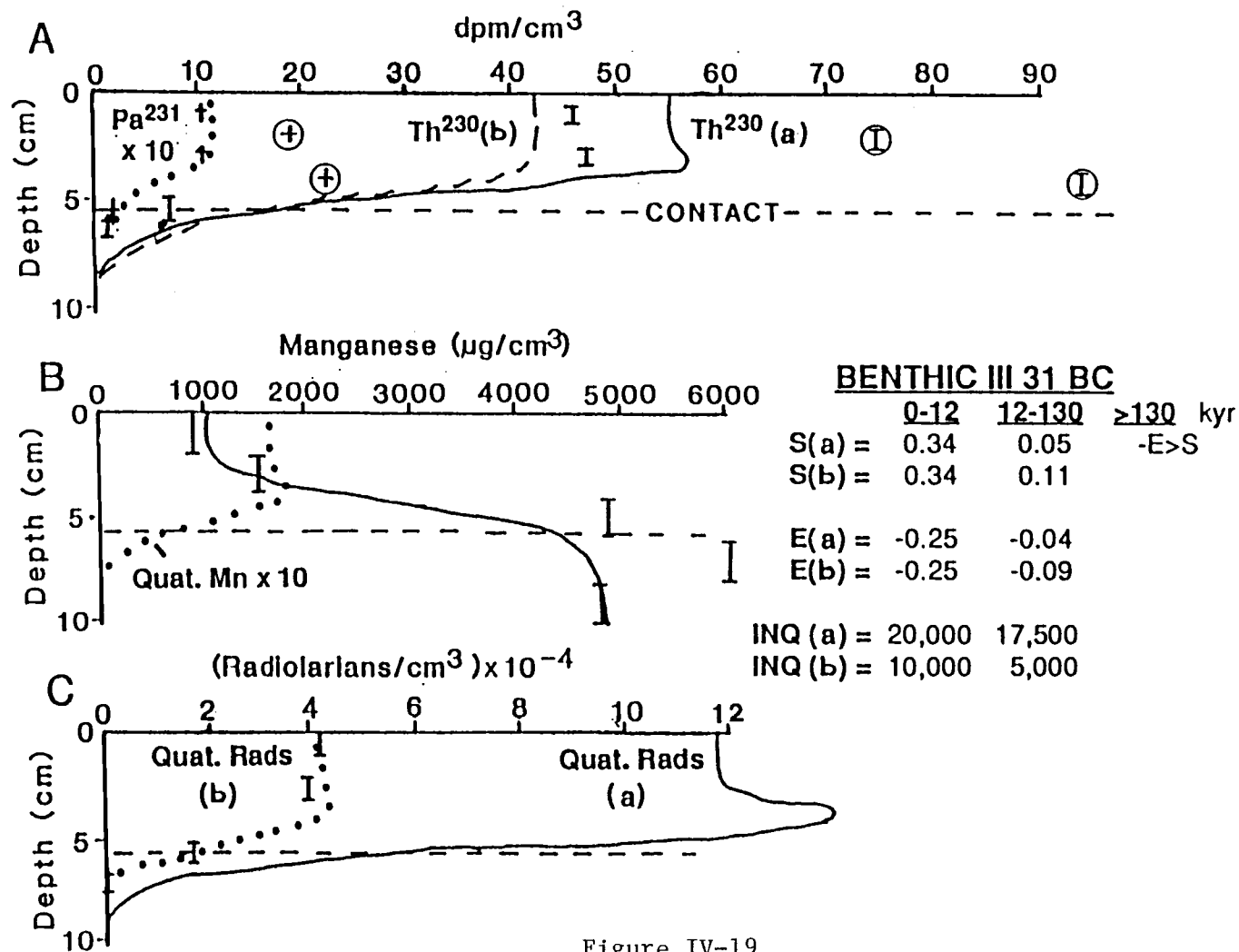


Figure IV-19

This result can be explained by the fact that opaline radiolarian shells are not fully conservative. Since we are dealing with inputs after they have been modified by dissolution, local environmental variations may have caused a difference in preservation. As discussed previously, Broecker and Peng (1982) suggest that net accumulation rate can affect the preservation of opal in sediments. Core 31 BC has a factor-of-four slower net accumulation rate than 47 BC, so the reduced opaline shell accumulation in the former case is consistent with this difference.

Kadko's (1983) application of the model to the data in core K7905 106 BC, taken from the western flank of the Site S basin, provides a fairly good fit to the  $^{230}\text{Th}$  values. However, the parameters used cannot account for the  $^{231}\text{Pa}$  data nor can they account for the radiolarian profiles. Here, we use model parameters (Figure IV-20) that provide a better fit to the  $^{231}\text{Pa}$  and conservative tracer profiles. To model these data and be consistent with model parameters used for 47 BC, a loss of 3 cm from the top of the core is necessary. This corresponds to a loss of the mixed layer, possibly during coring. As in 31 BC, it is necessary to use a Quaternary radiolarian input which is a factor-of-two less than in 47 BC. Again, we infer poorer opal preservation on the basin flanks than within the basin.

Although we have modelled only three cores, most of the near-surface sediment variations at the site are included. A consistent pattern of sedimentation for Site S emerges from these results. Prior to 130 kyr, this site was being eroded. The duration of this period of erosion is not well constrained by our data, but may have

Figure IV-20

Observed and modelled profiles of (A)  $^{230}\text{Th}$  and  $^{231}\text{Pa}$  and (B) radiolarian concentration for core K7905 106 BC from the western flank of the Site S basin. (A) As in Figure IV-14 with E and S values given in legend. Since E is negative, S includes sedimentation of Recent as well as reworked material. Modelled profiles (a) and (b) for  $^{231}\text{Pa}$  use input fluxes of  $0.3 \text{ dpm cm}^{-2} \text{ kyr}^{-1}$  (25% of production) and  $0.5 \text{ dpm cm}^{-2} \text{ kyr}^{-1}$  (42% of production), respectively. (B) As in Figure IV-15 using E and S values given (A). The best fit models show a core top loss of 3 cm. The horizontal dashed line represents the conformity between Units 2 and 4.

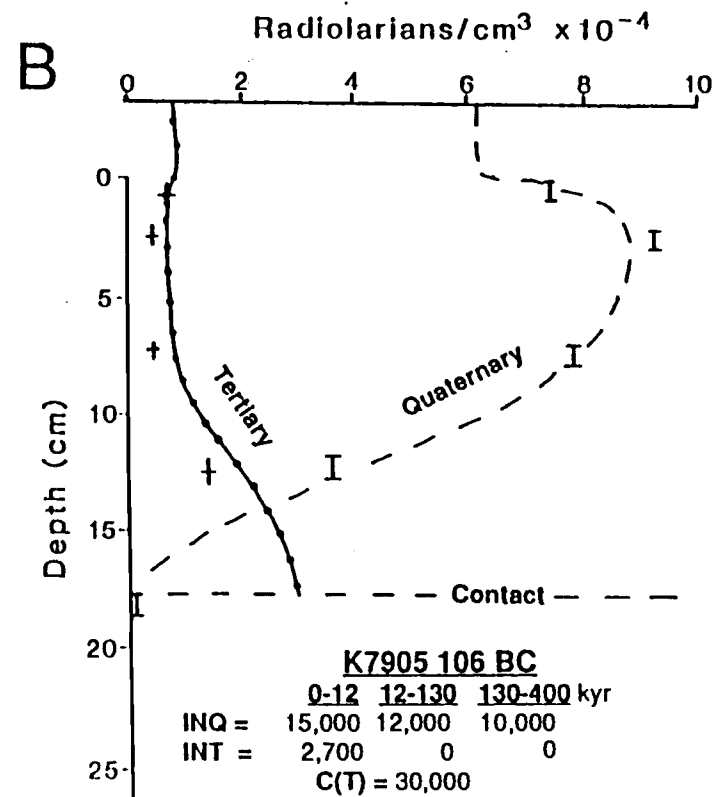
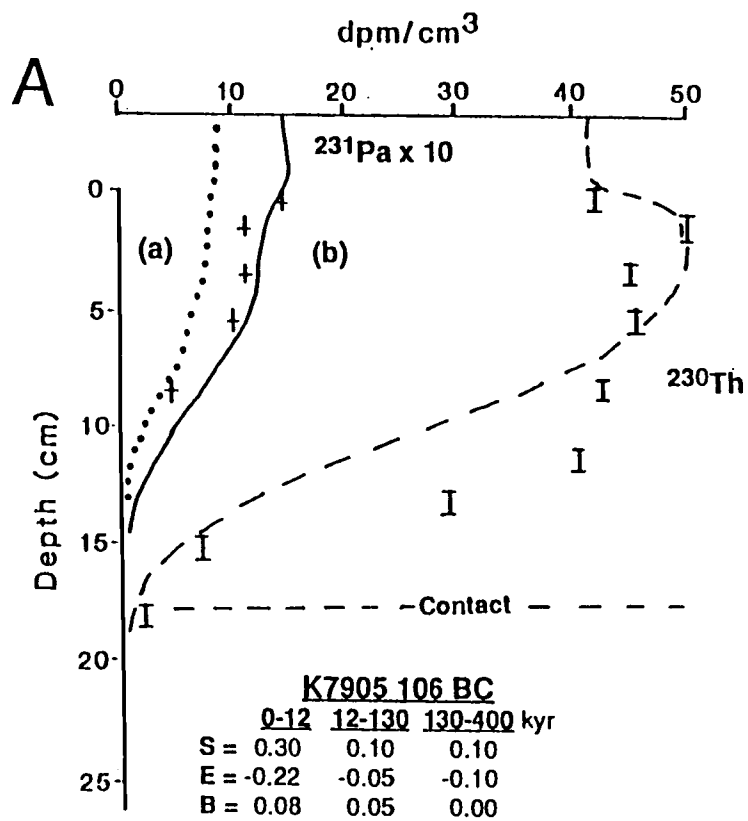


Figure IV-20

began as early as mid-Miocene at some locations. If the non-fossiliferous clay is a primary deposit, quiescent sedimentation (i.e., no erosion of the nannofossil ooze) is implied while it was accumulating. Starting 130,000 years ago, the basin cores and 106 BC have been accumulating sediment, whereas, 31 BC and similar locations continued to experience erosion. Since 12 kyr, the beginning of the Holocene, the rate of deposition has increased at this site. An observed increase in opal accumulation is responsible, in part, for the increase in the primary sedimentation rate. Whether this constitutes an increase in preservation or supply is uncertain. A change in source and/or current direction is necessary to account for the Recent input of reworked manganese. Finally, the net accumulation is quite variable across the site, with cores located on the flanks having accumulation rates more than a factor-of-three less than basin cores.

#### Sediment Trap - Surface Sediment Comparison

From the model results we conclude that the composition of near-surface sediment is strongly influenced by older reworked material. It is obvious, therefore, that a simple mass balance of water column particulate input, dissolution at the seafloor, and sediment accumulation is not applicable to this site (c.f. Fisher et al., 1986). An estimate of the amount of recycling of bioactive elements in the lower water column and surficial sediments can be made only by comparing the model input fluxes of Recent material and the measured water column fluxes.

No Recent calcium carbonate is preserved in sediments at Site S so all the measured flux ( $319-1419 \mu\text{g}\cdot\text{cm}^{-2}\cdot\text{yr}^{-1}$ , Table IV-4) must be recycled in the near-surface sediments and/or in the lower water column. For opal, the primary inputs used to model the observed profile in basin core 47 BC are only 2 and 5% of the mean trap-measured flux. Since much of the opal flux recorded by the trap deployment is due to diatoms (Pisias et al., 1986), the bulk of the opal recycling results from the dissolution of diatoms. Based on the radiolarian flux estimates of Pisias et al. (1986), 5-30% of the trap-measured radiolarian flux is preserved in the basin core. This preserved fraction is a factor-of-two less in cores from the flanks of the basin.

## CONCLUSIONS

This study illustrates that a combination of conservative tracers and radionuclides can be used to decipher the complex history of sedimentation in an area where there are multiple sources and erosion of sediments. Since the bottoms of ferromanganese nodules at this site are thought to derive transition metals from the sediments (Moore, et al., 1981), the model can help resolve the source of these metals. We conclude that much of the supply of metals is, in fact, from older reworked material. Also, a Recent change in sedimentation at the beginning of the Holocene is necessary to explain the observed properties of near-surface sediments at Site S.

Unlike other sites, the simple difference between water column fluxes measured by sediment traps and surface sediment accumulation rates is insufficient to define the recycling of biogenic components at Site S. A model of erosion and deposition, such as the one developed in this study, must first be used to partition "new" and reworked sediment before water column and sediment accumulation comparisons can be made.

Comparisons of the opal flux in the water column with the flux inputs to surface sediments shows that a basin core with a faster net accumulation rate preserves more of the opal flux than do cores from the flanks of the basin.



## REFERENCES

- Anderson, R.F., The marine geochemistry of thorium and protactinium, Ph.D. Thesis, Woods Hole Oceanographic Institution, Woods Hole, 1981.
- Broecker, W.S. and T.-H. Peng, Tracers in the Sea, Eldigio Press, Palisades, New York, 690 pp., 1982.
- Cochran, J.K., Particle mixing rates in sediments of the eastern equatorial Pacific: Evidence from  $^{210}\text{Pb}$ ,  $^{239,240}\text{Pu}$  and  $^{137}\text{Cs}$  distributions at MANOP sites, Geochim. Cosmochim. Acta, 49, 1195-1210, 1985.
- Criss, J.W., L.S. Birks and J.V. Gilfrich, Versatile X-ray analysis program combining fundamental parameters and empirical coefficients, Anal. Chem., 50, 33-37, 1978.
- Dymond, J., M. Lyle, B. Finney, D.Z. Piper, K. Murphy, R. Conard and N.G. Pissias, Ferromanganese nodules from MANOP Sites H, S and R - Control of mineralogical and chemical composition by multiple accretionary processes, Geochim. Cosmochim. Acta, 48, 931-949, 1984.
- Finney, B.P., Paleoclimatic influence on sedimentation and manganese nodule growth during the past 400,000 years at MANOP Site H (eastern equatorial Pacific), Ph.D. Thesis, Oregon State University, Corvallis, OR, 195 pp., 1986.
- Fischer, K., J. Dymond, M.W. Lyle, A. Soutar and S. Rau, The benthic cycle of copper: Evidence from sediment trap experiments in the eastern tropical North Pacific Ocean, Geochim. Cosmochim. Acta, 50, 1535-1543, 1986.

- Hays, J.D. and N.J. Shackleton, Globally synchronous extinction of the radiolarian Stylatractus universus, Geology, 4, 649-652, 1976.
- Heath, G.R., Mineralogy of Cenozoic deep-sea sediments from the equatorial Pacific Ocean, Geol. Soc. Am. Bull., 80, 1997-2018, 1969.
- Heath, G.R. and N.G. Pisias, A method for the quantitative estimation of clay minerals on North Pacific deep-sea sediments, Clays and Clay Min., 27, 175-184, 1979.
- Jahnke, R.A., D. Heggie, S.R. Emerson and V. Grundmanis, Pore waters of the central Pacific Ocean: Nutrient results, Earth Planet. Sci. Lett., 61, 233-256, 1982.
- Johnson, D.A., Ocean floor erosion in the equatorial Pacific, Geol. Soc. Am. Bull., 83, 3121-3144, 1972.
- Johnson, D.A. and T.C. Johnson, Sediment redistribution by bottom currents in the central Pacific, Deep-Sea Res., 17, 157-170, 1970.
- Kadko, D., A detailed study of some uranium series nuclides at an abyssal hill area near the East Pacific Rise at 8° 45'N, Earth Planet. Sci. Lett., 51, 115-131, 1980.
- Kadko, D., A multi-tracer approach to the study of erosion in the northeast equatorial Pacific, Earth Planet. Sci. Lett., 63, 13-33, 1983.
- Karas, M.C., Studies of manganese nodules using deep-tow photographs and side-looking sonars, S.I.O. Ref. 78-20, 1978.
- Krishnaswami, S., Authigenic transition elements in Pacific pelagic clays, Geochim. Cosmochim. Acta, 40, 425-434, 1976.

- Lyle, M., G.R. Heath and J.M. Robbins, Transport and release of transition elements during early diagenesis: Sequential leaching of sediments from MANOP Sites M and H, Part I: pH 5 acetic acid leach, Geochim. Cosmochim. Acta, 48, 1705-1715, 1984.
- Moore, T.C., Jr., Abyssal hills in the central equatorial Pacific: Sedimentation and stratigraphy, Deep-Sea Res., 17, 573-593, 1970.
- Moore, W.S., T.L. Ku, J.D. Macdougall, V.M. Burns, R. Burns, J. Dymond, M.W. Lyle and D.Z. Piper, Fluxes of metals to a manganese nodule: Radiochemical, chemical, structural and mineralogical studies, Earth Planet. Sci. Lett., 52, 151-171, 1981.
- Piper, D.Z., H.E. Cook and J.V. Gardner, Lithic and acoustic stratigraphy of the equatorial North Pacific: DOMES Sites A, B, and C, In: Marine Geology and Oceanography of the Pacific Manganese Nodule Province, J.L. Bischoff and D.Z. Piper, eds., pp. 309-348, 1979.
- Pisias, N.G., D.W. Murray and A.K. Roelofs, Radiolarian and silicoflagellate response to oceanographic changes associated with the 1983 El Niño, Nature, 320, 259-262, 1986.
- Riedel, W.R. and B.M. Funnell, Tertiary sediment cores and microfossils from the Pacific Ocean floor, Quarterly J. Geol. Soc. London, 120, 305-368, 1964.
- Robbins, J., G.R. Heath and M.W. Lyle, A sequential extraction procedure for partitioning elements among co-existing phases in marine sediments, College of Oceanography Ref. 83-3, Oregon State University, Corvallis, OR, 55 pp., 1984.

- Roelofs, A.K. and N.G. Pisias, Revised technique for preparing quantitative radiolarian slides from deep-sea sediments, Micropaleo, 32, 182-185, 1986.
- van Andel, T.H., G.R. Heath and T.C. Moore, Jr., Cenozoic Tectonics, sedimentation and paleoceanography of the central equatorial Pacific, Geol. Soc. Am. Mem., 143, 134 pp., 1975.
- von Stackelberg, U., Sedimentation, hiatuses and development of manganese nodules, Valdivia Site VA-13/2, N.C. Pacific, In: Marine Geology and Oceanography of the Pacific Manganese Nodule Province, J.L. Bischoff and D.Z. Piper, eds., pp. 559-586, 1979.

## BIBLIOGRAPHY

- Adelseck, C.G., Jr. and T.F. Anderson, The late Pleistocene record of productivity fluctuations in the eastern equatorial Pacific Ocean, Geology, 6, 388-391, 1978.
- Anderson, R.F. The marine geochemistry of thorium and protactinium. Ph.D. Thesis, Woods Hole Oceanographic Institution, Woods Hole, MA, 1981.
- Arrhenius, G., Sediment cores from the east Pacific, Pt. 1, In: Reports of the Swedish Deep-Sea Expeditions 1947-1948, edited by H. Pettersson, 5, p. 227, Elanders, Goteborg, 1952.
- Barber, R.T. and F.P. Chavez, Biological consequences of El Niño, Science, 222, 1203-1210, 1983.
- Berger, W.H., Deep-sea carbonates: Pleistocene dissolution cycles, J. Foram. Res., 3, 187-195, 1973.
- Berger, W.H., G.G. Adelseck, Jr. and L. Mayer, Distribution of carbonate in surface sediments of the Pacific Ocean, J. Geophys. Res., 81, 2617-2627, 1976.
- Berner, R., Phosphate removal from sea water by absorption on volcanogenic ferric oxides, Earth Planet. Sci. Lett., 18, 77-86, 1973.
- Bischoff, J.L., G.R. Heath and M. Leinen, Geochemistry of deep-sea sediments from the Pacific manganese nodule province: Domes sites A, B, and C, In: Marine Geology and Oceanography of the Pacific Manganese Nodule Province, edited by J.L. Bischoff and D.Z. Piper, Plenum Press, New York, pp. 397-436, 1979.

- Bonatti, E., Manganese fluctuations in Caribbean sediment cores due to post depositional remobilization, Bull. Mar. Sci., 21, 510-518, 1971.
- Bostrom, K., T. Karenen and S. Gartner, Provenance and accumulation rates of silica, Al, Ti, Fe, Mn, Cu, Ni, and Co in Pacific pelagic sediments, Chem. Geol., 11, 123-148, 1973.
- Boyle, E.A., Chemical accumulation variations under the Peru Current during the past 130,000 years, J. Geophys. Res., 88, 7667-7680, 1983.
- Broecker, W.S., Calcite accumulation rates and glacial to interglacial changes in oceanic mixing, In: The Late Cenozoic Ice Ages, edited by K.K. Turekian, pp. 239-265, Yale University, New Haven, CT, 1971.
- Broecker, W.S. and T.-H. Peng, Tracers in the Sea, Eldigio Press, Palisades, New York, 690 pp., 1982.
- Cane, M.A., Oceanographic events during El Niño, Science, 222, 1189-1195, 1983.
- Cochran, J.K. Particle mixing rates in sediments of the eastern equatorial Pacific: Evidence from  $^{210}\text{Pb}$ ,  $^{239,240}\text{Pu}$  and  $^{137}\text{Cs}$  distributions at MANOP Sites. Geochim. Cosmochim. Acta, 49, 1195-1210, 1985.
- Colley, S., J. Thompson, T.R.S. Wilson and N.C. higgs, Post-depositional migration of elements during diagenesis in brown clay and turbidite sequences in the northeast Atlantic, Geochim. Cosmochim. Acta, 48, 1223-1235, 1984.

- Criss, J.W., L.S. Birks and J.V. Gilfrich, Versatile X-ray analysis program combining fundamental parameters and empirical coefficients, Anal. Chem., 50, 33-37, 1978.
- Davies, T. and A.S. Laughton, Sedimentary processes in the north Atlantic, In: Initial Reports of the Deep Sea Drilling Project, edited by A.S. Laughton, W.A. Berggren, et al., U.S. Government Printing Office, Washington, DC, 12, 905-934, 1972.
- Dean, W.E., J.V. Gardner and P. Cepek, Tertiary carbonate-dissolution cycles on the Sierra Leone Rise, eastern equatorial Atlantic Ocean, Mar. Geol., 39, 81-101, 1981.
- Deuser, W.G., Seasonal and interannual variations in deep-water particle fluxes in the Sargasso Sea and their relation to surface hydrography, Deep-Sea Res., 33, 225-246, 1986.
- Deuser, W.G. and E.H. Ross, Seasonal change in the flux of organic carbon to the deep Sargasso Sea, Nature, 283, 364-365, 1980.
- Deuser, W.G., P.G. Brewer, T.D. Jickells and R.F. Commeau, Biological control of the removal of abiogenic particles from the surface ocean, Science, 219, 388-391, 1983.
- Dymond, J., Geochemistry of Nazca Plate surface sediments: An evaluation of hydrothermal, biogenic, detrital, and hydrogenous sources, In: Nazca Plate: Crustal Formation and Andean Convergence, edited by L.D. Kulm, J. Dymond et al., Geological Society of America Memoir, 154, pp. 133-174, 1981.

- Dymond, J., Sediment traps, particle fluxes, and benthic boundary layer processes, In: Global Ocean flux Study: Proceedings of a Workshop, September 10-14, 1984, National Academy of Science, Washington, DC, pp. 260-284, 1984.
- Dymond, J. and M. Lyle, Flux comparisons between sediments and sediment traps in the eastern tropical Pacific: Implications for atmospheric CO<sub>2</sub> variations during the Pleistocene, Limnol. Oceanogr., 30, 699-712, 1985.
- Dymond, J., M. Lyle, B. Finney, D.Z. Piper, K. Murphy, R. Conard and N.G. Pisias. Ferromanganese nodules from MANOP Sites H, S and R - Control of mineralogical and chemical composition by multiple accretionary processes. Geochim. Cosmochim. Acta, 48, 931-949, 1984.
- Emerson, S., Organic carbon preservation in marine sediments, In: The Carbon Cycle and Atmospheric CO<sub>2</sub>: Natural Variations Archean to Present, edited by E.T. Sundquist and W.S. Broecker, Geophysical Monograph 32, American Geophysical Union, Washington, DC, pp. 78-87, 1985.
- Emerson, S., K. Fischer, C. Reimers and D. Heggie, Organic carbon dynamics and preservation in deep-sea sediments, Deep-Sea Res., 32, 1-21, 1985.
- Finney, B.P., Paleoclimatic influence on sedimentation and manganese nodule growth during the past 400,000 years at MANOP Site H (eastern equatorial Pacific), Ph.D. Thesis, Oregon State University, Corvallis, 195 pp., 1986.



- Fischer, K., Particle fluxes to the eastern tropical Pacific Ocean - Sources and Processes, Ph.D. Thesis, Oregon State University, Corvallis, 225 pp., 1983.
- Fischer, K., J. Dymond, M. Lyle, A. Soutar and S. Rau, The benthic cycle of copper: Evidence from sediment trap experiments in the eastern tropical North Pacific Ocean, Geochim. Cosmochim. Acta, 50, 1535-1543, 1986.
- Fowler, S.W. and L.F. Small, Sinking rates of euphausiid fecal pellets, Limnol. Oceanogr., 17, 293-296, 1972.
- Froelich, P.N., M.L. Bender and G.R. Heath, Phosphorus accumulation rates in metalliferous sediments on the East Pacific Rise, Earth Planet. Sci. Lett., 34, 351-359, 1977.
- Froelich, P.N., M.L. Bender, N.A. Luedke, G.R. Heath and T. DeVries, The marine phosphorus cycle, Am. J. Sci., 282, 474-511, 1982.
- Gardner, J.V., High-resolution carbonate and organic-carbon stratigraphies for the late Neogene and Quaternary from the western Caribbean and eastern equatorial Pacific, In: Initial Reports of the Deep Sea Drilling Project, 68, pp. 347-364, 1982.
- Gardner, W.D., M.J. Richardson, K.R. Hinga and P.E. Biscaye, Resuspension measured with sediment traps in a high-energy environment, Earth Planet. Sci. Lett., 66, 262-278, 1983.
- Garrels, R.M. and F.T. MacKenzie, Evolution of Sedimentary Rocks, W.W. Norton & Co., New York, 397 pp., 1971.

- Hays, J.D., T. Saito, N.D. Opdyke and L.H. Burckle, Pliocene-Pleistocene sediments of the equatorial Pacific: Their paleomagnetic, biostratigraphic and climatic record, Geol. Soc. Am. Bull., 80, 1481-1514, 1969.
- Hays, J.D. and N.J. Shackleton, Globally synchronous extinction of the radiolarian Stylatractus universus, Geology, 4, 649-652, 1976.
- Heath, G.R. Mineralogy of Cenozoic deep-sea sediments from the equatorial Pacific Ocean. Geol. Soc. Am. Bull., 80, 1997-2018, 1969.
- Heath, G.R. and N.G. Pisias. A method for the quantitative estimation of clay minerals on North Pacific deep-sea sediments. Clays and Clay Min., 27, 175-184, 1979.
- Honjo, S. Biogenic carbonate particles in the Ocean: Do they dissolve in the water column? In: The Fate of Fossil Fuel CO<sub>2</sub> in the Oceans, edited by N.R. Anderson and A. Malahoff, Plenum Press, New York, pp. 269-294, 1977.
- Honjo, S., Seasonality and interaction of biogenic and lithogenic particulate flux at the Panama Basin, Science, 218, 883-884, 1982.
- Honjo, S., S.J. Manganini and J.J. Cole, Sedimentation of biogenic matter in the deep ocean, Deep-Sea Res., 29, 609-625, 1982.

- Imbrie, J., J.D. Hays, D.G. Martinson, A. McIntyre, A.C. Mix, J.J. Morley, N.G. Pisias, W.L. Prell, and N.J. Shackleton, The orbital theory of Pleistocene climate: support from a revised chronology of the marine  $\delta^{18}\text{O}$  record, in Milankovitch and Climate, Pt. I, edited by A. Berger, J. Imbrie et al., Reidel Pub. Co., Boston, pp. 269-305, 1984.
- Jahnke, R.A., D. Heggie, S.R. Emerson and V. Grundmanis, Pore waters of the central Pacific Ocean: Nutrient results, Earth Planet. Sci. Lett., 61, 233-256, 1982.
- Jenkins, G.M. and D.G. Watts, Spectral Analysis and its Applications, 525 pp., Holden-Day, San Francisco, 1968.
- Johnson, D.A. Ocean floor erosion in the equatorial Pacific. Geol. Soc. Am. Bull., 83, 3121-3144, 1972.
- Johnson, D.A. and T.C. Johnson. Sediment redistribution by bottom currents in the central Pacific. Deep-Sea Res., 17, 157-170, 1970.
- Kadko, D. A detailed study of some uranium series nuclides at an abyssal hill area near the East Pacific Rise at  $8^{\circ} 45' \text{N}$ . Earth Planet. Sci. Lett., 51, 115-131, 1980.
- Kadko, D. A multi-tracer approach to the study of erosion in the northeast equatorial Pacific. Earth Planet. Sci. Lett., 63, 13-33, 1983.
- Karas, M.C. Studies of manganese nodules using deep-tow photographs and side-looking sonars. S.I.O. Ref. 78-20, 1978.

- Keir, R.S. and W.H. Berger, Atmospheric CO<sub>2</sub> content in the last 120,000 years: The phosphate-extraction model, J. Geophys. Res., 88, 6027-6038, 1983.
- Koblentz-Mishke, O.J., V.V. Volkovinsky and J.G. Kabanova, Plankton primary production of the world oceans, In: Scientific Exploration of the South Pacific, edited by W.S. Wooster, National Academy of Sciences, Washington, DC, pp. 183-193, 1970.
- Kominz, M.A., G.R. Heath, T.-L. Ku and N.G. Pisias, Brunhes time scales and the interpretation of climatic change, Earth. Planet. Sci. Lett., 45, 394-410, 1979.
- Krishnaswami, S., Authigenic transition elements in Pacific pelagic clays, Geochim. Cosmochim. Acta, 40, 425-434, 1976.
- Ku, T.-L. and T. Oba, A method for quantitative evaluation of carbonate dissolution in deep-sea sediments and its application to paleoceanographic reconstruction, Quat. Res., 10, 112-129, 1978.
- Lampitt, R.S., Evidence for the seasonal deposition of detritus to the deep-sea floor and its subsequent resuspension, Deep-Sea Res., 32, 885-897, 1985.
- Leinen, M., A normative calculation technique for determining opal in deep-sea sediments, Geochim. Cosmochim. Acta, 41, 671-676, 1977.

Leinen, M., D. Cwienk, G.R. Heath, P.E. Biscaye, V. Kolla, J.

Thiede and J.P. Dauphin, Distribution of biogenic silica and quartz in recent deep sea sediments, Geology, 14, 199-203, 1986.

Lister, C.R.B., Control of pelagic sediment distribution by Internal waves of tidal period: Possible interpretation of data from the southern east Pacific rise, Mar. Geol., 20, 297-313, 1976.

Lowrie, A. and B.C. Heezen, Knoll and sediment drift near Hudson Canyon, Science, 157, 1552-1553, 1967.

Luz, B. and N.J. Shackleton,  $\text{CaCO}_3$  solution in the tropical Pacific during the past 130,000 years, In: Dissolution of Deep-Sea Carbonates, edited by W.V. Sliter, A.W.H. Be, et al., Cushman Found. Foram. Res., Special Publication, 13, 142-150, 1975.

Lyle, M. and J. Dymond, Metal accumulation rates in the Southeast Pacific: Errors introduced from assumed bulk densities, Earth Planet. Sci. Lett., 30, 164-168, 1976.

Lyle, M. and G.R. Heath, Carbonate sedimentation at MANOP Site C,  $1^\circ\text{N}$ ,  $139^\circ\text{W}$ , Equatorial Pacific (abstr.), Transactions, American Geophysical Union, EOS, 60, p. 850, 1979.

Lyle, M.W., G.R. Heath and J.M. Robbins, Transport and release of transition elements during early diagenesis: Sequential leaching of sediments from MANOP Sites M and H, Pt. 1, pH 5 acetic acid leach, Geochim. Cosmochim. Acta, 48, 1705-1715, 1984.

- Martinson, D.G., W. Menke and P. Stoffa, An inverse approach to signal correlation, J. Geophys. Res., 87, 4807-4818, 1982.
- Martinson, D.G., N.G. Pisias, J.D. Hays, T.C. Moore, J. Imbrie and N.J. Shackleton, Age dating and the orbital theory of the ice ages: Development of a high resolution 0-300 kyr chronostratigraphy, Quat. Res., in press.
- Mayer, L.A., The origin and geologic setting of high-frequency acoustic reflectors in deep-sea carbonates, Ph.D. Thesis, University of California, San Diego, 159 pp., 1979.
- Menard, H.W., Marine Geology of the Pacific, McGraw-Hill, 271 pp., 1964.
- Molina-Cruz, A., The relation of the southern tradewinds to upwelling processes during the last 75,000 years, Quat. Res., 8, 324-338, 1977.
- Moore, T.C., Jr. Abyssal hills in the central equatorial Pacific: Sedimentation and stratigraphy. Deep-Sea Res., 17, 573-593, 1970.
- Moore, T.C., Jr., N.G. Pisias and G.R. Heath, Climate changes and lags in Pacific carbonate preservation, sea surface temperature and global ice volume, In: The Fate of Fossil Fuel CO<sub>2</sub> in the Oceans, edited by N.R. Anderson and A. Malahoff, Plenum Press, New York, pp. 145-165, 1977.
- Moore, T.C., Jr. and G.R. Heath, Sea-floor sampling techniques, In: Chemical Oceanography, edited by J.P. Riley and R. Chester, Academic Press, New York, pp. 75-126, 1978.

- Moore, T.C., Jr., N.G. Pisias and D.A. Dunn, Carbonate time series of the Quaternary and Late Miocene sediments in the Pacific Ocean: A spectral comparison, Mar. Geol., 46, 217-233, 1982.
- Moore, W.S., T.L. Ku, J.D. Macdougall, V.M. Burns, R. Burns, J. Dymond, M.W. Lyle and D.Z. Piper. Fluxes of metals to a manganese nodule: Radiochemical, chemical, structural and mineralogical studies. Earth Planet. Sci. Lett., 52, 151-171, 1981.
- Morley, J.J. and J.D. Hays, Towards a high-resolution, global, deep-sea chronology for the last 750,000 years, Earth Planet. Sci. Lett., 53, 279-295, 1981.
- Müller, P.J. and E. Suess, Productivity, sedimentation rate and sedimentary organic matter in the oceans, 1, Organic carbon preservation, Deep-Sea Res., 26, 1347-1362, 1979.
- Müller, P.J., H. Erlenkeuser and R. von Grafenstein, Glacial-interglacial cycles in oceanic productivity inferred from organic carbon contents in eastern North Atlantic sediment cores, In: Coastal Upwelling: Its Sediment Record, Part B, edited by J. Thiede and E. Suess, pp. 365-398, 1983.
- Murray, D.W. and J. Dymond, The seasonal rain of microfossils and organic carbon to the deep sea in the equatorial Pacific (abstr.), Transactions, American Geophysical Union, EOS, 66, p. 1275, 1985.

- Nigrini, C.A., Radiolarian zones in the Quaternary of the equatorial Pacific Ocean, In: The Micropaleontology of the Oceans, edited by B.M. Funnell and W.R. Riedel, Cambridge University Press, Great Britain, pp. 443-461, 1971.
- Pedersen, T.F., Increased productivity in the eastern equatorial Pacific during the last glacial maximum (19,000 to 14,000 yrs B.P.), Geology, 11, 16-19, 1983.
- Peterson, M.N.A., Calcite: Rates of dissolution in a vertical profile in the central Pacific, Science, 154, 1542-1544, 1966.
- Piper, D.Z., H.E. Cook and J.V. Gardner. Lithic and acoustic stratigraphy of the equatorial North Pacific: DOMES Sites A, B, and C. In: Marine Geology and Oceanography of the Pacific Manganese Nodule Province, J.L. Bischoff and D.Z. Piper, eds., pp. 309-348, 1979.
- Pisias, N.G., Late Quaternary sediment of the Panama Basin: Sedimentation rates, periodicities, and controls of carbonate and opal accumulation, Geol. Soc. Am. Mem., 145, 375-391, 1976.
- Pisias, N.G. and W.L. Prell, Changes in calcium carbonate accumulation in the equatorial Pacific during the Late Cenozoic: Evidence from HPC Site 572, In: The Carbon Cycle and Atmospheric CO<sub>2</sub>: Natural Variations Archean to Present, Geophysical Monograph 32, American Geophysical Union, Washington, DC, pp. 443-454, 1985.



- Pisias, N.G., D.W. Murray and A.K. Roelofs, Radiolarian and silicoflagellate response to oceanographic changes associated with the 1983 El Niño, Nature, 320, 259-262, 1986.
- Pujos, A., Nannofossils from Quaternary deposits in the high-productivity area of the central equatorial Pacific, DSDP Leg 85, In: Initial Reports of the Deep Sea Drilling Project, 85, pp. 553-619, U.S. Government Printing Office, Washington, DC, 1985.
- Rea, D.K., Fluctuation in eolian sedimentation during the past five glacial-interglacial cycles: A preliminary examination of data from Deep-Sea Drilling Project Hole 503B, eastern equatorial Pacific, In: Initial Reports of the Deep Sea Drilling Project, 68, pp. 409-415, U.S. Government Printing Office, Washington, DC, 1982.
- Rea, D.K., L.W. Chambers, J.M. Chuey, T.R. Janecek, M. Leinen and N.G. Pisias, A 450,000-year record of cyclicity in oceanic and atmospheric processes from the eastern equatorial Pacific, Paleoceanography, in press.
- Reimers, C.E., S. Kalhorn, S. Emerson and K.H. Nealson, Oxygen consumption rates in pelagic sediments from the central Pacific: First estimates from microelectrode profiles, Geochim. Cosmochim. Acta, 48, 903-910, 1984.
- Riedel, W.R. and B.M. Funnell. Tertiary sediment cores and microfossils from the Pacific Ocean floor. Quarterly J. Geol. Soc. London, 120, 305-368, 1964.

- Robbins, J., G.R. Heath and M.W. Lyle, A sequential extraction procedure for partitioning elements among co-existing phases in marine sediments, College of Oceanography Ref. 84-3, Oregon State University, Corvallis, 55 pp, 1984.
- Roberts, D.G., N.G. Hogg, D.G. Bishop and C.G. Fleueller, Sediment distribution around moated seamounts in the Rockall Trough, Deep-Sea Res., 21, 175-184, 1974.
- Roelofs, A.K. and N.G. Pisias, Revised technique for preparing quantitative radiolarian slides from deep-sea sediments, Micropaleo., 32, 182-185, 1986.
- Romine, K., Late Quaternary history of atmospheric and oceanic circulation in the eastern equatorial Pacific, Mar. Micropaleo., 7, 163-187, 1982.
- Romine, K. and T.C. Moore, Jr., Radiolarian assemblage distributions and paleoceanography of the eastern equatorial Pacific Ocean during the last 127,000 years, Paleoceanogr. Paleoclim. Paleoecol., 35, 281-314, 1981.
- Rowe, G.T. and W.D. Gardner, Sedimentation rates on the slope water of the northwest Atlantic Ocean measured directly with sediment traps, J. Mar. Res., 37, 581-600, 1979.
- Sawlan, J.J. and J.W. Murray, Trace metal remobilization in the interstitial waters of red clay and hemipelagic marine sediments, Earth Planet. Sci. Lett., 64, 213-230, 1983.

- Schink, D.R., N.L. Guinasso, Jr. and K.A. Fanning, Processes affecting the concentration of silica at the sediment-water interface of the Atlantic Ocean, J. Geophys. Res., 8, 3013-3031, 1975.
- Schramm, C.T., Implications of radiolarian assemblages for the late Quaternary paleoceanography at the eastern equatorial Pacific, Quar. Res., 24, 204-218, 1985.
- Shackleton, N.J., and N.D. Opdyke, Oxygen isotope and paleomagnetic stratigraphy of equatorial Pacific core V28-238: Oxygen isotope temperatures and ice volumes on a  $10^5$  and  $10^6$  year scale, Quat. Res., 3, 39-55, 1973.
- Small, L.F., S.W. Fowler and M.Y. Unlu, Sinking rates of natural copepod fecal pellets, Mar. Biol., 51, 233-241, 1979.
- Spencer, D.W., P.G. Brewer, A. Fleer, S. Honjo, S. Krishnaswami and Y. Nozaki, Chemical fluxes from a sediment trap experiment in the deep Sargasso Sea, J. Mar. Res., 36, 493-523, 1978.
- Spiess, F.N. and M. Weydert, Cruise report: Rama Leg 1, MANOP Sites C and R, SIO Ref. 84-8, Marine Physical Laboratory, Scripps Institute of Oceanography, San Diego, CA, 23 pp., 1984.
- Takahashi, K., Radiolarian sinking population, standing stock and production rate, Mar. Micropaleo., 8, 171-181, 1983.
- Takahashi, K. and S. Honjo, Vertical flux of Radiolaria: A taxon-quantitative sediment trap study from the western tropical Atlantic, Micropaleontology, 27, 140-190, 1981.

- Thompson, P.R. and T. Saito, Pacific Pleistocene sediments: Planktonic foraminifera dissolution cycles and geochronology, Geology, 2, 333-335, 1974.
- Thunell, R.C., W.B. Curry and S. Honjo, Seasonal variation in the flux of planktonic foraminifera: Time-series sediment trap results from the Panama Basin, Earth Planet. Sci. Lett., 64, 44-55, 1983.
- Thunell, R.C. and L.A. Reynolds, Sedimentation of planktonic foraminifera: Seasonal changes in species flux in the Panama Basin, Micropaleontology, 30, 243-262, 1984.
- Uematsu, M., R.A. Duce, S. Nakaya and S. Tsunogai, Short-term temporal variability of eolian particles in surface waters of the Northwestern North Pacific, J. Geophys. Res., 90, 1167-1172, 1985a.
- Uematsu, M., R.A. Duce and J.M. Prosperó, Deposition of atmospheric mineral particles to the north Pacific Ocean, J. Atmos. Chem., 3, 123-138, 1985b.
- Valencia, M.J., Pacific Pleistocene paleoclimatic stratigraphies: A comparative analysis of results, Quat. Res., 8, 339-354, 1977.
- van Andel, T.H., G.R. Heath and T.C. Moore, Jr., Cenozoic Tectonics, sedimentation, and paleoceanography of the central equatorial Pacific, Geol. Soc. Am. Mem., 143, 134 pp., 1975.

- van Bennekom, A.J. and S.J. van der Gaast, Possible clay structures in frustules of living diatoms, Geochim. Cosmochim. Acta, 40, 1149-1152, 1976.
- Volat, J.-L., L. Pastouret and C. Vergnaud-Grazzini, Dissolution and carbonate fluctuations in Pleistocene deep-sea cores: A review, Mar. Geol., 34, 1028, 1980.
- von Stackelberg, U. Sedimentation, hiatuses and development of manganese nodules, Valdivia Site VA-13/2, N.C. Pacific. In: Marine Geology and Oceanography of the Pacific Manganese Nodule Province, J.L. Bischoff and D.Z. Piper, eds., pp. 559-586, 1979.
- Walsh, I., Resuspension and the rebound process: Implications of sediment trap studies in the Northern Pacific, M.S. Thesis, Oregon State University, Corvallis, 108 pp., 1985.
- Walsh, I., J. Dymond and R. Collier, Rates of recycling of biogenic components of fast settling particles derived from sediment trap experiments, Deep-Sea Res., submitted.
- Walsh, I., K. Fischer, D.W. Murray and J. Dymond, Evidence for resuspension of virgin particles from near-bottom sediment traps, Deep-Sea Res., submitted.
- Weliky, K., E. Suess, C.A. Ungerer, P.J. Müller and K. Fischer, Problems with accurate carbon measurements in marine sediments and particulate matter in seawater: A new approach, Limnol. Oceanogr., 28, 1252-1259, 1983.

## APPENDICES

## Appendix 1

## Chemical Data for Seven Site C Cores

Adjusted depths have been altered by subtracting the thickness of turbidites from appropriate intervals. Ages are from the linear extrapolation of the  $^{14}\text{C}$  GC age scale to each core based on the correlation of calcium carbonate concentration profiles. Elemental concentrations in weight % (salt corrected) were determined by XRF unless indicated.

K7905 16 GC

depth	adjusted depth	sample ID	age	salt	water content	dry bulk density	sum of oxides
(cm)	(cm)		(kyr)	%	%	(g/cm <sup>3</sup> )	
5.5	5.5	04999	3.20	4.4	56.9	0.605	97.0
10.5	10.5	04691	6.46	3.8	52.9	0.680	97.5
13.5	13.5	05002	8.42	3.8	52.8	0.680	97.5
17.5	17.5	05003	10.97	3.6	51.6	0.709	96.6
20.5	20.5	04693	12.92	3.5	50.9	0.724	97.1
24.5	24.5	05005	15.55	3.6	51.8	0.709	97.3
30.5	30.5	04694	19.54	3.7	52.4	0.694	95.6
34.5	34.5	05007	22.19	3.8	53.0	0.680	95.1
40.5	--	04695	--	3.6	51.8	0.709	96.6
45.5	38.5	05009	24.97	3.6	51.5	0.709	97.1
50.5	43.5	04696	28.51	3.4	50.2	0.740	95.9
55.5	48.5	05010	31.97	3.3	49.3	0.757	97.0
60.5	53.5	04697	35.31	3.3	49.3	0.757	96.0
65.5	58.5	05011	38.64	3.3	49.2	0.757	97.9
70.5	63.5	04698	42.07	3.0	47.1	0.812	96.1
75.5	68.5	05012	45.55	3.1	47.7	0.793	97.4
80.5	73.5	04699	49.10	3.1	48.0	0.793	97.1
85.5	78.5	05013	52.93	3.2	48.5	0.775	97.0
90.5	83.5	04700	57.10	3.0	46.7	0.812	96.3
96.5	89.5	05015	63.60	3.3	49.4	0.757	96.9
100.5	93.5	04701	68.95	3.9	53.9	0.666	97.7
103.5	96.5	05016	73.41	3.9	54.0	0.666	97.7
110.5	103.5	04702	86.03	4.8	59.1	0.564	99.2
120.5	113.5	04703	111.56	4.2	55.8	0.628	100.0
126.5	119.5	05018	124.66	4.1	54.9	0.641	99.7
133.5	126.5	05019	135.76	4.1	54.7	0.641	99.7
136.5	129.5	05020	139.66	4.1	54.9	0.641	99.6



## K7905 16 GC (continued)

depth (cm)	adjusted depth (cm)	sample ID	age (kyr)	salt %	water content %	dry bulk density (g/cm <sup>3</sup> )	sum of oxides
140.5	133.5	04705	144.30	4.1	54.9	0.641	98.8
144.5	137.5	05022	148.43	3.7	52.4	0.694	99.0
150.5	143.5	04706	154.83	3.5	50.8	0.724	98.3
156.5	149.5	05025	161.03	3.7	52.3	0.694	98.4
160.5	153.5	04707	165.36	3.2	48.8	0.775	97.0
163.5	156.5	05026	168.90	3.2	48.9	0.775	97.4
170.5	163.5	04708	177.60	3.7	50.6	0.724	96.2
176.5	169.5	05028	186.00	4.8	59.1	0.564	96.2
187.5	180.5	05029	203.16	4.1	55.1	0.641	96.7
190.5	183.5	04710	208.00	3.7	52.1	0.694	98.0
196.5	189.5	05030	--	3.3	49.6	0.757	98.0
200.5	193.5	04711	--	3.1	48.1	0.793	96.4
204.5	197.5	05031	--	3.4	50.3	0.740	97.7
207.5	200.5	05032	--	3.5	50.7	0.724	97.2
220.5	213.5	04712	--	4.0	54.3	0.653	97.5
224.5	217.5	05034	--	4.9	59.3	0.554	98.0
230.5	223.5	04713	--	4.6	57.8	0.584	98.7
234.5	227.5	05036	--	3.1	57.6	0.594	98.8
237.5	230.5	05037	--	3.8	52.5	0.694	97.9
247.5	240.5	05038	--	2.8	45.4	0.853	96.1
250.5	243.5	04715	--	2.9	46.3	0.832	96.0
256.5	249.5	05040	--	2.8	44.1	0.875	96.2
260.5	253.5	04716	--	2.7	44.3	0.875	96.7
263.5	256.5	05041	--	2.6	42.9	0.898	96.1
270.5	263.5	04718	--	3.3	49.5	0.757	95.7
276.5	269.5	05042	--	4.2	55.3	0.628	95.3

## K7905 16 GC

depth	Al	Si	P	Ti	Mn	Fe	Sr	Ba	opal	CaCO <sub>3</sub>	CaCO <sub>3</sub> (LECO)	C-org (LECO)
(cm)												
5.5	0.6420	9.4018	0.0475	0.0396	0.1808	0.5245	0.1175	0.1806	17.1	72.6	77.9	0.331
10.5	0.4974	8.0614	0.0413	0.0328	0.1467	0.4492	0.1229	0.1472	15.2	77.0	85.1	0.345
13.5	0.4593	6.7803	0.0374	0.0335	0.1429	0.4276	0.1252	0.1377	12.4	79.8	89.7	0.459
17.5	0.4173	5.9398	0.0344	0.0341	0.2871	0.3990	0.1273	0.1284	10.7	80.8	89.5	0.444
20.5	0.3847	5.3865	0.0334	0.0318	0.3220	0.3784	0.1265	0.1138	9.6	82.5	87.8	0.512
24.5	0.3849	4.9743	0.0333	0.0336	0.1004	0.3966	0.1288	0.1242	8.6	83.9	88.2	0.456
30.5	0.3733	4.2560	0.0336	0.0317	0.0438	0.3971	0.1294	0.1204	6.9	83.9	89.9	0.551
34.5	0.3372	4.4511	0.0322	0.0293	0.0407	0.3680	0.1191	0.1006	7.8	82.9	89.4	0.473
40.5	0.2246	1.6633	0.0267	0.0301	0.0437	0.3128	0.1096	0.0630	1.9	90.4	94.1	0.628
45.5	0.4122	3.5950	0.0310	0.0334	0.0658	0.3953	0.1277	0.1099	4.9	86.7	89.5	0.814
50.5	0.4037	3.4101	0.0310	0.0335	0.0575	0.3984	0.1276	0.1097	4.5	86.1	94.4	0.392
55.5	0.3794	3.5808	0.0301	0.0333	0.0657	0.3856	0.1295	0.0973	5.2	87.0	92.8	0.235
60.5	0.3145	3.6085	0.0299	0.0305	0.0488	0.3537	0.1281	0.0831	5.9	86.1	92.7	0.273
65.5	0.3186	3.7923	0.0293	0.0304	0.0610	0.3559	0.1299	0.0763	6.3	87.5	91.4	0.143
70.5	0.3024	3.0615	0.0274	0.0293	0.0641	0.3608	0.1303	0.0722	4.6	87.5	91.6	0.156
75.5	0.3307	3.4756	0.0301	0.0323	0.0698	0.3707	0.1447	0.0818	5.4	87.5	91.8	0.152
80.5	0.3197	3.3634	0.0291	0.0320	0.0703	0.3705	0.1436	0.0847	5.2	87.5	92.2	0.141
85.5	0.2851	2.9655	0.0279	0.0304	0.0742	0.3539	0.1435	0.0736	4.6	88.3	90.8	0.138
90.5	0.3454	3.3350	0.0316	0.0344	0.0866	0.3896	0.1446	0.0928	4.9	86.6	90.4	0.139
96.5	0.5473	4.9441	0.0383	0.0398	0.1073	0.4849	0.1403	0.1386	6.9	82.8	88.2	0.139
100.5	0.9074	7.6702	0.0503	0.0491	0.1550	0.6574	0.1316	0.2290	10.1	75.9	80.0	0.136
103.5	1.0442	8.8377	0.0556	0.0519	0.1647	0.7204	0.1286	0.2629	11.7	73.0	77.1	0.157
110.5	1.3217	11.1576	0.0595	0.0589	0.1397	0.8358	0.1207	0.3396	14.7	67.9	74.2	0.142
120.5	0.9364	11.1719	0.0484	0.0468	0.1770	0.6253	0.1292	0.2816	18.6	70.5	74.0	0.093
126.5	0.5170	9.4977	0.0367	0.0372	0.1544	0.4336	0.1317	0.1545	18.6	75.7	79.0	0.070
133.5	0.4844	7.8247	0.0346	0.0346	0.1232	0.4145	0.1321	0.1387	14.8	79.4	81.8	0.093
136.5	0.4824	7.5348	0.0386	0.0373	0.1203	0.4212	0.1342	0.1459	14.0	80.0	81.5	0.092
140.5	0.5999	7.9545	0.0425	0.0379	0.0915	0.4867	0.1337	0.1667	13.9	77.8	81.2	0.092
144.5	0.4988	7.7023	0.0402	0.0363	0.1436	0.4351	0.1343	0.1370	14.3	79.1	82.5	0.070
150.5	0.5497	6.5086	0.0370	0.0377	0.1671	0.4634	0.1384	0.1334	10.8	80.7	83.7	0.094

## K7905 16 GC (continued)

depth (cm)	Al	Si	P	Ti	Mn	Fe	Sr	Ba	opal	CaCO <sub>3</sub>	CaCO <sub>3</sub> (LECO)	C-org (LECO)
156.5	0.5550	7.6913	0.0375	0.0384	0.1173	0.4759	0.1371	0.1531	13.7	78.3	81.7	0.108
160.5	0.4935	5.0944	0.0369	0.0375	0.1086	0.4591	0.1438	0.1289	7.8	82.9	84.8	0.056
163.5	0.5537	5.3893	0.0394	0.0365	0.1195	0.4875	0.1443	0.1341	8.0	82.4	85.5	0.081
170.5	0.6527	6.0487	0.0433	0.0415	0.1183	0.5415	0.1440	0.1686	8.6	79.3	82.3	0.108
176.5	1.1410	10.3532	0.0561	0.0549	0.0927	0.8328	0.1314	0.3224	14.5	67.7	72.7	0.180
187.5	0.7122	7.2057	0.0463	0.0402	0.1195	0.5381	0.1394	0.2062	10.9	76.9	81.5	0.222
190.5	0.6576	6.6902	0.0450	0.0401	0.1285	0.5054	0.1438	0.1660	10.2	79.6	82.1	0.055
196.5	0.4697	6.3339	0.0388	0.0348	0.0852	0.4372	0.1452	0.1118	11.1	81.4	82.9	0.101
200.5	0.3689	4.5364	0.0344	0.0344	0.0705	0.4069	0.1467	0.0977	7.7	84.1	85.9	0.098
204.5	0.3853	5.1231	0.0350	0.0333	0.0704	0.4195	0.1435	0.0894	8.9	84.0	85.5	0.337
207.5	0.4341	5.2144	0.0382	0.0367	0.0801	0.4386	0.1430	0.1043	8.7	83.1	86.5	0.160
220.5	0.5815	6.8872	0.0440	0.0402	0.1097	0.5100	0.1378	0.1360	11.4	78.9	81.5	0.165
224.5	1.1719	10.7097	0.0666	0.0538	0.0734	0.7691	0.1308	0.2950	15.1	68.6	73.3	0.249
230.5	0.9930	9.7736	0.0579	0.0472	0.0578	0.7542	0.1348	0.2709	14.5	72.0	75.1	0.238
234.5	1.0233	9.9059	0.0552	0.0484	0.0870	0.6678	0.1369	0.2909	14.6	71.9	79.6	0.266
237.5	0.6683	6.8720	0.0443	0.0398	0.1085	0.5135	0.1489	0.2029	10.6	79.2	84.5	0.293
247.5	0.3518	3.7984	0.0325	0.0328	0.1870	0.3687	0.1569	0.0799	6.0	85.5	87.7	0.210
250.5	0.3668	4.0393	0.0354	0.0341	0.1372	0.3805	0.1566	0.0909	6.4	84.9	88.6	0.373
256.5	0.3521	3.5083	0.0299	0.0336	0.0647	0.3765	0.1577	0.0828	5.3	86.4	89.6	0.332
260.5	0.3405	3.1206	0.0286	0.0328	0.0680	0.3734	0.1584	0.0776	4.4	87.8	90.2	0.306
263.5	0.3179	2.8295	0.0277	0.0308	0.0679	0.3671	0.1595	0.0678	3.9	88.0	88.8	0.246
270.5	0.5500	4.3451	0.0352	0.0366	0.0713	0.4814	0.1417	0.1128	5.4	83.3	86.6	0.287
276.5	0.7978	6.2561	0.0415	0.0410	0.0746	0.5960	0.1334	0.1701	7.7	77.6	80.8	0.280

RAMA I 6 GC

depth (cm)	adjusted depth (cm)	sample ID	age (kyr)	salt %	water content %	dry bulk density (g/cm <sup>3</sup> )	sum of oxides
2.3	2.3	06871	1.09	3.9	53.4	0.666	93.6
5.0	5.0	06874	2.93	4.4	56.8	0.605	93.8
10.4	10.4	06880	6.64	4.5	57.6	0.594	93.5
14.9	14.9	06885	9.75	4.1	55.0	0.641	94.3
18.5	18.5	06889	12.19	3.2	48.6	0.775	95.6
20.3	20.3	06891	13.42	3.3	49.1	0.757	94.9
24.8	24.8	06896	16.48	4.0	54.3	0.653	95.1
30.2	30.2	06902	20.16	4.0	54.4	0.653	94.4
32.9	32.9	06905	21.94	4.0	54.2	0.653	95.4
40.1	40.1	06913	26.89	4.0	54.5	0.653	95.2
45.5	--	06919	--	3.6	51.5	0.709	93.6
50.0	--	06924	--	3.7	52.1	0.694	93.3
52.5	--	04966	--	2.5	42.7	0.922	94.4
70.5	--	04967	--	3.0	46.9	0.812	94.5
80.5	--	04968	--	3.2	48.6	0.775	94.6
90.5	--	04969	--	3.6	51.4	0.709	95.5
95.5	--	04970	--	3.7	52.1	0.694	95.8
100.5	--	04971	--	3.7	52.3	0.694	95.6
105.5	--	04972	--	3.8	53.2	0.680	95.2
110.5	--	04973	--	3.7	52.1	0.694	95.4
116.5	--	04974	--	4.3	56.3	0.617	94.7
121.5	--	04976	--	3.1	47.9	0.793	93.7
127.5	49.5	04979	33.08	3.5	50.8	0.724	95.2
133.5	55.5	04980	36.76	3.3	49.0	0.757	96.2
139.5	61.5	04982	40.43	2.7	44.1	0.875	94.7

RAMA I 6 GC (continued)

depth	adjusted	sample	age	salt	water	dry bulk	sum of
(cm)	depth	ID	(kyr)	%	content	density	oxides
	(cm)				%	(g/cm <sup>3</sup> )	
145.5	67.5	04983	44.18	2.7	44.3	0.875	95.4
151.5	73.5	04985	47.97	2.8	45.3	0.853	95.5
157.5	79.5	04987	52.08	2.8	45.4	0.853	94.7
163.5	85.5	04988	56.61	2.9	45.6	0.832	93.7
169.5	91.5	04990	62.91	2.9	45.7	0.832	94.5
175.5	97.5	04991	71.62	3.4	50.0	0.740	96.4
182.5	104.5	04992	86.65	3.9	53.8	0.666	97.0
188.5	110.5	04994	106.10	4.4	56.7	0.605	97.2
195.5	117.5	04996	126.60	3.4	50.3	0.740	95.9
200.5	122.5	04997	136.10	3.5	50.6	0.724	97.8
205.5	127.5	05708	143.90	3.5	50.7	0.724	94.8
209.5	131.5	05710	149.20	3.4	49.9	0.740	95.5
215.5	137.5	05713	157.90	2.9	46.0	0.832	93.6
219.5	141.5	05715	164.50	3.7	52.3	0.694	95.0
225.5	145.5	05718	177.60	4.5	57.4	0.594	97.0
229.5	--	05720	--	3.2	49.0	0.775	94.4
233.5	149.5	05722	183.30	4.9	59.7	0.554	96.2
235.5	151.5	05723	189.90	4.7	58.8	0.573	95.1
239.5	155.5	05725	206.10	3.4	50.3	0.740	92.0
245.5	161.5	05728	--	4.0	54.2	0.653	95.5
251.5	167.5	05731	--	4.8	58.8	0.564	97.8
265.5	181.5	05738	--	2.7	44.2	0.875	93.7
269.5	185.5	05740	--	2.9	45.9	0.832	94.0
275.5	191.5	05743	--	2.6	42.8	0.898	94.3
279.5	195.5	05745	--	2.9	46.0	0.832	95.2

## RAMA I 6 GC

depth (cm)	Al	Si	P	Ti	Mn	Fe	Sr	Ba	opal	CaCO <sub>3</sub>
2.3	0.6973	7.8982	0.0540	0.0431	0.1854	0.5970	0.1223	0.2046	12.8	72.3
5.0	0.6436	8.3131	0.0512	0.0427	0.1726	0.5757	0.1202	0.1888	14.4	71.8
10.4	0.6223	8.6530	0.0517	0.0423	0.1060	0.5740	0.1187	0.1873	15.5	70.9
14.9	0.4701	6.3547	0.0420	0.0401	0.1663	0.4978	0.1256	0.1469	11.2	77.4
18.5	0.3699	4.4327	0.0349	0.0328	0.4154	0.3968	0.1249	0.1026	7.4	82.7
20.3	0.3820	4.6289	0.0396	0.0363	0.2433	0.4338	0.1202	0.1095	7.8	81.9
24.8	0.4422	5.4641	0.0364	0.0341	0.1781	0.4291	0.1262	0.1357	9.2	80.3
30.2	0.4407	5.0787	0.0351	0.0338	0.1258	0.4316	0.1287	0.1290	8.4	80.4
32.9	0.4091	4.9249	0.0347	0.0318	0.1373	0.4080	0.1273	0.1183	8.3	81.8
40.1	0.3489	4.4560	0.0308	0.0320	0.0884	0.3797	0.1255	0.1064	7.7	83.0
45.5	0.3737	3.6507	0.0338	0.0331	0.0494	0.4085	0.1303	0.1203	5.4	83.3
50.0	0.3684	3.4580	0.0315	0.0318	0.0618	0.4151	0.1334	0.1205	5.0	83.4
52.5	0.3596	3.7791	0.0320	0.0337	0.0631	0.4145	0.1325	0.1237	5.9	84.0
70.5	0.3725	3.9535	0.0321	0.0319	0.0669	0.4231	0.1319	0.1157	6.1	83.6
80.5	0.3723	4.2027	0.0313	0.0348	0.0571	0.4565	0.1288	0.1196	6.8	82.9
90.5	0.3101	3.1080	0.0302	0.0296	0.0492	0.3486	0.1154	0.0734	4.7	86.1
95.5	0.2489	2.3305	0.0311	0.0305	0.0474	0.3275	0.1119	0.0626	3.4	88.1
100.5	0.2237	2.0654	0.0277	0.0296	0.0460	0.3112	0.1097	0.0585	3.0	88.5
105.5	0.1556	1.0543	0.0231	0.0305	0.0439	0.3031	0.1072	0.0490	1.1	90.4
110.5	0.1177	0.5058	0.0177	0.0285	0.0421	0.3174	0.1054	0.0333	0.1	91.7
116.5	0.1275	0.5481	0.0166	0.0290	0.0446	0.3091	0.1077	0.0392	0.1	90.8
121.5	0.3760	3.9066	0.0316	0.0309	0.0621	0.3847	0.1294	0.1057	6.0	82.7
127.5	0.3971	3.5012	0.0303	0.0336	0.0585	0.3778	0.1257	0.1193	4.8	85.0
133.5	0.3886	3.3439	0.0302	0.0319	0.0563	0.3747	0.1290	0.1014	4.5	86.5
139.5	0.3156	2.9954	0.0279	0.0316	0.0551	0.3652	0.1292	0.0899	4.3	86.3

## RAMA I 6 GC (continued)

depth (cm)	Al	Si	P	Ti	Mn	Fe	Sr	Ba	opal	CaCO <sub>3</sub>
145.5	0.2712	3.0032	0.0273	0.0294	0.0556	0.3485	0.1283	0.0691	4.8	87.0
151.5	0.3033	2.7597	0.0270	0.0318	0.0560	0.3493	0.1287	0.0776	3.8	87.3
157.5	0.3018	2.7735	0.0278	0.0310	0.0568	0.3645	0.1297	0.0816	3.9	86.5
163.5	0.2691	2.4931	0.0272	0.0309	0.0577	0.3628	0.1279	0.0747	3.6	86.3
169.5	0.3485	3.2428	0.0307	0.0324	0.0575	0.4252	0.1275	0.0910	4.6	85.0
175.5	0.8112	6.8480	0.0467	0.0433	0.0520	0.6618	0.1177	0.2037	9.0	77.1
182.5	1.0897	9.3805	0.0555	0.0526	0.0632	0.7692	0.1062	0.3191	12.6	70.7
188.5	0.8495	9.4212	0.0466	0.0454	0.0692	0.6307	0.1112	0.2683	15.1	71.9
195.5	0.5253	6.6980	0.0404	0.0352	0.1205	0.4690	0.1191	0.1585	11.5	78.1
200.5	0.5936	5.9304	0.0388	0.0381	0.1034	0.4922	0.1249	0.1503	8.9	81.4
205.5	0.5162	6.3857	0.0368	0.0364	0.0920	0.4921	0.1231	0.1464	10.8	77.8
209.5	0.6078	5.7397	0.0415	0.0386	0.0665	0.5573	0.1284	0.1566	8.3	79.5
215.5	0.6146	5.4611	0.0405	0.0387	0.1657	0.5321	0.1328	0.1706	7.5	78.2
219.5	0.6025	6.7029	0.0419	0.0379	0.1375	0.5186	0.1240	0.1949	10.8	76.8
225.5	0.5866	5.8371	0.0437	0.0370	0.0644	0.4719	0.1133	0.1851	8.7	80.0
229.5	0.3761	4.3399	0.0338	0.0322	0.0680	0.4267	0.1287	0.0920	7.1	82.6
233.5	1.1561	10.1681	0.0584	0.0557	0.0612	0.8407	0.1147	0.3069	13.9	67.9
235.5	1.0593	10.1752	0.0563	0.0538	0.0596	0.8126	0.1126	0.2957	14.9	67.3
239.5	0.5345	6.0835	0.0390	0.0378	0.0608	0.5239	0.1265	0.1471	9.9	75.7
245.5	0.6155	6.6057	0.0467	0.0401	0.0873	0.5329	0.1214	0.1642	10.4	77.4
251.5	0.9067	9.3526	0.0572	0.0454	0.0678	0.6478	0.1181	0.2169	14.3	72.4
265.5	0.3305	2.8992	0.0285	0.0317	0.0983	0.3786	0.1412	0.0828	3.9	85.3
269.5	0.4361	4.3753	0.0348	0.0320	0.0880	0.4246	0.1397	0.1122	6.6	82.0
275.5	0.3349	2.5584	0.0302	0.0322	0.0941	0.3826	0.1435	0.0705	3.1	86.7
279.5	0.4005	3.4613	0.0312	0.0341	0.0925	0.4135	0.1415	0.0897	4.7	85.3

## BENTHIC III 12 GC

depth (cm)	adjusted depth (cm)	sample ID	age (kyr)	salt %	water content %	dry bulk density (g/cm <sup>3</sup> )	sum of oxides
0.5	0.5	20080	0.30	4.5	57.5	0.594	94.8
5.5	5.5	20081	2.84	3.8	52.8	0.680	95.1
10.5	10.5	20082	5.38	3.4	50.1	0.740	94.4
15.5	12.5	20083	6.45	4.0	54.1	0.653	94.4
20.5	17.5	20084	9.07	3.6	51.3	0.709	94.6
25.5	22.5	20085	11.72	3.9	53.7	0.666	95.4
30.5	27.5	20086	14.46	3.6	51.7	0.709	95.1
35.5	32.5	20087	17.31	3.3	49.7	0.757	94.7
40.5	37.5	20088	20.28	3.5	50.5	0.724	94.2
45.5	--	20089	--	3.3	49.1	0.757	95.2
50.5	--	20090	--	3.7	52.5	0.694	96.1
55.5	--	20091	--	3.5	51.2	0.724	94.0
60.5	--	20092	--	3.9	54.0	0.666	96.0
65.5	--	20093	--	3.5	51.2	0.724	95.7
70.5	--	20094	--	3.2	48.8	0.775	96.2
75.5	--	20095	--	3.3	49.0	0.757	94.0
80.5	40.5	20096	22.08	3.4	50.0	0.740	95.1
85.5	45.5	20097	25.37	3.3	49.2	0.757	95.0
90.5	50.5	20098	28.90	3.2	48.3	0.775	95.9
95.5	55.5	20099	32.55	3.1	47.5	0.793	95.4
100.5	60.5	20100	36.35	3.2	48.2	0.775	95.6
105.5	65.5	20101	40.56	3.2	48.6	0.775	95.8
110.5	70.5	20102	45.36	3.1	47.5	0.793	95.6
114.5	75.5	20103	50.94	3.0	46.7	0.812	95.7
120.5	80.5	20104	57.79	3.1	47.6	0.793	95.6



## BENTHIC III 12 GC (continued)

depth (cm)	adjusted depth (cm)	sample ID	age (kyr)	salt %	water content %	dry bulk density (g/cm <sup>3</sup> )	sum of oxides
125.5	85.5	20105	67.83	3.5	50.9	0.724	96.6
130.5	90.5	20106	79.93	4.3	56.1	0.617	97.5
135.5	95.5	20107	94.16	4.7	58.8	0.573	97.8
140.5	100.5	20108	111.10	4.3	56.4	0.617	97.8
145.5	105.5	20109	124.00	4.0	54.5	0.653	97.7
150.5	110.5	20110	133.60	4.1	54.8	0.641	97.2
155.5	115.5	20111	141.60	3.9	54.0	0.666	97.1
160.5	120.5	20112	148.50	4.0	54.3	0.653	96.6
165.5	125.5	20113	156.00	3.4	50.1	0.740	94.9
170.5	130.5	20114	163.90	3.3	49.1	0.757	94.4
175.5	135.5	20115	173.50	3.6	51.7	0.709	95.7
180.5	138.5	20116	180.10	5.3	61.4	0.518	97.2
185.5	143.5	20117	192.70	5.5	62.4	0.502	96.3
190.5	148.5	20118	207.00	4.1	54.7	0.641	95.9
195.5	153.5	20119	221.00	3.6	51.3	0.709	94.7
200.5	158.5	20120	--	3.8	53.2	0.680	95.4
205.5	163.5	20121	--	3.7	52.0	0.694	95.7
210.5	168.5	20122	--	4.3	56.2	0.617	96.1
215.5	173.5	20123	--	5.4	61.9	0.510	97.2
220.5	178.5	20124	--	7.0	68.1	0.405	98.4
225.5	183.5	20125	--	4.8	59.2	0.564	96.2
230.5	188.5	20126	--	4.6	58.1	0.584	95.5
234.5	193.5	20127	--	4.2	55.7	0.628	94.8
240.5	198.5	20128	--	2.8	45.1	0.853	95.0
245.5	203.5	20129	--	2.9	46.1	0.832	95.1

## BENTHIC III 12 GC (continued)

depth	adjusted	sample	age	salt	water	dry bulk	sum of
(cm)	depth	ID	(kyr)	%	content	density	oxides
	(cm)				%	(g/cm <sup>3</sup> )	
250.5	208.5	20130	--	2.8	45.4	0.853	95.2
255.5	213.5	20131	--	2.5	42.4	0.922	95.8
260.5	218.5	20132	--	2.4	41.4	0.948	94.9
265.5	223.5	20133	--	3.2	48.9	0.775	94.0
270.5	228.5	20134	--	4.1	55.2	0.641	94.9
275.5	233.5	20135	--	4.4	56.9	0.605	95.3
280.5	238.5	20136	--	4.3	56.5	0.617	94.5
285.5	243.5	20137	--	5.0	60.0	0.545	93.6
290.5	248.5	20138	--	5.1	60.5	0.536	94.3
295.5	253.5	20139	--	3.5	51.2	0.724	95.3
300.5	258.5	20140	--	3.1	48.0	0.793	96.6
305.5	263.5	20141	--	3.0	46.6	0.812	96.0
309.5	267.5	20142	--	2.8	45.5	0.853	96.1

## BENTHIC III 12 GC

depth (cm)	Al	Si	P	Ti	Mn	Fe	Sr	Ba	opal	CaCO <sub>3</sub>
0.5	0.4629	6.6109	0.0415	0.0378	0.1379	0.4180	0.1217	0.1884	11.9	77.2
5.5	0.3689	6.0086	0.0360	0.0325	0.1167	0.3693	0.1253	0.1447	11.3	79.4
10.5	0.2631	4.0434	0.0289	0.0289	0.1065	0.3084	0.1216	0.0990	7.5	83.5
15.5	0.4171	4.4463	0.0378	0.0319	0.3881	0.3514	0.1268	0.1383	7.0	81.5
20.5	0.3292	4.4929	0.0297	0.0295	0.1478	0.3229	0.1271	0.1258	8.0	82.5
25.5	0.3920	4.7578	0.0362	0.0304	0.1156	0.3453	0.1270	0.1423	8.0	82.4
30.5	0.3281	4.0713	0.0313	0.0291	0.1030	0.3232	0.1296	0.1193	6.9	84.0
35.5	0.3226	3.5736	0.0318	0.0308	0.0549	0.3252	0.1308	0.1311	5.8	84.8
40.5	0.3239	3.3424	0.0302	0.0311	0.0591	0.3383	0.1310	0.1291	5.1	84.8
45.5	0.2998	3.2616	0.0302	0.0296	0.0585	0.3123	0.1221	0.1066	5.2	85.9
50.5	0.2957	3.3977	0.0296	0.0288	0.0543	0.2984	0.1183	0.0931	5.6	86.4
55.5	0.3278	3.5879	0.0304	0.0297	0.0549	0.3984	0.1334	0.1310	5.7	84.0
60.5	0.3424	2.9753	0.0281	0.0297	0.0501	0.2743	0.1249	0.1275	4.0	87.2
65.5	0.3467	2.9908	0.0286	0.0322	0.0472	0.2837	0.1265	0.1311	4.0	87.0
70.5	0.3042	2.8529	0.0269	0.0295	0.0461	0.3346	0.1279	0.0987	4.1	87.9
75.5	0.3086	3.6394	0.0303	0.0293	0.0715	0.3266	0.1289	0.1190	6.0	84.1
80.5	0.2895	3.3046	0.0303	0.0292	0.0573	0.3026	0.1216	0.1048	5.4	85.7
85.5	0.3180	3.1420	0.0293	0.0312	0.0582	0.3006	0.1248	0.1158	4.7	86.0
90.5	0.2478	2.6707	0.0267	0.0285	0.0469	0.3081	0.1285	0.0838	4.2	88.2
95.5	0.2663	2.7918	0.0266	0.0277	0.0493	0.3055	0.1304	0.0848	4.3	87.5
100.5	0.2557	2.8840	0.0262	0.0281	0.0501	0.2894	0.1273	0.0769	4.7	87.5
105.5	0.2496	2.9845	0.0262	0.0280	0.0550	0.2880	0.1299	0.0848	5.0	87.5
110.5	0.2470	2.6049	0.0268	0.0284	0.0555	0.2901	0.1291	0.0824	4.0	88.2
114.5	0.2514	2.7252	0.0293	0.0290	0.0509	0.2978	0.1302	0.0837	4.3	88.0
120.5	0.3754	3.4474	0.0348	0.0322	0.0793	0.3717	0.1269	0.1197	4.9	85.6

## BENTHIC III 12 GC (continued)

depth (cm)	Al	Si	P	Ti	Mn	Fe	Sr	Ba	opal	CaCO <sub>3</sub>
125.5	0.6665	5.9824	0.0457	0.0401	0.1201	0.5181	0.1188	0.2097	8.4	79.7
130.5	0.9627	8.4253	0.0532	0.0497	0.1339	0.6610	0.1112	0.3010	11.4	73.7
135.5	1.0105	10.4429	0.0534	0.0510	0.1393	0.6864	0.1083	0.4035	16.0	69.3
140.5	0.7472	9.2468	0.0462	0.0435	0.1271	0.5430	0.1141	0.3125	15.6	73.3
145.5	0.4364	7.0750	0.0352	0.0324	0.0922	0.3716	0.1166	0.1652	13.3	79.4
150.5	0.4044	5.9877	0.0386	0.0314	0.0729	0.3666	0.1201	0.1450	10.9	81.5
155.5	0.4191	6.5408	0.0396	0.0338	0.1063	0.3723	0.1207	0.1517	12.2	80.1
160.5	0.4498	5.8304	0.0350	0.0369	0.0875	0.4246	0.1226	0.1660	10.1	81.0
165.5	0.4121	4.2295	0.0384	0.0346	0.1357	0.3917	0.1287	0.1361	6.4	83.0
170.5	0.4914	4.5498	0.0390	0.0373	0.2058	0.4447	0.1290	0.1745	6.4	81.4
175.5	0.4954	5.3034	0.0378	0.0370	0.1414	0.4332	0.1283	0.1880	8.4	81.0
180.5	1.0106	8.9630	0.0558	0.0544	0.1487	0.7472	0.1147	0.3886	12.3	71.8
185.5	1.1724	10.8774	0.0608	0.0583	0.0860	0.8204	0.1108	0.4063	15.6	66.3
190.5	0.6949	6.7496	0.0470	0.0404	0.0637	0.6883	0.1248	0.2442	10.0	77.0
195.5	0.4808	5.1575	0.0417	0.0355	0.1795	0.4099	0.1273	0.1584	8.1	80.4
200.5	0.4696	5.1227	0.0388	0.0342	0.0763	0.4137	0.1279	0.1518	8.2	81.4
205.5	0.4290	4.8200	0.0371	0.0333	0.0621	0.3989	0.1290	0.1308	7.8	82.6
210.5	0.6227	6.6040	0.0449	0.0367	0.0887	0.4901	0.1212	0.2007	10.3	78.1
215.5	1.0327	9.6180	0.0574	0.0506	0.0743	0.6810	0.1132	0.3662	13.7	70.5
220.5	1.5875	13.2307	0.0755	0.0685	0.0978	0.9874	0.1024	0.4768	17.3	61.2
225.5	0.9005	8.0034	0.0535	0.0462	0.0787	0.6044	0.1205	0.3252	11.0	73.7
230.5	0.9577	8.3911	0.0549	0.0464	0.0884	0.7030	0.1166	0.3215	11.4	71.9
234.5	0.7723	6.9666	0.0491	0.0407	0.0957	0.5507	0.1281	0.2607	9.7	75.4
240.5	0.3267	3.0902	0.0313	0.0311	0.2513	0.3067	0.1429	0.0939	4.5	86.1
245.5	0.3482	3.8075	0.0327	0.0312	0.2101	0.3197	0.1427	0.1003	6.0	84.7

## BENTHIC III 12 GC (continued)

depth (cm)	Al	Si	P	Ti	Mn	Fe	Sr	Ba	opal	CaCO <sub>3</sub>
250.5	0.3172	3.1327	0.0296	0.0305	0.1311	0.3471	0.1429	0.0941	4.7	86.3
255.5	0.2893	2.4320	0.0267	0.0290	0.0794	0.3031	0.1450	0.0702	3.3	88.7
260.5	0.2926	2.3805	0.0273	0.0285	0.0764	0.3109	0.1454	0.0700	3.1	88.0
265.5	0.4860	4.0420	0.0331	0.0330	0.0739	0.4158	0.1374	0.1253	5.3	82.5
270.5	0.8221	6.2814	0.0420	0.0444	0.0972	0.5859	0.1306	0.2235	7.5	76.8
275.5	0.8932	6.7867	0.0445	0.0484	0.1099	0.6384	0.1303	0.2448	8.1	75.7
280.5	0.9529	7.0721	0.0487	0.0507	0.1552	0.6993	0.1291	0.2640	8.2	73.9
285.5	1.0226	7.6793	0.0529	0.0519	0.1302	0.7428	0.1262	0.3091	9.0	71.2
290.5	1.0611	8.3190	0.0546	0.0511	0.1129	0.7541	0.1242	0.3624	10.2	70.3
295.5	0.5290	4.7406	0.0373	0.0341	0.1139	0.4264	0.1328	0.1677	6.6	81.8
300.5	0.2693	2.9008	0.0276	0.0265	0.0480	0.3105	0.1303	0.0745	4.6	88.4
305.5	0.2609	2.9018	0.0268	0.0290	0.0475	0.3121	0.1300	0.0918	4.6	87.9
309.5	0.2716	2.9076	0.0274	0.0290	0.0478	0.3132	0.1289	0.0876	4.6	87.9

## BENTHIC III 18 GC

depth (cm)	adjusted depth (cm)	sample ID	age (kyr)	salt %	water content %	dry bulk density (g/cm <sup>3</sup> )	sum of oxides
0.5	0.5	20143	0.30	4.6	58.0	0.584	96.2
5.5	5.5	20144	4.32	4.5	57.4	0.594	97.5
10.5	10.5	20145	8.30	4.0	54.7	0.653	97.4
15.5	15.5	20146	12.31	3.5	51.1	0.724	97.0
20.5	20.5	20147	16.26	3.6	51.4	0.709	96.0
25.5	25.5	20148	20.22	3.7	52.5	0.694	95.9
30.5	30.5	20149	24.10	3.4	50.3	0.740	96.5
35.5	35.5	20150	28.10	3.4	49.9	0.740	96.5
40.5	40.5	20151	31.90	3.3	49.6	0.757	96.2
45.5	45.5	20152	35.46	3.2	48.9	0.775	96.0
50.5	50.5	20153	38.91	3.4	50.3	0.740	96.7
55.5	55.5	20154	42.38	3.3	49.6	0.757	96.5
60.5	60.5	20155	45.79	3.3	49.6	0.757	97.2
65.5	65.5	20156	49.18	3.5	50.6	0.724	96.5
70.5	70.5	20157	52.76	3.5	51.1	0.724	96.2
75.5	75.5	20158	56.40	3.3	49.1	0.757	96.0
80.5	80.5	20159	60.80	3.7	52.1	0.694	96.2
85.5	85.5	20160	66.07	4.3	56.0	0.617	97.1
90.5	90.5	20161	71.93	4.1	55.1	0.641	96.3
95.5	95.5	20162	78.45	4.3	56.1	0.617	97.3
100.5	100.5	20163	85.90	4.7	58.5	0.573	97.3
105.5	105.5	20164	94.05	4.9	59.3	0.554	98.1
110.5	110.5	20165	104.00	4.9	59.4	0.554	98.0
115.5	115.5	20166	113.40	4.5	57.3	0.594	98.2
120.5	120.5	20167	121.00	4.4	56.7	0.605	98.7
125.5	125.5	20168	127.90	4.5	57.2	0.594	99.1
130.5	130.5	20169	133.20	4.5	57.2	0.594	98.4
135.5	135.5	20170	138.20	4.5	57.2	0.594	99.3

## BENTHIC III 18 GC (continued)

depth (cm)	adjusted depth (cm)	sample ID	age (kyr)	salt %	water content %	dry bulk density (g/cm <sup>3</sup> )	sum of oxides
140.5	140.5	20171	142.70	4.1	54.8	0.641	98.6
145.5	145.5	20172	146.80	3.9	53.5	0.666	98.1
150.5	150.5	20173	151.30	3.8	53.3	0.680	97.9
155.5	155.5	20174	156.20	3.8	53.3	0.680	96.3
160.5	160.5	20175	161.80	4.3	56.2	0.617	98.1
165.5	165.5	20176	167.30	3.8	53.1	0.680	96.9
170.5	170.5	20177	175.00	3.8	53.3	0.680	95.6
175.5	175.5	20178	184.50	4.0	54.2	0.653	94.5
180.5	180.5	20179	196.30	4.0	54.5	0.653	96.1
185.5	185.5	20180	210.10	3.3	49.1	0.757	95.4
190.5	190.5	20181	--	3.3	49.3	0.757	95.8
195.5	195.5	20182	--	3.3	49.6	0.757	95.9
200.5	200.5	20183	--	3.6	51.5	0.709	96.4
205.5	205.5	20184	--	3.4	50.5	0.740	96.3
210.5	210.5	20185	--	4.0	54.5	0.653	96.7
215.5	215.5	20186	--	4.7	58.6	0.573	97.2
220.5	220.5	20187	--	5.3	61.4	0.518	97.9
225.5	225.5	20188	--	3.8	53.0	0.680	96.1
230.5	230.5	20189	--	3.8	53.2	0.680	95.8
235.5	235.5	20190	--	3.8	52.9	0.680	96.3
240.5	240.5	20191	--	3.4	50.5	0.740	95.4
245.5	245.5	20192	--	3.1	48.1	0.793	95.1
250.5	250.5	20193	--	2.7	44.0	0.875	95.2
255.5	255.5	20194	--	2.7	44.3	0.875	95.1
260.5	260.5	20195	--	2.6	42.9	0.898	95.0
265.5	265.5	20196	--	2.4	40.9	0.948	94.9
270.5	270.5	20197	--	2.4	41.0	0.948	95.2
275.5	275.5	20198	--	2.7	44.3	0.875	95.4

## BENTHIC III 18 GC

depth (cm)	Al	Si	P	Ti	Mn	Fe	Sr	Ba	opal	CaCO <sub>3</sub>
0.5	0.3918	5.3833	0.0356	0.0319	0.1309	0.3467	0.1168	0.1504	9.6	81.5
5.5	0.3448	5.4718	0.0323	0.0300	0.1326	0.3204	0.1172	0.1312	10.3	82.7
10.5	0.2739	4.7535	0.0283	0.0294	0.1753	0.2868	0.1209	0.1242	9.1	84.6
15.5	0.2724	3.4053	0.0290	0.0299	0.1565	0.2897	0.1271	0.1150	5.8	87.5
20.5	0.2681	2.9367	0.0262	0.0296	0.1243	0.2865	0.1243	0.1085	4.7	87.5
25.5	0.2871	2.8398	0.0277	0.0289	0.0857	0.2953	0.1284	0.1061	4.2	87.7
30.5	0.2728	2.7739	0.0264	0.0300	0.0963	0.2937	0.1276	0.0991	4.2	88.5
35.5	0.2267	2.6276	0.0251	0.0269	0.0566	0.2715	0.1284	0.0761	4.3	89.2
40.5	0.2019	2.2645	0.0259	0.0256	0.0533	0.2595	0.1285	0.0583	3.6	89.7
45.5	0.2145	2.4774	0.0253	0.0276	0.0592	0.2678	0.1290	0.0691	4.0	89.0
50.5	0.2173	2.8803	0.0252	0.0276	0.0577	0.2663	0.1296	0.0730	5.0	88.8
55.5	0.1982	2.6317	0.0242	0.0263	0.0646	0.2591	0.1274	0.0640	4.6	89.2
60.5	0.2129	3.0453	0.0254	0.0280	0.0615	0.2677	0.1279	0.0782	5.5	88.8
65.5	0.1999	2.7617	0.0254	0.0270	0.0623	0.2624	0.1279	0.0664	4.9	88.9
70.5	0.2144	2.3708	0.0259	0.0280	0.0605	0.2712	0.1271	0.0704	3.7	89.3
75.5	0.2393	2.6723	0.0272	0.0285	0.0594	0.2876	0.1286	0.0784	4.3	88.5
80.5	0.3606	3.6168	0.0306	0.0318	0.0625	0.3455	0.1245	0.1186	5.5	85.8
85.5	0.7521	6.7333	0.0441	0.0425	0.1059	0.5364	0.1145	0.2371	9.3	78.0
90.5	0.6112	6.0471	0.0417	0.0396	0.1081	0.4917	0.1187	0.2091	9.0	79.3
95.5	0.6355	6.2251	0.0400	0.0408	0.1421	0.4991	0.1160	0.2378	9.2	79.6
100.5	0.7759	8.1155	0.0433	0.0441	0.1524	0.5641	0.1111	0.3005	12.6	74.9
105.5	0.8043	9.1533	0.0433	0.0459	0.1015	0.5604	0.1084	0.2966	14.9	73.3
110.5	0.7434	9.1193	0.0426	0.0425	0.1613	0.5317	0.1124	0.3109	15.4	73.6
115.5	0.5695	8.4978	0.0378	0.0367	0.1761	0.4326	0.1150	0.2400	15.6	75.9
120.5	0.3307	6.9017	0.0309	0.0302	0.1536	0.3159	0.1186	0.1410	14.0	81.1
125.5	0.3046	7.2457	0.0287	0.0296	0.0834	0.3062	0.1162	0.1244	15.1	81.0
130.5	0.3066	6.0823	0.0303	0.0304	0.0904	0.3051	0.1168	0.1258	12.2	82.7
135.5	0.2999	6.9970	0.0319	0.0296	0.1112	0.2997	0.1157	0.1159	14.5	81.6



## BENTHIC III 18 GC (continued)

depth (cm)	Al	Si	P	Ti	Mn	Fe	Sr	Ba	opal	CaCO <sub>3</sub>
140.5	0.3130	6.3664	0.0328	0.0305	0.1300	0.3131	0.1183	0.1164	12.8	82.3
145.5	0.3123	5.4321	0.0341	0.0316	0.1466	0.3183	0.1188	0.1096	10.5	83.8
150.5	0.3277	5.7469	0.0320	0.0319	0.0795	0.3334	0.1213	0.1147	11.1	83.1
155.5	0.3383	5.5658	0.0315	0.0307	0.0587	0.3425	0.1212	0.1131	10.6	81.9
160.5	0.3629	7.8158	0.0320	0.0322	0.0505	0.3602	0.1215	0.1339	15.9	78.7
165.5	0.3196	5.4184	0.0323	0.0291	0.0689	0.3412	0.1254	0.1110	10.4	82.9
170.5	0.3887	5.3057	0.0361	0.0342	0.0623	0.3870	0.1251	0.1458	9.4	81.5
175.5	0.5373	6.2521	0.0380	0.0369	0.0612	0.4854	0.1222	0.1902	10.3	77.7
180.5	0.5992	6.5370	0.0404	0.0371	0.0787	0.4679	0.1249	0.2481	10.4	78.3
185.5	0.3795	4.2144	0.0349	0.0299	0.0729	0.3602	0.1294	0.1430	6.7	83.7
190.5	0.2973	3.7836	0.0318	0.0275	0.0827	0.3101	0.1268	0.0968	6.5	85.5
195.5	0.2783	4.3986	0.0315	0.0288	0.0667	0.3115	0.1290	0.1018	8.3	84.4
200.5	0.2591	4.4123	0.0299	0.0269	0.0603	0.3047	0.1288	0.0818	8.4	85.0
205.5	0.2736	4.0600	0.0326	0.0289	0.0641	0.3226	0.1277	0.0873	7.4	85.6
210.5	0.3565	5.7941	0.0353	0.0307	0.0692	0.3597	0.1238	0.1184	10.9	81.7
215.5	0.6626	8.5141	0.0484	0.0409	0.1130	0.5169	0.1165	0.2173	14.7	74.7
220.5	0.8076	10.0056	0.0548	0.0453	0.0690	0.5898	0.1147	0.2635	17.0	71.5
225.5	0.5763	5.7853	0.0464	0.0387	0.0716	0.4626	0.1300	0.1974	8.7	80.1
230.5	0.5251	5.7134	0.0434	0.0357	0.0842	0.4375	0.1314	0.1932	9.0	80.2
235.5	0.5338	5.6479	0.0412	0.0354	0.0815	0.4330	0.1324	0.1926	8.8	80.9
240.5	0.4152	5.1171	0.0354	0.0325	0.0932	0.3640	0.1360	0.1645	8.6	81.7
245.5	0.2895	3.4926	0.0299	0.0285	0.0938	0.3054	0.1406	0.1128	5.9	85.6
250.5	0.2054	2.1361	0.0267	0.0267	0.2103	0.2617	0.1435	0.0613	3.3	88.9
255.5	0.2304	2.8008	0.0285	0.0272	0.0817	0.2766	0.1449	0.0725	4.7	87.5
260.5	0.2216	2.4066	0.0283	0.0279	0.0631	0.2787	0.1448	0.0751	3.8	88.3
265.5	0.1904	1.8804	0.0255	0.0269	0.0636	0.2608	0.1469	0.0573	2.8	89.4
270.5	0.2355	2.0549	0.0265	0.0281	0.0617	0.2767	0.1444	0.0624	2.8	89.2
275.5	0.3484	3.1669	0.0296	0.0307	0.0583	0.3358	0.1418	0.0927	4.4	86.6

## BENTHIC III 21 GC

depth (cm)	adjusted depth (cm)	sample ID	age (kyr)	salt %	water content %	dry bulk density (g/cm <sup>3</sup> )	sum of oxides
0.5	0.5	20199	0.30	4.6	58.0	0.584	95.6
5.5	5.5	20200	3.20	4.4	57.0	0.605	95.8
10.5	10.5	20201	6.27	3.8	53.2	0.680	96.1
15.5	15.5	20202	9.30	3.6	51.9	0.709	96.3
20.5	20.5	20203	12.24	3.4	50.3	0.740	95.0
25.5	25.5	20204	15.25	3.8	52.8	0.680	96.1
30.5	30.5	20205	18.25	4.0	54.3	0.653	95.3
35.5	35.5	20206	21.19	4.1	55.2	0.641	96.0
40.5	40.5	20207	24.16	3.7	52.4	0.694	94.3
45.5	45.5	20208	27.22	3.9	53.8	0.666	96.1
50.5	50.5	20209	30.20	3.3	49.6	0.757	95.5
55.5	55.5	20210	32.99	3.3	49.5	0.757	96.0
60.5	60.5	20211	35.65	3.4	50.4	0.740	95.7
65.5	65.5	20212	38.27	3.2	48.9	0.775	94.8
70.5	70.5	20213	40.88	3.2	48.9	0.775	94.7
75.5	75.5	20214	43.47	3.3	49.7	0.757	95.7
80.5	80.5	20215	46.00	3.4	49.8	0.740	95.6
85.5	85.5	20216	48.50	3.3	49.5	0.757	95.2
90.5	90.5	20217	51.05	3.4	50.1	0.740	96.4
95.5	95.5	20218	53.67	3.4	49.9	0.740	96.2
100.5	100.5	20219	56.30	3.3	49.5	0.757	95.3
105.5	105.5	20220	59.31	3.7	52.6	0.694	96.0
110.5	110.5	20221	62.78	4.5	57.2	0.594	95.7
115.5	115.5	20222	66.58	5.3	61.7	0.518	96.6
125.5	125.5	20224	74.94	5.0	60.2	0.545	96.8
130.5	130.5	20225	79.66	5.0	59.9	0.545	96.1
134.5	134.5	20226	83.84	5.1	60.7	0.536	97.2
140.5	140.5	20227	90.62	4.7	58.6	0.573	96.3

## BENTHIC III 21 GC (continued)

depth (cm)	adjusted depth (cm)	sample ID	age (kyr)	salt %	water content %	dry bulk density (g/cm <sup>3</sup> )	sum of oxides
145.5	145.5	20228	97.03	4.5	57.2	0.594	97.1
150.5	150.5	20229	104.60	5.4	62.0	0.510	97.6
155.5	155.5	20230	111.60	5.4	62.1	0.510	98.8
160.5	160.5	20231	117.50	4.1	54.9	0.641	96.7
165.5	165.5	20232	123.10	4.0	54.6	0.653	96.0
170.5	170.5	20233	128.00	4.2	55.4	0.628	98.6
175.5	175.5	20234	132.10	4.3	55.9	0.617	98.0
180.5	180.5	20235	135.90	4.2	55.7	0.628	98.7
185.5	185.5	20236	139.60	4.3	56.0	0.617	99.1
190.5	190.5	20237	142.90	4.0	54.2	0.653	98.6
195.5	195.5	20238	145.90	4.2	55.6	0.628	98.9
200.5	200.5	20239	149.00	4.1	54.9	0.641	97.3
205.5	205.5	20240	152.20	4.2	55.3	0.628	97.0
210.5	210.5	20241	155.50	4.1	55.3	0.641	96.0
215.5	215.5	20242	158.70	4.5	57.3	0.594	96.2
220.5	220.5	20243	162.10	3.9	53.9	0.666	96.6
225.5	225.5	20244	165.70	3.8	52.7	0.680	96.1
230.5	230.5	20245	169.80	4.0	54.2	0.653	95.7
235.5	235.5	20246	174.10	3.9	53.9	0.666	94.3
240.5	240.5	20247	178.60	5.1	60.4	0.536	93.4
245.5	245.5	20248	183.60	7.7	70.3	0.371	96.1
250.5	250.5	20249	189.00	7.7	70.3	0.371	95.9
255.5	255.5	20250	194.70	9.1	74.1	0.317	97.2
260.5	260.5	20251	200.80	5.5	62.5	0.502	96.4
265.5	265.5	20252	206.80	4.4	56.7	0.605	95.6
270.5	270.5	20253	212.70	4.0	54.6	0.653	96.2
275.5	275.5	20254	--	4.1	55.1	0.641	95.6

## BENTHIC III 21 GC

depth (cm)	Al	Si	P	Ti	Mn	Fe	Sr	Ba	opal	CaCO <sub>3</sub>
0.5	0.5500	7.5024	0.0462	0.0340	0.1733	0.4139	0.1170	0.1981	13.2	75.6
5.5	0.5434	8.0883	0.0424	0.0328	0.1742	0.4104	0.1219	0.1946	14.8	74.8
10.5	0.4044	7.3864	0.0360	0.0299	0.2926	0.3397	0.1247	0.1628	14.5	77.1
15.5	0.3524	6.0308	0.0307	0.0285	0.4236	0.3061	0.1256	0.1353	11.6	80.3
20.5	0.3210	4.4108	0.0309	0.0310	0.4396	0.2996	0.1274	0.1368	7.9	82.6
25.5	0.3217	4.4094	0.0303	0.0289	0.3073	0.3042	0.1282	0.1276	7.8	83.9
30.5	0.3238	3.6551	0.0313	0.0309	0.0535	0.3109	0.1282	0.1335	6.0	85.0
35.5	0.3112	3.0637	0.0284	0.0305	0.0509	0.2937	0.1236	0.1158	4.5	86.9
40.5	0.3559	3.1385	0.0300	0.0311	0.0612	0.3146	0.1271	0.1363	4.3	85.1
45.5	0.3742	3.7829	0.0303	0.0306	0.0569	0.3182	0.1289	0.1307	5.8	85.4
50.5	0.3548	3.1768	0.0311	0.0290	0.0669	0.3235	0.1305	0.1109	4.4	86.3
55.5	0.3088	3.0254	0.0282	0.0285	0.0667	0.3058	0.1302	0.0973	4.5	87.3
60.5	0.2408	2.6708	0.0260	0.0272	0.0666	0.2704	0.1268	0.0769	4.3	88.1
65.5	0.2340	2.9125	0.0270	0.0270	0.0725	0.2704	0.1270	0.0754	5.0	86.7
70.5	0.2453	3.0582	0.0272	0.0272	0.1198	0.2765	0.1285	0.0846	5.2	86.2
75.5	0.2447	2.7468	0.0257	0.0282	0.0842	0.2798	0.1304	0.0822	4.4	87.9
80.5	0.2448	2.9219	0.0251	0.0254	0.0717	0.2794	0.1288	0.0722	4.9	87.5
85.5	0.2594	2.9157	0.0279	0.0304	0.0764	0.2902	0.1288	0.0904	4.7	87.0
90.5	0.2149	2.2152	0.0260	0.0275	0.0762	0.2674	0.1295	0.0728	3.4	90.0
95.5	0.2388	2.8624	0.0283	0.0279	0.0825	0.2811	0.1306	0.0796	4.8	88.2
100.5	0.3140	2.9851	0.0304	0.0312	0.0869	0.3279	0.1297	0.0958	4.3	86.7
105.5	0.4439	4.1524	0.0339	0.0352	0.1085	0.3951	0.1290	0.1346	6.0	84.2
110.5	0.8549	7.7318	0.0496	0.0454	0.2609	0.6090	0.1172	0.2604	10.8	73.9
115.5	1.1631	9.7445	0.0563	0.0528	0.1960	0.7575	0.1102	0.3386	12.8	68.9
125.5	1.0135	8.8326	0.0484	0.0477	0.1167	0.6832	0.1128	0.3051	12.0	71.9
130.5	0.9917	9.2550	0.0459	0.0513	0.1796	0.6567	0.1082	0.3264	13.2	70.2
134.5	1.1743	11.3004	0.0527	0.0543	0.1989	0.7510	0.1050	0.3804	16.5	66.2
140.5	1.0663	10.1468	0.0530	0.0499	0.1390	0.6998	0.1101	0.3515	14.8	68.5

## BENTHIC III 21 GC (continued)

depth (cm)	Al	Si	P	Ti	Mn	Fe	Sr	Ba	opal	CaCO <sub>3</sub>
145.5	1.0057	10.0299	0.0492	0.0480	0.1897	0.6508	0.1122	0.3388	15.1	69.7
150.5	1.2865	13.5521	0.0551	0.0538	0.2886	0.7619	0.1037	0.4432	21.0	61.2
155.5	0.9530	13.5538	0.0481	0.0458	0.3542	0.5731	0.1078	0.3737	24.4	63.7
160.5	0.6386	8.3058	0.0404	0.0359	0.3729	0.4219	0.1198	0.2213	14.8	74.5
165.5	0.5064	7.9941	0.0357	0.0319	0.2794	0.3628	0.1194	0.1573	15.0	75.3
170.5	0.3906	8.5307	0.0323	0.0325	0.3230	0.3222	0.1200	0.1440	17.5	77.1
175.5	0.3576	9.1104	0.0304	0.0292	0.1947	0.3144	0.1166	0.1284	19.2	75.6
180.5	0.3544	8.4978	0.0312	0.0305	0.1905	0.3089	0.1162	0.1368	17.8	77.6
185.5	0.3792	7.5159	0.0324	0.0319	0.1903	0.3182	0.1194	0.1428	15.1	80.0
190.5	0.3919	7.0738	0.0364	0.0328	0.3010	0.3273	0.1194	0.1358	13.8	80.4
195.5	0.3846	8.0148	0.0341	0.0297	0.0800	0.3285	0.1199	0.1275	16.2	79.0
200.5	0.4110	6.7256	0.0380	0.0332	0.1403	0.3574	0.1215	0.1393	12.8	79.9
205.5	0.4321	5.9918	0.0348	0.0333	0.0873	0.3712	0.1244	0.1331	10.7	81.2
210.5	0.4721	5.7993	0.0343	0.0322	0.0837	0.3942	0.1245	0.1433	9.8	80.5
215.5	0.4607	6.9936	0.0342	0.0375	0.0719	0.3810	0.1240	0.1678	12.9	78.1
220.5	0.4891	6.5345	0.0333	0.0337	0.0715	0.3494	0.1275	0.1441	11.4	79.6
225.5	0.4114	4.1811	0.0349	0.0324	0.0798	0.3833	0.1313	0.1255	6.3	84.4
230.5	0.5671	5.4175	0.0414	0.0392	0.2223	0.4588	0.1292	0.1836	7.9	80.3
235.5	0.6233	6.0379	0.0417	0.0402	0.0910	0.5133	0.1268	0.2041	8.9	77.6
240.5	0.9426	8.7117	0.0488	0.0511	0.0792	0.7293	0.1190	0.3125	12.4	69.2
245.5	1.7576	15.5181	0.0685	0.0762	0.0678	1.1685	0.1003	0.5916	21.3	53.0
250.5	1.7587	15.5074	0.0707	0.0775	0.0653	1.1522	0.0992	0.6061	21.2	52.7
255.5	1.9717	17.4501	0.0749	0.0819	0.0692	1.3093	0.0933	0.6702	24.0	48.6
260.5	1.0164	9.5912	0.0550	0.0511	0.0873	0.7095	0.1202	0.3622	13.8	70.1
265.5	0.7102	7.4885	0.0455	0.0423	0.0977	0.5310	0.1272	0.2505	11.6	75.4
270.5	0.5248	6.2706	0.0393	0.0329	0.1055	0.4307	0.1321	0.1851	10.9	79.4
275.5	0.6335	6.4293	0.0429	0.0391	0.2687	0.4910	0.1308	0.2330	10.2	77.7

## BENTHIC III 25 GC

depth	adjusted	sample	age	salt	water	dry bulk	sum of
(cm)	depth	ID	(kyr)	%	content	density	oxides
	(cm)				%	(g/cm <sup>3</sup> )	
0.5	0.5	20255	0.30	5.1	60.3	0.536	94.9
5.5	5.5	20256	3.61	5.0	60.2	0.545	96.5
10.5	10.5	20257	6.87	4.1	55.1	0.641	96.3
15.5	15.5	20258	10.18	3.8	53.2	0.680	94.9
20.5	20.5	20259	13.43	3.9	53.4	0.666	96.0
25.5	25.5	20260	16.73	4.2	55.7	0.628	96.2
30.5	--	20261	--	4.5	57.3	0.594	96.7
35.5	31.5	20262	20.67	4.4	56.6	0.605	95.5
40.5	36.5	20263	23.92	4.1	55.3	0.641	95.2
45.5	41.5	20264	27.31	3.8	52.7	0.680	95.5
50.5	46.5	20265	30.60	3.7	52.7	0.694	96.3
55.5	51.5	20266	33.69	3.7	52.3	0.694	97.2
60.5	56.5	20267	36.64	3.7	52.0	0.694	97.3
65.5	61.5	20268	39.58	3.4	50.1	0.740	96.2
70.5	66.5	20269	42.55	3.5	50.8	0.724	97.0
75.5	71.5	20270	45.46	3.6	51.6	0.709	96.6
85.5	81.5	20272	51.32	2.7	44.4	0.875	93.7
90.5	86.5	20273	54.37	3.7	52.7	0.694	96.0
95.5	91.5	20274	57.62	3.8	53.0	0.680	95.9
100.5	96.5	20275	61.56	4.7	58.5	0.573	96.1
105.5	101.5	20276	66.00	5.3	61.4	0.518	96.2
110.5	106.5	20277	70.87	6.2	65.4	0.452	98.2
115.5	111.5	20278	76.16	5.5	62.4	0.502	97.0
120.5	116.5	20279	82.09	5.8	63.9	0.480	97.3
125.5	121.5	20280	88.91	6.2	65.5	0.452	97.5

## BENTHIC III 25 GC (continued)

depth	adjusted	sample	age	salt	water	dry bulk	sum of
(cm)	depth	ID	(kyr)	%	content	density	oxides
	(cm)				%	(g/cm <sup>3</sup> )	
130.5	126.5	20281	96.15	5.6	62.7	0.494	96.6
135.5	131.5	20282	105.00	6.8	67.6	0.416	98.7
140.5	136.5	20283	113.10	5.5	62.6	0.502	97.8
145.5	141.5	20284	119.90	4.6	57.9	0.584	97.6
150.5	146.5	20285	126.10	4.5	57.3	0.594	97.4
155.5	151.5	20286	131.20	4.6	57.8	0.584	98.2
160.5	156.5	20287	135.70	4.6	58.1	0.584	97.7
165.5	161.5	20288	140.00	4.9	59.3	0.554	98.5
170.5	166.5	20289	143.90	4.3	56.2	0.617	97.0
175.5	171.5	20290	147.60	4.4	57.0	0.605	98.0
180.5	176.5	20291	151.50	4.3	56.3	0.617	96.8
185.5	181.5	20292	155.70	4.4	56.9	0.605	96.3
190.5	186.5	20293	159.90	4.4	57.0	0.605	97.0
195.5	191.5	20294	164.60	4.3	56.3	0.617	96.2
200.5	196.5	20295	170.10	4.3	55.9	0.617	95.0
205.5	201.5	20296	176.30	4.7	58.6	0.573	94.2
210.5	206.5	20297	183.50	6.3	65.8	0.440	94.1
215.5	211.5	20298	191.80	7.5	69.8	0.380	94.6
220.5	216.5	20299	201.20	5.0	60.1	0.545	96.7
225.5	221.5	20300	210.90	4.1	54.8	0.641	94.7
230.5	226.5	20301	--	4.6	58.2	0.584	96.3
235.5	231.5	20302	--	5.2	61.0	0.527	96.0
240.5	236.5	20303	--	4.5	57.5	0.594	95.0
245.5	241.5	20304	--	3.7	52.0	0.694	95.8
250.5	246.5	20305	--	4.0	54.0	0.653	96.5

BENTHIC III 25 GC (continued)

depth (cm)	adjusted depth (cm)	sample ID	age (kyr)	salt %	water content %	dry bulk density (g/cm <sup>3</sup> )	sum of oxides
255.5	251.5	20306	--	3.8	53.3	0.680	96.1
260.5	256.5	20307	--	3.7	52.4	0.694	95.8
265.5	261.5	20308	--	4.1	54.8	0.641	96.3
270.5	266.5	20309	--	4.6	57.8	0.584	96.1
275.5	271.5	20310	--	6.2	65.4	0.452	96.0
280.5	276.5	20311	--	8.1	71.5	0.354	97.2
284.5	280.5	20312	--	4.1	54.8	0.641	95.8



## BENTHIC III 25 GC

depth	Al	Si	P	Ti	Mn	Fe	Sr	Ba	opal	CaCO <sub>3</sub>
(cm)										
0.5	0.5430	7.9827	0.0476	0.0375	0.1959	0.4540	0.1176	0.2207	14.6	73.8
5.5	0.4798	8.3336	0.0448	0.0370	0.1897	0.4223	0.1198	0.2006	16.0	74.9
10.5	0.3328	6.9003	0.0359	0.0308	0.1481	0.3490	0.1265	0.1492	13.9	78.8
15.5	0.2819	4.4941	0.0309	0.0294	0.4899	0.3011	0.1268	0.1294	8.4	82.3
20.5	0.2687	4.1968	0.0301	0.0294	0.3815	0.3026	0.1260	0.1184	7.8	84.4
25.5	0.2687	3.5330	0.0312	0.0302	0.0418	0.3076	0.1288	0.1200	6.1	86.6
30.5	0.0916	0.8294	0.0178	0.0273	0.0358	0.2254	0.1075	0.0522	1.2	92.7
35.5	0.3033	3.2102	0.0291	0.0308	0.0858	0.3239	0.1275	0.1284	5.0	86.2
40.5	0.3080	3.0744	0.0295	0.0319	0.0622	0.3238	0.1279	0.1302	4.6	86.5
45.5	0.3117	2.9477	0.0292	0.0290	0.0648	0.3233	0.1300	0.1071	4.2	87.2
50.5	0.3077	3.1448	0.0503	0.0291	0.0705	0.3244	0.1282	0.1019	4.8	87.5
55.5	0.2393	2.9625	0.0276	0.0299	0.0637	0.2850	0.1293	0.0869	5.0	89.1
60.5	0.2214	2.6375	0.0271	0.0265	0.0666	0.2722	0.1300	0.0701	4.4	90.1
65.5	0.2453	2.6985	0.0280	0.0276	0.0778	0.2866	0.1317	0.0837	4.3	88.7
70.5	0.2281	2.6286	0.0261	0.0275	0.0705	0.2811	0.1291	0.0705	4.3	89.7
75.5	0.2201	2.7881	0.0251	0.0288	0.0731	0.2832	0.1325	0.0796	4.8	89.0
85.5	0.1643	2.2038	0.0273	0.0264	0.0646	0.2693	0.1299	0.0641	3.8	87.0
90.5	0.2305	2.8145	0.0288	0.0298	0.0775	0.3024	0.1308	0.0826	4.7	88.2
95.5	0.3188	3.4231	0.0328	0.0321	0.0936	0.3597	0.1280	0.1126	5.4	86.3
100.5	0.5621	5.8162	0.0427	0.0412	0.1268	0.4985	0.1202	0.1941	8.9	79.9
105.5	0.9585	8.7591	0.0546	0.0512	0.3007	0.7196	0.1131	0.3065	12.4	71.6
110.5	1.1675	10.4638	0.0577	0.0590	0.1458	0.8209	0.1054	0.3906	14.5	68.9
115.5	0.9488	9.0062	0.0504	0.0504	0.1130	0.7064	0.1109	0.3206	13.1	72.1
120.5	1.0113	10.2026	0.0500	0.0520	0.1657	0.7353	0.1054	0.3612	15.5	69.2
125.5	1.1282	11.5168	0.0524	0.0557	0.1260	0.7860	0.1024	0.3888	17.6	66.1
130.5	0.9297	10.1141	0.0508	0.0513	0.1546	0.6983	0.1109	0.3645	16.0	69.3
135.5	1.1235	13.4130	0.0561	0.0550	0.2227	0.7626	0.1041	0.4465	22.4	63.2
140.5	0.7442	11.6753	0.0467	0.0420	0.3401	0.5476	0.1101	0.3238	21.8	67.7

## BENTHIC III 25 GC (continued)

depth (cm)	Al	Si	P	Ti	Mn	Fe	Sr	Ba	opal	CaCO <sub>3</sub>
145.5	0.3987	8.2956	0.0348	0.0333	0.3008	0.3539	0.1203	0.1485	16.8	76.7
150.5	0.3100	8.0914	0.0312	0.0326	0.2547	0.3200	0.1177	0.1344	17.2	77.4
155.5	0.4183	7.5049	0.0363	0.0356	0.2028	0.3768	0.1169	0.1726	14.6	79.0
160.5	0.3195	6.8093	0.0321	0.0303	0.1391	0.3208	0.1182	0.1252	13.8	80.6
165.5	0.3360	7.7354	0.0343	0.0303	0.1459	0.3293	0.1179	0.1278	16.0	79.2
170.5	0.3458	6.4001	0.0361	0.0299	0.1366	0.3457	0.1215	0.1241	12.6	80.7
175.5	0.3778	6.6309	0.0379	0.0334	0.1508	0.3720	0.1240	0.1369	12.9	81.1
180.5	0.3726	5.6311	0.0351	0.0338	0.1034	0.3779	0.1255	0.1420	10.4	82.0
185.5	0.3826	5.8515	0.0337	0.0343	0.0816	0.3946	0.1245	0.1481	10.8	81.1
190.5	0.3829	6.4879	0.0345	0.0333	0.0743	0.3904	0.1256	0.1403	12.4	80.4
195.5	0.4061	5.4384	0.0369	0.0340	0.0765	0.4162	0.1302	0.1518	9.6	81.8
200.5	0.4581	4.8690	0.0390	0.0369	0.1153	0.4508	0.1278	0.1644	7.6	81.4
205.5	0.6345	6.3362	0.0451	0.0398	0.1242	0.5796	0.1264	0.2102	9.5	76.7
210.5	1.0813	10.7280	0.0557	0.0578	0.0877	0.8871	0.1130	0.4094	16.0	64.9
215.5	1.4486	12.9831	0.0654	0.0692	0.0789	1.0546	0.1053	0.5470	18.0	58.8
220.5	0.9064	8.9489	0.0530	0.0477	0.0902	0.6689	0.1228	0.3228	13.3	72.3
225.5	0.5830	6.2440	0.0413	0.0381	0.0997	0.4838	0.1281	0.2180	9.8	77.7
230.5	0.6404	7.0250	0.0431	0.0394	0.1973	0.4961	0.1271	0.2399	11.1	77.1
235.5	0.6770	7.2446	0.0442	0.0412	0.0976	0.5214	0.1276	0.2597	11.3	76.4
240.5	0.5631	5.7904	0.0432	0.0347	0.0766	0.4662	0.1287	0.1952	8.8	79.0
245.5	0.3808	4.5068	0.0408	0.0316	0.1858	0.3623	0.1328	0.1059	7.5	83.4
250.5	0.4102	5.1265	0.0396	0.0341	0.1715	0.3881	0.1307	0.1524	8.7	82.6
255.5	0.3085	4.6776	0.0344	0.0301	0.0857	0.3428	0.1336	0.0980	8.6	83.9
260.5	0.2532	3.8780	0.0309	0.0302	0.0805	0.3213	0.1316	0.0903	7.2	85.6
265.5	0.2917	4.1647	0.0334	0.0299	0.0897	0.3459	0.1284	0.0863	7.5	85.2
270.5	0.4237	5.8581	0.0394	0.0358	0.1347	0.4151	0.1247	0.1316	10.5	80.6
275.5	0.7858	9.7880	0.0546	0.0461	0.3013	0.6058	0.1148	0.2644	16.6	69.8
280.5	1.3695	14.4128	0.0709	0.0640	0.1442	0.9362	0.1040	0.4472	22.4	58.5
284.5	0.4197	7.4004	0.0395	0.0352	0.1980	0.3850	0.1224	0.1792	14.3	76.8

W8402 A 14 GC

depth (cm)	adjusted depth (cm)	sample ID	age (kyr)	salt %	water content %	dry bulk density (g/cm <sup>3</sup> )	sum of oxides
0.5	0.5	23766	0.30	5.6	62.7	0.494	97.2
3.5	3.5	23767	2.07	5.0	60.0	0.545	98.2
6.5	6.5	23768	3.85	4.6	57.7	0.584	97.5
9.5	9.5	23769	5.62	4.9	59.4	0.554	98.1
12.5	12.5	23770	7.40	4.6	57.8	0.584	98.7
15.5	15.5	23771	9.19	4.5	57.2	0.594	98.6
18.5	18.5	21772	10.95	4.2	55.9	0.628	97.8
21.5	21.5	23773	12.72	4.1	55.2	0.641	97.2
24.5	24.5	23774	14.50	4.1	55.0	0.641	98.0
27.5	27.5	23775	16.26	4.1	54.9	0.641	98.6
30.5	30.5	23776	18.05	4.1	55.2	0.641	97.9
33.5	33.5	23777	19.83	4.0	54.5	0.653	97.6
36.5	36.5	23778	21.55	3.8	52.9	0.680	97.0
39.5	39.5	23779	23.29	3.8	52.8	0.680	97.3
45.5	45.5	23780	26.93	3.6	51.3	0.709	97.3
51.5	51.5	23781	30.46	3.6	51.5	0.709	96.9
57.5	57.5	23782	33.73	3.3	49.2	0.757	96.4
63.5	63.5	23783	36.83	3.4	50.4	0.740	96.7
69.5	69.5	23784	39.88	3.3	49.5	0.757	95.6
75.5	75.5	23785	42.92	3.1	47.7	0.793	96.7
81.5	81.5	23786	45.84	3.4	49.8	0.740	95.5
87.5	87.5	23787	48.70	3.3	49.6	0.757	95.9
90.5	90.5	23788	50.13	3.4	49.9	0.740	96.1
93.5	93.5	23789	51.62	3.2	48.8	0.775	95.1
96.5	96.5	23790	53.10	3.3	49.7	0.757	95.7
99.5	99.5	23791	54.53	3.3	49.2	0.757	95.7

## W8402 A 14 GC (continued)

depth (cm)	adjusted depth (cm)	sample ID	age (kyr)	salt %	water content %	dry bulk density (g/cm <sup>3</sup> )	sum of oxides
102.5	102.5	23792	55.98	3.3	49.7	0.757	95.6
105.5	105.5	23793	57.56	3.4	50.3	0.740	95.8
108.5	108.5	23794	59.31	3.6	51.9	0.709	96.7
111.5	111.5	23795	61.17	4.0	54.1	0.653	96.0
114.5	114.5	23796	63.10	4.1	54.8	0.641	96.0
117.5	117.5	23797	65.13	4.4	56.9	0.605	95.4
120.5	120.5	23798	67.31	4.9	59.5	0.554	97.7
123.5	123.5	23799	69.52	4.6	57.7	0.584	95.9
126.5	126.5	23800	71.77	4.1	54.9	0.641	95.5
129.5	129.5	23801	74.13	4.3	56.3	0.617	95.8
131.5	131.5	23802	75.74	4.3	56.2	0.617	95.9
134.5	134.5	23803	78.24	4.2	55.7	0.628	96.0
138.5	138.5	23804	81.80	4.3	56.0	0.617	96.7
141.5	141.5	23805	84.71	4.5	57.5	0.594	95.8
144.5	144.5	23806	87.96	4.3	56.1	0.617	96.5
147.5	147.5	23807	90.81	4.5	57.1	0.594	96.2
150.5	150.5	23808	94.16	4.1	55.3	0.641	96.7
153.5	153.5	23809	97.90	4.3	56.2	0.617	96.5
156.5	156.5	23810	101.90	4.7	58.3	0.573	96.7
159.5	159.5	23811	106.10	4.5	57.5	0.594	96.7
162.5	162.5	23812	110.00	5.0	60.2	0.545	97.3
165.5	165.5	23813	113.40	4.8	59.0	0.564	98.3
168.5	168.5	23814	116.60	4.4	56.6	0.605	96.3
171.5	171.5	23815	119.80	4.0	54.0	0.653	96.3
174.5	174.5	23816	122.90	3.9	53.8	0.666	95.7
177.5	177.5	23817	125.70	3.9	54.0	0.666	96.0

## W8402 A 14 GC (continued)

depth (cm)	adjusted depth (cm)	sample ID	age (kyr)	salt %	water content %	dry bulk density (g/cm <sup>3</sup> )	sum of oxides
180.5	180.5	23818	128.40	4.3	55.9	0.617	96.2
183.5	183.5	23819	130.70	4.2	55.8	0.628	97.2
187.5	187.5	23820	133.60	3.9	54.0	0.666	98.9
189.5	189.5	23821	135.10	3.9	53.7	0.666	98.6
195.5	195.5	23822	139.30	4.0	54.4	0.653	96.9
201.5	201.5	23823	143.20	4.3	55.9	0.617	97.1
207.5	207.5	23824	146.60	4.2	55.8	0.628	96.6
213.5	213.5	23825	150.30	3.9	53.9	0.666	95.6
219.5	219.5	23826	154.20	4.2	55.7	0.628	96.1
225.5	225.5	23827	158.00	4.2	55.4	0.628	95.5
231.5	231.5	23828	162.00	4.3	56.5	0.617	95.8
237.5	237.5	23829	166.30	3.5	51.2	0.724	94.7
243.5	243.5	23830	171.20	3.8	53.0	0.680	94.1
249.5	249.5	23831	176.40	4.2	55.7	0.628	94.1
254.5	254.5	23832	181.10	6.1	65.0	0.459	93.9
261.5	261.5	23833	188.30	6.8	67.6	0.416	95.8
267.5	267.5	23834	195.00	7.1	68.6	0.400	95.6
273.5	273.5	23835	202.20	4.4	56.9	0.605	94.8
279.5	279.5	23836	209.30	3.9	53.4	0.666	94.2
283.5	283.5	23837	213.80	3.6	51.9	0.709	94.4
291.5	291.5	23838	222.60	4.0	54.3	0.653	94.2
297.5	297.5	23839	228.90	4.3	56.2	0.617	95.0
303.5	303.5	23840	234.60	5.4	62.1	0.510	96.3
309.5	309.5	23841	240.20	3.5	51.2	0.724	94.8
315.5	315.5	23842	246.40	3.6	51.4	0.709	94.1

## W8402 A 14 GC

depth	Al	Si	P	Ti	Mn	Fe	Sr	Ba	opal	CaCO <sub>3</sub>	CaCO <sub>3</sub> (LECO)	C-org (LECO)
(cm)												
0.5	0.4898	7.9940	0.0416	0.0348	0.1812	0.4065	0.1273	0.1995	15.1	76.2	79.82	0.304
3.5	0.4791	8.1044	0.0401	0.0324	0.1616	0.3793	0.1216	0.1847	15.5	77.1	81.98	0.252
6.5	0.4296	7.8760	0.0373	0.0327	0.1515	0.3621	0.1241	0.1796	15.4	77.5	81.39	0.231
9.5	0.3645	7.9592	0.0345	0.0302	0.1433	0.3292	0.1221	0.1554	16.3	77.9	83.05	0.226
12.5	0.3130	7.4818	0.0321	0.0320	0.2336	0.3013	0.1223	0.1525	15.6	79.7	84.13	0.182
15.5	0.3070	7.0678	0.0310	0.0291	0.1428	0.2990	0.1235	0.1339	14.5	80.8	88.09	0.182
18.5	0.3115	5.4732	0.0300	0.0299	0.2638	0.2983	0.1257	0.1353	10.5	83.4	91.00	0.152
21.5	0.3093	5.0862	0.0305	0.0285	0.5945	0.2783	0.1249	0.1236	9.6	83.0	89.08	0.152
24.5	0.2802	4.9583	0.0284	0.0284	0.2530	0.2814	0.1255	0.1090	9.6	84.7	92.63	0.205
27.5	0.3101	5.3687	0.0317	0.0290	0.2744	0.2970	0.1257	0.1244	10.4	84.2	91.41	0.180
30.5	0.3056	4.9005	0.0310	0.0301	0.0570	0.3101	0.1264	0.1205	9.2	85.0	91.81	0.345
33.5	0.3169	3.7426	0.0306	0.0293	0.0665	0.3075	0.1279	0.1165	6.2	87.2	92.27	0.289
36.5	0.3167	3.6875	0.0301	0.0278	0.0617	0.3072	0.1266	0.1152	6.0	86.7	91.92	0.246
39.5	0.3101	3.5547	0.0298	0.0299	0.0615	0.3024	0.1276	0.1140	5.7	87.4	94.94	0.214
45.5	0.3261	3.5597	0.0298	0.0312	0.0730	0.3081	0.1276	0.1184	5.6	87.3	90.66	0.162
51.5	0.3061	3.4694	0.0292	0.0292	0.0707	0.3087	0.1292	0.0973	5.6	87.2	92.28	0.135
57.5	0.2285	2.9053	0.0260	0.0275	0.0658	0.2736	0.1264	0.0782	5.0	88.4	95.60	0.110
63.5	0.2168	3.0042	0.0280	0.0269	0.0705	0.2618	0.1273	0.0729	5.4	88.4	92.13	0.101
69.5	0.2375	2.8401	0.0262	0.0281	0.0777	0.2666	0.1297	0.0729	4.7	87.7	93.20	0.101
75.5	0.2375	2.5694	0.0260	0.0262	0.0879	0.2750	0.1313	0.0660	4.0	89.4	93.70	0.084
81.5	0.2296	2.9738	0.0248	0.0274	0.0911	0.2679	0.1288	0.0778	5.2	87.2	93.27	0.111
87.5	0.2375	3.1881	0.0255	0.0270	0.0847	0.2645	0.1272	0.0753	5.5	87.1	93.36	0.113
90.5	0.2703	3.2421	0.0288	0.0277	0.0743	0.2832	0.1292	0.0821	5.4	87.2	92.99	0.130
93.5	0.2238	2.0875	0.0253	0.0285	0.0810	0.2587	0.1280	0.0664	3.0	88.9	95.19	0.092
96.5	0.2384	2.4550	0.0271	0.0268	0.0799	0.2715	0.1287	0.0677	3.7	88.5	94.14	0.108
99.5	0.2524	2.6549	0.0298	0.0271	0.0759	0.2805	0.1287	0.0703	4.1	88.0	92.89	0.154
102.5	0.2819	3.2743	0.0298	0.0276	0.0883	0.2985	0.1266	0.0833	5.6	86.5	91.15	0.142

## W8402 A 14 GC (continued)

depth (cm)	Al	Si	P	Ti	Mn	Fe	Sr	Ba	opal	CaCO <sub>3</sub>	CaCO <sub>3</sub> (LECO)	C-org (LECO)
105.5	0.3758	3.5453	0.0337	0.0321	0.1008	0.3458	0.1261	0.1062	5.1	85.5	90.61	0.187
108.5	0.4748	4.5300	0.0356	0.0360	0.1068	0.4005	0.1257	0.1471	6.6	83.8	88.49	0.202
111.5	0.6884	6.3499	0.0436	0.0401	0.1406	0.5136	0.1216	0.1909	9.0	78.1	83.02	0.158
114.5	0.7126	6.5674	0.0445	0.0415	0.1622	0.5371	0.1221	0.2226	9.3	77.5	82.10	0.107
117.5	0.9407	7.9426	0.0502	0.0463	0.1839	0.6452	0.1152	0.2799	10.4	72.8	79.14	0.176
120.5	1.1892	9.5179	0.0578	0.0533	0.2393	0.7489	0.1115	0.3534	11.9	70.4	74.96	0.130
123.5	1.0017	8.2033	0.0490	0.0467	0.1700	0.6552	0.1125	0.2972	10.5	72.5	77.65	0.100
126.5	0.8339	7.0668	0.0434	0.0448	0.1367	0.5859	0.1180	0.2601	9.3	75.5	78.98	0.112
129.5	0.8553	7.3749	0.0446	0.0454	0.1014	0.5844	0.1151	0.2565	9.9	74.8	80.64	0.121
131.5	0.9149	7.8159	0.0463	0.0448	0.1086	0.6125	0.1141	0.2615	10.3	73.9	78.10	0.125
134.5	0.8471	7.8532	0.0443	0.0446	0.1364	0.5847	0.1140	0.2641	11.2	74.1	80.28	0.086
138.5	0.9758	9.0427	0.0450	0.0465	0.1697	0.6353	0.1101	0.3054	12.8	71.7	78.40	0.094
141.5	1.0621	10.2575	0.0468	0.0487	0.1484	0.6940	0.1080	0.3383	15.0	67.7	71.73	0.105
144.5	0.9025	8.8478	0.0450	0.0454	0.1223	0.6155	0.1130	0.2939	13.1	72.3	77.78	0.098
147.5	0.8693	8.7862	0.0442	0.0429	0.0804	0.5947	0.1144	0.2877	13.3	72.3	73.93	0.156
150.5	0.7964	8.1845	0.0429	0.0441	0.1402	0.5565	0.1156	0.2819	12.4	74.4	81.18	0.152
153.5	0.9183	9.2324	0.0460	0.0468	0.1724	0.6149	0.1142	0.3158	13.9	71.2	80.29	0.180
156.5	1.0857	10.9407	0.0528	0.0510	0.2135	0.6903	0.1107	0.3722	16.5	66.9	76.68	0.122
159.5	0.9808	10.5782	0.0492	0.0467	0.2186	0.6278	0.1102	0.3255	16.4	68.2	75.08	0.125
162.5	0.9865	12.3395	0.0487	0.0448	0.2696	0.6210	0.1075	0.3420	21.0	64.8	71.92	0.116
165.5	0.7517	10.7451	0.0424	0.0386	0.3929	0.4793	0.1145	0.2811	19.3	70.1	76.50	0.167
168.5	0.6541	8.6973	0.0403	0.0366	0.3766	0.4300	0.1154	0.2322	15.2	73.0	81.62	0.161
171.5	0.5603	7.1245	0.0367	0.0332	0.4839	0.3672	0.1195	0.1868	12.2	76.9	83.66	0.166
174.5	0.4733	6.9315	0.0335	0.0329	0.4571	0.3250	0.1208	0.1514	12.5	77.1	85.14	0.155
177.5	0.4478	7.2960	0.0327	0.0328	0.3025	0.3220	0.1202	0.1556	13.8	77.0	84.63	0.119
180.5	0.3831	8.0398	0.0306	0.0308	0.2642	0.2979	0.1183	0.1479	16.3	75.8	83.21	0.155
183.5	0.3866	8.5969	0.0301	0.0287	0.2336	0.2787	0.1159	0.1254	17.6	75.8	84.04	0.171

## W8402 A 14 GC (continued)

depth	Al	Si	P	Ti	Mn	Fe	Sr	Ba	opal	CaCO <sub>3</sub>	CaCO <sub>3</sub> (LECO)	C-org (LECO)
(cm)												
187.5	0.3920	8.8535	0.0305	0.0294	0.1956	0.2753	0.1171	0.1249	18.2	77.0	83.67	0.172
189.5	0.3983	7.9297	0.0300	0.0286	0.0950	0.2942	0.1148	0.1230	15.8	78.7	83.09	0.158
195.5	0.3788	5.9764	0.0317	0.0298	0.1627	0.3399	0.1181	0.1187	11.1	81.0	86.50	0.165
201.5	0.3582	7.8728	0.0322	0.0281	0.1737	0.2898	0.1161	0.1242	16.1	77.3	84.48	0.127
207.5	0.3516	8.0439	0.0319	0.0268	0.0995	0.3006	0.1155	0.1118	16.6	76.6	84.86	0.172
213.5	0.4289	5.5660	0.0352	0.0310	0.1421	0.3474	0.1227	0.1115	9.6	80.6	79.79	0.146
219.5	0.3805	5.4602	0.0343	0.0311	0.0919	0.3552	0.1233	0.1161	9.9	81.6	85.94	0.173
225.5	0.3963	6.1220	0.0342	0.0338	0.0860	0.3645	0.1236	0.1422	11.3	79.6	85.74	0.184
231.5	0.4017	6.4269	0.0337	0.0335	0.0816	0.3739	0.1250	0.1405	12.1	79.1	89.58	0.243
237.5	0.3793	4.4715	0.0360	0.0345	0.0953	0.3828	0.1314	0.1460	7.4	82.5	89.04	0.131
243.5	0.4678	4.9409	0.0388	0.0369	0.3123	0.4312	0.1273	0.1600	7.7	80.2	84.85	0.133
249.5	0.5957	6.4173	0.0425	0.0426	0.4678	0.5082	0.1245	0.2249	10.0	76.1	82.70	0.203
254.5	1.0585	10.9258	0.0545	0.0567	0.0861	0.8369	0.1149	0.3760	16.7	64.1	73.76	0.227
261.5	1.4562	13.6498	0.0650	0.0678	0.0773	1.0204	0.1065	0.4862	19.5	58.3	64.02	0.363
267.5	1.4694	14.0378	0.0630	0.0678	0.0773	0.9990	0.1070	0.4906	20.4	57.4	63.63	0.473
273.5	0.8179	7.8123	0.0467	0.0460	0.1006	0.5951	0.1265	0.2940	11.4	73.2	81.08	0.200
279.5	0.5832	6.1198	0.0395	0.0362	0.0993	0.4681	0.1288	0.2068	9.5	77.5	84.45	0.117
283.5	0.5048	4.9851	0.0378	0.0333	0.1189	0.4223	0.1327	0.1712	7.4	80.5	89.73	0.139
291.5	0.5884	5.8936	0.0434	0.0355	0.4643	0.4424	0.1287	0.1947	8.8	77.4	83.99	0.119
297.5	0.5829	5.9494	0.0392	0.0347	0.0951	0.4451	0.1289	0.1909	9.0	78.7	86.61	0.150
303.5	0.6946	8.6135	0.0419	0.0378	0.0798	0.4872	0.1251	0.2434	14.5	73.5	78.57	0.187
309.5	0.4149	4.1986	0.0368	0.0309	0.0966	0.3624	0.1320	0.1273	6.3	83.0	91.33	0.112
315.5	0.3633	4.1958	0.0356	0.0325	0.2358	0.3308	0.1318	0.1083	6.9	82.4	91.34	0.108
321.5	0.3299	4.2367	0.0351	0.0300	0.1250	0.3272	0.1323	0.1046	7.3	83.2	93.03	0.161
327.5	0.2642	4.1047	0.0315	0.0288	0.0889	0.3097	0.1325	0.0953	7.7	84.1	93.98	0.144
332.5	0.2366	3.7049	0.0302	0.0299	0.0958	0.2983	0.1294	0.0818	6.9	85.4	93.23	0.118



## APPENDIX 2

## BENTHIC III 28 BC

Depth (cm)	Sample I.D.	Na	Mg	Al	Si	P	S	K	Ca	Ti	Cr
1.0	24503	0.2015	2.0707	7.3264	30.9588	0.1608	0.2261	2.3760	0.7196	0.3918	0.0063
3.0	24504	0.2940	2.0310	7.3342	31.0361	0.1611	0.2082	2.4056	0.7138	0.4028	0.0062
5.0	24505	0.0000	2.0419	7.2646	30.7362	0.1532	0.2224	2.4090	0.7128	0.4000	0.0071
7.0	24506	0.3714	1.9981	7.2931	30.7648	0.1506	0.1811	2.4168	0.6925	0.4041	0.0071
9.0	24507	0.3147	2.0395	7.3945	31.0189	0.1648	0.1757	2.4899	0.6764	0.4200	0.0074
11.0	24508	0.3056	2.0334	7.3665	30.7217	0.1516	0.1702	2.5111	0.6777	0.4176	0.0078
13.0	24509	0.2203	2.0534	7.4514	30.8730	0.1495	0.1809	2.5313	0.6882	0.4248	0.0073
15.0	24510	0.1765	2.0513	7.3445	30.2764	0.1580	0.1910	2.5082	0.7093	0.4153	0.0077
17.0	24511	0.3274	2.0880	7.4897	30.5777	0.1921	0.1840	2.5240	0.7443	0.4178	0.0083
19.0	25065	0.1437	2.0475	7.3854	30.3005	0.1869	0.1992	2.4979	0.7372	0.4096	0.0075
23.0	25067	0.2680	2.0951	7.4659	30.1785	0.2056	0.1927	2.4726	0.7531	0.4025	0.0084
25.0	25068	0.3013	2.0684	7.4776	30.2909	0.2111	0.1922	2.4855	0.7621	0.4054	0.0072
27.0	25069	0.1691	2.2128	7.5132	30.1299	0.2253	0.1962	2.5044	0.7931	0.4059	0.0067
29.0	25070	0.2753	2.1826	7.5956	30.1183	0.2610	0.1945	2.4965	0.8269	0.4073	0.0078
31.0	25071	0.2227	2.1066	7.5546	30.2744	0.2158	0.2120	2.5189	0.7518	0.4081	0.0064
33.0	25072	0.2543	2.1221	7.5933	30.3131	0.2525	0.1871	2.5285	0.8316	0.4142	0.0065
35.0	25073	0.2582	2.1971	7.7118	30.0795	0.2556	0.1825	2.5298	0.8413	0.4153	0.0069
37.0	25074	0.1382	2.2415	7.5703	29.5946	0.2899	0.2339	2.4734	0.8874	0.4079	0.0066

# BENTHIC III 28 BC

Depth (cm)	Mn	Co	Fe	Ni	Cu	Zn	Rb	Sr	Ba	Opal	CaCO <sub>3</sub>	Salt %	H <sub>2</sub> O %	Mn-ex	Dry Density (g/cm <sup>3</sup> )	Sum of Oxides
1.0	0.2881	4.8601	0.0050	0.0149	0.0399	0.0168	0.0116	0.0289	0.5410	15.1	0.0	11.7	79.5	0.2561	0.2560	96.7
3.0	0.2798	0.0168	4.9595	0.0053	0.0155	0.0405	0.0117	0.0295	0.5611	15.3	0.0	10.6	77.6	0.2478	0.2750	97.1
5.0	0.2578	4.9840	0.0052	0.0146	0.0398	0.0166	0.0118	0.0289	0.5595	15.1	0.0	8.4	73.0	0.2258	0.3210	96.0
7.0	0.2227	5.0783	0.0050	0.0135	0.0383	0.0166	0.0119	0.0282	0.5329	14.9	0.0	9.8	76.2	0.1907	0.2890	96.5
9.0	0.1556	5.2366	0.0045	0.0115	0.0360	0.0167	0.0119	0.0272	0.4924	14.8	0.0	9.2	74.8	0.1236	0.3030	97.4
11.0	0.1147	5.2955	0.0045	0.0109	0.0350	0.0174	0.0121	0.0267	0.4601	14.3	0.0	8.1	72.1	0.0827	0.3300	96.7
13.0	0.1151	5.2763	0.0045	0.0109	0.0355	0.0173	0.0123	0.0276	0.4837	13.9	0.0	7.3	69.7	0.0831	0.3540	97.2
15.0	0.0868	5.2518	0.0043	0.0102	0.0347	0.0172	0.0123	0.0280	0.4969	13.3	0.0	7.2	69.3	0.0548	0.3580	95.6
17.0	0.0847	5.3644	0.0043	0.0097	0.0356	0.0169	0.0119	0.0289	0.5324	12.8	0.1	7.9	71.5	0.0527	0.3360	97.1
19.0	0.0735	5.2152	0.0039	0.0091	0.0349	0.0164	0.0119	0.0285	0.5042	13.0	0.1	7.0	68.7	0.0415	0.3640	95.7
21.0	0.0481	5.2750	0.0037	0.0089	0.0370	0.0167	0.0118	0.0307	0.5962	12.1	0.1	7.8	71.4	0.0161	0.3370	96.0
23.0	0.0479	5.2463	0.0037	0.0083	0.0353	0.0166	0.0121	0.0299	0.5666	12.3	0.2	8.0	71.8	0.0159	0.3330	96.3
27.0	0.0458	5.6979	0.0042	0.0094	0.0410	0.0173	0.0117	0.0315	0.6330	11.5	0.2	6.7	67.9	0.0138	0.3720	96.9
29.0	0.0483	5.4632	0.0040	0.0093	0.0479	0.0174	0.0117	0.0338	0.6755	10.7	0.3	6.9	68.4	0.0163	0.3670	97.0
31.0	0.0517	5.2443	0.0035	0.0083	0.0406	0.0167	0.0121	0.0313	0.6184	11.5	0.1	6.9	68.3	0.0197	0.3680	96.4
33.0	0.0574	5.3064	0.0036	0.0087	0.0414	0.0169	0.0121	0.0310	0.6084	11.3	0.3	6.8	68.0	0.0254	0.3710	97.0
35.0	0.0461	5.3814	0.0040	0.0094	0.0476	0.0177	0.0120	0.0325	0.6571	9.7	0.4	7.0	68.9	0.0161	0.3620	97.1
37.0	0.0475	5.2930	0.0036	0.0090	0.0525	0.0185	0.0114	0.0345	0.7143	9.7	0.5	5.9	64.7	0.0155	0.4040	95.7

## BENTHIC III 31 BC

Depth (cm)	Sample I.D.	Na	Mg	Al	Si	P	S	K	Ca	Ti	Cr
1.0	23512	0.7986	2.0787	7.5185	31.5701	0.1961	0.2007	2.3870	0.7853	0.4013	0.0063
3.0	24513	0.4259	2.0510	7.4036	31.1625	0.2088	0.2155	2.3660	0.8220	0.3960	0.0058
5.0	24514	0.5459	2.2245	7.6176	30.7348	0.2764	0.2540	2.4878	0.9848	0.4086	0.0056
7.0	24515	0.8282	2.5525	7.9538	28.4208	0.3900	0.3556	2.5980	1.1521	0.4052	0.0056
9.0	24516	0.6513	3.1207	8.1324	28.4153	0.4565	0.5045	2.2743	1.4104	0.3897	0.0048
11.0	24517	0.7372	3.3787	8.2768	28.9973	0.4376	0.5215	2.1464	1.5513	0.3857	0.0047
13.0	24518	0.8839	3.2033	8.2151	28.8868	0.4701	0.5059	2.1799	1.4541	0.3807	0.0054
15.0	24519	0.5003	3.1515	8.1156	29.1054	0.4582	0.5068	2.2114	1.4446	0.3833	0.0048
17.0	24520	0.7238	3.4919	8.4218	29.1308	0.4883	0.5714	2.0920	1.6299	0.3672	0.0035
19.0	24521	0.9948	3.5768	8.4949	29.3429	0.5498	0.5693	2.0904	1.6808	0.3706	0.0036
21.0	24522	0.5861	3.3396	8.0311	28.1816	0.4953	0.4540	2.0749	1.6571	0.3667	0.0047
23.0	24523	0.7210	3.3442	8.1385	28.4954	0.5232	0.4834	2.1005	1.6506	0.3689	0.0045

# BENTHIC III 31 BC

Depth (cm)	Rn	Fe	Co	Ni	Cu	Zn	Rb	Sr	Ba	Opal	CaCO <sub>3</sub>	Salt %	H <sub>2</sub> O %	Mn-ex	Dry Density (g/cm <sup>3</sup> )	Sum of Oxides
1.0	0.3870	4.9666	0.0059	0.0181	0.0442	0.0169	0.0121	0.0308	0.5716	15.0	0.2	12.6	80.8	0.3550	0.2430	99.8
3.0	0.3987	4.9421	0.0060	0.0182	0.0442	0.0169	0.0117	0.0308	0.5723	15.0	0.3	11.1	78.6	0.3667	0.2650	98.2
5.0	1.6271	4.8250	0.0175	0.0399	0.1000	0.0196	0.0098	0.0376	0.8573	12.2	0.7	9.2	74.9	1.5951	0.3020	101.0
7.0	1.5039	5.0703	0.0179	0.0398	0.1141	0.0219	0.0091	0.0506	1.2670	3.4	1.1	5.8	64.5	1.4719	0.4060	99.0
9.0	1.4116	5.3765	0.0165	0.0350	0.1092	0.0247	0.0081	0.0630	1.7365	1.9	1.8	7.7	70.9	1.3796	0.3420	101.3
11.0	1.1646	5.6590	0.0137	0.0274	0.0964	0.0260	0.0085	0.0666	1.9124	2.1	2.2	10.3	77.0	1.1326	0.2810	103.7
13.0	0.9919	5.5469	0.0112	0.0228	0.0843	0.0245	0.0085	0.0677	1.9655	2.4	1.9	11.1	78.5	0.9599	0.2660	102.7
15.0	1.0475	5.4974	0.0107	0.0237	0.0837	0.0238	0.0089	0.0624	1.7677	3.8	1.9	10.4	77.3	1.0155	0.2780	102.2
17.0	1.5533	5.4716	0.0134	0.0292	0.0965	0.0252	0.0077	0.0725	2.2310	1.2	2.4	11.2	78.6	1.5213	0.2650	105.3
19.0	1.7819	5.4927	0.0148	0.0326	0.1001	0.0259	0.0069	0.0720	2.2505	1.1	2.5	11.7	79.5	1.7499	0.2560	107.1
21.0	2.1189	5.4866	0.0182	0.0362	0.1008	0.0267	0.0074	0.0510	1.6129	2.2	2.4	10.5	77.4	2.0869	0.2770	104.4
23.0	1.9023	5.4440	0.0170	0.0360	0.1011	0.0261	0.0076	0.0580	1.7607	2.1	2.4	11.0	78.4	1.8703	0.2670	103.3

## BENTHIC III 35 BC

---

Depth (cm)	Sample I.D.	Na	Mg	Al	Si	P	S	K	Ca	Ti	Cr
1.0	24524	0.8222	2.1123	7.6146	31.3423	0.1357	0.1772	2.3752	0.6403	0.3963	0.0059
3.0	24525	0.3542	2.0516	7.4512	31.5082	0.1454	0.1972	2.4471	0.6606	0.4122	0.0068
5.0	24526	0.0417	2.0489	7.3373	31.3588	0.1448	0.2198	2.4462	0.6740	0.4111	0.0059
7.0	24527	0.2152	2.0344	7.3491	31.3520	0.1430	0.2027	2.4663	0.6730	0.4145	0.0069
9.0	24528	0.2996	2.0420	7.3820	30.8428	0.1469	0.1898	2.4863	0.6756	0.4127	0.0071
11.0	24529	0.2421	2.1417	7.5822	30.6874	0.1756	0.2025	2.5180	0.7274	0.4151	0.0071
13.0	24530	0.1841	2.0385	7.3654	30.7045	0.1482	0.1747	2.5021	0.6600	0.4146	0.0091
15.0	24531	0.3696	2.1416	7.4796	30.3753	0.2052	0.1828	2.4879	0.7410	0.4153	0.0077
17.0	24532	0.2924	2.0601	7.5252	30.9378	0.1662	0.1664	2.5168	0.7135	0.4179	0.0073
19.0	24533	0.3023	2.0128	7.3737	30.8690	0.1741	0.1744	2.4792	0.7144	0.4088	0.0070
21.0	24534	0.1310	2.2047	7.6725	30.2288	0.1792	0.2168	2.5082	0.7251	0.4183	0.0071
23.0	24535	0.1167	2.3274	7.8642	30.0823	0.1906	0.2360	2.5481	0.7605	0.4277	0.0075
25.0	24536	0.0688	2.2303	7.6965	30.3953	0.2017	0.2257	2.5137	0.7663	0.4140	0.0066
27.0	24537	0.1926	2.3157	7.7503	30.3111	0.2343	0.2472	2.4887	0.8026	0.4170	0.0079
29.0	24538	0.2296	2.4345	7.9017	30.1646	0.2466	0.2577	2.4995	0.8689	0.4223	0.0072
31.0	24539	0.1572	2.4105	7.8710	29.9344	0.1978	0.2559	2.4929	0.7890	0.4165	0.0075

# BENTHIC III 35 BC

Depth (cm)	Mn	Fe	Co	Ni	Cu	Zn	Rb	Sr	Ba	Opal	CaCO <sub>3</sub>	Salt %	H <sub>2</sub> O %	Mn-ex	Dry Density (g/cm <sup>3</sup> )	Sum of Oxides
1.0	0.2253	4.8219	0.0046	0.0129	0.0369	0.0161	0.0122	0.0281	0.5115	13.7	0.0	15.4	84.2	0.1933	0.2090	98.6
3.0	0.1904	5.0664	0.0046	0.0123	0.0381	0.0168	0.0122	0.0278	0.5262	15.5	0.0	11.4	79.0	0.1584	0.2610	98.4
5.0	0.1722	5.0862	0.0044	0.0117	0.0378	0.0164	0.0121	0.0279	0.5253	16.1	0.0	9.2	74.9	0.1402	0.3020	97.4
7.0	0.1715	5.1522	0.0046	0.0120	0.0377	0.0169	0.0119	0.0274	0.4979	16.0	0.0	8.9	74.1	0.1395	0.3100	97.7
9.0	0.1246	5.2124	0.0041	0.0106	0.0379	0.0166	0.0120	0.0283	0.5054	14.4	0.0	8.3	72.6	0.0926	0.3250	96.9
11.0	0.0820	5.3114	0.0039	0.0096	0.0448	0.0174	0.0120	0.0324	0.6060	12.4	0.1	7.4	70.0	0.0500	0.3510	97.4
13.0	0.0949	5.1881	0.0042	0.0096	0.0361	0.0172	0.0122	0.0276	0.4927	14.2	0.0	7.6	70.8	0.0629	0.3430	96.3
15.0	0.0779	5.3222	0.0039	0.0096	0.0421	0.0169	0.0117	0.0302	0.5859	12.5	0.1	8.1	72.0	0.0459	0.3310	96.8
17.0	0.0595	5.2889	0.0037	0.0086	0.0375	0.0165	0.0120	0.0283	0.5178	13.4	0.0	7.8	71.1	0.0275	0.3400	97.6
19.0	0.0603	5.2189	0.0035	0.0082	0.0356	0.0163	0.0119	0.0273	0.5169	14.6	0.0	8.2	72.3	0.0283	0.3280	96.9
21.0	0.0480	5.3498	0.0036	0.0087	0.0476	0.0182	0.0118	0.0318	0.6469	10.4	0.1	7.6	70.7	0.0160	0.3440	96.6
23.0	0.0558	5.4481	0.0039	0.0100	0.0546	0.0185	0.0123	0.0344	0.7072	8.4	0.2	7.5	70.2	0.0238	0.3490	97.2
25.0	0.0502	5.3858	0.0036	0.0091	0.0479	0.0173	0.0121	0.0331	0.6823	10.6	0.2	7.4	70.0	0.0182	0.3510	97.2
27.0	0.0516	5.4149	0.0038	0.0095	0.0551	0.0184	0.0115	0.0339	0.7698	10.0	0.3	7.0	68.8	0.0196	0.3630	97.7
29.0	0.0494	5.5017	0.0039	0.0104	0.0615	0.0194	0.0114	0.0344	0.7836	8.2	0.4	7.4	70.0	0.0174	0.3510	98.3
31.0	0.0491	5.4685	0.0039	0.0106	0.0585	0.0193	0.0116	0.0342	0.7497	8.0	0.2	7.6	70.7	0.0171	0.3440	97.2

K7905 47 BC

Depth (cm)	Sample I.D.	Na	Mg	Al	Si	P	S	K	Ca	Ti	Cr
1.0	03556	0.6239	1.9724	7.1961	31.6116	0.1803	0.1907	2.3801	0.7495	0.3943	0.0064
3.0	03557	0.1576	1.9019	6.8709	30.4056	0.1854	0.2201	2.3664	0.7673	0.3919	0.0074
5.0	03558	0.1097	1.8778	6.8061	30.0781	0.1616	0.1867	2.3507	0.7126	0.3885	0.0074
7.0	03559	0.3108	1.8912	6.8340	29.9785	0.1605	0.2228	2.4038	0.7175	0.3945	0.0062
9.0	03560	0.1977	1.9399	6.9513	30.0688	0.1371	0.1753	2.4484	0.6536	0.4023	0.0068
11.0	03561	0.3415	2.0037	7.2715	30.8044	0.1598	0.1861	2.4841	0.7000	0.4070	0.0064
13.0	03562	0.2317	1.9562	7.0011	30.0683	0.1456	0.1764	2.4648	0.6818	0.4048	0.0072
15.0	03563	0.3268	1.9438	7.0280	29.6318	0.1802	0.1611	2.4493	0.7642	0.3970	0.0078
17.0	03564	0.2835	1.8598	6.8109	28.4979	0.1765	0.1698	2.3926	0.7368	0.3938	0.0068
19.0	03565	0.4671	1.9587	7.1756	29.5089	0.1982	0.2266	2.4571	0.7655	0.3958	0.0074
21.0	03566	0.3489	1.9946	7.2597	30.1033	0.1800	0.2041	2.4785	0.7393	0.4006	0.0072
23.0	03567	0.3162	1.9059	6.9441	28.6178	0.1991	0.1692	2.4028	0.7724	0.3939	0.0078
25.0	02568	0.2565	2.0116	7.2351	28.9596	0.2076	0.1736	2.4720	0.8032	0.4045	0.0069
27.0	03569	0.3252	2.1334	7.5236	30.1139	0.2397	0.2167	2.4964	0.8506	0.4125	0.0071
29.0	03570	0.2193	2.2515	7.5045	29.5334	0.2748	0.2675	2.4433	0.9066	0.4091	0.0073
31.0	03571	0.1066	2.2203	7.4820	29.5188	0.2435	0.2685	2.5018	0.8629	0.4135	0.0081



K7905 47 BC

Depth (cm)	Mn	Fe	Co	Ni	Cu	Zn	Rb	Sr	Ba	Opal	CaCO <sub>3</sub>	Salt %	H <sub>2</sub> O %	Mn-ex	Dry Density (g/cm <sup>3</sup> )	Sum of Oxides
1.0	0.2637	4.9354	0.0053	0.0146	0.0402	0.0217	0.0112	0.0284	0.5243	25.1	0.1	10.2	76.4	0.2317	0.2870	98.4
3.0	0.2249	4.9261	0.0051	0.0138	0.0393	0.0183	0.0121	0.0289	0.5265	24.5	0.2	7.2	68.9	0.1929	0.3620	94.5
5.0	0.1924	4.9287	0.0048	0.0135	0.0384	0.0185	0.0119	0.0280	0.5223	24.1	0.0	7.9	71.0	0.1604	0.3410	93.3
7.0	0.1389	5.0350	0.0042	0.0111	0.0360	0.0191	0.0120	0.0274	0.4840	23.7	0.0	6.8	67.7	0.1069	0.3740	93.5
9.0	0.0967	5.0740	0.0041	0.0100	0.0336	0.0179	0.0125	0.0268	0.4498	23.1	0.0	6.2	65.6	0.0647	0.3950	93.7
11.0	0.0775	5.1019	0.0041	0.0092	0.0323	0.0176	0.0124	0.0271	0.4876	22.5	0.0	6.9	67.9	0.0455	0.3720	96.4
13.0	0.0836	5.1526	0.0044	0.0091	0.0311	0.0188	0.0124	0.0270	0.4952	22.7	0.0	5.8	63.8	0.0516	0.4130	94.1
15.0	0.0655	5.1941	0.0043	0.0092	0.0324	0.0204	0.0122	0.0291	0.5095	21.4	0.2	6.3	65.8	0.0335	0.3930	93.6
17.0	0.0730	5.2434	0.0041	0.0096	0.0360	0.0184	0.0128	0.0313	0.5704	20.2	0.1	7.0	68.4	0.0410	0.3670	90.6
19.0	0.0541	5.1123	0.0038	0.0087	0.0365	0.0177	0.0124	0.0315	0.6102	19.9	0.2	6.3	65.6	0.0221	0.3950	93.9
21.0	0.0663	5.1415	0.0041	0.0095	0.0371	0.0186	0.0126	0.0311	0.5793	20.8	0.1	7.2	68.9	0.0343	0.3620	95.1
23.0	0.0517	5.3874	0.0039	0.0089	0.0377	0.0180	0.0121	0.0307	0.5670	19.4	0.2	6.6	66.9	0.0197	0.3820	91.5
25.0	0.0483	5.4221	0.0037	0.0086	0.0419	0.0200	0.0119	0.0313	0.5927	18.1	0.3	6.2	65.3	0.0163	0.3980	93.2
27.0	0.0454	5.3496	0.0038	0.0083	0.0454	0.0192	0.0120	0.0322	0.6496	18.9	0.4	6.9	67.8	0.0134	0.3730	96.7
29.0	0.0465	5.3128	0.0038	0.0096	0.0585	0.0195	0.0119	0.0359	0.7705	17.5	0.5	5.9	64.1	0.0145	0.4100	95.7
31.0	0.0475	5.3494	0.0037	0.0086	0.0483	0.0194	0.0123	0.0329	0.6477	17.7	0.4	5.7	63.1	0.0155	0.4200	95.2

## K7905 82 GC

Depth (cm)	Sample I.D.	Na	Mg	Al	Si	P	S	K	Ca	Ti	Cr
0.5	26016	0.5048	1.9522	7.1824	31.5910	0.2303	0.1729	2.3890	0.8055	0.4010	0.0063
5.5	26018	0.2983	1.9332	7.0868	31.0631	0.1790	0.1594	2.4142	0.7259	0.4033	0.0086
8.5	26019	0.3309	1.9951	7.3522	31.1440	0.1706	0.1535	2.5188	0.7060	0.4224	0.0074
11.5	26020	0.3841	1.9973	7.3299	30.7166	0.1804	0.1479	2.4997	0.7195	0.4125	0.0073
14.5	26021	0.3783	2.0345	7.4419	31.0661	0.1870	0.1479	2.5284	0.7341	0.4190	0.0076
17.5	26022	0.2206	2.0181	7.3680	30.9950	0.1783	0.1714	2.4871	0.7167	0.4111	0.0070
20.5	26023	0.3814	2.0396	7.4486	30.6695	0.2018	0.1557	2.4938	0.7548	0.4090	0.0076
23.5	26024	0.2496	2.0952	7.6717	30.7218	0.1841	0.1675	2.5645	0.7305	0.4222	0.0080
29.5	26025	0.1101	2.1130	7.6640	30.4264	0.1875	0.1786	2.5553	0.7346	0.4210	0.0070
35.5	26026	0.3100	2.2299	7.8644	30.8495	0.2286	0.1604	2.5685	0.8060	0.4307	0.0087
41.5	26027	0.3960	2.3760	7.9699	30.5790	0.2522	0.1905	2.5457	0.8376	0.4382	0.0088
47.5	26028	0.1635	2.3739	7.8043	30.1691	0.2422	0.2096	2.5045	0.8424	0.4200	0.0084
53.5	26029	0.2694	2.4679	7.8985	30.2611	0.2301	0.1910	2.5528	0.8196	0.4259	0.0072
59.5	26030	0.3784	2.4197	7.9074	30.0440	0.2562	0.1719	2.5067	0.8582	0.4240	0.0077
65.5	26031	0.2674	2.3762	7.8399	30.0251	0.2464	0.1724	2.5225	0.8340	0.4281	0.0080
71.5	26032	0.3402	2.3998	7.7836	29.9284	0.2318	0.1711	2.5024	0.8078	0.4232	0.0072
77.5	26033	0.1872	2.4168	7.9122	30.2520	0.2284	0.1585	2.5439	0.8043	0.4358	0.0068
83.5	26034	0.3107	2.3947	7.8578	29.9083	0.2466	0.1575	2.5348	0.8332	0.4290	0.0069
89.5	26035	0.5795	2.3633	7.8299	29.9834	0.3146	0.1496	2.4896	0.9918	0.4197	0.0060
95.5	26036	0.1797	2.3721	7.7364	29.9526	0.2604	0.1666	2.4956	0.8892	0.4273	0.0074
101.5	26037	0.2682	2.3230	7.6987	29.5885	0.2997	0.1526	2.4551	0.9669	0.4160	0.0063
107.5	26038	0.2974	2.3408	7.7198	29.5035	0.2901	0.1454	2.4847	0.9266	0.4184	0.0069
113.5	26039	0.3581	2.3646	7.6391	29.7087	0.3177	0.1540	2.4723	0.9907	0.4151	0.0063
119.5	26040	0.2547	2.3867	7.7881	29.8467	0.3223	0.1780	2.5142	1.0067	0.4250	0.0056
125.5	26041	0.3555	2.4057	7.8294	29.4012	0.3479	0.1978	2.5207	1.0410	0.4308	0.0066
131.5	26042	0.3196	2.3726	7.6692	29.3800	0.3696	0.2041	2.4966	1.0915	0.4179	0.0078
137.5	26043	0.3422	2.3844	7.7792	29.6537	0.3589	0.2028	2.4996	1.0759	0.4157	0.0064
143.5	26044	0.3190	2.3616	7.7244	29.1502	0.3461	0.2070	2.4797	1.0758	0.4063	0.0058
149.5	26045	0.4253	2.3757	7.7569	29.6721	0.4040	0.1978	2.5103	1.1811	0.4117	0.0045
155.5	26046	0.5086	2.3862	7.7677	29.4452	0.4625	0.2214	2.5438	1.3196	0.4042	0.0051
161.5	26047	0.5435	2.4163	7.9050	29.4512	0.4368	0.2292	2.6245	1.2316	0.4162	0.0054
167.5	26048	0.6484	2.3826	7.9958	28.9644	0.4028	0.2137	2.6766	1.1861	0.4164	0.0068
173.5	26049	0.6413	2.3723	7.9654	29.3672	0.4324	0.2043	2.6372	1.2327	0.4170	0.0051
179.5	26050	0.6509	2.3503	7.8295	28.9002	0.4202	0.1805	2.6279	1.1960	0.4124	0.0051
185.5	26051	0.8281	2.3325	8.0084	28.6418	0.4482	0.1596	2.6580	1.2556	0.4046	0.0056
191.5	26052	0.8550	2.4105	7.9821	27.8848	0.4215	0.1729	2.6519	1.2338	0.3934	0.0064
197.5	26053	1.1617	2.6070	8.0760	27.9341	0.5123	0.2468	2.6763	1.4710	0.3979	0.0053
209.5	26055	1.3965	3.0775	8.1522	27.8711	0.6645	0.3607	2.3072	1.8842	0.3725	0.0040
215.5	26056	2.0700	3.3560	8.7049	28.9372	0.6869	0.5115	2.2634	1.8803	0.3822	0.0038
221.5	26057	1.5207	3.2102	8.2436	28.0508	0.6988	0.4103	2.1879	1.9413	0.3760	0.0051
227.5	26058	2.0840	3.2667	8.2756	28.1288	0.6897	0.3897	2.1680	1.8879	0.3773	0.0041
233.5	26059	2.2026	3.4388	8.7172	29.0694	0.6613	0.4442	2.1820	1.8105	0.3870	0.0054

## K7905 82 GC

Depth (cm)	Mn	Fe	Co	Ni	Cu	Zn	Rb	Sr	Ba	Opal	CaCO <sub>3</sub>	Salt %	H <sub>2</sub> O %	Mn-ex	Dry Density (g/cm <sup>3</sup> )	Sum of Oxides
0.5	0.3043	5.0269	0.0050	0.0159	0.0438	0.0169	0.0119	0.0282	0.5309	18.0	0.3	10.3	77.1	0.2723	0.2800	98.7
5.5	0.2958	5.1092	0.0049	0.0137	0.0396	0.0169	0.0118	0.0276	0.5051	17.5	0.1	8.8	74.0	0.1938	0.3110	96.7
8.5	0.1613	5.2814	0.0046	0.0122	0.0380	0.0175	0.0122	0.0274	0.4987	15.4	0.0	8.5	73.1	0.1293	0.3200	97.8
11.5	0.0914	5.2792	0.0041	0.0097	0.0360	0.0173	0.0122	0.0272	0.5011	14.6	0.0	8.2	72.4	0.0594	0.3270	96.8
14.5	0.0736	5.3206	0.0039	0.0096	0.0373	0.0169	0.0125	0.0282	0.5329	14.6	0.1	8.5	73.2	0.0416	0.3190	98.0
17.5	0.1582	5.2136	0.0043	0.0126	0.0391	0.0169	0.0120	0.0288	0.5796	14.9	0.0	8.0	71.7	0.1262	0.3340	97.3
20.5	0.0704	5.2905	0.0036	0.0087	0.0406	0.0168	0.0122	0.0300	0.5982	13.4	0.1	8.3	72.7	0.0384	0.3240	97.2
23.5	0.0526	5.3681	0.0035	0.0091	0.0418	0.0165	0.0126	0.0299	0.5689	11.7	0.1	8.4	72.9	0.0206	0.3220	97.7
29.5	0.0496	5.3436	0.0035	0.0086	0.0429	0.0171	0.0127	0.0303	0.5679	10.9	0.1	7.6	70.8	0.0176	0.3430	96.9
35.5	0.0514	5.5178	0.0035	0.0093	0.0505	0.0182	0.0125	0.0323	0.6521	10.3	0.3	9.5	75.5	0.0194	0.2960	99.3
41.5	0.0523	5.5084	0.0039	0.0108	0.0603	0.0195	0.0119	0.0352	0.8203	8.7	0.3	9.1	74.6	0.0203	0.3050	99.5
47.5	0.0484	5.4550	0.0043	0.0116	0.0563	0.0198	0.0119	0.0356	0.8202	9.1	0.4	8.8	73.8	0.0164	0.3130	97.8
53.5	0.0479	5.9233	0.0044	0.0126	0.0541	0.0196	0.0122	0.0335	0.7514	8.5	0.3	9.2	74.9	0.0159	0.3020	99.1
59.5	0.0470	5.6245	0.0041	0.0120	0.0653	0.0208	0.0114	0.0304	0.6780	8.0	0.4	8.9	74.2	0.0150	0.3090	98.3
65.5	0.0497	5.5954	0.0038	0.0123	0.0599	0.0209	0.0119	0.0310	0.6515	8.4	0.3	8.4	73.0	0.0177	0.3210	97.8
71.5	0.0521	5.7401	0.0044	0.0156	0.0601	0.0222	0.0115	0.0303	0.6228	8.7	0.3	9.6	75.7	0.0201	0.2940	97.7
77.5	0.0542	5.6431	0.0045	0.0159	0.0636	0.0228	0.0118	0.0299	0.6087	8.4	0.3	9.7	75.8	0.0222	0.2930	98.3
83.5	0.0556	5.6592	0.0043	0.0152	0.0617	0.0223	0.0118	0.0283	0.5656	8.0	0.3	9.1	74.6	0.0236	0.3050	97.7
89.5	0.0509	5.5772	0.0040	0.0132	0.0644	0.0205	0.0115	0.0294	0.5488	8.4	0.7	9.9	76.3	0.0189	0.2880	98.4
95.5	0.0508	5.5502	0.0040	0.0135	0.0691	0.0210	0.0116	0.0287	0.5213	9.2	0.5	9.2	74.7	0.0188	0.3040	97.2
101.5	0.0486	5.5063	0.0040	0.0126	0.0737	0.0210	0.0116	0.0286	0.4737	8.5	0.7	9.3	75.1	0.0166	0.3000	96.5
107.5	0.0466	5.5408	0.0041	0.0125	0.0708	0.0214	0.0116	0.0284	0.4902	8.1	0.6	8.9	74.0	0.0146	0.3110	96.4
113.5	0.0460	5.7205	0.0043	0.0123	0.0677	0.0208	0.0113	0.0293	0.5206	9.4	0.7	8.7	73.6	0.0140	0.3150	97.3
119.5	0.0481	5.5698	0.0043	0.0131	0.0696	0.0212	0.0116	0.0311	0.5902	8.4	0.8	8.4	72.9	0.0161	0.3220	97.8
125.5	0.5458	5.4545	0.0168	0.0268	0.0858	0.0211	0.0108	0.0333	0.6920	7.0	0.9	8.2	72.3	0.5138	0.3280	98.0
131.5	0.5423	5.4339	0.0127	0.0249	0.0786	0.0210	0.0108	0.0328	0.6800	8.3	1.0	7.9	71.6	0.5103	0.3350	97.6
137.5	0.3034	5.4714	0.0089	0.0198	0.0758	0.0211	0.0109	0.0323	0.6762	8.0	1.0	8.1	72.2	0.2714	0.3290	98.1
143.5	0.2790	5.4466	0.0086	0.0192	0.0741	0.0208	0.0109	0.0322	0.6709	7.3	1.0	8.2	72.4	0.2470	0.3270	96.7
149.5	0.1114	5.5737	0.0054	0.0143	0.0706	0.0209	0.0109	0.0328	0.6304	8.2	1.2	8.8	73.9	0.0794	0.3120	98.3
155.5	0.0559	5.4653	0.0039	0.0125	0.0719	0.0210	0.0106	0.0361	0.7344	7.7	1.6	8.0	71.7	0.0239	0.3340	98.4
161.5	0.0623	5.6094	0.0042	0.0138	0.0707	0.0219	0.0113	0.0369	0.7977	6.4	1.4	7.8	71.2	0.0303	0.3390	98.9
167.5	0.0776	5.6173	0.0042	0.0124	0.0698	0.0212	0.0111	0.0355	0.7389	4.5	1.2	7.7	71.0	0.0456	0.3410	97.9
173.5	0.2206	5.6052	0.0069	0.0160	0.0719	0.0211	0.0108	0.0356	0.7238	5.7	1.4	7.5	70.5	0.1886	0.3460	99.0
179.5	0.4680	5.5823	0.0120	0.0228	0.0739	0.0211	0.0109	0.0326	0.6194	5.7	1.3	7.4	70.2	0.4360	0.3490	97.9
185.5	0.8922	5.5976	0.0132	0.0301	0.0764	0.0222	0.0106	0.0324	0.5968	3.5	1.4	8.2	72.5	0.8602	0.3260	98.8
191.5	3.3731	5.1775	0.0135	0.0770	0.1050	0.0256	0.0090	0.0331	0.6510	1.9	1.4	7.1	69.2	3.3411	0.3590	100.5
197.5	3.1438	5.2573	0.0082	0.0797	0.0952	0.0267	0.0082	0.0422	0.9846	1.1	2.0	9.0	74.3	3.1118	0.3080	102.5
209.5	2.9753	5.2373	0.0060	0.0685	0.0834	0.0297	0.0073	0.0482	1.4545	0.4	3.0	13.9	82.6	2.9433	0.2250	104.7
215.5	2.5454	5.1074	0.0051	0.0613	0.0766	0.0283	0.0070	0.0713	2.3682	0.0	3.0	15.9	84.7	2.5134	0.2040	109.6
221.5	2.0727	5.2528	0.0055	0.0551	0.0739	0.0295	0.0073	0.0498	1.5401	0.1	3.2	14.9	83.7	2.0407	0.2140	104.4
227.5	1.9548	5.1667	0.0061	0.0559	0.0713	0.0301	0.0074	0.0484	1.5281	0.0	3.0	16.6	85.3	1.9228	0.1980	105.0
233.5	1.8085	5.1231	0.0056	0.0502	0.0706	0.0300	0.0077	0.0518	1.7988	0.0	2.8	17.3	86.0	1.7765	0.1910	108.1

## K7905 97 GC

Depth (cm)	Sample I.D.	Na	Mg	Al	Si	P	S	K	Ca	Ti	Cr
0.5	26060	0.6499	2.1339	7.6941	30.1096	0.2977	0.1744	2.5711	0.9713	0.4196	0.0061
3.5	26061	0.7028	2.2742	7.8391	28.6861	0.3158	0.1706	2.6315	1.0275	0.4049	0.0057
6.5	26062	0.5286	2.3143	7.9304	29.2143	0.3181	0.1961	2.6584	1.0541	0.4099	0.0061
9.5	26063	0.5010	2.3331	7.8969	29.0098	0.3403	0.2353	2.6621	1.0830	0.4040	0.0043
12.5	26064	0.5042	2.2879	7.8569	29.3003	0.3132	0.1750	2.6593	1.0478	0.4135	0.0055
15.5	26065	0.8583	2.3656	8.0168	28.2759	0.3633	0.1810	2.6892	1.1532	0.3988	0.0053
18.5	26066	0.6087	2.3269	7.9327	28.5831	0.3557	0.1629	2.6703	1.0879	0.4055	0.0066
21.5	26067	0.6378	2.3807	7.9543	28.2355	0.3643	0.2145	2.6807	1.1413	0.3956	0.0050
24.5	26068	0.8317	2.3833	8.0685	28.5666	0.3921	0.1739	2.6868	1.1859	0.4050	0.0043
30.5	26069	0.7777	2.3765	7.9932	28.2811	0.3689	0.1995	2.6741	1.1653	0.3963	0.0037
36.5	26070	0.5848	2.2918	7.8992	29.2366	0.3266	0.1685	2.6621	1.0525	0.4114	0.0069
42.5	26071	0.7020	2.4070	8.0121	28.1930	0.3847	0.2121	2.6727	1.1843	0.3977	0.0046
48.5	26072	0.7608	2.4062	8.0913	28.7291	0.3887	0.1766	2.7083	1.1676	0.4071	0.0045
54.5	26073	0.7294	2.3404	7.8912	28.1697	0.3756	0.1757	2.6465	1.1657	0.3953	0.0053
60.5	26074	0.7763	2.3910	8.0657	28.5910	0.4012	0.1698	2.6910	1.1959	0.4036	0.0036
66.5	26075	0.7545	2.3534	7.9682	28.3171	0.3714	0.1779	2.6712	1.1624	0.4014	0.0081
72.5	26076	0.7409	2.3564	7.9537	28.2138	0.3723	0.1751	2.6541	1.1624	0.3976	0.0046
78.5	26077	0.7274	2.3706	7.9972	28.4651	0.3666	0.1868	2.6778	1.1519	0.4014	0.0056
84.5	26078	0.6380	2.3777	7.9314	28.1939	0.3697	0.2248	2.6709	1.1347	0.3989	0.0047
90.5	26079	0.7599	2.3422	7.9101	28.1261	0.3495	0.1883	2.6404	1.1129	0.3945	0.0055
96.5	26080	0.7104	2.3859	8.0139	28.4328	0.3349	0.2097	2.6636	1.0823	0.4023	0.0042
102.5	26081	0.8524	2.3936	8.0985	28.7465	0.3451	0.2002	2.6915	1.1052	0.4075	0.0040
108.5	26082	0.7389	2.3914	7.9759	28.2678	0.3230	0.2321	2.6269	1.0660	0.3955	0.0049
114.5	26083	0.7520	2.4214	8.0955	28.7447	0.3234	0.2247	2.6605	1.0765	0.4063	0.0039
120.5	26084	0.6220	2.4244	8.0429	28.6007	0.3078	0.2611	2.6359	1.0669	0.4015	0.0048
126.5	26085	1.4112	2.4267	8.2972	29.1246	0.3495	0.1468	2.6159	1.0874	0.4128	0.0052
132.5	26086	1.1402	2.4068	8.1743	28.9859	0.3392	0.1891	2.6361	1.0826	0.4087	0.0047
138.5	26087	0.7319	2.4081	7.9612	28.3016	0.3220	0.2508	2.6146	1.0706	0.3952	0.0043
144.5	26088	0.7522	2.4235	8.0721	28.7373	0.2712	0.2378	2.6282	1.0380	0.4000	0.0044
150.5	26089	1.0660	2.4249	8.2519	29.1940	0.3461	0.1777	2.6465	1.0804	0.4069	0.0036
156.5	26090	0.9901	2.4597	8.2533	29.2397	0.3604	0.1885	2.6618	1.1170	0.4080	0.0043
162.5	26091	0.7826	2.4120	7.9873	28.4551	0.3367	0.2261	2.6018	1.0857	0.3934	0.0057
168.5	26092	0.8863	2.4563	8.1552	28.9535	0.3645	0.2440	2.6473	1.1268	0.4001	0.0039
174.5	26093	1.0913	2.3866	8.0868	28.7583	0.3526	0.1966	2.6159	1.0975	0.4013	0.0045
180.5	26094	1.0343	2.3844	8.0416	28.6391	0.3497	0.2039	2.6359	1.1171	0.3992	0.0046
186.5	26095	1.0614	2.3838	8.0418	28.7239	0.3532	0.1934	2.6277	1.1330	0.4025	0.0046
192.5	26096	0.7608	2.4203	7.9094	28.5719	0.2847	0.2356	2.6600	1.0636	0.4073	0.0036
198.5	26097	1.1845	2.3534	8.0037	28.4783	0.3318	0.1588	2.5927	1.0880	0.4024	0.0055

## K7905 97 GC

Depth (cm)	Br	Fe	Co	Ni	Cu	Zn	Rb	Sr	Ba	Opal	CaCO <sub>3</sub>	Salt %	H <sub>2</sub> O %	Mn-ex	Dry Density (g/cm <sup>3</sup> )	Sum of Oxides
0.5	0.4675	5.3863	0.0060	0.0192	0.0588	0.0192	0.0116	0.0317	0.6526	9.9	0.7	9.7	75.9	0.3905	0.2920	98.6
3.5	0.5648	5.4794	0.0069	0.0215	0.0751	0.0203	0.0108	0.0340	0.7243	5.1	0.8	8.8	74.0	0.5328	0.3110	96.8
6.5	0.6693	5.4659	0.0073	0.0240	0.0777	0.0206	0.0110	0.0343	0.7023	5.7	0.9	8.7	73.7	0.5883	0.3140	98.1
9.5	0.7528	5.4667	0.0078	0.0270	0.0854	0.0205	0.0104	0.0346	0.7324	5.5	1.0	7.8	71.3	0.7608	0.3380	98.0
12.5	0.6812	5.4838	0.0076	0.0259	0.0753	0.0203	0.0110	0.0318	0.6125	6.5	0.9	8.1	72.0	0.6492	0.3310	98.1
15.5	1.2924	5.4962	0.0107	0.0426	0.0972	0.0235	0.0097	0.0339	0.7310	2.6	1.2	8.2	72.2	1.2604	0.3290	98.3
18.5	1.0048	5.5196	0.0083	0.0342	0.0820	0.0220	0.0103	0.0322	0.6674	4.0	1.0	8.1	72.2	0.9728	0.3290	97.7
21.5	1.2295	5.4836	0.0081	0.0393	0.0888	0.0225	0.0099	0.0338	0.7119	3.0	1.1	7.0	68.9	1.1975	0.3620	97.6
24.5	1.2836	5.5523	0.0077	0.0408	0.0878	0.0232	0.0096	0.0331	0.7210	2.9	1.2	8.1	72.0	1.2516	0.3310	99.2
30.5	1.1495	5.5530	0.0077	0.0401	0.0858	0.0226	0.0097	0.0329	0.6909	2.8	1.2	8.0	71.7	1.1175	0.3340	98.0
36.5	0.6470	5.5629	0.0068	0.0241	0.0766	0.0208	0.0109	0.0332	0.6827	5.9	0.9	7.9	71.5	0.6150	0.3360	98.3
42.5	1.2772	5.5126	0.0082	0.0405	0.0879	0.0233	0.0098	0.0340	0.7468	2.4	1.2	7.1	69.3	1.2452	0.3580	98.1
48.5	1.0908	5.5971	0.0077	0.0393	0.0842	0.0226	0.0102	0.0339	0.7116	3.1	1.2	7.9	71.4	1.0588	0.3370	99.3
54.5	1.0805	5.5778	0.0077	0.0400	0.0843	0.0229	0.0097	0.0328	0.6435	3.4	1.2	7.5	70.2	1.0485	0.3400	97.3
60.5	1.0815	5.6348	0.0079	0.0405	0.0855	0.0225	0.0099	0.0333	0.6607	3.0	1.3	7.7	71.1	1.0495	0.3400	99.0
66.5	1.0225	5.6310	0.0078	0.0379	0.0850	0.0223	0.0094	0.0325	0.6380	3.1	1.2	7.6	70.6	0.9905	0.3450	97.8
72.5	1.0210	5.6103	0.0079	0.0397	0.0841	0.0223	0.0097	0.0323	0.6050	3.0	1.2	7.5	70.5	0.9890	0.3460	97.5
78.5	0.9453	5.6758	0.0080	0.0372	0.0842	0.0222	0.0097	0.0321	0.6313	3.2	1.1	7.3	69.6	0.9133	0.3550	98.1
84.5	0.9859	5.6377	0.0078	0.0397	0.0833	0.0216	0.0097	0.0329	0.6989	3.1	1.1	6.2	66.0	0.9539	0.3910	97.3
90.5	0.9206	5.6533	0.0079	0.0362	0.0821	0.0221	0.0095	0.0329	0.6843	3.1	1.0	7.3	69.9	0.8886	0.3520	97.0
96.5	0.9046	5.6737	0.0077	0.0365	0.0830	0.0219	0.0098	0.0335	0.7617	3.0	1.0	7.0	68.7	0.8726	0.3640	97.9
102.5	0.9415	5.7342	0.0080	0.0376	0.0849	0.0222	0.0097	0.0334	0.7702	3.1	1.0	7.5	70.4	0.9095	0.3470	99.2
108.5	0.8856	5.6310	0.0077	0.0382	0.0828	0.0221	0.0096	0.0341	0.8058	2.9	0.9	7.0	68.9	0.8536	0.3620	97.3
114.5	0.8718	5.7026	0.0076	0.0398	0.0857	0.0225	0.0099	0.0343	0.7919	3.1	1.0	7.2	69.4	0.8398	0.3570	98.8
120.5	0.7891	5.6538	0.0075	0.0366	0.0831	0.0222	0.0097	0.0344	0.8517	3.2	0.9	6.6	67.4	0.7571	0.3770	98.0
126.5	0.9368	5.8427	0.0080	0.0461	0.0804	0.0228	0.0098	0.0331	0.7527	2.3	1.0	9.8	76.1	0.9048	0.2900	101.2
132.5	0.6679	5.8421	0.0078	0.0357	0.0830	0.0226	0.0097	0.0326	0.7145	3.0	1.0	8.7	73.7	0.6309	0.3140	99.8
138.5	0.8468	5.6421	0.0077	0.0436	0.0858	0.0221	0.0097	0.0339	0.7988	3.1	0.9	6.9	68.3	0.8148	0.3680	97.3
144.5	0.8584	5.6383	0.0078	0.0423	0.0863	0.0219	0.0097	0.0337	0.7947	3.3	0.9	6.6	67.3	0.8264	0.3780	98.4
150.5	0.9321	5.7259	0.0077	0.0445	0.0881	0.0224	0.0098	0.0342	0.8177	2.9	1.0	8.7	73.8	0.9001	0.3130	100.7
156.5	0.9307	5.7104	0.0079	0.0442	0.0880	0.0218	0.0099	0.0345	0.8323	3.0	1.1	8.4	72.9	0.8987	0.3220	100.9
162.5	0.8726	5.5862	0.0074	0.0410	0.0854	0.0217	0.0093	0.0350	0.9266	3.3	1.0	7.5	70.4	0.8406	0.3470	97.9
168.5	0.8503	5.6318	0.0076	0.0376	0.0855	0.0215	0.0095	0.0363	0.9711	3.1	1.1	7.5	70.4	0.8183	0.3470	99.8
174.5	0.9003	5.6972	0.0077	0.0392	0.0858	0.0225	0.0097	0.0363	0.9187	3.2	1.0	8.3	72.5	0.8683	0.3260	99.4
180.5	1.0070	5.6835	0.0078	0.0428	0.0869	0.0224	0.0095	0.0351	0.8603	3.3	1.1	7.5	70.3	0.9750	0.3480	99.2
186.5	1.0998	5.7134	0.0078	0.0497	0.0900	0.0229	0.0098	0.0348	0.8146	3.4	1.1	7.7	71.0	1.0678	0.3410	99.6
192.5	1.0748	5.6657	0.0075	0.0527	0.0918	0.0224	0.0098	0.0333	0.7181	4.2	0.9	5.5	62.9	1.0428	0.4220	98.1
198.5	1.3188	5.6772	0.0097	0.0631	0.1062	0.0231	0.0097	0.0335	0.7722	3.2	1.0	8.1	72.1	1.3468	0.3300	99.2

# K7905 106 BC

Depth	Mn	Fe	Co	Ni	Cu	Zn	Rb	Sr	Ba	Opal	CaCO <sub>3</sub>	Salt	H <sub>2</sub> O	Mn-ex	Dry Density	Sum of Oxides
(cm)												%	%		(g/cm <sup>3</sup> )	
1.0	0.4579	5.4158	0.0062	0.0210	0.0464	0.0171	0.0093	0.0235	0.5630	20.7	1.8	28.7	92.0	0.4259	0.1310	159.5
3.0	0.4733	5.0549	0.0058	0.0191	0.0433	0.0178	0.0115	0.0303	0.5919	21.1	2.3	15.8	84.2	0.3473	0.2090	107.8
5.0	0.3298	4.7534	0.0059	0.0176	0.0400	0.0194	0.0121	0.0316	0.5711	22.4	1.8	6.5	66.6	0.2978	0.3850	90.3
7.0	0.3138	4.9461	0.0056	0.0174	0.0403	0.0171	0.0122	0.0315	0.5587	21.6	2.1	10.9	77.7	0.2818	0.2740	97.0
9.0	0.2638	4.9530	0.0055	0.0166	0.0397	0.0181	0.0124	0.0317	0.5477	21.1	2.7	7.9	70.9	0.2568	0.3420	91.9
11.0	0.2446	5.2759	0.0053	0.0145	0.0374	0.0175	0.0109	0.0277	0.5153	19.1	2.9	18.4	86.5	0.2126	0.1860	120.5
13.0	0.1646	4.9681	0.0045	0.0111	0.0351	0.0164	0.0119	0.0329	0.5053	20.0	3.7	9.3	74.6	0.1326	0.3050	95.9
15.0	0.1465	5.0455	0.0047	0.0096	0.0378	0.0174	0.0102	0.0316	0.6014	17.5	4.7	19.7	87.5	0.1145	0.1760	125.2
17.0	0.1574	4.4395	0.0042	0.0096	0.0374	0.0163	0.0105	0.0483	0.7013	20.6	9.2	7.5	70.0	0.1254	0.3510	96.5
19.0	0.0971	1.7303	0.0009	0.0062	0.0160	0.0088	0.0050	0.1124	0.3547	10.0	51.5	3.9	53.6	0.0651	0.5150	89.2
21.0	0.0827	0.9605	0.0002	0.0053	0.0101	0.0059	0.0036	0.1304	0.2244	6.0	68.7	3.0	47.2	0.0507	0.5790	90.1
23.0	0.0499	0.3556	0.0000	0.0037	0.0036	0.0033	0.0024	0.1445	0.1485	3.3	82.5	2.3	40.2	0.0179	0.6490	91.9
25.0	0.0483	0.2741	0.0000	0.0042	0.0036	0.0029	0.0021	0.1459	0.1136	2.7	84.5	2.1	37.8	0.0163	0.6730	92.3
27.0	0.0511	0.2774	0.0000	0.0048	0.0036	0.0033	0.0020	0.1431	0.1197	2.9	83.3	2.1	38.2	0.0191	0.6690	91.3

APPENDIX 3

## Radiolarian and clay mineral data for Site S cores

Core	Depth (cm)	Quaternary Rads <sup>a</sup> ( $\times 10^{-5}$ rads $\cdot$ g $^{-1}$ )	Tertiary Rads <sup>a</sup> ( $\times 10^{-5}$ rads $\cdot$ g $^{-1}$ )	Illite (%)	Smectite (%)
K7905 47	0-1	2.48	0.37	32	2.6
	5-6	4.27	0.23	28	2.7
	9-10	3.96	0.24	25	3.2
	16-19	1.85	0.42	36	4.1
	23-24	0.93	0.66	23	3.2
	30-31	0.17	0.84	44	5.7
K7905 106	0-1	2.94	0.26	29	1.6
	2-3	3.25	0.20	30	1.2
	7-8	2.55	0.19	36	1.7
	12-13	1.20	0.47	30	-
	24-25	0.0	5.23	0.9	5.7
	26-27	0.0	6.35	-	-
BENTHIC 28	0-1	3.09	0.55	16	1.2
	5-6	2.77	0.49	71	2.1
	8-9	2.32	0.58	22	0.7
	12-13	1.26	0.30	23	1.0
	15-16	0.95	0.69	28	3.5
	18-19	1.22	0.75	39	3.9
BENTHIC 31	24-25	1.11	1.25	67	2.8
	0-1	1.77	0.10	25	0.8
	2-3	1.53	0.32	35	1.2
	5-6	0.63	0.25	21	8.6
K7905 82	9-10	0.00	0.01	8.6	8.8
	3-4	1.77	0.28	34	1.2
	14-15	(87) <sup>b</sup>	(13) <sup>b</sup>	28	2.3
	26-27	--	--	25	3.6
	32-33	(40) <sup>b</sup>	(60) <sup>b</sup>	22	2.0
	36-39	(44) <sup>b</sup>	(56) <sup>b</sup>	33	4.2
	44-45	( 3) <sup>b</sup>	(97) <sup>b</sup>	30	2.2
	56-57	0.0	0.82	26	4.2
	80-81	0.0	1.03	14	8.5
	161-162	0.0	0.95	18	6.1
PLEIADES 125 <sup>c</sup>	230-231	0.0	0.0	3.7	4.2
	88-90	0.0	14.3	--	--
PLEIADES 119 <sup>d</sup>	398-400	0.0	22.6	--	--
	110-111	0.0	12.4	--	--
BENTHIC 30 <sup>f</sup>	60-61	0.0	10.8	0.0	14

<sup>a</sup>Corrected for calcium carbonate.

<sup>b</sup>Values are percent of Quaternary plus Tertiary radiolarians, no estimates of radiolarians  $\cdot$  g $^{-1}$  are made.

<sup>c</sup>11° 03.0'N, 140° 03.1'W; 4801 m; 89.9% CaCO<sub>3</sub>; T. tuberosa Zone.

<sup>d</sup>11° 02.9'N, 140° 03.3'W; 4780 m; 90.0% CaCO<sub>3</sub>; S. delmontensis Zone.

<sup>e</sup>11° 01.16'N, 140° 05.56'W; 4909 m; 87.9% CaCO<sub>3</sub>; S. delmontensis Zone.

<sup>f</sup>11° 01.16'N, 140° 03.38'W; 4857 m; 60.5% CaCO<sub>3</sub>; C. tetrapera Zone.



## APPENDIX 4

Radionuclide determination (in  $\text{dpm}\cdot\text{g}^{-1}$ ) for core  
BENTHIC III 31 BC<sup>a</sup>

Depth cm	$^{230}\text{Th}$	$^{227}\text{Th}^b$
0.5 - 1.5	$187.6 \pm 1.0$	$4.68 \pm 0.13$
1.5 - 2.5	$299.5 \pm 1.6$	$7.33 \pm 0.20$
2.5 - 3.5	$176.6 \pm 0.8$	$3.88 \pm 0.10$
3.5 - 4.5	$348.7 \pm 1.6$	$7.39 \pm 0.19$
5 - 6	$21.8 \pm 0.3$	$0.62 \pm 0.05$
7 - 8	$8.0 \pm 0.2$	$0.18 \pm 0.04$
8 - 9	$5.1 \pm 0.2$	$0.01 \pm 0.04$

<sup>a</sup>Data provided by D. Kadko, Oregon State University.

<sup>b</sup>We assume  $^{227}\text{Th} = ^{231}\text{Pa}$ .